Advances in Sparse Array Signal Processing and its Applications 2022

Lead Guest Editor: Xiaofei Zhang
Guest Editors: Wang Zheng and Junpeng Shi

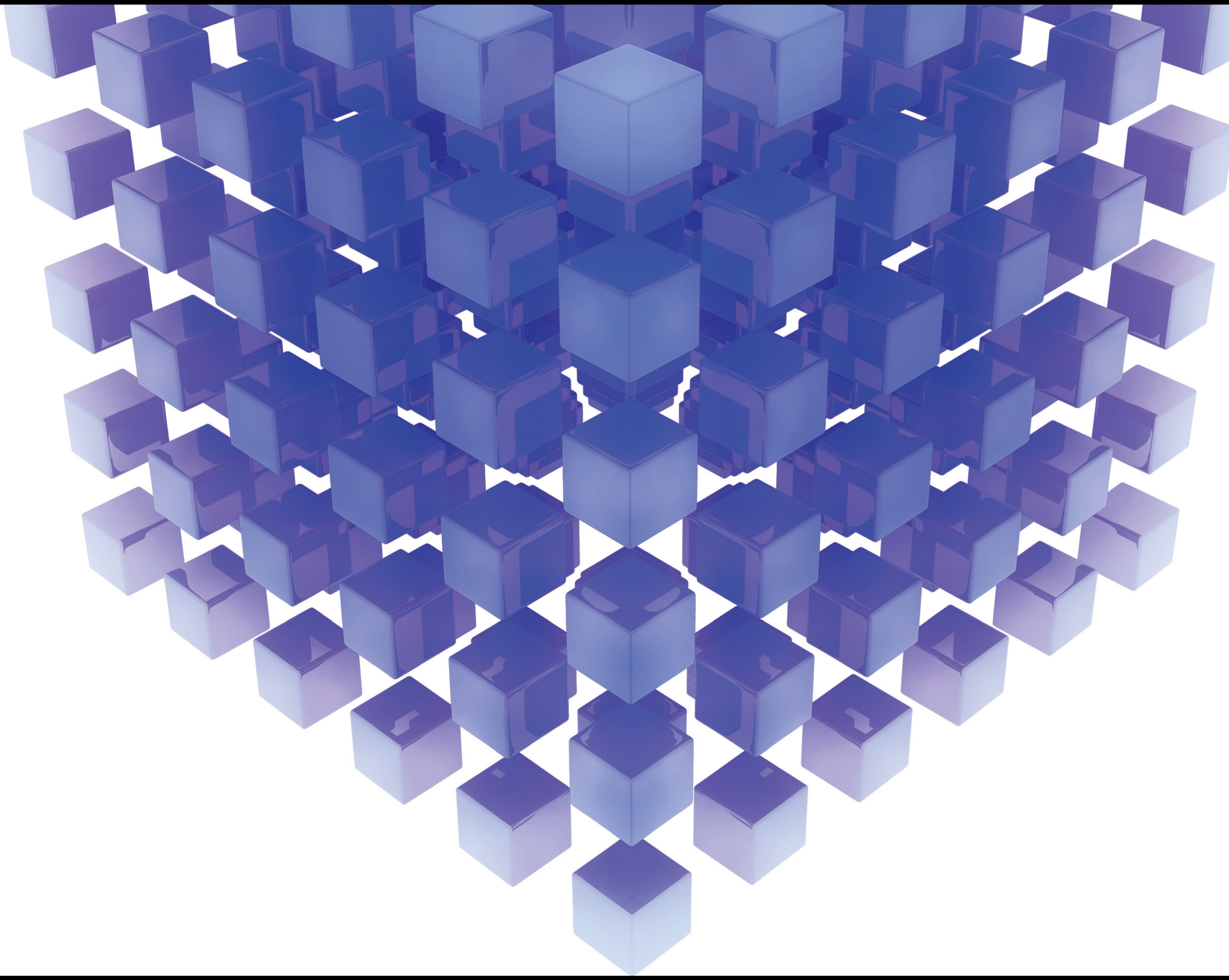

Advances in Sparse Array Signal Processing and its Applications 2022

Mathematical Problems in Engineering

Advances in Sparse Array Signal Processing and its Applications 2022

Lead Guest Editor: Xiaofei Zhang
Guest Editors: Wang Zheng and Junpeng Shi

Paolo Boscariol, Italy
Daniela Boso, Italy
Guillermo Botella-Juan, Spain
Abdesselem Boulkroune, Algeria
Boulaïd Boulkroune, Belgium
Fabio Bovenga, Italy
Francesco Braghin, Italy
Ricardo Branco, Portugal
Julien Bruchon, France
Matteo Bruggi, Italy
Michele Brun, Italy
Maria Elena Bruni, Italy
Maria Angela Butturi, Italy
Bartłomiej Błachowski, Poland
Dhanamjayulu C, India
Raquel Caballero-Águila, Spain
Filippo Cacace, Italy
Salvatore Caddemi, Italy
Zuowei Cai, China
Roberto Caldelli, Italy
Francesco Cannizzaro, Italy
Maosen Cao, China
Ana Carpio, Spain
Rodrigo Carvajal, Chile
Caterina Casavola, Italy
Sara Casciati, Italy
Federica Caselli, Italy
Carmen Castillo, Spain
Inmaculada T. Castro, Spain
Miguel Castro, Portugal
Giuseppe Catalanotti, United Kingdom
Alberto Cavallo, Italy
Gabriele Cazzulani, Italy
Fatih Vehbi Celebi, Turkey
Miguel Cerrolaza, Venezuela
Gregory Chagnon, France
Ching-Ter Chang, Taiwan
Kuei-Lun Chang, Taiwan
Qing Chang, USA
Xiaoheng Chang, China
Prasenjit Chatterjee, Lithuania
Kacem Chehdi, France
Peter N. Cheimets, USA
Chih-Chiang Chen, Taiwan
He Chen, China
Kebing Chen, China
Mengxin Chen, China
Shyi-Ming Chen, Taiwan
Xizhong Chen, Ireland
Xue-Bo Chen, China
Zhiwen Chen, China
Qiang Cheng, USA
Zeyang Cheng, China
Luca Chiapponi, Italy
Francisco Chicano, Spain
Tirivanhu Chinyoka, South Africa
Adrian Chmielewski, Poland
Seongim Choi, USA
Gautam Choubey, India
Hung-Yuan Chung, Taiwan
Yusheng Ci, China
Simone Cinquemani, Italy
Roberto G. Citarella, Italy
Joaquim Ciurana, Spain
John D. Clayton, USA
Piero Colajanni, Italy
Giuseppina Colicchio, Italy
Vassilios Constantoudis, Greece
Enrico Conte, Italy
Alessandro Contento, USA
Mario Cools, Belgium
Gino Cortellessa, Italy
Carlo Cosentino, Italy
Paolo Crippa, Italy
Erik Cuevas, Mexico
Guozeng Cui, China
Mehmet Cunkas, Turkey
Giuseppe D'Aniello, Italy
Peter Dabnichki, Australia
Weizhong Dai, USA
Zhifeng Dai, China
Purushothaman Damodaran, USA
Sergey Dashkovskiy, Germany
Adiel T. De Almeida-Filho, Brazil
Fabio De Angelis, Italy
Samuele De Bartolo, Italy
Stefano De Miranda, Italy
Filippo De Monte, Italy

José António Fonseca De Oliveira Correia, Portugal
Jose Renato De Sousa, Brazil
Michael Defoort, France
Alessandro Della Corte, Italy
Laurent Dewasme, Belgium
Sanku Dey, India
Gianpaolo Di Bona, Italy
Roberta Di Pace, Italy
Francesca Di Puccio, Italy
Ramón I. Diego, Spain
Yannis Dimakopoulos, Greece
Hasan Dinçer, Turkey
José M. Domínguez, Spain
Georgios Dounias, Greece
Bo Du, China
Emil Dumic, Croatia
Madalina Dumitriu, United Kingdom
Premraj Durairaj, India
Saeed Eftekhar Azam, USA
Said El Kafhali, Morocco
Antonio Elipe, Spain
R. Emre Erkmen, Canada
John Escobar, Colombia
Leandro F. F. Miguel, Brazil
FRANCESCO FOTI, Italy
Andrea L. Facci, Italy
Shahla Faisal, Pakistan
Giovanni Falsone, Italy
Hua Fan, China
Jianguang Fang, Australia
Nicholas Fantuzzi, Italy
Muhammad Shahid Farid, Pakistan
Hamed Faroqi, Iran
Yann Favennec, France
Fiorenzo A. Fazzolari, United Kingdom
Giuseppe Fedele, Italy
Roberto Fedele, Italy
Baowei Feng, China
Mohammad Ferdows, Bangladesh
Arturo J. Fernández, Spain
Jesus M. Fernandez Oro, Spain
Francesco Ferrise, Italy
Eric Feulvarch, France
Thierry Floquet, France
Eric Florentin, France
Gerardo Flores, Mexico
Antonio Forcina, Italy
Alessandro Formisano, Italy
Francesco Franco, Italy
Elisa Francomano, Italy
Juan Frausto-Solis, Mexico
Shujun Fu, China
Juan C. G. Prada, Spain
HECTOR GOMEZ, Chile
Matteo Gaeta, Italy
Mauro Gaggero, Italy
Zoran Gajic, USA
Jaime Gallardo-Alvarado, Mexico
Mosè Gallo, Italy
Akemi Gálvez, Spain
Maria L. Gandarias, Spain
Hao Gao, Hong Kong
Xingbao Gao, China
Yan Gao, China
Zhiwei Gao, United Kingdom
Giovanni Garcea, Italy
José García, Chile
Harish Garg, India
Alessandro Gasparetto, Italy
Stylianos Georgantzinos, Greece
Fotios Georgiades, India
Parviz Ghadimi, Iran
Ştefan Cristian Gherghina, Romania
Georgios I. Giannopoulos, Greece
Agathoklis Giaralis, United Kingdom
Anna M. Gil-Lafuente, Spain
Ivan Giorgio, Italy
Gaetano Giunta, Luxembourg
Jefferson L.M.A. Gomes, United Kingdom
Emilio Gómez-Déniz, Spain
Antonio M. Gonçalves de Lima, Brazil
Qunxi Gong, China
Chris Goodrich, USA
Rama S. R. Gorla, USA
Veena Goswami, India
Xunjie Gou, Spain
Jakub Grabski, Poland

George A. Papakostas, Greece
Xosé M. Pardo, Spain
You-Jin Park, Taiwan
Manuel Pastor, Spain
Pubudu N. Pathirana, Australia
Surajit Kumar Paul, India
Luis Payá, Spain
Igor Pažanin, Croatia
Libor Pekař, Czech Republic
Francesco Pellicano, Italy
Marcello Pellicciari, Italy
Jian Peng, China
Mingshu Peng, China
Xiang Peng, China
Xindong Peng, China
Yuexing Peng, China
Marzio Pennisi, Italy
Maria Patrizia Pera, Italy
Matjaz Perc, Slovenia
A. M. Bastos Pereira, Portugal
Wesley Peres, Brazil
F. Javier Pérez-Pinal, Mexico
Michele Perrella, Italy
Francesco Pesavento, Italy
Francesco Petrini, Italy
Hoang Vu Phan, Republic of Korea
Lukasz Pieczonka, Poland
Dario Piga, Switzerland
Marco Pizzarelli, Italy
Javier Plaza, Spain
Goutam Pohit, India
Dragan Poljak, Croatia
Jorge Pomares, Spain
Hiram Ponce, Mexico
Sébastien Poncet, Canada
Volodymyr Ponomaryov, Mexico
Jean-Christophe Ponsart, France
Mauro Pontani, Italy
Sivakumar Poruran, India
Francesc Pozo, Spain
Aditya Rio Prabowo, Indonesia
Anchasa Pramuanjaroenkij, Thailand
Leonardo Primavera, Italy
B Rajanarayan Prusty, India
Krzysztof Puszynski, Poland
Chuan Qin, China
Dongdong Qin, China
Jianlong Qiu, China
Giuseppe Quaranta, Italy
DR. RITU RAJ, India
Vitomir Racic, Italy
Carlo Rainieri, Italy
Kumbakonam Ramamani Rajagopal, USA
Ali Ramazani, USA
Angel Manuel Ramos, Spain
Higinio Ramos, Spain
Muhammad Afzal Rana, Pakistan
Muhammad Rashid, Saudi Arabia
Manoj Rastogi, India
Alessandro Rasulo, Italy
S.S. Ravindran, USA
Abdolrahman Razani, Iran
Alessandro Reali, Italy
Jose A. Reinoso, Spain
Oscar Reinoso, Spain
Haijun Ren, China
Carlo Renno, Italy
Fabrizio Renno, Italy
Shahram Rezapour, Iran
Ricardo Riaza, Spain
Francesco Riganti-Fulginei, Italy
Gerasimos Rigatos, Greece
Francesco Ripamonti, Italy
Jorge Rivera, Mexico
Eugenio Roanes-Lozano, Spain
Ana Maria A. C. Rocha, Portugal
Luigi Rodino, Italy
Francisco Rodríguez, Spain
Rosana Rodríguez López, Spain
Francisco Rossomando, Argentina
Jose de Jesus Rubio, Mexico
Weiguo Rui, China
Rubén Ruiz, Spain
Ivan D. Rukhlenko, Australia
Dr. Eswaramoorthi S., India
Weichao SHI, United Kingdom
Chaman Lal Sabharwal, USA
Andrés Sáez, Spain

Bekir Sahin, Turkey
Laxminarayan Sahoo, India
John S. Sakellariou, Greece
Michael Sakellariou, Greece
Salvatore Salamone, USA
Jose Vicente Salcedo, Spain
Alejandro Salcido, Mexico
Alejandro Salcido, Mexico
Nunzio Salerno, Italy
Rohit Salgotra, India
Miguel A. Salido, Spain
Sinan Salih, Iraq
Alessandro Salvini, Italy
Abdus Samad, India
Sovan Samanta, India
Nikolaos Samaras, Greece
Ramon Sancibrian, Spain
Giuseppe Sanfilippo, Italy
Omar-Jacobo Santos, Mexico
J Santos-Reyes, Mexico
José A. Sanz-Herrera, Spain
Musavarah Sarwar, Pakistan
Shahzad Sarwar, Saudi Arabia
Marcelo A. Savi, Brazil
Andrey V. Savkin, Australia
Tadeusz Sawik, Poland
Roberta Sburlati, Italy
Gustavo Scaglia, Argentina
Thomas Schuster, Germany
Hamid M. Sedighi, Iran
Mijanur Rahaman Seikh, India
Tapan Senapati, China
Lotfi Senhadji, France
Junwon Seo, USA
Michele Serpilli, Italy
Silvestar Šesnić, Croatia
Gerardo Severino, Italy
Ruben Sevilla, United Kingdom
Stefano Sfarra, Italy
Dr. Ismail Shah, Pakistan
Leonid Shaikhet, Israel
Vimal Shanmuganathan, India
Prayas Sharma, India
Bo Shen, Germany
Hang Shen, China
Xin Pu Shen, China
Dimitri O. Shepelsky, Ukraine
Jian Shi, China
Amin Shokrollahi, Australia
Suzanne M. Shontz, USA
Babak Shotorban, USA
Zhan Shu, Canada
Angelo Sifaleras, Greece
Nuno Simões, Portugal
Mehakpreet Singh, Ireland
Piyush Pratap Singh, India
Rajiv Singh, India
Seralathan Sivamani, India
S. Sivasankaran, Malaysia
Christos H. Skiadas, Greece
Konstantina Skouri, Greece
Neale R. Smith, Mexico
Bogdan Smolka, Poland
Delfim Soares Jr., Brazil
Alba Sofi, Italy
Francesco Soldovieri, Italy
Raffaele Solimene, Italy
Yang Song, Norway
Jussi Sopanen, Finland
Marco Spadini, Italy
Paolo Spagnolo, Italy
Ruben Specogna, Italy
Vasilios Spitas, Greece
Ivanka Stamova, USA
Rafał Stanisławski, Poland
Miladin Stefanović, Serbia
Salvatore Strano, Italy
Yakov Strelniker, Israel
Kangkang Sun, China
Qiuqin Sun, China
Shuaishuai Sun, Australia
Yanchao Sun, China
Zong-Yao Sun, China
Kumarasamy Suresh, India
Sergey A. Suslov, Australia
D.L. Suthar, Ethiopia
D.L. Suthar, Ethiopia
Andrzej Swierniak, Poland
Andras Szekrenyes, Hungary
Kumar K. Tamma, USA

Yong (Aaron) Tan, United Kingdom
Marco Antonio Taneco-Hernández, Mexico
Lu Tang, China
Tianyou Tao, China
Hafez Tari, USA
Alessandro Tasora, Italy
Sergio Teggi, Italy
Adriana del Carmen Téllez-Anguiano, Mexico
Ana C. Teodoro, Portugal
Efstathios E. Theotokoglou, Greece
Jing-Feng Tian, China
Alexander Timokha, Norway
Stefania Tomasiello, Italy
Gisella Tomasini, Italy
Isabella Torcicollo, Italy
Francesco Tornabene, Italy
Mariano Torrisi, Italy
Thang nguyen Trung, Vietnam
George Tsiatas, Greece
Le Anh Tuan, Vietnam
Nerio Tullini, Italy
Emilio Turco, Italy
Ilhan Tuzcu, USA
Efstratios Tzirtzilakis, Greece
FRANCISCO UREÑA, Spain
Filippo Ubertini, Italy
Mohammad Uddin, Australia
Mohammad Safi Ullah, Bangladesh
Serdar Ulubeyli, Turkey
Mati Ur Rahman, Pakistan
Panayiotis Vafeas, Greece
Giuseppe Vairo, Italy
Jesus Valdez-Resendiz, Mexico
Eusebio Valero, Spain
Stefano Valvano, Italy
Carlos-Renato Vázquez, Mexico
Martin Velasco Villa, Mexico
Franck J. Vernerey, USA
Georgios Veronis, USA
Vincenzo Vespri, Italy
Renato Vidoni, Italy
Venkatesh Vijayaraghavan, Australia
Anna Vila, Spain
Francisco R. Villatoro, Spain
Francesca Vipiana, Italy
Stanislav Vítek, Czech Republic
Jan Vorel, Czech Republic
Michael Vynnycky, Sweden
Mohammad W. Alomari, Jordan
Roman Wan-Wendner, Austria
Bingchang Wang, China
C. H. Wang, Taiwan
Dagang Wang, China
Guoqiang Wang, China
Huaiyu Wang, China
Hui Wang, China
J.G. Wang, China
Ji Wang, China
Kang-Jia Wang, China
Lei Wang, China
Qiang Wang, China
Qingling Wang, China
Weiwei Wang, China
Xinyu Wang, China
Yong Wang, China
Yung-Chung Wang, Taiwan
Zhenbo Wang, USA
Zhibo Wang, China
Waldemar T. Wójcik, Poland
Chi Wu, Australia
Qiuhong Wu, China
Yuqiang Wu, China
Zhibin Wu, China
Zhizheng Wu, China
Michalis Xenos, Greece
Hao Xiao, China
Xiao Ping Xie, China
Qingzheng Xu, China
Binghan Xue, China
Yi Xue, China
Joseph J. Yame, France
Chuanliang Yan, China
Xinggang Yan, United Kingdom
Hongtai Yang, China
Jixiang Yang, China
Mijia Yang, USA
Ray-Yeng Yang, Taiwan

Contents

Hindawi
Mathematical Problems in Engineering
Volume 2023, Article ID 7199603, 13 pages
https://doi.org/10.1155/2023/7199603

Research Article

Real-Valued Weighted Subspace Fitting Algorithm for DOA Estimation with Block Sparse Recovery

Liangliang Li,[1] Xianpeng Wang ,[1] Jinmei Shi,[2] and Xiang Lan[1]

[1]*State Key Laboratory of Marine Resource Utilization in South China Sea and School of Information and Communication Engineering, Hainan University, Haikou 570228, China*
[2]*College of Information Engineering, Hainan Vocational University of Science and Technology, Haikou 571158, China*

Correspondence should be addressed to Xianpeng Wang; wxpeng2016@hainanu.edu.cn

Received 5 April 2022; Accepted 26 May 2022; Published 12 January 2023

Academic Editor: Wang Zheng

In this paper, the problem of direction-of-arrival (DOA) estimation for strictly noncircular sources under the condition of unknown mutual coupling is concerned, and then a robust real-valued weighted subspace fitting (WSF) algorithm is proposed via block sparse recovery. Inspired by noncircularity, the real-valued coupled extended array output with double array aperture is first structured via exploiting the real-valued conversion. Then, an efficient real-valued block extended sparse recovery model is constructed by performing the parameterized decoupling operation to avoid the unknown mutual coupling and noncircular phase effects. Thereafter, the WSF framework is investigated to recover the real-valued block sparse matrix, where the spectrum of real-valued NC MUSIC-like is utilized to design a weighted matrix for strengthening the solutions sparsity. Eventually, DOA estimation is achieved based on the support set of the reconstructed block sparse matrix. Owing to the combination of noncircularity, parametrized decoupling thought, and reweighted strategy, the proposed method not only effectively achieves high-precision estimation, but also efficiently reduces the computational complexity. Plenty of simulation results demonstrate the effectiveness and efficiency of the proposed method.

1. Introduction

Thanks to the growing maturity of array signal processing technology, parameter estimation gradually occupies an important position in the fields of vehicle positioning, radar, medical diagnosis, and so on [1]. As one of the bases for parameter estimation, direction-of-arrival (DOA) estimation has been a hot topic for decades accompanied by a series of work [2–4]. Afterwards, benefiting from the increasing development of multiple-input multiple-output (MIMO) technique, MIMO radar architectures have been developed to provide high degrees of freedom (DOF) and resolution for DOA estimation [5]. Unfortunately, the distance between sensors decreases as the number of antennas increases for a fixed array aperture. It means that it is quite possible for closely-spaced sensors to suffer from the unknown mutual coupling effect. Thereby, it is worthwhile to study DOA estimation with strong robustness. In this way, this paper mainly investigates the robust DOA estimation of strictly noncircular sources with unknown mutual coupling.

Generally speaking, many DOA estimation attempts can be roughly divided into subspace-based methods [6–9] and sparse signal recovery (SSR) methods [10–13]. Multiple signal classification (MUSIC) method [6] uses the decoupled noise subspace to first achieve super-resolution direction finding, different from estimation of signal parameters via rotational invariance techniques (ESPRIT) algorithm [7] based on the decoupled signal subspace. It should be pointed out that these approaches have difficulty in achieving satisfactory performance under low signal-to-noise ratio (SNR), insufficient snapshots, or correlated sources. Thereafter, sparse recovery technique offers a feasible perspective to overcome these drawbacks, which can be categorized into norm optimization estimators [10, 11] and sparse Bayesian learning (SBL) approaches [12, 13]. Furthermore, it has been demonstrated that SSR algorithms are better than subspace-based methods in challenging circumstances, such as unsatisfactory SNR or inadequate snapshots [14].

It can be found that the above methods study circular signals by default. However, in recent years, DOA estimation of noncircular sources has received extensive attention in parameter estimation [15]. This is largely due to its wide distribution and natural superiorities. To the best of our knowledge, noncircular sources are commonly seen in practical communication systems [16], such as amplitude modulation (AM) and binary phase shift keying (BPSK). More importantly, noncircular sources can achieve higher accuracy and detect more targets than the default circular sources [17]. Subsequently, numerous algorithms [18–24] have been presented for noncircular sources that show the advantage in accuracy. On the one hand, there are lots of attempts achieved by subspace technology [18–20]. As shown in [18], noncircular MUSIC (NC MUSIC) algorithm is derived via combining noncircularity with MUSIC principle. Whereas, large-scale spectral peak search results in relatively high computational complexity. After that, noncircular root MUSIC (NC Root-MUSIC) approach [19] and noncircular conjugate ESPRIT (NC C-ESPRIT) algorithm [20] are introduced for tackling the above problem. On the other hand, DOA estimation for noncircular sources is implemented from the perspective of sparse reconstruction [21–24]. In [21, 22], the joint sparsity-aware schemes for array and monostatic MIMO radar system are put forward, respectively. With the in-depth research on sparsity, not only block sparsity but also rank sparsity are simultaneously utilized to model a nuclear norm penalty framework for enhancing the solutions sparsity [23]. Although this method has superiorities in estimation accuracy and resolution, it is computationally expensive. Thereby, a unitary nuclear norm minimization strategy [24] is further presented to reduce the computational complexity.

It is noted that the array manifolds of the above methods are normally assumed to be ideal. Nevertheless, such hypothesis may not be applicable to practice due to the existence of array manifold perturbations, like mutual coupling [25, 26]. It is generally believed that there may be unknown mutual coupling between closely-spaced antennas affected by the interaction of space electromagnetic fields [26]. This perturbation leads to undesired array manifold, thereby degrading or even invalidating the estimation performance of these approaches. Afterwards, a large number of calibration ideas are designed to deal with the problem of unknown mutual coupling [27–38].

For one thing, a series of calibrations [27–34] for circular sources have been attempted to estimate DOAs. In [27], the unknown mutual coupling is modeled as a complex band symmetric Toeplitz structure, and then additional auxiliary sensors are added to compensate. Similarly, the selection matrix is further designed by setting the antennas at both ends of the original array to be auxiliary sensors [28]. Unfortunately, these approaches can only maintain normal direction finding at the expense of array aperture. For preserving the array aperture as much as possible, the parameterized decoupling idea [29] is introduced to decouple the angle parameter and mutual coupling coefficients. Although this method uses whole data, its application scope is still limited because it belongs to subspace-based methods. Different from these efforts using subspace technology, relevant works [30–34] on sparse recovery have also been carried out. As introduced in [30], a revised l_1-SVD (singular value decomposition) algorithm is structured by designing a specific selection matrix in array. Analogously, the selection matrix is further implanted into the MIMO framework [31]. Actually, both the auxiliary sensors and the selection matrix can be regarded as two embodiments of array compensation. But they all sacrifice the array aperture. Aiming at this drawback, an effective block sparse recovery (BSR) approach [32] is presented by replacing array compensation with parameterized decoupling. Moreover, a reweighted BSR algorithm [33] and a weighted subspace fitting (WSF) method [34] are further reported for acquiring higher accuracy.

For another, some studies [35–40] on noncircular sources have been done to estimate DOAs. In [35], a selection matrix is first constructed to remove the negative influence so as to directly apply ESPRIT principle. Similar to [27, 28], it is achieved at the expense of array aperture. Subsequently, an efficient real-valued rank reduction method [36] using MUSIC principle is derived to effectively avoid the unknown mutual coupling effect and protect the precious array aperture. However, these methods are still subject to the limitations of subspace technology, unlike robust SSR algorithms. In view of this shortcoming, the joint reweighted sparsity-inducing scheme based on SVD principle [37] and WSF principle [38] are put forward, respectively. Whereas, their computational complexity is relatively higher than that of subspace-based methods in [35, 36].

In this work, an efficient real-valued WSF algorithm with block sparse recovery is presented for DOA estimation of strictly noncircular sources under unknown mutual coupling. First, a real-valued block extended sparse recovery model is formed to avoid the unknown mutual coupling and noncircular phase effects. Subsequently, the regularization framework between sparsity penalty and subspace fitting error is investigated. Finally, a real-valued reweighted block sparse recovery approach is explored to achieve WSF for DOA estimation. The proposed method effectively maintains high accuracy and efficiently reduces the computational load. The simulation results confirm the correctness of the above deduce.

The main contributions of the proposed method are summarized as follows:

(a) Perform a real-valued conversion to reduce the computational burden, and then construct a real-valued coupled extended data by exploiting noncircularity.

(b) Eliminate the unknown mutual coupling and noncircular phase interferences through parameterized decoupling operation without array aperture loss.

(c) Structure a real-valued noncircular MUSIC-like (NC MUSIC-like) weighted matrix to enhance the solutions sparsity.

Table 1: Some important notations.

Notations	Definitions
$(\cdot)^T$, $(\cdot)^*$ and $(\cdot)^H$	Transpose, conjugate, and conjugate-transpose operations
$(\cdot)^\dagger$ and $\lvert\cdot\rvert$	Pseudo-inverse and absolute value operations
$\mathrm{Re}[\cdot]$ and $\mathrm{Im}[\cdot]$	Real and imaginary part operations
$\mathbf{0}_{M\times K}$	$M\times K$ dimensional zero matrix
$\mathbf{I}_M$	$M\times M$ dimensional identity matrix
$\mathrm{diag}\{\cdot\}$ and $\mathrm{blkdiag}\{\cdot\}$	Diagonalization and block diagonalization operations
$\mathbf{E}\{\cdot\}$	Mathematical expectation operation
$\mathrm{tr}\{\cdot\}$ and $\det\{\cdot\}$	Trace and determinant operations
$\lVert\cdot\rVert_0$, $\lVert\cdot\rVert_1$, and $\lVert\cdot\rVert_2$	l_0-norm, l_1-norm, and l_2-norm
$\lVert\cdot\rVert_F$	Frobenius norm

(d) Develop a robust real-valued WSF framework to estimate DOAs by block sparse recovery.

It is noted that some important notations adopted in this article are defined in Table 1.

2. Data Model for DOA Estimation

2.1. Problem Formulation. Suppose that K far-field uncorrelated narrowband NC sources $\{s_{d,k}\}_{k=1}^{K}$ incident on a uniform linear array (ULA) equipped with M omnidirectional antennas. The distinct DOAs can be denoted as $\boldsymbol{\theta} = [\theta_1, \theta_2, \ldots, \theta_K]$. Then, the array output in the ideal environment can be structured as

$$\mathbf{x}(t) = \mathbf{A}\mathbf{s}_d(t) + \mathbf{n}(t), \tag{1}$$

where $\mathbf{x}(t) = [x_1(t), x_2(t), \ldots, x_M(t)]^{\mathrm{T}} \in \mathbb{C}^{M\times 1}$ is the received data. $\mathbf{n}(t) = [n_1(t), n_2(t), \ldots, n_M(t)]^{\mathrm{T}} \in \mathbb{C}^{M\times 1}$ stands for the complex additive Gaussian white noise vector with zero mean. Meanwhile, $\mathbf{s}_d(t) = [s_{d,1}(t), s_{d,2}(t), \ldots, s_{d,K}(t)]^{\mathrm{T}} \in \mathbb{C}^{K\times 1}$ means the noncircular signal vector. $\mathbf{A} = [\mathbf{a}(\theta_1), \mathbf{a}(\theta_2), \ldots, \mathbf{a}(\theta_K)] \in \mathbb{C}^{M\times K}$ indicates the ideal array manifold matrix. As the k th column of matrix $\mathbf{A}$, $\mathbf{a}(\theta_k)$ is known as array manifold corresponding to k th target and satisfies $\mathbf{a}(\theta_k) = [1, \rho(\theta_k), \ldots, \rho^{M-1}(\theta_k)]^{\mathrm{T}} \in \mathbb{C}^{M\times 1}$, where $\rho(\theta_k) = e^{j\nu(\theta_k)}$ with $\nu(\theta_k) = -2\pi\, d/\lambda_n \sin(\theta_k)$. d represents the distance between adjacent antennas and λ_n denotes the signal wavelength. Obviously, the data model in (1) is not affected by any array manifold perturbations, such as mutual coupling [37] and gain-phase error [9]. Unfortunately, as the number of antennas increases, the distance between sensors decreases. Hence, due to the fact that space electromagnetic field interacts with each other, closely-spaced antennas are vulnerable to unknown mutual coupling, as illustrated in Figure 1.

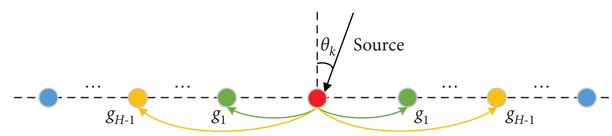

Figure 1: Mutual coupling model of ULA.

It has been demonstrated that the mutual coupling coefficients between antennas are inversely proportional to their spacing. That is to say, the larger the sensors spacing, the weaker the mutual coupling effect, and the smaller the corresponding coefficients. Moreover, when the antennas are far enough away from each other, it is reasonable to ignore the impact of unknown mutual coupling. Then, a structure of complex banded symmetric Toeplitz in [27] is utilized to model the mutual coupling matrix (MCM), i.e.,

$$\mathbf{G} = \mathrm{Toeplitz}\Big(\big[1, g_1, \ldots, g_{H-1}, \mathbf{0}_{1\times(M-H)}\big]\Big) = \begin{bmatrix} 1 & g_1 & \cdots & g_{H-1} & & & & & \\ g_1 & 1 & g_1 & \cdots & g_{H-1} & & \mathbf{0} & & \\ \vdots & \ddots & \ddots & \ddots & \ddots & \ddots & & & \\ g_{H-1} & \cdots & g_1 & 1 & g_1 & \cdots & g_{H-1} & & \\ & \ddots & \vdots & \ddots & \ddots & \ddots & \ddots & \ddots & \\ & & g_{H-1} & \cdots & g_1 & 1 & g_1 & \cdots & g_{H-1} \\ & \mathbf{0} & & \ddots & \vdots & \ddots & \ddots & \ddots & \vdots \\ & & & & g_{H-1} & \cdots & g_1 & 1 & g_1 \\ & & & & & g_{H-1} & \cdots & g_1 & 1 \end{bmatrix}, \tag{2}$$

where $\{g_c\}_{c=1}^{H-1}$ refer to the unknown nonzero mutual coupling coefficients, whose c th element $g_c = \lambda_c e^{j\varphi_c}$ is made up of amplitude coefficient λ_c and phase coefficient φ_c, respectively. It can be clearly seen that there are H nonzero mutual coupling coefficients, which satisfy $0 < |g_{H-1}| < |g_{H-2}| <, \ldots, < |g_2| < |g_1| < |g_0| = 1$. Then, the

(1) **Input:** The actual received signal $\mathbf{y}(t)$ in (6);
(2) Extract the real and imaginary parts of $\mathbf{y}(t)$ based on (7) and (8) to formulate the real-valued coupled extended array output $\mathbf{y}_{RI}(t)$ in (10);
(3) Calculate the sampling covariance matrix $\mathbf{R}$ of $\mathbf{y}_{RI}(t)$ by (13);
(4) Perform eigenvalue decomposition on $\mathbf{R}$ to acquire the signal subspace $\mathbf{E}_s$ and the noise subspace $\mathbf{E}_n$ in (14);
(5) Construct the optimal weighted matrix $\mathbf{W}_{\text{opt}}$ according to (14);
(6) Form the over-complete dictionary $\overline{\mathbf{A}}_{RI}$ in (26) by sparsely representing $\overline{\mathbf{T}}(\theta_k)$ of $\widehat{\mathbf{A}}_{RI}$ in (21) to develop a sparse representation model in (27);
(7) Structure the real-valued NC MUSIC-like weighted matrix $\mathbf{D}$ adopting (33) to enhance the solutions sparsity;
(8) Design the reweighted regularized framework based on WSF principle in (35);
(9) **Output:** The reconstructed real-valued sparse vector $\mathbf{r}^{l_2}$;
(10) Perform a 1-D spectrum search to find the K maximum values for DOA estimation.

Algorithm 1: Real-valued weighted subspace fitting algorithm with block sparse recovery.

ideal array manifold is affected by the unknown mutual coupling in antennas, which should be revised as

$$\hat{\mathbf{a}}(\theta_k) = \mathbf{G}\mathbf{a}(\theta_k). \tag{3}$$

Thereby, the practical array output under the condition of unknown mutual coupling can be written as

$$\mathbf{y}(t) = \mathbf{G}\mathbf{A}\mathbf{s}_d(t) + \mathbf{n}(t), \tag{4}$$

where $\mathbf{y}(t) = [y_1(t), y_2(t), \ldots, y_M(t)]^{\mathbf{T}} \in \mathbb{C}^{M\times 1}$ represents the actual received data disturbed by unknown mutual coupling, unlike $\mathbf{x}(t)$ in (1).

According to the above introduction, $\mathbf{s}_d(t)$ denotes the noncircular source, which means that its noncircular rate ξ ranges from 0 to 1, including the upper limit [38]. When referring to the maximum noncircular rate $\xi = 1$, the radiation signal can be defined as the strictly noncircular source, like AM modulation signal. In this paper, strictly noncircular sources are considered. It has revealed in [22] that the complex strictly NC source $\mathbf{s}_d(t)$ in (4) can be further expressed as

$$\mathbf{s}_d(t) = \mathbf{\Phi}\mathbf{s}(t), \tag{5}$$

where $\mathbf{\Phi} = \operatorname{diag}(e^{j\phi_1}, e^{j\phi_2}, \ldots, e^{j\phi_K}) \in \mathbb{C}^{K\times K}$ stands for the rotation phase shift matrix corresponding to $\boldsymbol{\phi} = [\phi_1, \phi_2, \ldots, \phi_K]$, which can be arbitrary for each source. $\mathbf{s}(t) = [s_1(t), s_2(t), \ldots, s_K(t)]^{\mathbf{T}} \in \mathbb{R}^{K\times 1}$ is the real-valued signal vector corresponding to the complex-valued vector $\mathbf{s}_d(t)$. In this way, taking (5) back to (4), the actual array output can be represented as

$$\mathbf{y}(t) = \mathbf{G}\mathbf{A}\mathbf{s}_d(t) + \mathbf{n}(t) = \mathbf{G}\mathbf{A}\mathbf{\Phi}\mathbf{s}(t) + \mathbf{n}(t). \tag{6}$$

2.2. Real-Valued Conversion for Noncircular Sources. In view of the noncircularity advantages, many researches on noncircular sources directly construct the extended signal model achieved by the received data and its conjugate form. However, the data belongs to the complex domain, which inevitably leads to the high computational burden. Different from the above classical processing in the complex domain, a real-valued conversion is first applied to the received data for structuring an extended data model in the real domain [36]. Thanks to the real-valued transformation, the computation load is greatly reduced to accelerate the direction finding speed. Then, following the idea in [36], the real and imaginary parts of the actual array output can be extracted as

$$\begin{aligned}\mathbf{y}_R(t) &= \operatorname{Re}[\mathbf{y}(t)] \\ &= \frac{[\mathbf{y}(t) + \mathbf{y}^*(t)]}{2} \\ &= \left[\frac{(\mathbf{G}\mathbf{A}\mathbf{\Phi} + \mathbf{G}^*\mathbf{A}^*\mathbf{\Phi}^*)}{2}\right]\mathbf{s}(t) + \operatorname{Re}[\mathbf{n}(t)] \\ &= \mathbf{A}_R\mathbf{s}(t) + \mathbf{n}_R(t),\end{aligned} \tag{7}$$

$$\begin{aligned}\mathbf{y}_I(t) &= \operatorname{Im}[\mathbf{y}(t)] \\ &= \frac{[\mathbf{y}(t) - \mathbf{y}^*(t)]}{2j} \\ &= \left[\frac{(\mathbf{G}\mathbf{A}\mathbf{\Phi} - \mathbf{G}^*\mathbf{A}^*\mathbf{\Phi}^*)}{2j}\right]\mathbf{s}(t) + \operatorname{Im}[\mathbf{n}(t)] \\ &= \mathbf{A}_I\mathbf{s}(t) + \mathbf{n}_I(t),\end{aligned} \tag{8}$$

where $\mathbf{n}_R(t) \in \mathbb{R}^{M\times 1}$ and $\mathbf{n}_I(t) \in \mathbb{R}^{M\times 1}$ express the real and imaginary components achieved by the complex noise vector $\mathbf{n}(t) \in \mathbb{C}^{M\times 1}$. $\mathbf{A}_R = [\mathbf{a}_R(\theta_1, \phi_1, \mathbf{G}), \mathbf{a}_R(\theta_2, \phi_2, \mathbf{G}), \ldots, \mathbf{a}_R(\theta_K, \phi_K, \mathbf{G})] \in \mathbb{R}^{M\times K}$ and $\mathbf{A}_I = [\mathbf{a}_I(\theta_1, \phi_1, \mathbf{G}), \mathbf{a}_I(\theta_2, \phi_2, \mathbf{G}), \ldots, \mathbf{a}_I(\theta_K, \phi_K, \mathbf{G})] \in \mathbb{R}^{M\times K}$ are the virtual coupled array manifold matrices of $\mathbf{y}_R(t)$ and $\mathbf{y}_I(t)$, respectively. Moreover, as one of the columns in $\mathbf{A}_R$ and $\mathbf{A}_I$, $\mathbf{a}_R(\theta, \phi, \mathbf{G})$ and $\mathbf{a}_I(\theta, \phi, \mathbf{G})$ simultaneously contain the unknown mutual coupling coefficients and noncircular phase. They can be represented as

$$\begin{aligned}\mathbf{a}_R(\theta, \phi, \mathbf{G}) &= \frac{\left(\mathbf{G}\mathbf{a}(\theta)e^{j\phi} + \mathbf{G}^*\mathbf{A}^*(\theta)e^{-j\phi}\right)}{2}, \\ \mathbf{a}_I(\theta, \phi, \mathbf{G}) &= \frac{\left(\mathbf{G}\mathbf{a}(\theta)e^{j\phi} - \mathbf{G}^*\mathbf{A}^*(\theta)e^{-j\phi}\right)}{2j}.\end{aligned} \tag{9}$$

Combining (7) and (8), a real-valued coupled extended signal model can be designed as

$$\begin{aligned}\mathbf{y}_{RI}(t) &= \begin{bmatrix}\mathbf{y}_R(t)\\ \mathbf{y}_I(t)\end{bmatrix}\\ &= \begin{bmatrix}\mathbf{A}_R\\ \mathbf{A}_I\end{bmatrix}\mathbf{s}(t) + \begin{bmatrix}\mathbf{n}_R(t)\\ \mathbf{n}_I(t)\end{bmatrix}\\ &= \mathbf{A}_{RI}\mathbf{s}(t) + \mathbf{n}_{RI}(t),\end{aligned} \tag{10}$$

where $\mathbf{A}_{RI} = [\mathbf{a}_{RI}(\theta_1, \phi_1, \mathbf{G}), \mathbf{a}_{RI}(\theta_2, \phi_2, \mathbf{G}), \ldots, \mathbf{a}_{RI}(\theta_K, \phi_K, \mathbf{G})] \in \mathbb{R}^{2M\times K}$ is the real-valued coupled extended steering matrix. Each column in $\mathbf{A}_{RI}$ denotes the coupled extended array manifold and takes the following structure:

$$\mathbf{a}_{RI}(\theta, \phi, \mathbf{G}) = \begin{bmatrix}\mathbf{a}_R(\theta, \phi, \mathbf{G})\\ \mathbf{a}_I(\theta, \phi, \mathbf{G})\end{bmatrix}. \tag{11}$$

Then, the covariance matrix of $\mathbf{y}_{RI}(t)$ can be written as

$$\hat{\mathbf{R}} = \mathrm{E}\left\{\mathbf{y}_{RI}(t)\mathbf{y}_{RI}^H(t)\right\} = \mathbf{A}_{RI}\mathbf{R}_s\mathbf{A}_{RI}^H + \sigma^2\mathbf{I}_{2M}, \tag{12}$$

where σ^2 expresses the corresponding noise power. $\mathbf{R}_s = \mathrm{E}\{\mathbf{s}(t)\mathbf{s}^H(t)\}$ indicates the signal covariance matrix, whose rank K' rests with the source correlation. This paper assumes $K' = K$ because of the uncorrelated sources presupposition. In fact, $\hat{\mathbf{R}}$ can only be obtained when the number of snapshots approaches infinity. However, it is clearly unavailable and eventually replaced by its maximum likelihood estimation $\mathbf{R}$ in reality. $\mathbf{R}$ can be computed by finite snapshots T, which takes the following form:

$$\mathbf{R} = \frac{1}{T}\sum_{t=1}^{T}\mathbf{y}_{RI}(t)\mathbf{y}_{RI}^H(t), \tag{13}$$

where $\mathbf{R}$ refers to the sampling covariance matrix. Then, applying eigenvalue decomposition to $\mathbf{R}$, yields

$$\mathbf{R} = \sum_{m=1}^{2M}\lambda_m\boldsymbol{\delta}_m\boldsymbol{\delta}_m^H = \mathbf{E}_s\boldsymbol{\Omega}_s\mathbf{E}_s^H + \mathbf{E}_n\boldsymbol{\Omega}_n\mathbf{E}_n^H, \tag{14}$$

where $\{\lambda_m\}_{m=1}^{2M}$ mean the eigenvalues and satisfy $\lambda_1 \geq \lambda_2 \geq, \ldots, \geq \lambda_K > \lambda_{K+1} =, \ldots, = \lambda_{2M}$. $\{\boldsymbol{\delta}_m\}_{m=1}^{2M}$ are the eigenvectors corresponding to the eigenvalues $\{\lambda_m\}_{m=1}^{2M}$. What is more, K larger eigenvalues and their corresponding eigenvectors are utilized to formulate the diagonal matrix $\boldsymbol{\Omega}_s$ and the signal subspace $\mathbf{E}_s$, respectively, i.e., $\boldsymbol{\Omega}_s = \mathrm{diag}\{\lambda_1, \lambda_2, \ldots, \lambda_K\} \in \mathbb{R}^{K\times K}$ and $\mathbf{E}_s = [\boldsymbol{\delta}_1, \boldsymbol{\delta}_2, \ldots, \boldsymbol{\delta}_K] \in \mathbb{R}^{2M\times K}$. In like manner, the diagonal matrix $\boldsymbol{\Omega}_n = \mathrm{diag}\{\lambda_{K+1}, \lambda_{K+2}, \ldots, \lambda_{2M}\} \in \mathbb{R}^{(2M-K)\times(2M-K)}$ and the noise subspace $\mathbf{E}_n = [\boldsymbol{\delta}_{K+1}, \boldsymbol{\delta}_{K+2}, \ldots, \boldsymbol{\delta}_{2M}] \in \mathbb{R}^{2M\times(2M-K)}$ are composed of $2M - K$ smaller eigenvalues and the corresponding eigenvectors [38].

As introduced in [39], the steering matrix spans the same range subspace as the signal subspace. Similarly, the signal subspace $\mathbf{E}_s$ lies in the range space of the real-valued coupled extended steering matrix $\mathbf{A}_{RI}$, which indicates that $\mathbf{E}_s$ and $\mathbf{A}_{RI}$ satisfy

$$\mathbf{E}_s = \mathbf{A}_{RI}\mathbf{U}. \tag{15}$$

where $\mathbf{U}$ denotes a column full rank matrix with $K \times K$ dimension. Unfortunately, it is hard for (15) to estimate $\mathbf{U}$ due to the coexistence of unknown parameters, such as mutual coupling coefficients and noncircular phase. Thereby, a robust estimator should be designed to overcome these disturbances.

2.3. Parameterized Decoupling Operation.

It is noted that the real-valued coupled extended array manifold in (11) is affected by unknown mutual coupling and noncircular phase, resulting in the failure of many existing ideal direction finding algorithms. Inspired by [36], the parameterized decoupling thought in the real domain is exploited to deal with the above problem.

Through parameterizing the virtual coupled array manifolds $\mathbf{a}_R(\theta, \phi, \mathbf{G})$ and $\mathbf{a}_I(\theta, \phi, \mathbf{G})$, yields

$$\begin{aligned}\mathbf{a}_R(\theta, \phi, \mathbf{G}) &= \frac{\left(\mathbf{G}\mathbf{a}(\theta)e^{j\phi} + \mathbf{G}^*\mathbf{a}^*(\theta)e^{-j\phi}\right)}{2}\\ &= \overset{\frown}{\boldsymbol{\Psi}}(\theta, \phi, \mathbf{G})\overset{\frown}{\mathbf{T}}(\theta)\overset{\frown}{\boldsymbol{\Sigma}}(\theta, \phi, \mathbf{G}) - \breve{\boldsymbol{\Psi}}(\theta, \phi, \mathbf{G})\breve{\mathbf{T}}(\theta)\breve{\boldsymbol{\Sigma}}(\theta, \phi, \mathbf{G}),\end{aligned} \tag{16}$$

$$\begin{aligned}\mathbf{a}_I(\theta, \phi, \mathbf{G}) &= \frac{\left(\mathbf{G}\mathbf{a}(\theta)e^{j\phi} - \mathbf{G}^*\mathbf{a}^*(\theta)e^{-j\phi}\right)}{2j}\\ &= \breve{\boldsymbol{\Psi}}(\theta, \phi, \mathbf{G})\overset{\frown}{\mathbf{T}}(\theta)\breve{\boldsymbol{\Sigma}}(\theta, \phi, \mathbf{G}) + \overset{\frown}{\boldsymbol{\Psi}}(\theta, \phi, \mathbf{G})\breve{\mathbf{T}}(\theta)\overset{\frown}{\boldsymbol{\Sigma}}(\theta, \phi, \mathbf{G}),\end{aligned} \tag{17}$$

where

$$\widehat{\mathbf{T}}(\theta)=\begin{bmatrix}1 & & & & & & \\ & \cos(\nu(\theta)) & & & & \mathbf{0} & \\ & & \ddots & & & & \\ & & & \cos((H-1)\nu(\theta)) & & & \\ & & & \vdots & & & \\ & \mathbf{0} & & \cos((M-H)\nu(\theta)) & & & \\ & & & & \ddots & & \\ & & & & & & \cos((M-1)\nu(\theta))\end{bmatrix},$$

$$\breve{\mathbf{T}}(\theta)=\begin{bmatrix}0 & & & & & & \\ & \sin(\nu(\theta)) & & & & \mathbf{0} & \\ & & \ddots & & & & \\ & & & \sin((H-1)\nu(\theta)) & & & \\ & & & \vdots & & & \\ & \mathbf{0} & & \sin((M-H)\nu(\theta)) & & & \\ & & & & \ddots & & \\ & & & & & & \sin((M-1)\nu(\theta))\end{bmatrix}, \tag{18}$$

$$\widehat{\Psi}(\theta,\phi,\mathbf{G})=\sum_{c=1-H}^{H-1}\lambda_{|c|}\cos\left(\varphi_{|c|}+\phi+c\cdot\nu(\theta)\right),$$

$$\breve{\Psi}(\theta,\phi,\mathbf{G})=\sum_{c=1-H}^{H-1}\lambda_{|c|}\sin\left(\varphi_{|c|}+\phi+c\cdot\nu(\theta)\right),$$

$$\widehat{\boldsymbol{\Sigma}}(\theta,\phi,\mathbf{G})=\left[\widehat{\tau}_1(\theta),\ldots,\widehat{\tau}_{H-1}(\theta),1,\widehat{\sigma}_1(\theta),\ldots,\widehat{\sigma}_{H-1}(\theta)\right]^T,$$

$$\breve{\boldsymbol{\Sigma}}(\theta,\phi,\mathbf{G})=\left[\breve{\tau}_1(\theta),\ldots,\breve{\tau}_{H-1}(\theta),1,\breve{\sigma}_1(\theta),\ldots,\breve{\sigma}_{H-1}(\theta)\right]^T,$$

$$\widehat{\tau}_h(\theta)=\frac{\widehat{\Psi}(\theta,\phi,\mathbf{G})-\sum_{c=h}^{H-1}\lambda_c\cos\left(\varphi_c+\phi-c\cdot\nu(\theta)\right)}{\widehat{\Psi}(\theta,\phi,\mathbf{G})},$$

$$\breve{\tau}_h(\theta)=\frac{\breve{\Psi}(\theta,\phi,\mathbf{G})-\sum_{c=h}^{H-1}\lambda_c\sin\left(\varphi_c+\phi-c\cdot\nu(\theta)\right)}{\breve{\Psi}(\theta,\phi,\mathbf{G})},$$

$$\widehat{\sigma}_h(\theta)=\frac{\widehat{\Psi}(\theta,\phi,\mathbf{G})-\sum_{c=H-h}^{H-1}\lambda_c\cos\left(\varphi_c+\phi+c\cdot\nu(\theta)\right)}{\widehat{\Psi}(\theta,\phi,\mathbf{G})},$$

$$\breve{\sigma}_h(\theta)=\frac{\breve{\Psi}(\theta,\phi,\mathbf{G})-\sum_{c=H-h}^{H-1}\lambda_c\sin\left(\varphi_c+\phi+c\cdot\nu(\theta)\right)}{\breve{\Psi}(\theta,\phi,\mathbf{G})},$$

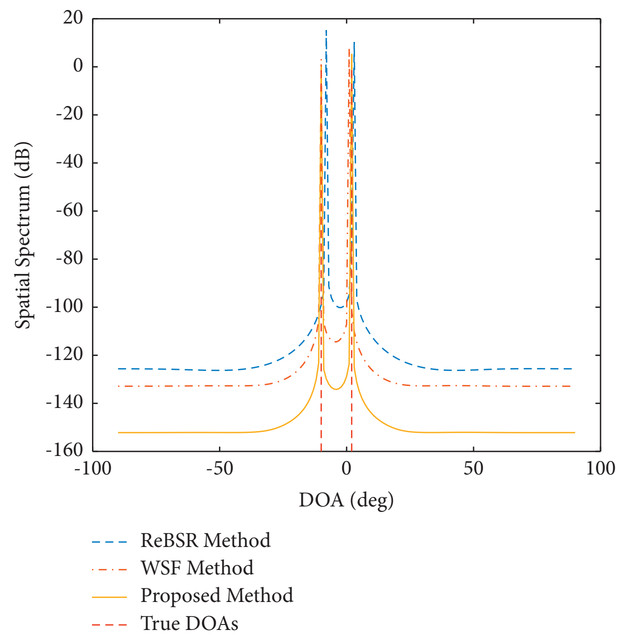

FIGURE 2: The spatial spectra for all methods.

where $h = 1, 2, \ldots, H-1$. $\widehat{\mathbf{T}}(\theta) \in \mathbb{R}^{M\times(2H-1)}$ and $\breve{\mathbf{T}}(\theta) \in \mathbb{R}^{M\times(2H-1)}$ are the real-valued block matrices and only depend on angle information. For briefness, $F = 2H-1$ is defined in what follows.

It is worth emphasizing that $\widehat{\Psi}(\theta, \phi, \mathbf{G})$ and $\breve{\Psi}(\theta, \phi, \mathbf{G})$ stand for two constants. They rely on three parameters, i.e., angle parameter, mutual coupling coefficients, and noncircular phase. Additionally, $\widehat{\Psi}(\theta, \phi, \mathbf{G}) \neq 0$ and $\breve{\Psi}(\theta, \phi, \mathbf{G}) \neq 0$ occur with extremely high probability except for a few very special circumstances. Thereby, this article defaults $\widehat{\Psi}(\theta, \phi, \mathbf{G}) \neq 0$ and $\breve{\Psi}(\theta, \phi, \mathbf{G}) \neq 0$.

Then, bringing (16) and (17) back to (11), $\mathbf{a}_{RI}(\theta, \phi, \mathbf{G}) \in \mathbb{R}^{2M\times 1}$ can be decoupled as

$$\begin{aligned}
\mathbf{a}_{RI}(\theta, \varphi, \mathbf{G}) &= \begin{bmatrix} \mathbf{a}_R(\theta, \varphi, \mathbf{G}) \\ \mathbf{a}_I(\theta, \varphi, \mathbf{G}) \end{bmatrix} \\
&= \begin{bmatrix} \widehat{\Psi}(\theta, \varphi, \mathbf{G})\widehat{\mathbf{T}}(\theta)\widehat{\boldsymbol{\Sigma}}(\theta, \varphi, \mathbf{G}) - \breve{\Psi}(\theta, \varphi, \mathbf{G})\breve{\mathbf{T}}(\theta)\breve{\boldsymbol{\Sigma}}(\theta, \varphi, \mathbf{G}) \\ \breve{\Psi}(\theta, \varphi, \mathbf{G})\widehat{\mathbf{T}}(\theta)\breve{\boldsymbol{\Sigma}}(\theta, \varphi, \mathbf{G}) + \widehat{\Psi}(\theta, \varphi, \mathbf{G})\breve{\mathbf{T}}(\theta)\widehat{\boldsymbol{\Sigma}}(\theta, \varphi, \mathbf{G}) \end{bmatrix}, \\
&= \underbrace{\begin{bmatrix} \widehat{\mathbf{T}}(\theta) & -\breve{\mathbf{T}}(\theta) \\ \breve{\mathbf{T}}(\theta) & \widehat{\mathbf{T}}(\theta) \end{bmatrix}}_{\overline{\mathbf{T}}(\theta)} \underbrace{\begin{bmatrix} \widehat{\Psi}(\theta, \varphi, \mathbf{G})\widehat{\boldsymbol{\Sigma}}(\theta, \varphi, \mathbf{G}) \\ \breve{\Psi}(\theta, \varphi, \mathbf{G})\breve{\boldsymbol{\Sigma}}(\theta, \varphi, \mathbf{G}) \end{bmatrix}}_{\boldsymbol{\Lambda}(\theta,\varphi,\mathbf{G})}
\end{aligned} \tag{19}$$

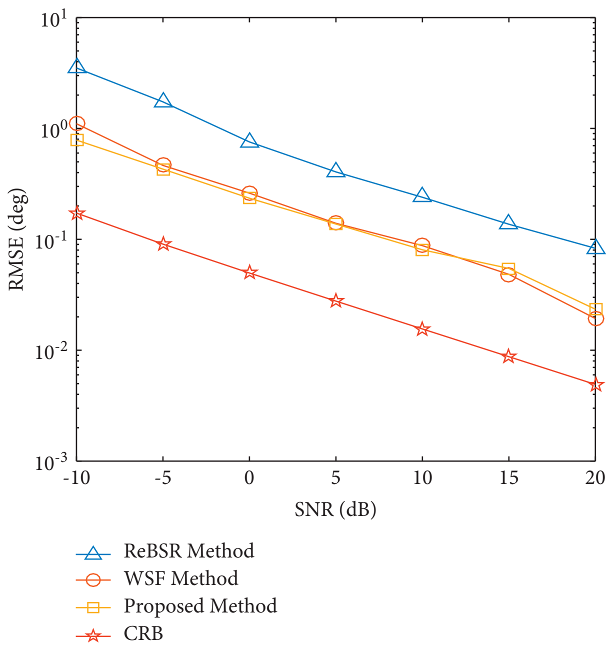

Figure 3: RMSE versus SNR for all methods.

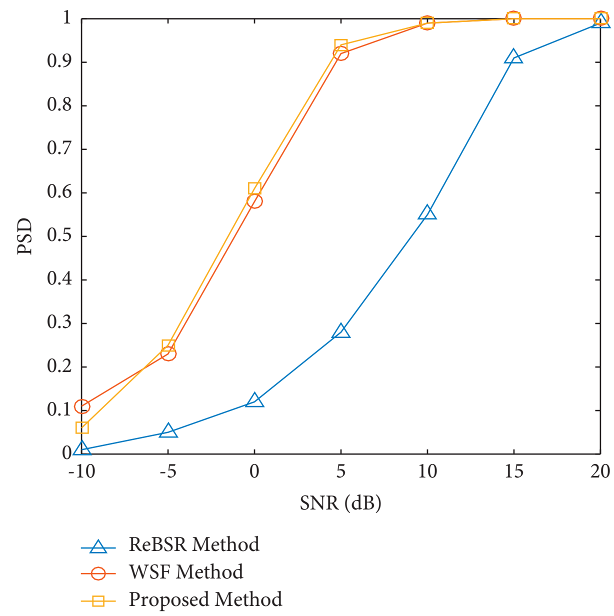

Figure 4: PSD versus SNR for all methods.

where $\overline{\mathbf{T}}(\theta) \in \mathbb{R}^{2M\times 2F}$ and $\boldsymbol{\Lambda}(\theta,\phi,\mathbf{G}) \in \mathbb{R}^{2F\times 1}$ are block matrix and block vector, respectively. It can be discovered that the real-valued coupled extended array manifold $\mathbf{a}_{RI}(\theta,\phi,\mathbf{G}) \in \mathbb{R}^{2M\times 1}$ is decoupled into two parts: $\overline{\mathbf{T}}(\theta)$ and $\boldsymbol{\Lambda}(\theta,\phi,\mathbf{G})$. $\overline{\mathbf{T}}(\theta)$ only rests with angle parameter. Therefore, it can be seemed as a new decoupled extended steering vector, similar to $\mathbf{a}_{RI}(\theta,\phi,\mathbf{G}) \in \mathbb{R}^{2M\times 1}$ in (11). While $\boldsymbol{\Lambda}(\theta,\phi,\mathbf{G})$ subjects to the interferences of unknown mutual coupling and noncircular phase.

According to (19), the coupled signal model in (10) can be further decoupled as

$$\begin{aligned}\mathbf{y}_{RI}(t) &= \begin{bmatrix}\mathbf{y}_R(t)\\ \mathbf{y}_I(t)\end{bmatrix} = \begin{bmatrix}\mathbf{A}_R\\ \mathbf{A}_I\end{bmatrix}\mathbf{s}(t) + \begin{bmatrix}\mathbf{n}_R(t)\\ \mathbf{n}_I(t)\end{bmatrix}\\ &= \mathbf{A}_{RI}\mathbf{s}(t) + \mathbf{n}_{RI}(t) = \hat{\mathbf{A}}_{RI}\boldsymbol{\Delta}\mathbf{s}(t) + \mathbf{n}_{RI}(t)\\ &= \hat{\mathbf{A}}_{RI}\mathbf{s}_{RI}(t) + \mathbf{n}_{RI}(t),\end{aligned} \tag{20}$$

where

$$\begin{aligned}\hat{\mathbf{A}}_{RI} &= \left[\overline{\mathbf{T}}(\theta_1), \overline{\mathbf{T}}(\theta_2), \ldots, \overline{\mathbf{T}}(\theta_K)\right] \in \mathbb{R}^{2M\times 2FK},\\ \boldsymbol{\Delta} &= \operatorname{blkdiag}\{\boldsymbol{\Lambda}(\theta_1,\varphi_1,\mathbf{G}), \boldsymbol{\Lambda}(\theta_2,\varphi_2,\mathbf{G}), \ldots, \boldsymbol{\Lambda}(\theta_K,\varphi_K,\mathbf{G})\},\end{aligned} \tag{21}$$

where $\hat{\mathbf{A}}_{RI}$ denotes the real-valued block extended array manifold matrix formed by $\overline{\mathbf{T}}(\theta_k)\,(k = 1, 2, \ldots, K)$. It separates angle parameter from disturbance factors, such as mutual coupling coefficients and noncircular phase, making it only depend on DOAs information. The block diagonal matrix $\boldsymbol{\Delta} \in \mathbb{R}^{2FK\times K}$ is combined with the real signal vector $\mathbf{s}(t)$ to construct a novel block signal vector $\mathbf{s}_{RI}(t)$. i.e., $\mathbf{s}_{RI}(t) = \boldsymbol{\Delta}\mathbf{s}(t) \in \mathbb{R}^{2FK\times 1}$. It can be found that the $(2Fk - 2F + 1)$ th to $(2Fk)$ th rows in $\mathbf{s}_{RI}(t)$ correspond to k th element in $\mathbf{s}(t)$. Besides, both the new extended array manifold matrix $\hat{\mathbf{A}}_{RI}$ and the corresponding signal vector $\mathbf{s}_{RI}(t)$ in (20) have block structures for each target, unlike the original coupled extended steering matrix $\mathbf{A}_{RI}$ and the signal vector $\mathbf{s}(t)$ in (10).

3. Real-Valued Weighted Subspace Fitting with Block Sparse Recovery

3.1. The Subspace Fitting Framework with Optimal Weighted Matrix. It has been analyzed that the real-valued coupled extended array manifold matrix $\mathbf{A}_{RI}$ still spans the same range subspace as the signal subspace $\mathbf{E}_s$. Through combining the basic theory of linear algebra and the fact that $\boldsymbol{\Delta}$ in (21) is a column full rank matrix, it can be deduced that the signal subspace $\mathbf{E}_s$ is a subset of the range space of the real-valued block extended array manifold matrix $\hat{\mathbf{A}}_{RI}$, which satisfies

$$\mathbf{E}_s = \mathbf{A}_{RI}\mathbf{U} = \hat{\mathbf{A}}_{RI}\boldsymbol{\Delta}\mathbf{U} = \hat{\mathbf{A}}_{RI}\hat{\mathbf{U}}, \tag{22}$$

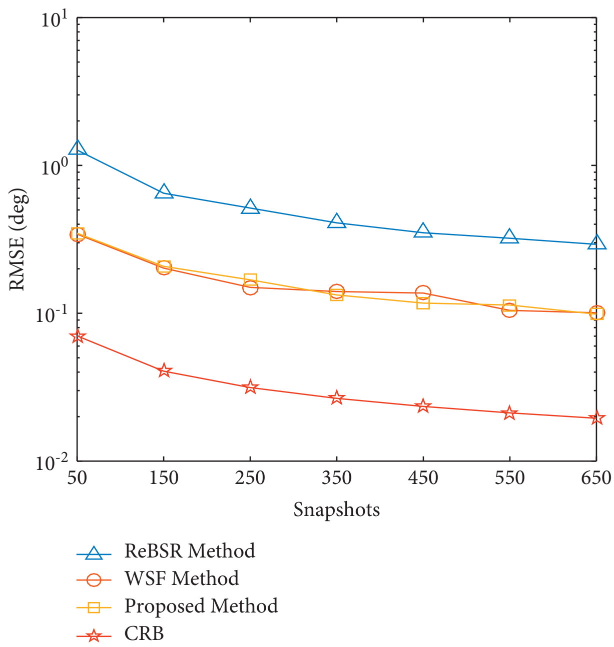

Figure 5: RMSE versus snapshots for all methods.

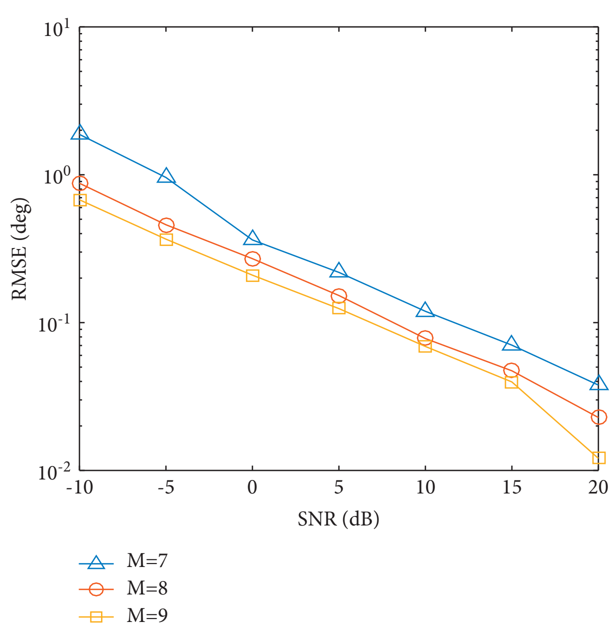

Figure 6: RMSE of the proposed method versus SNR for different number of antennas.

where $\hat{\mathbf{U}} = \Delta\mathbf{U} \in \mathbb{R}^{2FK\times K}$ is a block diagonal matrix with column full rank and consists of K subblocks $\hat{\mathbf{U}}_k\,(k = 1, 2, \ldots, K)$. As the k th subblock, $\hat{\mathbf{U}}_k$ is composed of the $(2Fk - 2F + 1)$ th to $(2Fk)$ th rows in $\hat{\mathbf{U}}$ corresponding to k th row in $\mathbf{U}$. Whereas, (22) will be invalid when there are disturbances such as noise in the array output.

As revealed in [39], numerous prevalent works on DOA estimation can be viewed as the subspace fitting problem in a general sense. Then, a subspace fitting framework is given as follows:

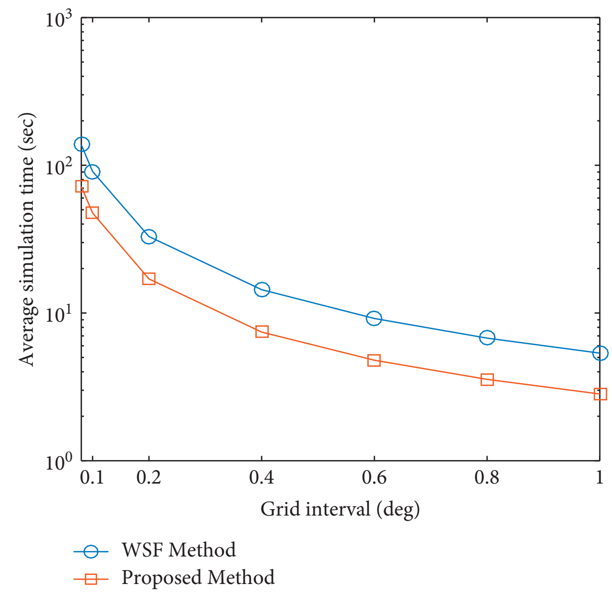

Figure 7: Average simulation time versus grid interval.

$$[\hat{\theta}, \mathbf{U}] = \underset{\theta,\tilde{\mathbf{U}}}{\arg\min} \left\| \mathbf{E}_s \mathbf{W}^{1/2} - \hat{\mathbf{A}}_{RI}(\theta)\tilde{\mathbf{U}} \right\|_F^2, \tag{23}$$

where $\hat{\mathbf{A}}_{RI}$ is parameterized by θ. $\mathbf{W} \in \mathbb{R}^{K\times K}$ represents a positive definite weighted matrix depending on the distinct calculation ways and affecting the asymptotic characteristics of fitting error. According to [39], it has been revealed that there exists an optimal weighted matrix that asymptotically minimizes the fitting error variance in the target directions and satisfies $\mathbf{W}_{opt} = (\mathbf{\Omega}_s - \hat{\sigma}^2 \mathbf{I}_K)^2 \mathbf{\Omega}_s^{-1}$. $\hat{\sigma}^2$ denotes any consistent estimate of noise variance, which can be achieved by averaging $2M - K$ smaller eigenvalues of $\mathbf{R}$. Highlighting that when $\mathbf{W} = \mathbf{W}_{opt}$, (23) describes the optimal subspace fitting issue, defined as weighted subspace fitting (WSF) problem [40].

It is emphasized that $\hat{\mathbf{A}}_{RI}$ and $\tilde{\mathbf{U}}$ can be separated in the process of subspace fitting [38]. Meanwhile, the parameter we care about is $\hat{\mathbf{A}}_{RI}$, not $\tilde{\mathbf{U}}$. Therefore, the least square solution of $\tilde{\mathbf{U}}$ can be solved by fixing $\hat{\mathbf{A}}_{RI}$. i.e.,

$$\mathbf{U} = \hat{\mathbf{A}}_{RI}^{\dagger}(\theta)\mathbf{E}_s\mathbf{W}^{1/2}. \tag{24}$$

Then bringing (24) back to (23), yields

$$\begin{aligned} \hat{\theta} &= \underset{\theta}{\arg\min}\, \mathrm{tr}\left\{ \mathbf{P}^{\perp}_{\hat{\mathbf{A}}_{RI}(\theta)} \mathbf{E}_s \mathbf{W}_{opt} \mathbf{E}_s^H \right\} \\ &= \underset{\theta}{\arg\min}\, \Upsilon(\theta), \end{aligned} \tag{25}$$

where $\mathbf{P}^{\perp}_{\hat{\mathbf{A}}_{RI}(\theta)} = \mathbf{I}_{2M} - \mathbf{P}_{\hat{\mathbf{A}}_{RI}(\theta)} = \mathbf{I}_{2M} - \hat{\mathbf{A}}_{RI}(\theta)\hat{\mathbf{A}}_{RI}^{\dagger}(\theta)$.

In order to deeply study the subspace fitting issue structured by (25) from the perspective of sparse reconstruction, the spatial domain is evenly discretized to form an over-complete dictionary $\overline{\mathbf{A}}_{RI}$. $\overline{\mathbf{A}}_{RI}$ takes the following form:

$$\overline{\mathbf{A}}_{RI} = \left[\overline{\mathbf{T}}(\overline{\theta}_1), \overline{\mathbf{T}}(\overline{\theta}_2), \ldots, \overline{\mathbf{T}}(\overline{\theta}_N) \right] \in \mathbb{R}^{2M\times 2FN}, \tag{26}$$

where $\overline{\boldsymbol{\theta}} = \{\overline{\theta}_1, \overline{\theta}_2, \ldots, \overline{\theta}_N\}$ represents a sampling grid point set and N indicates the number of grid points. It is noted that compared with M and K, N is sufficiently large in this paper, so that the grid-off issue is not considered here. Through combining (22) with $\mathbf{W}_{opt}$, $\mathbf{E}_s\mathbf{W}_{\mathrm{opt}}^{1/2} = \hat{\mathbf{A}}_{RI}\hat{\mathbf{U}}\mathbf{W}_{\mathrm{opt}}^{1/2} = \hat{\mathbf{A}}_{RI}\tilde{\mathbf{U}}$ can be structured. However, it should be pointed out that such relationship is mathematically strict only under the condition of infinite snapshots. Then, based on the over-complete dictionary in (26), $\mathbf{E}_s\mathbf{W}_{\mathrm{opt}}^{1/2}$ can be sparsely represented as

$$\mathbf{E}_s\mathbf{W}_{\mathrm{opt}}^{1/2} = \overline{\mathbf{A}}_{RI}\overline{\mathbf{U}}, \tag{27}$$

where $\overline{\mathbf{U}} = [\overline{\mathbf{U}}_{\overline{\theta}_1}^{\mathbf{T}}, \overline{\mathbf{U}}_{\overline{\theta}_2}^{\mathbf{T}}, \ldots, \overline{\mathbf{U}}_{\overline{\theta}_N}^{\mathbf{T}}]^{\mathbf{T}}$ denotes a block sparse matrix, whose n th subblock $\overline{\mathbf{U}}_{\overline{\theta}_n}$ is made up of the $(2Fn - 2F + 1)$ th to $(2Fn)$ th rows of $\overline{\mathbf{U}}$. Furthermore, the subblocks corresponding to the desired DOAs in $\overline{\mathbf{U}}$ are equal to those in $\tilde{\mathbf{U}}$, while the rest are zero. i.e.,

$$\overline{\mathbf{U}}_{\overline{\theta}_n} = \begin{cases} \tilde{\mathbf{U}}_{\theta_k}, & \overline{\theta}_n \in \{\theta_1, \theta_2, \ldots, \theta_K\} \\ \mathbf{0}, & \overline{\theta}_n \notin \{\theta_1, \theta_2, \ldots, \theta_K\} \end{cases}, \tag{28}$$

where $n = 1, 2, \ldots, N$ and $k = 1, 2, \ldots, K$.

According to (28), it is known that there are only K nonzero subblocks in $\overline{\mathbf{U}}$ due to the existence of K targets. Therefore, the DOA estimation issue can be transformed into a block sparse recovery problem, in which DOAs can be estimated by determining the positions of nonzero subblocks in $\overline{\mathbf{U}}$.

It can be discovered that block sparse matrix $\overline{\mathbf{U}}$ is critical for direction finding, which can be reconstructed via minimizing l_0-norm. Then, a l_0-norm optimization scheme is formed as

$$\min\left\|\mathbf{r}^{l_2}\right\|_0 \text{s.t. } \mathbf{E}_s\mathbf{W}_{opt}^{1/2} = \overline{\mathbf{A}}_{RI}\overline{\mathbf{U}}, \tag{29}$$

where a column vector $\mathbf{r}^{l_2} = [r_1^{l_2}, r_2^{l_2}, \ldots, r_N^{l_2}]^{\mathbf{T}}$ is introduced to describe sparsity. $r_n^{l_2}$ is the n th element in $\mathbf{r}^{l_2}$ and corresponds to the n th subblock of $\overline{\mathbf{U}}$, which can be computed by the l_2-norm of the $(2Fn - 2F + 1)$ th to $(2Fn)$ th rows in $\overline{\mathbf{U}}$. That is to say, $r_n^{l_2} = \sqrt{\sum_{a=2Fn-2F+1}^{2Fn}\sum_{b=1}^{K}(\overline{\mathbf{U}}_{a,b})^2}$, in which $\overline{\mathbf{U}}_{a,b}$ represents the element located at the a th row and b th column of $\overline{\mathbf{U}}$. Evidently, the sparsity of vector $\mathbf{r}^{l_2}$ is the same as that of the block sparse matrix $\overline{\mathbf{U}}$.

In general, l_0-norm penalty can accurately describe the solutions sparsity in the process of sparse recovery. Whereas, l_0-norm penalty is a nondeterministic polynomial (NP)-hard and nonconvex combinatorial optimization problem, so it is mathematically intractable. In this way, l_0-norm convex relaxes to l_1-norm to solve the above problem. Moreover, considering the fitting error caused by finite snapshots, the l_1-norm penalty framework is ultimately restructured as

$$\min\left\|\mathbf{r}^{l_2}\right\|_1 \text{s.t. } \left\|\mathbf{E}_s\mathbf{W}_{\mathrm{opt}}^{1/2} - \overline{\mathbf{A}}_{RI}\overline{\mathbf{U}}\right\|_F \le \varepsilon, \tag{30}$$

where the regularization parameter ε means the upper limit of the subspace fitting error, that is utilized to guarantee robust DOA estimation. Inspired by (25), it is known that the subspace fitting error is equal to $\sqrt{\Upsilon(\theta)}$. It has been derived that function $(2T/\hat{\sigma}^2)\Upsilon(\theta)$ asymptotically follows chi-square distribution with $2K'(2M - K)$ degrees of freedom when θ refers to the true DOAs [40]. Thereby, $\sqrt{\Upsilon(\theta)} \le \varepsilon$ with a high confidence interval $1 - \overline{\rho}$ is calculated to determine parameter ε, in which $\overline{\rho} = 0.001$ is chosen in this paper.

3.2. Reweighted Block Sparse Recovery for DOA Estimation. Through the sparse recovery framework achieved by l_1-norm constrained optimization in (30), DOA estimation can indeed be obtained. However, l_1-norm penalty is only the convex approximation of l_0-norm minimization, resulting in limited recovery accuracy. Specifically speaking, the penalty imposed on larger coefficients is heavier than that imposed on smaller coefficients in the l_1-norm penalty framework, unlike the democratic l_0-norm constraint. Then, a weighted matrix is introduced to enhance the solutions sparsity, where the weights can be determined by constructing the penalty factors. Therefore, l_1-norm can approximate l_0-norm as much as possible.

Following the principle of MUSIC-like approach in [36, 38], the orthogonality between the real-valued block extended array manifold and the noise subspace can be utilized to formulate a novel real-valued NC MUSIC-like spectrum function. The spectrum function can be expressed as

$$Z_{\mathrm{MUSIC}}(\theta) = \frac{1}{\det\left(\overline{\mathbf{T}}^H(\theta)\mathbf{E}_n\mathbf{E}_n^H\overline{\mathbf{T}}(\theta)\right)}. \tag{31}$$

Inspired by the discretized sampling gird points $\overline{\boldsymbol{\theta}} = \{\overline{\theta}_1, \overline{\theta}_2, \ldots, \overline{\theta}_N\}$, the orthogonality between the over-complete dictionary and its noise subspace can be exploited to structure the weights. First, the over-complete dictionary in (26) can be categorized into two groups: $\overline{\mathbf{A}}_{RI} = [\overline{\mathbf{A}}_{RI1}, \overline{\mathbf{A}}_{RI2}]$. It is supposed that $\overline{\mathbf{A}}_{RI1}$ is composed of K block steering matrices corresponding to the interested DOAs, while $\overline{\mathbf{A}}_{RI2}$ is formed by residual $N - K$ subblocks. Then based on (31), the initial weights can be represented as

$$\hat{d}_n = \det\left\{\overline{\mathbf{T}}^H(\overline{\theta}_n)\mathbf{E}_n\mathbf{E}_n^H\overline{\mathbf{T}}(\overline{\theta}_n)\right\} n = 1, 2, \ldots, N, \tag{32}$$

where the weight $\hat{d}_n$ indicates the determinant value corresponding to $\overline{\theta}_n$. Then, a weighted matrix can be structured as

$$\mathbf{D} = \mathrm{diag}\{\mathbf{d}\}, \tag{33}$$

where $\mathbf{D} \in \mathbb{R}^{N\times N}$ denotes a weighted matrix that depends on the vector $\mathbf{d}$. Furthermore, $\mathbf{d}$ relates to the initial weights $\hat{d}_n (n = 1, 2, \ldots, N)$ and takes the following form:

$$\begin{aligned} \mathbf{d} &= [\mathbf{d}_1, \mathbf{d}_2] \\ &= [\overline{d}_1, \overline{d}_2, \ldots, \overline{d}_N] \\ &= \frac{[\hat{d}_1, \hat{d}_2, \ldots, \hat{d}_N]}{\max[\hat{d}_1, \hat{d}_2, \ldots, \hat{d}_N]}. \end{aligned} \tag{34}$$

It can be concluded that if the number of snapshots is sufficiently large, the weights in $\mathbf{d}_1$ corresponding to the interested DOAs are more likely to be zero, which are smaller than those in $\mathbf{d}_2$. Through exploiting the weighted matrix, larger coefficients are preserved by smaller weights, while smaller coefficients close to zero are punished by larger weights. Therefore, no matter how large or small the coefficients are, they can be punished more democratically, behaving like the fair l_0-norm penalty. Eventually, by embedding the weighted matrix $\mathbf{D}$, the reweighted scheme based on l_1-norm optimization can be constructed as

$$\begin{aligned} &\min \left\| \mathbf{D}\mathbf{r}^{l_2} \right\|_1, \\ &\text{s.t.} \quad \left\| \mathbf{E}_s \mathbf{W}_{\text{opt}}^{1/2} - \overline{\mathbf{A}}_{RI} \overline{\mathbf{U}} \right\|_F \leq \varepsilon. \end{aligned} \tag{35}$$

Thanks to second order cone (SOC) programming packages, like CVX, the optimization problem given in (35) can be successfully addressed. In this way, DOAs can be effectively estimated by detecting the positions of nonzero values in the reconstructed sparse vector $\mathbf{r}^{l_2}$.

Up to now, an efficient real-valued weighted subspace fitting algorithm with block sparse recovery has been proposed for DOA estimation of strictly noncircular sources with unknown mutual coupling, which can be summarized as algorithm 1.

4. Simulation and Analysis

In this section, plenty of simulations are implemented and the corresponding results are exhibited to demonstrate the superior performance of the proposed method.

4.1. Simulation Scene. To demonstrate the superiority of the proposed method, the reweighted BSR method in [33] (defined as ReBSR method) and the joint reweighted sparsity-inducing method based on WSF principle in [38] (defined as WSF method) are chosen as the comparison methods. Meanwhile inspired by the Cramer–Rao bound (CRB) for noncircular signals of MIMO radar in [22], the array CRB is redrived for noncircular sources under unknown mutual coupling in this paper. In addition, the root mean square error (RMSE) is used to evaluate the estimation performance of all algorithms, which can be achieved by

$$\text{RMSE} = \sqrt{\frac{1}{JK} \sum_{j=1}^{J} \sum_{k=1}^{K} \left(\theta_{j,k} - \theta_k\right)^2}, \tag{36}$$

where θ_k stands for the real DOAs of k th target and $\theta_{j,k}$ is estimated by θ_k in the j th Monte Carlo experiment. K refers to the number of radiating sources. The number of Monte Carlo experiments is set as $J = 100$.

In what follows, it is assumed that $M = 8$ antennas form a ULA, each of them is separated by half-wavelength spacing. There are $K = 2$ narrowband uncorrelated strictly noncircular sources incident on the ULA from different directions in the far field, whose DOAs are denoted as $\theta_1 = -10^\circ$ and $\theta_2 = 2^\circ$, respectively. Additionally, the mutual coupling matrix consists of $H = 3$ nonzero coefficients including $g_1 = 0.6864 - j0.0919$ and $g_2 = 0.2079 - j0.0603$. The entire spatial domain from -90° to 90° is uniformly sampled at the grid interval of 0.1°.

4.2. Simulation Results. Figure 2 gives the spatial spectra for all different methods, in which SNR is set to −5 dB and the number of snapshots is fixed at 100. According to Figure 2, it can be observed that all methods form spectral peaks at the true DOAs positions. That is to say, these algorithms can realize direction finding of noncircular sources in the case of unknown mutual coupling. Furthermore, ReBSR method has the least shape peaks, the highest side-lobe, and the farthest from the real DOAs, while the proposed approach has the sharpest peaks, the lowest side-lobe, and the closest to the desirable DOAs. In this way, the proposed method outperforms other approaches in terms of resolution and accuracy.

Figures 3 and 4 indicate RMSE versus SNR and PSD versus SNR for distinct algorithms, respectively. In Figure 3, the number of snapshots is chosen as $\mathbf{T} = 100$. On the one hand, as displayed in Figure 3, the RMSE of these methods gradually decreases as SNR increases. Therefore, these methods can achieve improved performance by enhancing the signal environment. Moreover, the main difference between the proposed method and WSF algorithm is whether to perform real-valued conversion, so its impact on the estimation accuracy may not be obvious. In other words, it is reasonable to assume that their performance is similar. At the same time, the RMSE of ReBSR algorithm is larger than that of other noncircular methods, which is mainly due to its inability to take advantage of noncircularity, unlike the other two noncircular algorithms. On the other hand, as given in Figure 4, PSD refers to the successful detection rate for all Monte Carlo running experiments. And when the error absolute value between the true DOA θ_k and the estimated DOA θ_k is less than 0.3°, the target detection is considered successful. From Figure 4, within the selected SNR range, the PSD of the proposed method and WSF approach are much higher than that of ReBSR algorithm. Additionally, they can be the first to achieve 100% PSD compared to ReBSR method. In conclusion, the proposed method has advantage over ReBSR algorithm and similar performance to WSF approach.

Figure 5 depicts RMSE versus snapshots for distinct methods, when SNR is fixed at SNR = 0 dB. As shown in Figure 5, the overall simulation trend is similar to that of Figure 3. As the number of snapshots increases, the RMSE of all distinct approaches decreases. Furthermore, in terms of estimation accuracy, the proposed method is similar to WSF algorithm, better than ReBSR approach and closer to CRB.

Figure 6 shows RMSE of the proposed method versus SNR for different number of antennas, in which $\mathbf{T} = 100$. From Figure 6, the RMSE is the largest when $M = 7$, while the RMSE is the smallest when $M = 9$, which means that if SNR is fixed, the RMSE of the proposed method decreases with the increase of the number of sensors. However, it is worth highlighting that the more sensors, the higher the estimation accuracy, the heavier the computational load, and even the stronger the antennas interaction. In other words, it is better to make a trade-off between effectiveness and efficiency.

Figure 7 reveals the average simulation time required for the two noncircular methods versus gird interval, where SNR and snapshots are set to SNR = 0 dB and $\mathbf{T} = 100$, respectively. In Figure 7, whether the proposed method or WSF algorithm, the larger the grid interval, the shorter the simulation time and the lower the computational burden. This is mainly because the number of sampling grid points decreases as the grid interval increases. In addition, it is evident that the proposed method requires much less time than WSF algorithm, which means that the proposed method is superior to WSF algorithm in simulation time, although they all belong to noncircular algorithms. The main reason is that the proposed method converts complex domain date into real domain data to speed up direction finding for meeting the real-time requirement as much as possible, different from WSF approach in the complex domain. In this way, it takes less time to efficiently achieve high-precision DOA estimation, which is more suitable for practical applications.

5. Conclusion

In this paper, the scenario of strictly noncircular sources in the presence of unknown mutual coupling is concerned, and then a real-valued reweighted block sparse recovery framework achieved by WSF principle is structured for DOA estimation. In the proposed method, a real-valued coupled extended array output is first constructed by connecting the real and imaginary parts of the received data. Then, the real-valued block extended sparse recovery model is formed by exploiting the parameterized decoupling thought to avoid the influences of unknown mutual coupling and noncircular phase. Afterwards, a robust WSF approach is explored to recover the real-valued block sparse matrix for DOA estimation, where a real-valued NC MUSIC-like weighted matrix is further embedded to reinforce the solutions sparsity. Additionally, the upper bound of subspace fitting error is reported as well. Thanks to noncircularity, parameterized decoupling operation, and reweighted measure, the proposed method can not only provide desirable estimation accuracy, but also bear low computational burden. Extensive experiment results validate the effectiveness and efficiency of the proposed method for strictly noncircular sources with unknown mutual coupling.

Data Availability

No data were used to support this study.

Conflicts of Interest

The authors declare that there are no conflicts of interest regarding the publication of this paper.

Acknowledgments

This work was supported by the Key Research and Development Program of Hainan Province (No. ZDYF2020019), the National Natural Science Foundation of China (Nos. 61861015 and 61961013), the National Key Research and Development Program of China (Nos. 2019CXTD400 and SQ2020YFF0405680), and Hainan Province Graduate Student Innovation Research Project (No. Qhyb2021-08).

References

[1] X. Wang, L. T. Yang, D. Meng, M. Dong, K. Ota, and H. Wang, "Multi-uav cooperative localization for marine targets based on weighted subspace fitting in sagin environment," *IEEE Internet of Things Journal*, vol. 9, no. 8, pp. 5708–5718, 2022.

[2] Y. Guo, X. Wang, X. Lan, and T. Su, "Traffic target location estimation based on tensor decomposition in intelligent transportation system," *IEEE Transactions on Intelligent Transportation Systems*, 2022.

[3] X. Wang, Y. Zhu, M. Huang, J. Wang, L. Wan, and G. Bi, "Unitary matrix completion-based doa estimation of noncircular signals in nonuniform noise," *IEEE Access*, vol. 7, pp. 73719–73728, 2019.

[4] J. Cong, X. Wang, C. Yan, L. T. Yang, M. Dong, and K. Ota, "Crb weighted source localization method based on deep neural networks in multi-uav network," *IEEE Internet of Things Journal*, 2022.

[5] X. Wang, W. Wang, and G. Bi, "Low complexity subspace approach for direction finding in bistatic mimo radar," in *Proceedings of the 2015 IEEE 6th International Workshop on Computational Advances in Multi-Sensor Adaptive Processing (CAMSAP)*, pp. 317–320, Cancun, Mexico, December 2015.

[6] R. Schmidt, "Multiple emitter location and signal parameter estimation," *IEEE Transactions on Antennas and Propagation*, vol. 34, no. 3, pp. 276–280, 1986.

[7] R. Roy and T. Kailath, "Esprit-estimation of signal parameters via rotational invariance techniques," *IEEE Transactions on Acoustics, Speech, &;Signal Processing*, vol. 37, no. 7, pp. 984–995, 1989.

[8] J. Li, D. Li, D. Jiang, and X. Zhang, "Extended-aperture unitary root music-based doa estimation for coprime array," *IEEE Communications Letters*, vol. 22, no. 4, pp. 752–755, 2018.

[9] L. Li, T. Fu, Y. Yang, M. Huang, Z. Han, and J. Li, "Joint angle estimation and array calibration using eigenspace in monostatic mimo radar," *IEEE Access*, vol. 8, pp. 60645–60652, 2020.

[10] W. Wang and R. Wu, "High resolution direction of arrival (doa) estimation based on improved orthogonal matching pursuit (omp) algorithm by iterative local searching," *Sensors*, vol. 13, no. 9, pp. 11167–11183, 2013.

[11] J. Yin and T. Chen, "Direction-of-arrival estimation using a sparse representation of array covariance vectors," *IEEE Transactions on Signal Processing*, vol. 59, no. 9, pp. 4489–4493, 2011.

[12] M. E. Tipping, "Sparse bayesian learning and the relevance vector machine," *Journal of Machine Learning Research*, vol. 1, pp. 211–244, 2001.

[13] H. Wang, L. Wan, M. Dong, K. Ota, and X. Wang, "Assistant vehicle localization based on three collaborative base stations

via sbl-based robust doa estimation," *IEEE Internet of Things Journal*, vol. 6, no. 3, pp. 5766–5777, 2019.

[14] X. Wang, W. Wang, J. Liu, X. Li, and J. Wang, "A sparse representation scheme for angle estimation in monostatic mimo radar," *Signal Processing*, vol. 104, pp. 258–263, 2014.

[15] H. Chen, C. Hou, W. Liu, W. P. Zhu, and M. N. S. Swamy, "Efficient two-dimensional direction-of-arrival estimation for a mixture of circular and noncircular sources," *IEEE Sensors Journal*, vol. 16, no. 8, pp. 2527–2536, Apr, 2016.

[16] F. Barbaresco and P. Chevalier, "Noncircularity exploitation in signal processing overview and application to radar," in *Proceedings of the 2008 IET Waveform Diversity &; Digital Radar Conference - Day 1:Waveform Diversity &; Design*, pp. 1–6, London, December 2008.

[17] J. Steinwandt, F. Roemer, M. Haardt, and G. Del Galdo, "R-dimensional esprit-type algorithms for strictly second-order non-circular sources and their performance analysis," *IEEE Transactions on Signal Processing*, vol. 62, no. 18, pp. 4824–4838, 2014.

[18] H. Abeida and J.-P. Delmas, "Music-like estimation of direction of arrival for noncircular sources," *IEEE Transactions on Signal Processing*, vol. 54, no. 7, pp. 2678–2690, 2006.

[19] P. Chargé, Y. Wang, and J. Saillard, "A non-circular sources direction finding method using polynomial rooting," *Signal Processing*, vol. 81, no. 8, pp. 1765–1770, 2001.

[20] W. Wang, X. Wang, H. Song, and Y. Ma, "Conjugate esprit for doa estimation in monostatic mimo radar," *Signal Processing*, vol. 93, no. 7, pp. 2070–2075, 2013.

[21] Z.-M. Liu, Z.-T. Huang, Y.-Y. Zhou, and J. Liu, "Direction-of-arrival estimation of noncircular signals via sparse representation," *IEEE Transactions on Aerospace and Electronic Systems*, vol. 48, no. 3, pp. 2690–2698, 2012.

[22] X. Wang, W. Wang, X. Li, Q. Liu, and J. Liu, "Sparsity-aware doa estimation scheme for noncircular source in mimo radar," *Sensors*, vol. 16, no. 4, p. 539, 2016.

[23] X. Wang, L. Wang, X. Li, and G. Bi, "Nuclear norm minimization framework for doa estimation in mimo radar," *Signal Processing*, vol. 135, pp. 147–152, 2017.

[24] X. Wang, M. Huang, X. Wu, and G. Bi, "Direction of arrival estimation for mimo radar via unitary nuclear norm minimization," *Sensors*, vol. 17, no. 4, p. 939, 2017.

[25] Z. Zheng, C. Yang, W.-Q. Wang, and H. C. So, "Robust doa estimation against mutual coupling with nested array," *IEEE Signal Processing Letters*, vol. 27, pp. 1360–1364, 2020.

[26] T. Svantesson, "Modeling and estimation of mutual coupling in a uniform linear array of dipoles," in *Proceedings of the 1999 IEEE International Conference on Acoustics, Speech, and Signal Processing. Proceedings. ICASSP99 (Cat. No. 99CH36258)*, vol. 5, pp. 2961–2964, Phoenix, AZ, USA, March 1999.

[27] Z. Ye and C. Liu, "On the resiliency of music direction finding against antenna sensor coupling," *IEEE Transactions on Antennas and Propagation*, vol. 56, no. 2, pp. 371–380, 2008.

[28] Z. Zheng, J. Zhang, and J. Zhang, "Joint dod and doa estimation of bistatic mimo radar in the presence of unknown mutual coupling," *Signal Processing*, vol. 92, no. 12, pp. 3039–3048, 2012.

[29] B. Liao, Z.-G. Zhang, and S.-C. Chan, "Doa estimation and tracking of ulas with mutual coupling," *IEEE Transactions on Aerospace and Electronic Systems*, vol. 48, no. 1, pp. 891–905, 2012.

[30] J. Dai, D. Zhao, and X. Ji, "A sparse representation method for doa estimation with unknown mutual coupling," *IEEE Antennas and Wireless Propagation Letters*, vol. 11, pp. 1210–1213, 2012.

[31] J. Liu, X. Wang, and W. Zhou, "Covariance vector sparsity-aware doa estimation for monostatic mimo radar with unknown mutual coupling," *Signal Processing*, vol. 119, pp. 21–27, 2016.

[32] Q. Wang, T. Dou, H. Chen, W. Yan, and W. Liu, "Effective block sparse representation algorithm for doa estimation with unknown mutual coupling," *IEEE Communications Letters*, vol. 21, no. 12, pp. 2622–2625, 2017.

[33] X. Wang, D. Meng, M. Huang, and L. Wan, "Reweighted regularized sparse recovery for doa estimation with unknown mutual coupling," *IEEE Communications Letters*, vol. 23, no. 2, pp. 290–293, 2019.

[34] D. Meng, X. Wang, M. Huang, L. Wan, and B. Zhang, "Robust weighted subspace fitting for doa estimation via block sparse recovery," *IEEE Communications Letters*, vol. 24, no. 3, pp. 563–567, 2020.

[35] J. Xie, L. Wang, and J. Su, "Efficient doa estimation algorithm for noncircular sources under unknown mutual coupling," *IEEE Sensors Letters*, vol. 2, no. 3, pp. 1–4, 2018.

[36] J. Xie, L. Wang, and Y. Wang, "Efficient real-valued rank reduction algorithm for doa estimation of noncircular sources under mutual coupling," *IEEE Access*, vol. 6, pp. 64450–64460, 2018.

[37] L. Li, D. Luo, G. Bi, X. Wang, and D. Meng, "Joint sparsity-inducing doa estimation for strictly noncircular sources with unknown mutual coupling," in *Proceedings of the 2020 IEEE 11th Sensor Array and Multichannel Signal Processing Workshop (SAM)*, pp. 1–4, Hangzhou, China, June 2020.

[38] L. Li, T. Fu, X. Wang, M. Huang, L. Wan, and Y. Yang, "Doa estimation of strictly noncircular sources in wireless sensor array network via block sparse representation," *IEEE Access*, vol. 8, pp. 47500–47508, 2020.

[39] M. Viberg and B. Ottersten, "Sensor array processing based on subspace fitting," *IEEE Transactions on Signal Processing*, vol. 39, no. 5, pp. 1110–1121, 1991.

[40] M. Viberg, B. Ottersten, and T. Kailath, "Detection and estimation in sensor arrays using weighted subspace fitting," *IEEE Transactions on Signal Processing*, vol. 39, no. 11, pp. 2436–2449, 1991.

Hindawi
Mathematical Problems in Engineering
Volume 2022, Article ID 8800833, 9 pages
https://doi.org/10.1155/2022/8800833

Research Article

The Limited Aperture Sparse Array for DOA Estimation of Coherent Signals: A Mutual-Coupling-Optimized Array and Coherent DOA Estimation Algorithm

Yu Zhang ,[1,2] Meng Yang,[1,2] Xiaofei Zhang,[1,2] Shengxinlai Han,[1,2] and Jinke Cao[1,2]

[1]*College of Electronic and Information Engineering, Nanjing University of Aeronautics and Astronautics, Nanjing 211106, China*
[2]*Key Laboratory of Dynamic Cognitive System of Electromagnetic Spectrum Space (Nanjing University of Aeronautics and Astronautics), Ministry of Industry and Information Technology, Nanjing 211106, China*

Correspondence should be addressed to Yu Zhang; yyzz@nuaa.edu.cn

Received 28 July 2022; Revised 9 September 2022; Accepted 19 September 2022; Published 5 October 2022

Academic Editor: Abdul Qadeer Khan

The paper investigates DOA estimation of coherent Signals with the limited aperture sparse array. Mutual coupling between the sensors of the array cannot be ignored in practical radar with a limited aperture of array sensors, which will result in a degradation in the performance of Direction of Arrival (DOA) estimation. This paper proposes a Mutual-coupling-optimized array (MCOA) with a limited aperture in this scenario to reduce the mutual coupling effect. Firstly, we prove the sparse uniform linear array (SULA) has the smallest mutual coupling leakage when the array aperture and the number of sensors is determined. Secondly, we modify the spacing of the array sensors in SULA to make sure that the spacing between all array sensors and the reference sensor are coprime aiming to estimate DOA without spatial aliasing. Thirdly, we give an expression for the array element spacing arrangement with reduced mutual coupling leakage. Finally, the coherent signals are well resolved by the Sparse Bayesian Learning (SBL) algorithm. Numerous simulations are conducted to validate the advantages of the proposed array compared to several sparse arrays for estimating coherent signals in the presence of mutual coupling.

1. Introduction

The problem of Direction of Arrival (DOA) estimation has attracted a lot of attention in the fields of radar, sonar, navigation, and astronomy [1–7], where the antenna arrays are utilized for collecting the spatial sampling of incident signals. Scholars propose many DOA estimation algorithms based on the uniform linear array (ULA), such as multiple signal classification (MUSIC) [5], estimation of signal parameters via rotational invariance techniques (ESPRIT) [6], propagator method (PM) [8], and parallel factor (PARAFAC) technique [9].

However, the above-given algorithm is predicated on the assumption that the incident signals are uncorrelated. The received signals are typically coherent and the rank of the covariance matrix is insufficient due to the impact of the transmission environment in actual applications. The aforementioned DOA estimation algorithm will be invalid at this time [10]. To tackle this problem, some decoherence algorithms are proposed to deal with coherent signals. The most representative method is the spatial smoothing (SS) method [11], which regards ULA as many subarrays with the same array flow type and then averages the covariance matrix of each subarray to obtain the full rank covariance matrix. Later, people proposed the Forward/backward spatial smoothing techniques [12], improved spatial smoothing techniques [13] on this basis of SS and make a series of improvement on these algorithms [14]. In [15], the authors were devoted to establishing more accurate conditions by studying the positive definiteness of smoothed target covariance matrix. There are also algorithms that reconstruct the covariance matrix of the received signal, such as SVD algorithms and the Toeplitz decoherence method [16]. These methods estimate coherent signals at the expense of array aperture, which reduces DOA estimation performance. The compressed sensing (CS) algorithms [17–19] can estimate DOA by exploiting the sparsity of the target in the spatial domain without taking into account the coherence of the signals. In [20], an iterative adaptive approach (IAA) is given for the beamforming design based on the sparsity. In [21], the Orthogonal Matching Pursuit (OMP) is used to recover the spare signal with high probability, but the accuracy of OMP is lower than that of MUSIC. In [22], both the Sparse Bayesian Learning (SBL) and the relevance vector machine (RVM) are proposed. The weakness of CS algorithms is that they are more complex than the previously described DOA estimating techniques. The traditional DOA estimation algorithms are generally considered based on ULA, but sparse linear arrays are seldom utilized.

Recently, sparse arrays such as Nested arrays (NA) [23] and coprime arrays (CA) [24] have attracted wide attention because such sparse arrays can achieve $O(M^2)$ degrees of freedoms (DOFs) with only M antenna sensors. Though the DOA estimation performance of NA is better than that of CA, the mutual coupling leakage of NA is much greater than that of CA due to the influence of the dense ULA subarray, which reduces performance in the presence of mutual coupling. Despite the array positions of CA and NA can be expressed in closed-form, their continuous degrees of freedom are not the greatest. In comparison to CA and NA, the minimum redundant array (MRA) [25] has the most continuous degrees of freedom, allowing it to use more virtual arrays. However, MRA lacks a closed-form expression for the locations of its sensors, and its array design requires a significant amount of complicated calculations.

The aperture of the array is usually limited in most applications, and the number of array elements is fixed. Because the spacing between the array elements is relatively close, the mutual coupling effect cannot be ignored. ULA and traditional sparse arrays will fail to estimate the DOA of coherent signals and the research of DOA estimation in this situation is relatively few. Though there are some methods [26–28] proposed to mitigate the mutual coupling effects by utilizing a complex mutual coupling model, these methods estimate mutual coupling coefficients at the cost of increased complexity and decreased degree of freedom (DOFs). Therefore, it is a good choice to consider how to reduce the mutual coupling effect when designing the array. Under the restrictions of a set array aperture and a number of array sensors, this paper determines the array design approach with the least mutual coupling leakage, and we further propose a Mutual-coupling-Optimized Array (MCOA) based on the theory of estimating DOA without spatial aliasing [29, 30]. To estimate the DOA of coherent signals, we use the sparse Bayesian learning-based (SBL) compressed sensing algorithm. In particular, we summarize our main contributions as follows:

(1) We propose a mutual-coupling-optimized array under the restriction of a fixed number of sensors and fixed array aperture. Then, we prove that the mutual coupling leakage of the suggested array is smaller than that of conventional sparse arrays and that it can estimate DOA without spatial aliasing.

(2) We employ the SBL algorithm to estimate coherent DOA for the proposed array and compare the SBL algorithm with other algorithms to demonstrate that the estimation performance of the SBL algorithm is better than other algorithms including OMP and IAA.

The remainder of this paper is given as follows: we provide the mathematical model of the sparse array and the definition of mutual coupling matrix in Section 2. In Section 3, we present how to design the mutual coupling optimized array with a limited aperture. Section 4 introduces the specific steps of the sparse Bayesian learning algorithm. Section 5 analyses the CRB of the array in this context. Section 6 verifies the theoretical performance of the proposed array through simulation analysis while Section 7 concludes this paper.

Notations: scalars, vectors, matrices, and sets are denoted by lowercase letters a, lowercase letters in boldface $\mathbf{a}$, uppercase letters in boldface $\mathbf{A}$, and letters in blackboard boldface $\mathbb{A}$, respectively. $\mathbf{A}^T$, $\mathbf{A}^*$, and $\mathbf{A}^H$ are the transpose, complex conjugate, and complex conjugate transpose of $\mathbf{A}$. $\mathrm{Tr}[\cdot]$ denotes the trace operator for a matrix. $\|\cdot\|_F$ represents the Frobenius norm and $\mathrm{diag}(\cdot)$ represents the matrix formed by the diagonal elements of the matrix. $[\mathbf{A}]_{i,j}$ denotes the (i, j) entry of $\mathbf{A}$. $\gcd(n_1, n_2, \cdots, n_M)$ denotes the greatest common divisor of the elements.

2. Mathematical Model

Consider a sparse array consisting of M sensors as shown in Figure 1, and the position of the ith sensor is denoted by $z_i d$ with $d = \lambda/2$, z_i represents the distance of the i- th sensor relative to the reference sensor and λ stands for the wavelength. Suppose that there are K far-field narrowband coherent signals from different directions $\theta = [\theta_1, \theta_2, \cdots, \theta_K]$ $\sqrt{b^2 - 4ac}$ with powers $\mathbf{p} = [\sigma_1^2, \sigma_2^2, \cdots, \sigma_K^2]$ impinge on this sparse array. The received signal of the array can be expressed as follows [2]:

$$\mathbf{X}_0 = \mathbf{AS} + \mathbf{N}, \tag{1}$$

where $\mathbf{A} = [\mathbf{a}(\theta_1), \mathbf{a}(\theta_2), \cdots, \mathbf{a}(\theta_K)]$ represents the direction matrix and $\mathbf{a}(\theta_i) = [1, e^{j2\pi z_2 d \sin\theta_i/\lambda}, \cdots, e^{j2\pi z_M d \sin\theta_i/\lambda}]^T$ denotes the direction vector of the ith signal. λ is the wavelength of the signal. $\mathbf{S} = [\alpha_1, \alpha_2, \cdots, \alpha_K]\mathbf{s}_0 \in \mathbb{C}^{M\times J}$ means the narrowband coherent signals with J snapshots, where $\mathbf{s}_0$ is the generate signals and α_i stands for the complex constant. $\mathbf{N} \in \mathbb{C}^{M\times J}$ represents the additive white Gaussian noise vector with noise variance σ^2.

There is coupling between the array elements. The received signal model is expressed as follows [28]:

$$\mathbf{X} = \mathbf{CAS} + \mathbf{N}, \tag{2}$$

where $\mathbf{C}$ is the mutual coupling matrix. The mutual coupling matrix can be modelled as a B-banded symmetric Toeplitz

Figure 1: Array model.

matrix according to the assumption in the following equation [28]:

$$[\mathbf{C}]_{p,q} = \begin{cases} 0, & \left|z_p - z_q\right| > B \\ c_{\left|z_p - z_q\right|} & \left|z_p - z_q\right| \le B, \end{cases} \tag{3}$$

where $1 > |c_1| > \cdots > c_B > 0$, $c_1 = c_0 e^{j\pi/3}$, $c_s = c_1 e^{-j(s-1)/8}/s$, $s \in (0, B]$. c_0 is the mutual coupling constant and B denotes the maximum spacing of sensor pairs with mutual coupling. In addition, the mutual coupling is evaluated by the coupling leakage, i.e.,

$$\gamma = \frac{\|\mathbf{C} - \operatorname{diag}(\mathbf{C})\|_F}{\|\mathbf{C}\|_F}. \tag{4}$$

3. Mutual-Coupling-Optimized Array with Limited Aperture

In this section, we first show that the mutual coupling leakage of the sparse and uniform linear array is the smallest under the condition of finite aperture and number of elements. Then, we discussed how to change the position of the array elements, so that the mutual coupling leakage is still small, and there is no spatial aliasing in DOA estimation.

3.1. A Minimum Mutual Coupling Leakage Array. Considering the M- element array with an array aperture of N, we propose an array which has no spatial aliasing in DOA estimation and has the smaller mutual coupling leakage than most sparse arrays.

Lemma 1. *For an M element array with an array aperture of N, the mutual coupling leakage is minimized if and only if the array elements are equally spaced.*

$$z_{i+1}d - z_i d = z_i d - z_{i-1} d = \frac{N}{(M-1)}, \quad i = 2, 3, \cdots, M-1. \tag{5}$$

Proof. According to equation (3), the mutual coupling matrix can be expressed as follows:

$$\mathbf{C} = \begin{bmatrix} c_0 & c_{z_2 - z_1} & \cdots & c_{z_M - z_1} \\ c_{z_2 - z_1} & c_0 & \cdots & c_{z_M - z_2} \\ \vdots & \vdots & \ddots & \vdots \\ c_{z_M - z_1} & c_{z_M - z_2} & \cdots & c_0 \end{bmatrix}. \tag{6}$$

Then, the expression of the coupling leakage can be calculated as follows:

$$\gamma = \frac{\|\mathbf{C} - \operatorname{diag}(\mathbf{C})\|_F}{\|\mathbf{C}\|_F} = \frac{\sqrt{2\sum_{i=1}^{M-1}\sum_{j=i+1}^{M}\left|c_{z_j - z_i}\right|^2}}{\sqrt{M_{|c_0|}^2 + 2\sum_{i=1}^{M-1}\sum_{j=i+1}^{M}\left|c_{z_j - z_i}\right|^2}}, \tag{7}$$

where

$$\sum_{i=1}^{M-1}\sum_{j=i+1}^{M}\left|c_{z_j - z_i}\right|^2 = \left|c_1\right|^2 \sum_{i=1}^{M-1}\sum_{j=i+1}^{M}\frac{1}{\left(z_j d - z_i d\right)^2} = \left|c_1\right|^2 S, \tag{8}$$

where $S = \sum_{i=1}^{M-1}\sum_{j=i+1}^{M}(z_j d - z_i d)^{-2}$. The value of z_i, $i = 1, 2, \cdots, M$ corresponding to the minimum value of S is the position of each array sensor when the mutual coupling leakage is minimum.

Denote the $M-1$ array spacings as $x_1, x_2, \cdots, x_{M-1}$ respectively. Then,

$$\begin{aligned} S &= \sum_{i=1}^{M-1}\sum_{j=i+1}^{M}\left(z_j d - z_i d\right)^{-2} = \sum_{i=1}^{M-1}\left(z_{i+1}d - z_i d\right)^{-2} \\ &\quad + \sum_{i=1}^{M-2}\left(z_{i+2}d - z_i d\right)^{-2} + \cdots + \sum_{i=1}^{1}\left(z_M d - z_i d\right)^{-2} \\ &= \sum_{i=1}^{M-1} x_i^{-2} + \sum_{i=1}^{M-2}\left(x_i + x_{i+1}\right)^{-2} + \cdots \\ &\quad + \sum_{i=1}^{1}\left(x_i + x_{i+1} + \cdots + x_{i+(M-2)}\right)^{-2}. \end{aligned} \tag{9}$$

Calculate the minimum value of S by Lagrange multiplier method.

$$g\left(x_1, \cdots, x_{M-1}, \mu\right) = S + \mu\left(x_1 + x_2 + \cdots + x_{M-1} - N\right). \tag{10}$$

Take the partial derivative of each variable in the function and set the result equal to zero.

$$\begin{cases} \dfrac{\partial g(x_1,\cdots,x_{M-1},\mu)}{\partial x_1} = 0 \\ \vdots \\ \dfrac{\partial g(x_1,\cdots,x_{M-1},\mu)}{\partial x_{M-1}} = 0 \\ \dfrac{\partial g(x_1,\cdots,x_{M-1},\mu)}{\partial \mu} = 0. \end{cases} \tag{11}$$

There is an extreme point in (10) when $x_1 = x_2 = \cdots = x_{M-1} = N/(M-1)$ and the cost function S has a minimum value at this time. Therefore, the value of z_i, $\quad i = 1, 2, \cdots, M$ corresponding to the minimum value of S is the position of each array element in the array when the mutual coupling leakage is minimum. From the above-given discussion, it can be seen that the M elements array with an aperture of the array N reach the minimum mutual coupling leakage when (5) holds. The array designed in (5) is a sparse uniform line array (SULA) when $N > (M-1)\lambda$.

However, SULA will cause spatial aliasing during DOA estimation [29] because the spacing of the adjacent sensors are larger than half-wavelength. Next, we discuss how to fine-tune the position of SULA's array elements to solve the angular ambiguity problem and maintain the advantage of low mutual coupling leakage. □

3.2. B Mutual-Coupling-Optimized Array (MCOA). Suppose that the first sensor is located at the origin without loss of generality, then the position of the array can be expressed as follows:

$$\mathbb{Z} = \{0, z_2, \cdots, z_M\} d. \tag{12}$$

In order to facilitate the subsequent discussion, z_i needs to be adjusted to integer by choosing an appropriate d.

Theorem 1 (see [29]). *ie array manifold* $\mathbf{a}(\theta) = [1, e^{j2\pi z_2 \sin\theta/\lambda}, \dots, e^{j2\pi z_M \sin\theta/\lambda}]^T$ *is invertible if and only if the sensor locations* z_i *(assumed integers) are coprime.*

$$\gcd(z_2, z_3, \cdots, z_M) = 1. \tag{13}$$

According to Theorem 1, we design the array structure as follows:

$$\mathbf{d} = [x_1, x_2, \dots, x_{M-1}] = \begin{cases} \Big[a-1, \underbrace{a, \dots, a}_{[(M-2)/2]}, a+1, a, \dots, a\Big], & N = a(M-1), \\ \Big[a, \dots, \underbrace{a+1, \dots, a+1}_{b}, \dots, a\Big], & N = a(M-1) + b,\ b < M-1, \end{cases} \tag{14}$$

where $\mathbf{d}_{1\times(M-1)}$ represent the spacing of adjacent sensors in array and a, b are integers.

In fact, the different arrangement order of elements in $\mathbf{d}$ will also cause the structural change of $\mathbb{Z}$, which leads to different mutual coupling leakage. Due to the large number of repetitions of elements in $\mathbf{d}$, there will be many repeated combinations of corresponding $\mathbb{Z}$. Obviously, when the larger distance between adjacent sensors in the center of the array, the mutual coupling between the middle sensors and the sensors on both sides can be effectively reduced so that the mutual coupling leakage of the whole array degrades significantly. This is the reason why we make $\mathbf{d}$ as (14). The relationship between $\mathbb{Z}$ and $\mathbf{d}$ is $z_{i+1} - z_i = d_i$, then the expression of the array position $\mathbb{Z}$ can be written as follows:

$$\mathbb{Z} = \begin{cases} \{0, a-1, 2a-1, \cdots, N\} d, & N = a(M-1), \\ \{0, a, \cdots, ka+1, \cdots, N\} d, & N = a(M-1) + b, b < N+1. \end{cases} \tag{15}$$

We will prove that the position in (15) satisfies Theorem 1 in the following part.

Proof. When $N = a(M-1)$, then

$$\begin{aligned} \gcd(2a-1, a-1) &= \gcd(a-1, 2a-1 \bmod a-1) \\ &= 1 \\ &= 1, \end{aligned} \tag{16}$$

where $a \bmod b$ represents the remainder of dividing a by b.

When $N = a(M-1) + b, b < N+1$, then.

$$\begin{aligned} \gcd(a, ka+1) &= \gcd(a, ka+1 \bmod a) \\ &= \gcd(a, 1) = 1. \end{aligned} \tag{17}$$

In summary $\gcd(z_2, z_3, \cdots, z_M) = 1$, that is, the designed array structure satisfies Theorem 1. Suppose that an antenna array with array aperture $N = 8\lambda$ and the number of sensors

$M = 8$ needs to be designed. According to (15), since N is not divisible by $M-1$, we can calculate that $\mathrm{N} = 2(M-1)+2$ with $a=2, b=2$ and write the expression of $\mathbf{d}$ and $\mathbb{Z}$.

$$\begin{aligned} \mathbf{d} &= [2,2,3,3,2,2,2], \\ \mathbb{Z} &= \{0,2,4,7,10,12,14,16\}d. \end{aligned} \tag{18}$$

Figure 2 shows the example of the above MCOA. The array structure is very similar to that of the SULA. There are five spacing between the sensors are 2 d and the remaining two are 3 d. We place the 3 d in the middle of the array to make the mutual coupling between the middle sensors and sensor on both sides decreasing, which effectively reduces the coupling leakage of the whole array. The array locations also satisfy Theorem 1.

$$\gcd(2,4,7,10,12,14,16) = 1. \tag{19}$$

□

4. Sparse Bayesian-Based Compressed Sensing Method

In the sparse signal representation framework [23, 24], the direction matrix $\mathbf{A}$ in (2) should be replaced by a transfer matrix $\mathbf{A}_g$, thus the signal model in (2) can be rewritten as follows:

$$\mathbf{X} = \mathbf{C}\mathbf{A}_g\mathbf{S}_g + \mathbf{N}, \tag{20}$$

where $\mathbf{S}_g = [\mathbf{s}_1, \cdots, \mathbf{s}_J] \in \mathbb{C}^{G\times J}$ represent the complex signal amplitudes containing G DOAs and J snapshots. The transfer matrix $\mathbf{A}_g = [\mathbf{a}_1, \cdots, \mathbf{a}_G] \in \mathbb{C}^{M\times G}$ consists of all hypothetical DOAs. The likelihood function of the received signal $\mathbf{X}$ can be represented as follows:

$$p\left(\mathbf{X}|\mathbf{S}_g;\sigma^2\right) = \frac{\exp\left(-1/\sigma^2\left\|\mathbf{X}-\mathbf{C}\mathbf{A}_g\mathbf{S}_g\right\|_F^2\right)}{\left(\pi\sigma^2\right)^{NL}}. \tag{21}$$

The SBL algorithm treats $\mathbf{s}$ as a zero mean complex Gaussian random vector with unknown diagonal covariance $\Gamma = \mathrm{diag}(\gamma_1, \cdots, \gamma_M) = \mathrm{diag}(\gamma)$. The prior model is given by the following equation:

$$p\left(\mathbf{S}_g\right) = \prod_{j=1}^{J} p\left(\mathbf{s}_j\right) = \prod_{j=1}^{J} \mathrm{AC}(0,\Gamma). \tag{22}$$

For Gaussian prior and likelihood, the evidence $p(\mathbf{X})$ is Gaussian and represented as follows:

$$p(\mathbf{X}) = \int p\left(\mathbf{S}_g\right)p\left(\mathbf{X}|\mathbf{S}_g\right)d\mathbf{S}_g = \prod_{j=1}^{J}\mathrm{AC}\left(\mathbf{x}_j;\mathbf{0},\Sigma_{\mathbf{x}}\right), \tag{23}$$

where $\Sigma_{\mathbf{x}} = \sigma^2\mathbf{I} + \mathbf{C}\mathbf{A}_g\Gamma\mathbf{A}_g^H\mathbf{C}^H$ and $\mathbf{I}$ stands for the identity matrix of order $M\times M$. The SBL algorithm is to estimate the diagonal entries of Γ by maximizing the evidence

$$(\widehat{\gamma}_1,\cdots,\widehat{\gamma}_M) = \arg\max_{\gamma}\left\{-\sum_{j=1}^{J}\mathbf{x}_j^H\Sigma_y^{-1}\mathbf{x}_j - L\log\left|\Sigma_{\mathbf{x}}\right|\right\}, \tag{24}$$

the derivative of (24) is

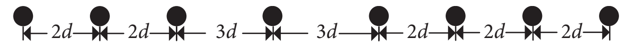

Figure 2: MCOA array with an array aperture of 8 wavelengths and a sensor count of 8.

$$\begin{aligned} &\frac{\partial\left(-\sum_{j=1}^{J}\mathbf{x}_j^H\sum_y^{-1}\mathbf{x}_j - L\log\left|\Sigma_{\mathbf{x}}\right|\right)}{\partial\gamma_m} \\ &= tr\left(\mathbf{X}^H\sum_{\mathbf{x}}^{-1}\mathbf{a}_m\mathbf{a}_m^H\sum_{\mathbf{x}}^{-1}\mathbf{X}\right) - L\mathbf{a}_m^H\Sigma_{\mathbf{x}}^{-1}\mathbf{a}_m \\ &= \left\|\mathbf{X}^H\sum_{\mathbf{x}}^{-1}\mathbf{a}_m\right\|_2^2 - L\mathbf{a}_m^H\sum_{\mathbf{x}}^{-1}\mathbf{a}_m \\ &= \left(\frac{\gamma_m^{\mathrm{old}}}{\gamma_m^{\mathrm{new}}}\right)^2\left\|\mathbf{X}^H\sum_{\mathbf{x}}^{-1}\mathbf{a}_m\right\|_2^2 - L\mathbf{a}_m^H\sum_{\mathbf{x}}^{-1}\mathbf{a}_m. \end{aligned} \tag{25}$$

The factor $(\gamma_m^{\mathrm{old}}/\gamma_m^{\mathrm{new}})^2$ is introduced to obtain an iterative equation in γ_m. Equate the derivatives to zero and we can get the fixed-point update rule [1, 2, 4].

$$\begin{aligned} \gamma_m^{\mathrm{new}} &= \gamma_m^{\mathrm{old}}\frac{1}{L}\frac{\left\|\mathbf{X}^H\sum_{\mathbf{x}}^{-1}\mathbf{a}_m\right\|_2^2}{\mathbf{a}_m^H\sum_{\mathbf{x}}^{-1}\mathbf{a}_m} \\ &= \gamma_m^{\mathrm{old}}\frac{\mathrm{Tr}\left[\mathbf{S}_{\mathbf{x}}\sum_{\mathbf{x}}^{-1}\mathbf{a}_m\mathbf{a}_m^H\Sigma_{\mathbf{x}}^{-1}\right]}{\mathbf{a}_m^H\sum_{\mathbf{x}}^{-1}\mathbf{a}_m}. \end{aligned} \tag{26}$$

where $\mathbf{S}_{\mathbf{x}} = 1/J\mathbf{X}\mathbf{X}^H$ is the sample covariance matrix.

The main steps of the SBL algorithm are summarized as follows:

Step 1: Set the parameters as $\varepsilon = 10^{-3}$ and get the input data $\mathbf{X}, \mathbf{A}_g, \sigma^2, k_{\max}$;

Step 2: Initialization the parameters $\gamma_m^{\mathrm{old}} = 1, \forall m$;

Step 3: Calculate $\Sigma_{\mathbf{x}} = \sigma^2\mathbf{I} + \mathbf{C}\mathbf{A}\Gamma^{\mathrm{old}}\mathbf{A}^H\mathbf{C}^H$;

Step 4: Update γ_m^{new} by using equation (27);

Step 5: Set $\gamma^{\mathrm{old}} = \gamma^{\mathrm{new}}, \Gamma^{\mathrm{old}} = \mathrm{diag}(\gamma^{\mathrm{old}}), k = k+1$;

Step 6: If $\|\gamma^{new}-\gamma^{\mathrm{old}}\|_1/\|\gamma^{\mathrm{old}}\|_1 > \varepsilon$ and $k < k_{\max}$, go back to step 3;

Step 7: The K largest peaks in γ are the required DOA values.

5. Performance Analysis

5.1. Comparison of Mutual Coupling Leakage between Different Arrays with the Same Aperture. We select some sparse arrays for comparison. In order to make the array aperture of all arrays consistent, we compress the element spacing of CA and ECA. The result is shown in Table 1, it can be seen that the mutual coupling leakage of the proposed array is the smallest except SULA, and its mutual coupling leakage is very close to SULA.

5.2. Crarmer–Rao Bound (CRB). According to the knowledge of the literature [32], the Crarmer–Rao Bound (CRB) matrix can be represented as follows:

Table 1: Comparison of mutual coupling leakage of different arrays.

	Array aperture	d	$\mathbb{Z}$	Mutual coupling leakage
Proposed	8 λ	0.5 λ	0,2,4,7,10,12,14,16	0.0826
CA	8 λ	0.5 λ	0 4 5 8 10 12 15 16	0.1076
ECA	8 λ	0.4444 λ	0 2 4 5 6 8 13 18	0.1140
NA	8 λ	0.4211 λ	0 1 2 3 7 11 15 19	0.1194
SULA	8 λ	1.1429 λ	0 1 2 3 4 5 6 7	0.0806
ULA	3.5 λ	0.5 λ	0 1 2 3 4 5 6 7	0.1819

$$CRB = \frac{\sigma_n^2}{2J}\left\{\mathrm{Re}\left[\mathbf{D}^H \prod_{\mathbf{A}}^{\perp} \mathbf{D}\widehat{P}^T\right]\right\}^{-1}, \tag{27}$$

where $\mathrm{Re}[\cdot]$ stands for the operation of taking the real part, $\mathbf{A}$ represents the manifold matrix of the array, $\Pi_{\mathbf{A}}^{\perp} = \mathbf{I} - \mathbf{A}(\mathbf{A}^H\mathbf{A})^{-1}\mathbf{A}^H$ is the orthogonal projection of $\mathbf{A}$, and $\mathbf{I}$ stands for the identity matrix of order $M \times M$, $\widehat{P} = 1/J\sum_{t=1}^{J} s(t)s^H(t)$, σ_n^2 denotes the average power of signal source, $\mathbf{D}$ can be written as follows:

$$\mathbf{D} = \left[\frac{\partial \mathbf{a}(\theta_1)}{\partial\theta_1}, \frac{\partial \mathbf{a}(\theta_2)}{\partial\theta_2}, \dots, \frac{\partial \mathbf{a}(\theta_K)}{\partial\theta_K}\right], \tag{28}$$

where $\mathbf{a}(\theta_K)$ denotes steering vector.

5.3. Computational Complexity. In this section, we provide the complexity of the SBL method compared with OMP and MUSIC. Assuming that the number of array elements is M, there are G grid points and J snapshots, the maximum number of iterations is $k_{\max}$, then the computational complexity of main operations are as follows: (a) calculate the covariance matrix: $O(M^2J)$; (b) update the $\Sigma_{\mathbf{x}}$ in Step 3: $O(2M^2G + G^2M + M^3)$; (C) update γ_m^{new} in Step 4: $O[G(2M^3 + 3M^2 + M)]$. The computational complexity of SBL is $O[M^2J + k_{\max}(2GM^3 + 5GM^2 + G^2M + GM + M^3)]$.

6. Simulation Results

In this part, we provide numerical simulations of the performance of the proposed MCOA as well as a comparison with the other sparse arrays and the CRB. The array aperture is limited to 8 wavelengths and the number of array sensors is 8. Two coherent signals with equal power impinge on the array with directions $\theta_1 = 10°$, $\theta_2 = 40°$, and the correlation coefficient is set to $[\alpha_1, \alpha_2] = [1, e^{j\pi/4}]$. Define the Root Mean Square Error (RMSE) of the DOA estimates as follows:

$$\mathrm{RMSE} = \sqrt{\frac{1}{K}\frac{1}{Q}\sum_{k=1}^{K}\sum_{q=1}^{Q}\left(\widehat{\theta}_{q,k} - \theta_k\right)^2}, \tag{29}$$

where Q and K are the number of Monte Carlo trials and the total number of coherent signals, respectively. $\widehat{\theta}_{q,k}$ means the qth estimate of the real angle θ_k . Unless other stated, we assume that the mutual coupling constant is $c_0 = 0.12$ and the maximum spacing of sensor pairs is $B = 100$. For each Figure, 1000 Monte Carlo simulations were run to estimate the Root Mean Square Error (RMSE).

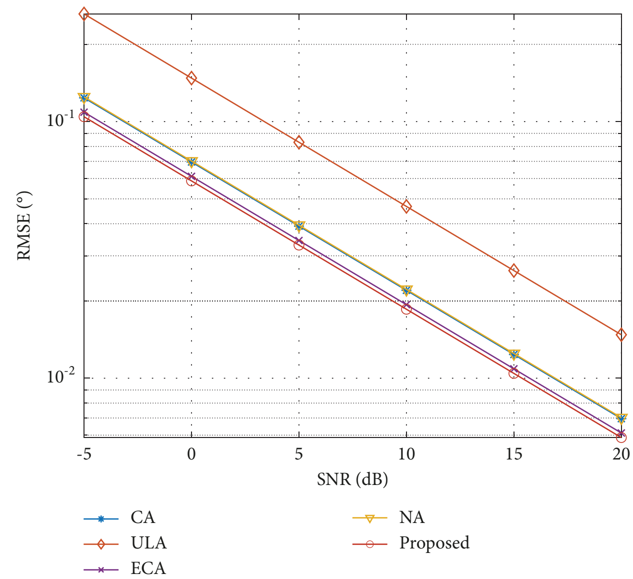

Figure 3: CRB comparison of different arrays.

First, we compare the CRB of different arrays in Figure 3. The result shows that the CRB of the coprime array is very close to the CRB of the proposed array, but the CRB of the proposed array is the smallest among all arrays, which indicates that its performance is optimal.

Figure 4 depicts the spatial spectrum of the SBL method with the proposed array. The signal-to-noise ratio (SNR) is 10 dB and the snapshot is $J = 200$. There are many spectral peaks in the estimation result, but the peak of the incident signal is the highest, which is 40 dB higher than other spectral peaks. It shows that the estimation result of this method is accurate enough to be used for the coherent signal estimation when there is mutual coupling between array sensors.

The proposed array is also compared with other arrays with different SNRs in Figure 5. The SNR varies from −5 dB to 20 dB and the number of snapshots is $J = 200$. All five kinds of arrays can accurately estimate the incident angle of the relevant signals. Due to the influence of mutual coupling, the angle estimation of the CA and ULA decreases greatly, and their RMSE value is larger than the proposed array. Because the influence of mutual coupling leakage is less than that of other arrays, the proposed array can better estimate the DOA of coherent signals.

Figure 6 shows the performance of different arrays with snapshots changing, the coherent signal is consistent with the previous simulation and the SNR is 5 dB. The snapshot varies from 10 to 600. When the snapshot is less than 100, all five arrays cannot work well and the performance is not good enough. However, the RMSE of all the arrays reduces with the snapshot increasing. When the snapshot is larger than 100, the curve of RMSE of the CA and ULA is almost a straight line, because the impact of the mutual coupling leakage at this time is greater than the performance

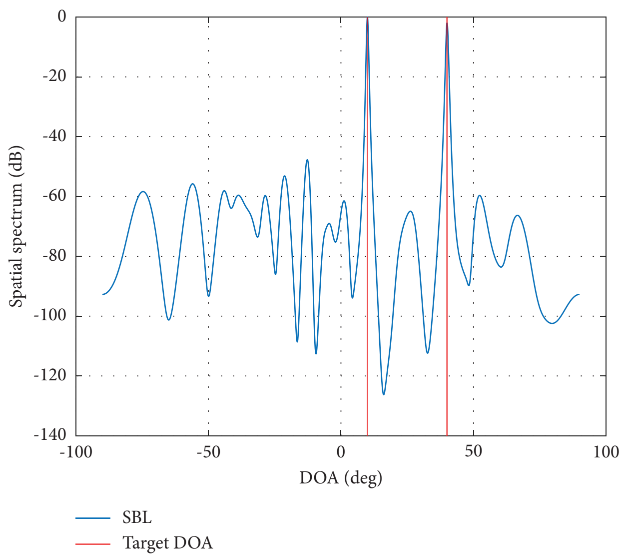

Figure 4: The spatial spectrum for DOA estimation.

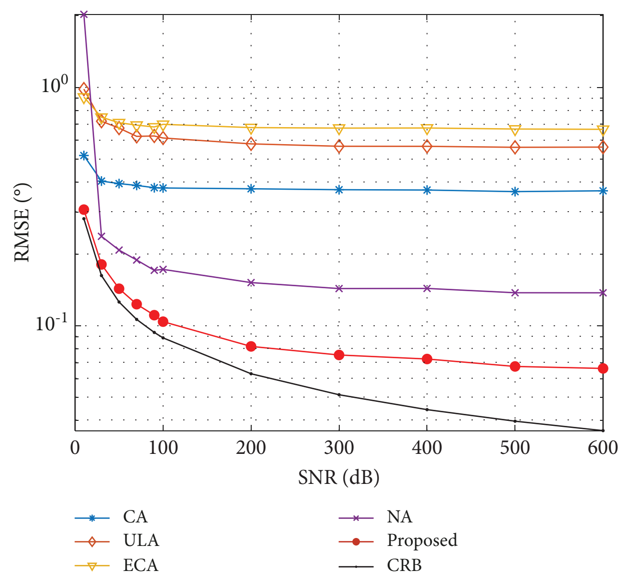

Figure 6: The DOA estimation performance with different snapshots.

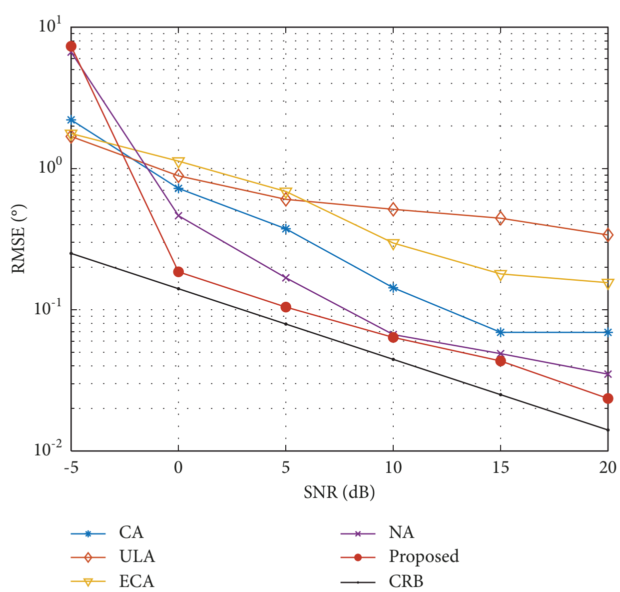

Figure 5: The DOA estimation performance with different SNRs.

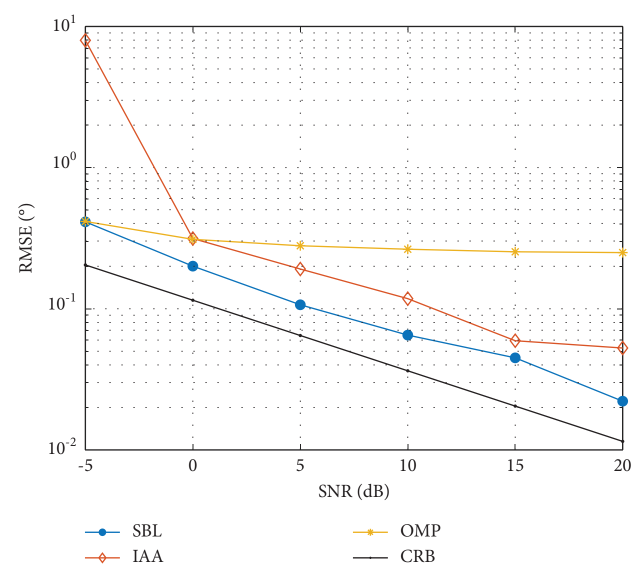

Figure 7: Comparison of RMSE of different algorithms with SNR.

improvement brought about by the increase of snapshots. On the other hand, the performance of the proposed array and NA is better than the other three arrays, and the proposed array has the best performance because the mutual coupling leakage of the proposed array is the smallest among these arrays.

Finally, we compared the SBL algorithm with two other compressed sensing algorithms including the IAA [20] and the OMP [21]. In Figure 7, the SNR changes from −5 dB to 20 dB and the snapshot is 200. The other simulation conditions were the same as before. At low SNR, the SBL has the same performance as IAA and OMP, but when the SNR increases, the performance of OMP hardly improves, and the performance of IAA is better than OMP. The curve of SBL is smoother than the other two algorithms, which means that in this case, its performance is more stable than other algorithms.

7. Conclusions

In this paper, the mutual coupling optimization array with a given number of sensors under the condition of the finite aperture is studied. Compared with the sparse arrays including CA, NA, and ECA, the mutual coupling leakage of the proposed array is smaller. When there is mutual coupling between array sensors, we apply the SBL to DOA estimation of coherent signals and compare its performance with other compressed sensing methods including IAA and OMP. Finally, various simulations are carried out to prove the superior performance of the proposed array for estimating coherent signals in the condition of mutual coupling. In fact, this paper mainly focuses on the coherent signal estimation problem of the sparse array in the 1D-DOA case. By using the previous related research, this result can be extended to an L-shaped array to realize DOA estimation of coherent signal in the 2D-DOA case. Reference [31].

Data Availability

The data used to support the findings of this study are included within the article.

Conflicts of Interest

The authors declare that they have no conflicts of interest.

Acknowledgments

This work was supported by China NSF (Grant nos. 61971217, 61971218, and 61631020), Jiangsu NSF (Grant no. BK20200444), the fund of Sonar Technology Key Laboratory (Research on the theory and algorithm of signal processing for two-dimensional underwater acoustics coprime array) and the fund of Sonar technology key laboratory (Range estimation and location technology of passive target via multiple array combination), Jiangsu Key Research and Developement Project (Grant no. BE2020101), and National Key Research and Development Project (Grant no. 2020YFB1807602).

References

[1] J. Li, Q. Zhang, W. Deng, Y. Tang, X. Zhang, and Q. Wu, "Source direction finding and direct localization exploiting UAV array with unknown gain-phase errors," *IEEE Internet of Things Journal*, vol. 2022, Article ID 3181450, p. 1, 2022.

[2] J. Li, P. Li, P. Li, L. Tang, X. Zhang, and Q. Wu, "Self-position awareness based on cascade direct localization over multiple source data," *IEEE Transactions on Intelligent Transportation Systems*, vol. 1, 9 pages, 2022.

[3] Y. Qian, Z. Yang, and H. Zeng, "Direct position determination for augmented coprime arrays via weighted subspace data fusion method," *Mathematical Problems in Engineering*, vol. 2021, Article ID 2825025, p. 1, 2021.

[4] S. E. Nai, W. Ser, Z. L. Yu, and H. Chen, "Iterative robust minimum variance beamforming," *IEEE Transactions on Signal Processing*, vol. 59, no. 4, pp. 1601–1611, April 2011.

[5] R. Schmidt, "Multiple emitter location and signal parameter estimation," *IEEE Transactions on Antennas and Propagation*, vol. 34, no. 3, pp. 276–280, March 1986.

[6] R. Roy and T. Kailath, "ESPRIT-estimation of signal parameters via rotational invariance techniques," *IEEE Transactions on Acoustics, Speech, & Signal Processing*, vol. 37, no. 7, pp. 984–995, 1989.

[7] C. Zhou, Y. Gu, S. He, and Z. Shi, "A robust and efficient algorithm for coprime array adaptive beamforming," *IEEE Transactions on Vehicular Technology*, vol. 67, no. 2, pp. 1099–1112, 2018.

[8] S. Marcos, A. Marsal, and M. Benidir, "The propagator method for source bearing estimation," *Signal Processing*, vol. 42, no. 2, pp. 121–138, 1995.

[9] N. D. Sidiropoulos, G. B. Giannakis, and R. Bro, "Blind PARAFAC receivers for DS-CDMA systems," *IEEE Transactions on Signal Processing*, vol. 48, no. 3, pp. 810–823, March 2000.

[10] F. Wen, J. Shi, and Z. Zhang, "Generalized spatial smoothing in bistatic EMVS-MIMO radar," *Signal Processing*, vol. 193, Article ID 108406, 2022.

[11] T.-J. Shan, M. Wax, and T. Kailath, "On spatial smoothing for direction-of-arrival estimation of coherent signals," *IEEE Transactions on Acoustics, Speech, & Signal Processing*, vol. 33, no. 4, pp. 806–811, August 1985.

[12] S. U. Pillai and B. H. Kwon, "Forward/backward spatial smoothing techniques for coherent signal identification," *IEEE Transactions on Acoustics, Speech, & Signal Processing*, vol. 37, no. 1, pp. 8–15, 1989.

[13] W. Du and R. L. Kirlin, "Improved spatial smoothing techniques for DOA estimation of coherent signals," *IEEE Transactions on Signal Processing*, vol. 39, no. 5, pp. 1208–1210, May 1991.

[14] W. X. Du and R. L. Kirlin, "Improved spatial smoothing techniques for DOA estimation of coherent signals," *IEEE Transactions on Signal Processing*, vol. 39, no. 5, pp. 1208–1210, 1991.

[15] J. Shi, Z. Yang, and Y. Liu, "On parameter identifiability of diversity-smoothing-based MIMO radar," *IEEE Transactions on Aerospace and Electronic Systems*, vol. 58, no. 3, pp. 1660–1675, 2022.

[16] F.-M. Han and X.-Da Zhang, "An ESPRIT-like algorithm for coherent DOA estimation," *IEEE Antennas and Wireless Propagation Letters*, vol. 4, pp. 443–446, 2005.

[17] Z. Yang and L. Xie, "Exact joint sparse frequency recovery via optimization methods," *IEEE Transactions on Signal Processing*, vol. 64, no. 19, pp. 5145–5157, 2016.

[18] Z. Yang and L. Xie, "Enhancing sparsity and resolution via reweighted atomic norm minimization," *IEEE Transactions on Signal Processing*, vol. 64, no. 4, pp. 995–1006, 2016.

[19] Y. Yu, A. P. Petropulu, and H. V. Poor, "Measurement matrix design for compressive sensing–based MIMO radar," *IEEE Transactions on Signal Processing*, vol. 59, no. 11, pp. 5338–5352, 2011.

[20] L. Du, T. Yardibi, J. Li, and P. Stoica, "Review of user parameter-free robust adaptive beamforming algorithms," in *Proceedings of the 2008 42nd Asilomar Conference on Signals, Systems and Computers*, pp. 363–367, Beijing China, June 2008.

[21] S. K. Sahoo and A. Makur, "Signal recovery from random measurements via extended orthogonal matching Pursuit," *IEEE Transactions on Signal Processing*, vol. 63, no. 10, pp. 2572–2581, 2015.

[22] M. E. Tipping, "Sparse Bayesian learning and the relevance vector machine," *Journal of Machine Learning Research*, vol. 1, pp. 211–244, 2001.

[23] P. Pal and P. P. Vaidyanathan, "Nested arrays: a novel approach to array processing with enhanced degrees of freedom," *IEEE Transactions on Signal Processing*, vol. 58, no. 8, pp. 4167–4181, Aug, 2010.

[24] P. P. Vaidyanathan and P. Pal, "Sparse sensing with Co-prime samplers and arrays," *IEEE Transactions on Signal Processing*, vol. 59, no. 2, pp. 573–586, 2011.

[25] A. Moffet, "Minimum-redundancy linear arrays," *IEEE Transactions on Antennas and Propagation*, vol. 16, no. 2, pp. 172–175, 1968.

[26] Z. Ye, J. Dai, X. Xu, and X. Wu, "DOA estimation for uniform linear array with mutual coupling," *IEEE Transactions on*

Aerospace and Electronic Systems, vol. 45, no. 1, pp. 280–288, 2009.

[27] J. Dai, D. Zhao, and X. Ji, "A sparse representation method for DOA estimation with unknown mutual coupling," *IEEE Antennas and Wireless Propagation Letters*, vol. 11, pp. 1210–1213, 2012.

[28] B. Liao, Z.-G. Zhang, and S.-C. Chan, "DOA estimation and tracking of ULAs with mutual coupling," *IEEE Transactions on Aerospace and Electronic Systems*, vol. 48, no. 1, pp. 891–905, 2012.

[29] P. P. Vaidyanathan and P. Pal, "Why does direct-MUSIC on sparse-arrays work?" in *Proceedings of the 2013 Asilomar Conference on Signals, Systems and Computers*, pp. 2007–2011, Pacific Grove, CA, USA, May 2013.

[30] P. P. Vaidyanathan and P. Pal, "Direct-MUSIC on sparse arrays," in *Proceedings of the 2012 International Conference on Signal Processing and Communications (SPCOM)*, pp. 1–5, Bangalore, India, August 2012.

[31] C. L. Liu and P. P. Vaidyanathan, "Super nested arrays: linear sparse arrays with reduced mutual coupling—Part I: fundamentals," *IEEE Transactions on Signal Processing*, vol. 64, no. 15, pp. 3997–4012, 2016.

[32] X. Lai, W. Chen, B. Li, and H. Zeng, "Improved DFT method for DOA estimation with extended coprime array:based on large difference coarray," *International Journal of Electronics*, vol. 2021, no. 5, Article ID 1941289, pp. 733–747, 2022.

Hindawi
Mathematical Problems in Engineering
Volume 2022, Article ID 9982817, 12 pages
https://doi.org/10.1155/2022/9982817

Research Article

Direct Position Determination of Noncircular Sources with Multiple Nested Arrays via Weighted Subspace Data Fusion

Yang Qian[1,2] **Xinlei Shi**[1,2] **Haowei Zeng**[1,2] **and Xudong Dong**[1,2]

[1] *College of Electronic Information Engineering, Nanjing University of Aeronautics and Astronautics, Nanjing 211106, China*
[2] *Key Laboratory of Dynamic Cognitive System of Electromagnetic Spectrum Space (Nanjing University of Aeronautics and Astronautics), Ministry of Industry and Information Technology, Nanjing 211106, China*

Correspondence should be addressed to Yang Qian; qianyang@nuaa.edu.cn

Received 27 May 2022; Revised 23 July 2022; Accepted 30 July 2022; Published 20 September 2022

Academic Editor: Junpeng Shi

Direct position determination (DPD) of noncircular (NC) sources for multiple nested arrays (NA) is researched in this study. For noncircular sources, the dimension reduction method is used to decrease the computing complexity and remove the noncircular phase. Furthermore, nested array and noncircular sources extend spatial degree of freedom. Due to inferior stability and noise susceptibility of original algorithm, we propose SNR weighted subspace data fusion (W-SDF) algorithm. Each observation station places a nested array, spatial smoothing technology, and sum and difference co-array are used to deal with the nested array. Simulation results show that under nested array and noncircular sources, the proposed W-SDF algorithm has decreased the complexity of the algorithm and improved the location accuracy, degree of freedom, and resolution.

1. Introduction

In modern wireless location system, the focus of research is fast and accurate signal location [1]. The traditional positioning technology system is mostly a two-step estimation mode such as the correlation measurement, time difference of arrival (TDOA), frequency difference of arrival (FDOA), and energy gain. Therefore, location information is extracted from the signal data radiated by the target [2]. Then, the position parameters of the target are obtained from the above observations. The two-step positioning method has the characteristics of decentralization and does not need to transmit all signal data to the same central station for processing [3]. Therefore, it has low requirements for communication transmission bandwidth and calculation, which is convenient for engineering implementation [4]. From the positioning principle, the two-step positioning method is difficult to obtain the asymptotically optimal estimation accuracy, because it has experienced many processing links [5]. In addition, the two-step positioning is easy to lose the correlation of multiple stations, and the lost information is difficult to make up in the second-step positioning link [6]. In order to avoid the above problems, the direct position determination method is proposed. The core idea is to directly obtain the position information of the target from the original sampling signal without estimating the intermediate observation value. This principle avoids the problem of data association [7–10]. Therefore, direct positioning method has higher estimation accuracy and resolution [11–14].

Nowadays, there have been few reports about sparse array for direct determination position. In 2010, professor P. Pal proposed the nested array structure [15]. The nested array can greatly increase the degree of freedom of the array than the uniform linear array (ULA) [16–21]. In 2011, professor P. Pal proposed the coprime array structure, which is basically the same as the nested array structure. The obtained array degree of freedom is less than the nested array, but more sparse than the nested array [22]. J. Galy used the noncircular features of sources to increase the performance of DOA estimation. J. Galy proposed the MUSIC algorithm for noncircular sources, which pioneered the application of noncircular sources in spatial spectrum estimation [23]. Yin applied the noncircular features of sources to direct positioning field with a moving array. The noncircular signal improves spatial degree of freedom and increases the positioning accuracy [24]. Zhang et al. applied the noncircular characteristics of sources to direct positioning with a moving coprime array [25]. At present, noncircular signal is rarely applied in direct positioning with multiple nested arrays [26–29]. Therefore, it is very important to study the noncircular sources for direct positioning with multiple nested arrays.

In this study, we use the noncircular sources characteristic to expand the spatial degree of freedom. The dimension method is used to decrease the computing complexity. In this study, the nested array is introduced into direct positioning. Therefore, array aperture is extended and the spatial smoothing method is adopted. Because the traditional SDF method is easily affected by noise and has inferior stability, the weighted SDF method is proposed [8]. Therefore, we can obtain high positioning accuracy.

The main contributions are as follows:

(1) We apply noncircular sources and the dimensionality reduction method to the direct location with noncircular sources to reduce the computational complexity and remove the phase of noncircular sources.
(2) We place a nested array on each observation station and use spatial smoothing technology and sum and difference co-array to deal with the nested array to expand the array aperture.
(3) We assign a weight to each station to improve the positioning accuracy because the SDF algorithm is vulnerable to noise and poor stability. Therefore, SNR weighted SDF loss function is set up.

The composition is as below. In Section 2, we expound on a direct position determination model, a common two-level nested array, and some notions about noncircular sources. In the next section, we depict spatial smoothing technology and SNR weighted SDF algorithm. In Section 4, we analyze the performance about the W-SDF algorithm and expound on its advantages from degree of freedom, computing complexity, and positioning accuracy. In Section 5, we emulate the weighted SDF algorithm and compare the performance of proposed algorithm with that of other algorithms. The last section summarizes this study.

Notations. $(\bullet)^H$, $(\bullet)^T$, and $(\bullet)^*$ mean conjugate transpose, transpose, and conjugate. The symbol $\otimes$ and $\mathrm{vec}(\bullet)$ mean the Kronecker product and matrix vectorization. I_n means an $n \times n$ unit matrix and $E(\bullet)$ means the mathematical expectation.

2. Preliminaries

In this section, we expound on a common two-level nested array and some notions about noncircular sources. Then, we describe multiple nested arrays combination direct positioning model.

2.1. Two-Level Nested Array Model. In Figure 1, the ordinary two-level nested array has $H = 6$ array elements, the dense uniform linear array (ULA) has $M = 3$ array elements, and the sparse array has $N = 3$ array elements. Uniform linear array element interval is $d_1 = d$, and sparse linear array element interval is $d_2 = 4d$, where $d = \lambda/2$, and λ expresses as signal wavelength. Figure 2 shows the positive sum co-array (a), the negative sum co-array (b), and difference co-array (c). Successive fictitious elements are placing from $-11d$ to $11d$.

2.2. Direct Position Determination Model. Direct position determination scenario is shown in Figure 3. Q independent narrow-band noncircular sources are in far-field X-Y plane. Multiple sources are $\mathbf{p}_q = [x_q, y_q]^T$ $(q = 1, 2, \ldots Q)$. L nested arrays with $H = M + N$ array elements are placing at L stations $\mathbf{u}_l = [x_{ul}, y_{ul}]^T$ $(l = 1, 2, \ldots, L)$.

The output signal of the $lth\,(l = 1, 2, \ldots, L)$ array at the $kth\,(k = 1, 2, 3 \ldots K)$ sampling snapshot time can be indicated as follows [9]:

$$\mathbf{r}_l(k) = \sum_{q=1}^{Q} \mathbf{a}_l(\mathbf{p}_q) f_{l,q}(k) + \mathbf{n}_l(k), \tag{1}$$

where $f_{l,q}(k)$ means the source waveform, $\mathbf{n}_l(k)$ means the noise vector for the lth station, and $\mathbf{a}_l(\mathbf{p}_q)$ means the orientation vector. This is all depending on the arrival direction orientation of the signal $\theta_l(\mathbf{p}_q)$ [9]:

$$\begin{aligned} \theta_l(\mathbf{p}_q) &= \arctan \frac{\mathbf{x}_{ul}(1) - \mathbf{p}_q(1)}{\mathbf{y}_{ul}(2) - \mathbf{p}_q(2)}, \\ \mathbf{a}_l(\mathbf{p}_q) &= \left[1, e^{-j2\pi d \sin\theta_l(\mathbf{p}_q)}, \ldots, e^{-j2\pi(H-1)d\sin\theta_l(\mathbf{p}_q)}\right]^T. \end{aligned} \tag{2}$$

Equation (1) can be indicated as follows [9]:

$$\mathbf{r}_l(k) = \mathbf{A}_l(\mathbf{p})\mathbf{f}_l(\mathbf{k}) + \mathbf{n}_l(k), \tag{3}$$

where

$$\begin{aligned} \mathbf{A}_l(\mathbf{p}) &= \left[\mathbf{a}_l(\mathbf{p}_1), \mathbf{a}_l(\mathbf{p}_2), \ldots, \mathbf{a}_l(\mathbf{p}_Q)\right], \\ \mathbf{f}_l(k) &= \left[f_{l,1}(k), f_{l,2}(k), \ldots, f_{l,Q}(k)\right]^T, \\ \mathbf{p} &= \left[\mathbf{p}_1^{\mathbf{T}}, \mathbf{p}_2^{\mathbf{T}}, \ldots, \mathbf{p}_Q^{\mathbf{T}}\right]^T, \\ \mathbf{n}_l(k) &= \left[\mathbf{n}_{l,1}(k), \mathbf{n}_{l,2}(k), \ldots, \mathbf{n}_{l,H}(k)\right]^T. \end{aligned} \tag{4}$$

2.3. Noncircular Sources Model. The sources studied in this study are noncircular sources. Reference [29] shows that any digital modulated signal $f(t)$ in the complex plane expression is obtained as follows:

$$f(t) = \sigma e^{-j\varphi}\left(\sqrt{\frac{1+k}{2}} f_1(t) + j\sqrt{\frac{1-k}{2}} f_Q(t)\right), \tag{5}$$

where φ is rotation phase, $k\,(0 \le k \le 1)$ controls signal amplitude, signal power $E\{|f(t)^2|\} = \sigma^2$, $f_1(t)$ and $f_Q(t)$ are

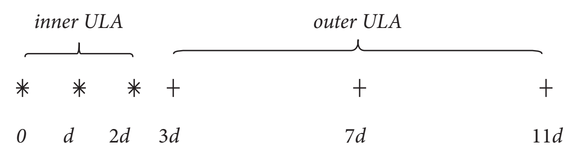

Figure 1: Two-level nested array.

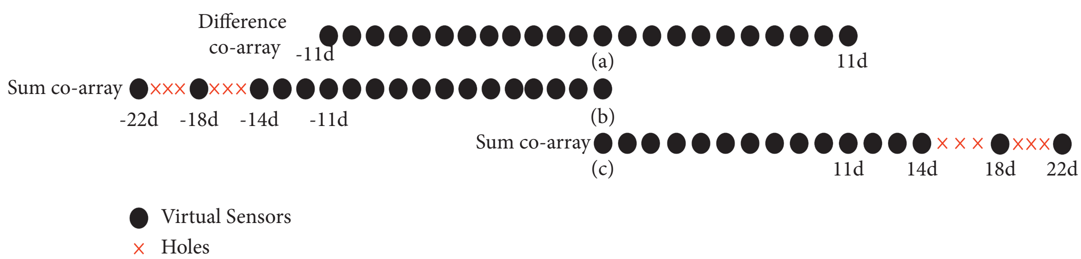

Figure 2: Difference co-array and sum co-array.

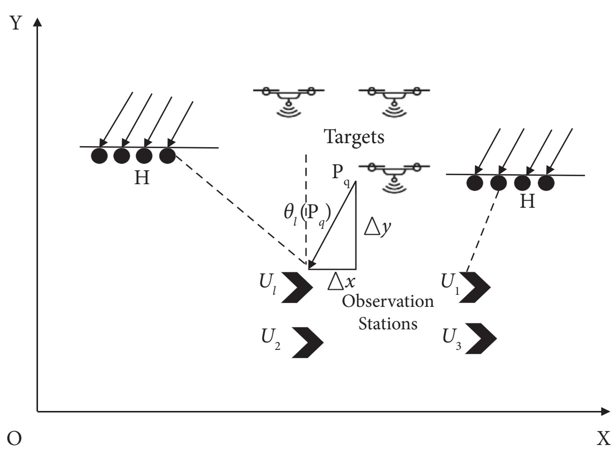

Figure 3: Multiple arrays combination positioning scene.

unit codirectional component and unit orthogonal component, satisfying $E\{|f_1(t)|^2\} = 1$, $E\{|f_Q(t)|^2\} = 1$, and $E\{f_1(t)f_Q(t)\} = 0$. When $k = 0$, the sources are called circular sources; when $k \neq 0$, the sources are called noncircular sources.

In order to measure the degree of noncircular for sources, literature [26–28] give the definition of noncircular sources:

$$E\left[\mathbf{f}_l(k)\mathbf{f}_l^{\mathbf{H}}(k)\right] = \rho e^{j\varphi} E\left[\mathbf{f}_l(k)\mathbf{f}_l^T(k)\right], \tag{6}$$

where φ denotes the noncircular phase, and ρ denotes the noncircular rate of the value in 0–1. In particular, when $\rho = 1$, the signal was called strictly noncircular sources.

According to reference [27], noncircular sources can be indicated as follows:

$$\mathbf{f}(t) = \mathbf{\Phi}\mathbf{f}^0(t), \tag{7}$$

where

$$\mathbf{\Phi} = \begin{bmatrix} e^{-j\varphi_1} & 0 & \ldots & 0 \\ 0 & e^{-j\varphi_2} & \ldots & . \\ . & . & . & . \\ 0 & . & 0 & e^{-j\varphi_Q} \end{bmatrix}, \tag{8}$$

where $\mathbf{f}^0(t)$ means the real part of the signal.

According to equation (7), equation (4) can be indicated as follows:

$$\mathbf{r}_l(k) = \mathbf{A}_l(\mathbf{p})\mathbf{\Phi}\mathbf{f}_l^0(k) + \mathbf{n}_l(k), \tag{9}$$

where

$$\mathbf{f}_l^0(k) = \left[f_{l,1}^{(0)}(k), f_{l,2}^{(0)}(k), \ldots, f_{l,Q}^{(0)}(k)\right]^T. \tag{10}$$

3. The Proposed W-SDF Algorithm

In this section, we elaborate steps of weighted SDF algorithm, the process of spatial smoothing technology, and SNR weighting process.

3.1. Covariance Vectorization Signal. On the basis of the features of noncircular sources, we make use of dimension reduction method to decrease computational complexity and remove noncircular phase. We combine the SDF algorithm for direct position determination to obtain spectral peak search function.

We use features of noncircular sources to expand the received signal vector as follows [9]:

$$\mathbf{z}_l(k) = \begin{bmatrix} \mathbf{r}_1(k) \\ \mathbf{r}_1^*(k) \end{bmatrix} = \begin{bmatrix} \mathbf{A}_l(\mathbf{p})\mathbf{f}_l(k) \\ \mathbf{A}_l^*(\mathbf{p})\mathbf{f}_l^*(k) \end{bmatrix} + \begin{bmatrix} \mathbf{n}_l(k) \\ \mathbf{n}_l^*(k) \end{bmatrix}. \tag{11}$$

It can be obtained from equation (7):

$$\mathbf{f}_l^*(k) = \mathbf{\Phi}^*\mathbf{f}_l^{(0)}(k) = \mathbf{\Phi}^*\mathbf{\Phi}^{-1}\mathbf{f}_l(k) = \left(\mathbf{\Phi}^*\right)^2\mathbf{f}_l(k). \tag{12}$$

Then, equation (11) can be indicated as follows:

$$\mathbf{z}_l(k) = \begin{bmatrix} \mathbf{A}_l(\mathbf{p}) \\ \mathbf{A}_l^*(\mathbf{p})\mathbf{\Phi}^*\mathbf{\Phi}^* \end{bmatrix}\mathbf{f}_l(k) + \begin{bmatrix} \mathbf{n}_l(k) \\ \mathbf{n}_l^*(k) \end{bmatrix} = \mathbf{C}_l(\mathbf{p})\mathbf{f}_l(k) + \begin{bmatrix} \mathbf{n}_l(k) \\ \mathbf{n}_l^*(k) \end{bmatrix}, \quad (13)$$

where

$$\% \ \mathbf{C}_l(\mathbf{p}) = \begin{bmatrix} \mathbf{A}_l(\mathbf{p}) \\ \mathbf{A}_l(\mathbf{p})\mathbf{\Phi}^*\mathbf{\Phi}^* \end{bmatrix} = \left[\mathbf{c}_l(\mathbf{p}_1), \mathbf{c}_l(\mathbf{p}_2), \ldots \mathbf{c}_l(\mathbf{p}_Q)\right], \quad (14)$$

where

$$\mathbf{c}_l(\mathbf{p}_q) = \begin{bmatrix} \mathbf{a}_l(\mathbf{p}) \\ \mathbf{a}_l(\mathbf{p})e^{j2\varphi_q} \end{bmatrix}. \quad (15)$$

The covariance matrix is as follows:

$$\mathbf{R}_l = \frac{1}{K}\sum_{k=1}^{K}\mathbf{Z}_l(k)\mathbf{Z}_l^H(k) = \sum_{i=1}^{q}\sigma_{l,q}^2\mathbf{c}_l(\mathbf{p}_q)\mathbf{c}_l^H(\mathbf{p}_q) + \sigma_n^2\mathbf{I}, \quad (16)$$

where $\sigma_{l,q}^2$ means the power of the qth radiate source and σ_n^2 means noise power. For making use of features of nested array, we make the covariance matrix vector as follows [28]:

$$\begin{aligned} \mathbf{z}_l &= vec(\mathbf{R}_l) \\ &= vec\sum_{i}^{D}\sigma_{l,q}^2\mathbf{c}_l(\mathbf{p}_q)\mathbf{c}_l^H(\mathbf{p}_q) + \sigma_n^2\widetilde{I} \\ &= \mathbf{H}_l(\mathbf{p})\boldsymbol{\mu} + \sigma_n^2\widetilde{\mathbf{I}}, \end{aligned} \quad (17)$$

where μ is the signal power vector and

$$\begin{aligned} \mathbf{H}_l(\mathbf{p}) &= \left[\mathbf{c}_l^*(\mathbf{p}_1)\otimes\mathbf{c}_l(\mathbf{p}_1), c_l^*(\mathbf{p}_2)\otimes\mathbf{c}_l(\mathbf{p}_2), \ldots, \mathbf{c}_l^*(\mathbf{p}_Q) \otimes\mathbf{c}_l(\mathbf{p}_Q)\right], \\ \widetilde{\mathbf{I}} &= vec(\mathbf{I}_H), \end{aligned} \quad (18)$$

where

$$\begin{aligned} \left[\mathbf{c}_l^*(\mathbf{p}_q)\otimes\mathbf{c}_l(\mathbf{p}_q)\right] &= \begin{bmatrix} \mathbf{a}_l(\mathbf{p}_q) \\ \mathbf{a}_l^*(\mathbf{p}_q)e^{j2\varphi_q} \end{bmatrix}^* \otimes \begin{bmatrix} \mathbf{a}_l(\mathbf{p}_q) \\ \mathbf{a}_l^*(\mathbf{p}_q)e^{j2\varphi_q} \end{bmatrix} \\ &= \begin{bmatrix} \mathbf{a}_l^*(\mathbf{p}_q)\otimes\mathbf{a}_l(\mathbf{p}_q) \\ \mathbf{a}_l^*(\mathbf{p}_q)\otimes\mathbf{a}_l^*(\mathbf{p}_q)e^{j2\varphi_q} \\ \mathbf{a}_l(\mathbf{p}_q)\otimes\mathbf{a}_l(\mathbf{p}_q)e^{-j2\varphi_q} \\ \mathbf{a}_l(\mathbf{p}_q)\otimes\mathbf{a}_l^*(\mathbf{p}_q) \end{bmatrix} = \begin{bmatrix} p_1 \\ p_2 \\ p_3 \\ p_4 \end{bmatrix}, \end{aligned} \quad (19)$$

where $p_1 = \mathbf{a}_l^*(\mathbf{p}_q)\otimes\mathbf{a}_l(\mathbf{p}_q)$, $p_2 = \mathbf{a}_l^*(\mathbf{p}_q)\otimes\mathbf{a}_l^*(\mathbf{p}_q)e^{j2\varphi_q}$, $p_3 = \mathbf{a}_l(\mathbf{p}_q)\otimes\mathbf{a}_l(\mathbf{p}_q)e^{-j2\varphi_q}$, and $p_4 = \mathbf{a}_l(\mathbf{p}_q)\otimes\mathbf{a}_l^*(\mathbf{p}_q)$. In Figure 4, the successive array elements of difference co-array are in range of $[-(M_1-1)d, (M_1-1)d]$, where $M_1 = MN + N$, $M = 4$, $N = 4$. DIFF I and DIFF II represent difference co-array. The successive array elements of sum co-array are in range of $[-(M_2-1)d, 0]$ and $[0, (M_2-1)d]$, where $M_2 = MN + M + N$. SUM I and SUM II represent sum co-array.

After the elements are sorted and duplicated according to the phase, the two vectors can be regarded as a direction vector of continuous difference co-array DCA:

$$\mathbf{c}_d(\mathbf{p}_q) = e^{-j2\pi U_d d\sin\theta_l(\mathbf{p}_q)/\lambda}, \quad (20)$$

where $U_d = \langle -R_1, R_1\rangle$, $R_1 = MN + N - 1$.

The equivalent received signal of DCA can be obtained as follows:

$$\mathbf{b}_d = \mathbf{H}_d\boldsymbol{\gamma} + \sigma_n^2\mathbf{u}, \quad (21)$$

where $\mathbf{H}_d = [\,\mathbf{c}_d(\mathbf{p}_1) \ \ \mathbf{c}_d(\mathbf{p}_2) \ \ \ldots \ \ \mathbf{c}_d(\mathbf{p}_Q)\,]$ is direction matrix of DCA. $\boldsymbol{\gamma}$ is equivalent incident signal vector. $\mathbf{u}$ is vector with only the middle $R_1 + 1$ elements of 1 and other elements of $\mathbf{u}$ are 0.

The elements are sorted and removed according to phase. After repetition, the direction vectors can be indicated as follows, respectively:

$$\begin{aligned} \mathbf{c}_s^-(\mathbf{p}_q) &= e^{-j2\pi U_s^- d\sin\theta_l(p_q)/\lambda}e^{j2\varphi_q}, \\ \mathbf{c}_s^+(\mathbf{p}_q) &= e^{-j2\pi U_d d\sin\theta_l(p_q)/\lambda}e^{-j2\varphi_q}, \end{aligned} \quad (22)$$

where $U_s^- = \langle -R_3, R_2\rangle$, $R_2 = 0$, and $R_3 = MN + M + N - 1$.

The equivalent received sources of SCA I and the equivalent received sources of SCA II can be obtained as follows:

$$\begin{aligned} \mathbf{b}_s^- &= \mathbf{H}_s^-\boldsymbol{\gamma}, \\ \mathbf{b}_s^+ &= \mathbf{H}_s^+\boldsymbol{\gamma}, \end{aligned} \quad (23)$$

where $\mathbf{H}_s^- = [\,\mathbf{c}_s^-(\mathbf{p}_1) \ \ \mathbf{c}_s^-(\mathbf{p}_2) \ \ \ldots \ \ \mathbf{c}_s^-(\mathbf{p}_Q)\,]$ is directional matrix of SCA I and $\mathbf{H}_s^+ = [\,\mathbf{c}_s^+(\mathbf{p}_1) \ \ \mathbf{c}_s^+(\mathbf{p}_2) \ \ \ldots \ \ \mathbf{c}_s^+(\mathbf{p}_Q)\,]$ is directional matrix of SCA II.

3.2. Spatial Smoothing Technology. Different from the traditional spatial smoothing of the full array, this section carries out the strategy of backward spatial smoothing for the continuous difference co-array DCA and the negative and positive semiaxis continuous sum co-array SCA I and SCA II respectively.

In Figure 4, for successive difference co-array DCA, we divide DCA into $R_1 + 1$ equivalent subarrays, which has $R_1 + 1$ elements each. The corresponding received signal can be indicated as follows [9]:

$$\mathbf{b}_{di} = \widetilde{\mathbf{H}}_d\mathbf{\Psi}^{i-1}\boldsymbol{\gamma} + \sigma_n^2\widetilde{\mathbf{u}}_i, \quad (24)$$

where b_{di} means $ith\,(i = 1, 2, \ldots, R_1 + 1)$ subarray, $\widetilde{\mathbf{u}}_i$ means the vector that the ith element value is 1, and the other element values are all 0 [9]. $\widetilde{\mathbf{H}}_d = [\widetilde{\mathbf{c}}_d(\mathbf{p}_1),$

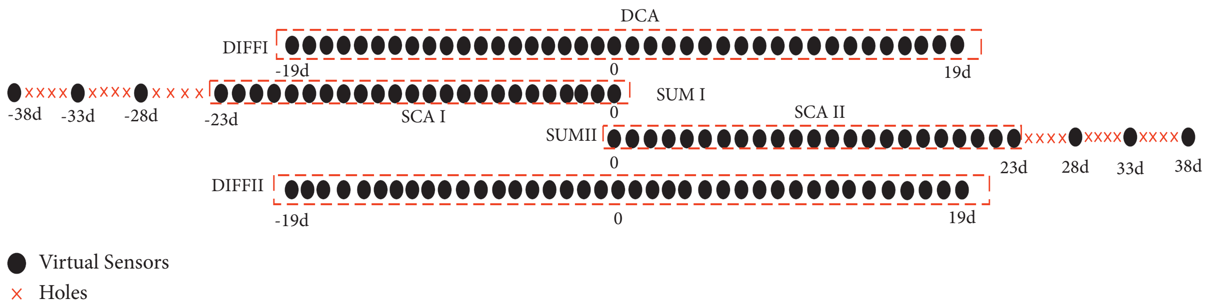

Figure 4: Array graph of sum and difference co-array.

$\tilde{\mathbf{c}}_d(\mathbf{p}_2), \ldots, \tilde{\mathbf{c}}_d(\mathbf{p}_q)]$ means the orientation matrix of SS-DCA, and its qth orientation vector can be indicated as follows [9]:

$$\tilde{\mathbf{c}}_d(\mathbf{p}_q) = \left[1, e^{-j\pi \sin\theta_l(\mathbf{p}_q)}, e^{-j2\pi \sin\theta_l(\mathbf{p}_q)}, \ldots, e^{-jR_1\pi \sin\theta_l(\mathbf{p}_q)}\right]^T, \tag{25}$$

$$\boldsymbol{\Psi} = diag\left\{e^{j\pi \sin\theta_l(\mathbf{p}_1)}, e^{j\pi \sin\theta_l(\mathbf{p}_2)}, \ldots, e^{j\pi \sin\theta_l(\mathbf{p}_Q)}\right\}. \tag{26}$$

The received sources of $R_1 + 1$ subarrays are connected together, and equation (26) shows received sources matrix after spatial smoothing $\mathbf{B}_d \in C^{(R_1+1)\times(R_1+1)}$:

$$\begin{aligned} \mathbf{B}_d &= \left[\mathbf{b}_{d1}, \mathbf{b}_{d2}, \ldots, \mathbf{b}_{d(R_1+1)}\right] \\ &= \tilde{\mathbf{H}}_d\left[\boldsymbol{\gamma}, \boldsymbol{\Psi\gamma}, \ldots, \boldsymbol{\Psi}^{R_1}\boldsymbol{\gamma}\right] + \sigma_n^2 I_{R_1+1} \\ &= \tilde{\mathbf{H}}_d\tilde{\mathbf{S}} + \sigma_n^2\mathbf{I}_{R_1+1}, \end{aligned} \tag{27}$$

where $\tilde{\mathbf{S}} = [\boldsymbol{\gamma}, \boldsymbol{\Psi\gamma}, \ldots, \boldsymbol{\Psi}^{R_1}\boldsymbol{\gamma}]$, and $\mathbf{B}_d$ means the received sources of the first smooth subarray SS-DCA. Element location range of SS-DCA is $\langle 0, R_1\rangle$.

For successive sum co-array, they are divided into $R_1 + 1$ subarray. The number of elements of each subarray is $R_3 - R_2 - R_1 + 1$. After divided, the $ith(i = 1, 2, \ldots, R_1 + 1)$ received sources of the SCA I and received sources of SCA II are as follows [9]:

$$\begin{aligned} \mathbf{b}_{si}^- &= \widetilde{\mathbf{H}_s^-}\boldsymbol{\Psi}^{i-1}\boldsymbol{\gamma}, \\ \mathbf{b}_{si}^+ &= \widetilde{\mathbf{H}_s^+}\boldsymbol{\Psi}^{i-1}\boldsymbol{\gamma}, \end{aligned} \tag{28}$$

where $\widetilde{\mathbf{H}_s^-} = [\tilde{\mathbf{c}}_s^-(\mathbf{p}_1), \tilde{\mathbf{c}}_s^-(\mathbf{p}_2), \ldots, \tilde{\mathbf{c}}_s^-(\mathbf{p}_q)]$, the array elements location range of SS-SCA I is $\langle -(R_3 - R_1), 0\rangle$, and the corresponding qth orientation vector can be indicated as follows:

$$\tilde{\mathbf{c}}_s^-(\mathbf{p}_q) = \left[e^{j(R3-R_1)\pi \sin\theta_l(\mathbf{p}_q)}e^{j2\varphi_q}, \ldots, e^{j\pi \sin\theta_l(\mathbf{p}_q)}e^{j2\varphi_q}, e^{j2\varphi_q}\right]^T, \tag{29}$$

where $\widetilde{\mathbf{H}_s^+} = [\tilde{\mathbf{c}}_s^+(\mathbf{p}_1), \tilde{\mathbf{c}}_s^+(\mathbf{p}_2), \ldots, \tilde{\mathbf{c}}_s^+(\mathbf{p}_q)]$, the array elements location range of SS-SCA II is $\langle R_1, R_3\rangle$, and the corresponding qth orientation vector can be indicated as follows:

$$\tilde{\mathbf{c}}_s^+(\mathbf{p}_q) = \left[e^{-jR_1\pi \sin\theta_l(\mathbf{p}_q)}e^{-j2\varphi_q}, e^{-j(R_1+1)\pi \sin\theta_l(\mathbf{p}_q)}e^{-j2\varphi_q}, \ldots, e^{-jR_3\pi \sin\theta_l(\mathbf{p}_q)}e^{-j2\varphi_q}\right]^T. \tag{30}$$

The received sources matrix of SS-SCA I and the received sources matrix of SS-SCA II are indicated as follows:

$$\begin{aligned} \mathbf{B}_s^- &= \left[\mathbf{b}_{s1}^-, \mathbf{b}_{s2}^-, \ldots, \mathbf{b}_{s(R_1+1)}^-\right] = \widetilde{\mathbf{H}_s^-}\tilde{\mathbf{S}}, \\ \mathbf{B}_s^+ &= \left[\mathbf{b}_{s1}^+, \mathbf{b}_{s2}^+, \ldots, \mathbf{b}_{s(R_1+1)}^+\right] = \widetilde{\mathbf{H}_s^+}\tilde{\mathbf{S}}. \end{aligned} \tag{31}$$

The received signal consists of $\mathbf{B}_s^-, \mathbf{B}_d, \mathbf{B}_s^+$, as shown in the following equation:

$$\tilde{\mathbf{B}} = \begin{bmatrix} \mathbf{B}_s^- \\ \mathbf{B}_d \\ \mathbf{B}_s^+ \end{bmatrix} = \begin{bmatrix} \tilde{\mathbf{H}}_s^- \\ \tilde{\mathbf{H}}_d \\ \tilde{\mathbf{H}}_s^+ \end{bmatrix}\tilde{S} + \begin{bmatrix} \mathbf{O}_{(R_3-R_1+1)\times(R_1+1)} \\ \sigma_n^2\mathbf{I}_{R_1+1} \\ \mathbf{O}_{(R_3-R_1+1)\times(R_1+1)} \end{bmatrix} = \tilde{\mathbf{H}}\tilde{\mathbf{S}} + \mathbf{U}, \tag{32}$$

where $\tilde{\mathbf{H}} = \left[\tilde{\mathbf{c}}(\mathbf{p}_1) \;\; \tilde{\mathbf{c}}(\mathbf{p}_2) \;\; \ldots \;\; \tilde{\mathbf{c}}(\mathbf{p}_q)\right]$ is direction matrix of SDCA, and SDCA denotes fictitious array after spatial smoothing and corresponding qth orientation vector can be indicated as follows:

$$\tilde{\mathbf{c}}(\mathbf{p}) = \begin{bmatrix} \tilde{\mathbf{c}}_s^- \\ \tilde{\mathbf{c}}_d \\ \tilde{\mathbf{c}}_s^+ \end{bmatrix}. \tag{33}$$

As shown in Figure 5, a longer fictitious array is set up. There are 28 array elements after spatial smoothing, where $M = 4, N = 4$.

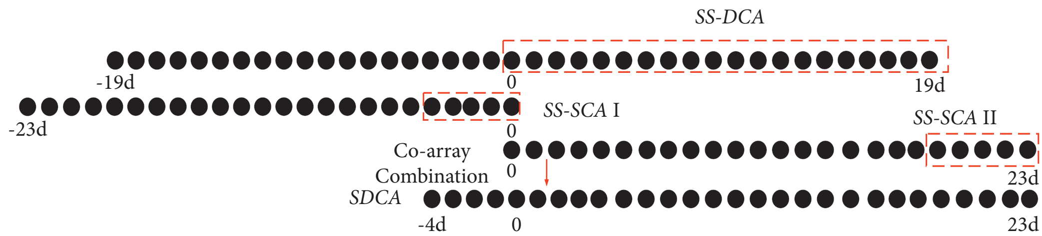

Figure 5: Nested array framework graph after spatial smoothing.

Firstly, the estimated value of the covariance matrix of the smoothed SDCA received signal is calculated as follows:

$$\mathbf{R}_Y = \frac{1}{\mathbf{R}_1 + 1}\widetilde{\mathbf{Y}}\widetilde{\mathbf{Y}^{\mathbf{H}}}. \tag{34}$$

The noise subspace $\mathbf{E}_l^n$ can be obtained by eigenvalue decomposition $\mathbf{R}_Y$. $(\mathbf{E}_l^n)^H\widetilde{\mathbf{c}}(\mathbf{p}_q) = 0$, so cost function of noncircular sources is as follows:

$$f_{NC-S\,DF}(\mathbf{p},\varphi) = \arg\max \frac{1}{\sum_{l=1}^{L}\widetilde{\mathbf{c}}(\mathbf{p},\varphi)^H\mathbf{E}_l^n(\mathbf{E}_l^n)^H\widetilde{\mathbf{c}}(\mathbf{p},\varphi)}. \tag{35}$$

This study makes use of dimension reduction method to decrease the computational complexity and eliminate the noncircular phase. The qth direction is shown in the following equation:

$$\widetilde{\mathbf{c}}(\mathbf{p}_q,\varphi_q) = \begin{bmatrix} e^{j(R_3-R_1)\pi\sin\theta_l(\mathbf{p}_q)}e^{j2\varphi_q} \\ \vdots \\ e^{j\pi\sin\theta_l(\mathbf{p}_q)} \\ e^{j2\varphi_q} \\ \hline 1 \\ e^{-j\pi\sin\theta_l(\mathbf{p}_q)} \\ \vdots \\ e^{-jR_1\pi\sin\theta_l(\mathbf{p}_q)} \\ \hline e^{-jR_1\pi\sin\theta_l(\mathbf{p}_q)}e^{-j2\varphi_q} \\ \vdots \\ e^{-jR_3\pi\sin\theta_l(\mathbf{p}_q)}e^{-j2\varphi_q} \end{bmatrix} = \begin{bmatrix} e^{j(R_3-R_1)\pi\sin\theta_l(\mathbf{p}_q)} & & \\ \cdots & & \\ e^{j\pi\sin\theta_l(\mathbf{p}_q)} & & \\ 1 & & \\ & 1 & \\ & e^{-j\pi\sin\theta_l(\mathbf{p}_q)} & \\ & \cdots & \\ & e^{-jR_1\pi\sin\theta_l(\mathbf{p}_q)} & \\ & & e^{-jR_1\pi\sin\theta_l(\mathbf{p}_q)} \\ & & e^{-j(R_1+1)\pi\sin\theta_l(\mathbf{p}_q)} \\ & & \cdots \\ & & e^{-jR_3\pi\sin\theta_l(\mathbf{p}_q)} \end{bmatrix} \begin{bmatrix} e^{j2\varphi_q} \\ 1 \\ e^{-j2\varphi_q} \end{bmatrix}$$

$$= \mathbf{\Theta}(\mathbf{p}_q)\boldsymbol{\phi}(\varphi_q). \tag{36}$$

Finally, we can obtain separation matrix $\boldsymbol{\phi}(\varphi_q) = \left[e^{j2\varphi_q}\ 1\ e^{-j2\varphi_q}\right]^T$. We set up $\mathbf{e} = [0\ 1\ 0]^T$ to decrease searching dimension. So, it can eliminate noncircular phase. $\mathbf{\Theta}(\mathbf{p}_q)$ is another separation matrix.

Therefore, we can set up the cost function of RD-SDF algorithm as follows:

$$f_{RD-SDF}(\mathbf{p}) = \arg\max\sum_{l=1}^{L}\mathbf{e}^H\left(\mathbf{\Theta}^H(\mathbf{p})\mathbf{E}_l^n(\mathbf{E}_l^n)^H\mathbf{\Theta}(\mathbf{p})\right)^{-1}\mathbf{e}. \tag{37}$$

Because SDF only makes use of noise subspace, it is sensitive to external factors, such as few snapshots or low signal-to-noise ratio. Therefore, we assign a weight to each observation station to improve positioning accuracy and set up the following cost function:

$$f_{W-SDF}(\mathbf{p}) = \arg\max \sum_{l=1}^{L} w_l e^H \left(\Theta^H(\mathbf{p})\mathbf{E}_l^n (E_l^n)^H \Theta(\mathbf{p})\right)^{-1} e, \tag{38}$$

where w_l means the weight of the lth station.

3.3. The Proposed SNR Weighted SDF. In view of the energy allocation principle on account of the water injection theory, the routes with good quality are distributed more power and the routes with poor quality are distributed less power. According to this principle, we can acquire the maximum route capacity. Due to inferior stability and noise susceptibility of ordinary algorithm, we propose SNR weighted method. For the sake of cutting down the total error, we devise a weight that increases as the error decreases.

Assuming that the noise is irrelevant and the sources and noise are mutually independent. Therefore, the covariance matrix can be reconstructed, and covariance matrix can be indicated as follows:

$$\widehat{\mathbf{R}}_l = \frac{1}{K}\sum_{k=1}^{K}\left(\sum_{q=1}^{Q}\mathbf{g}_{l,q}^2 W_q \mathbf{b}_l(\mathbf{p})\mathbf{b}_l^H(\mathbf{p}) + \sigma_n^2 \mathbf{I}_{V\times V}\right), \tag{39}$$

where $\mathbf{I}_{V\times V}$ is unit matrix of $V\times V$, where $V = MN + N$. The power of different emitter sources in the same array or different arrays in the same emitter source is decided by the sources power W_q and unknown parameters $g_{l,q}$.

Received sources covariance matrix are separated into two sections [8]:

$$\begin{aligned}\widehat{\mathbf{R}}_l = \mathbf{R}_s + \mathbf{R}_n = \mathbf{A}_l(\mathbf{p})diag\left(\left[W_{l,1},\ldots,W_{l,Q}\right]\right)\mathbf{A}_l^H(\mathbf{p})\\ + \sigma_n^2\mathbf{I}_{V\times V}.\end{aligned} \tag{40}$$

Therefore, the eigenvalue can be indicated as follows [8]:

$$\lambda_{l,i} = \begin{cases}\sigma_{y_i}^2 + \sigma_n^2, & 1\le i\le Q,\\ \sigma_n^2, & Q+1\le i\le V,\end{cases} \tag{41}$$

where $\sigma_{y_i}^2$, $1\le i\le Q$ are Q eigenvalues of $\mathbf{R}_s$, and we use them represent the power of the received sources. According to equation (41), the estimated noise power can be obtained for the lth observation station as follows:

$$\widehat{\sigma}_{nl}^2 = \frac{1}{V-Q}\sum_{i=Q+1}^{V}\lambda_{l,i}. \tag{42}$$

According to (42), we can get the power of the lth station as below

$$\widehat{W}_l = \sum_{i=1}^{Q}\left(\lambda_{l,i} - \widehat{\sigma}_{nl}^2\right). \tag{43}$$

The received signal with large signal-to-noise ratio will engender smaller position error. So, we should distribute larger weight to the location. The cost function is set up as follows:

$$f_{SW-SDF}(\mathbf{p}) = \arg\max\sum_{l=1}^{L}\frac{\widehat{W_l}}{\widehat{\sigma}_{nl}^2}\mathbf{e}^H\left(\mathbf{\Theta}^H(\mathbf{p})\mathbf{a}_j^H(\mathbf{p})\mathbf{E}_l^n(\mathbf{E}_l^n)^H(\mathbf{p})\mathbf{a}_j\mathbf{\Theta}(\mathbf{p})^{-1}\mathbf{e}\right). \tag{44}$$

Through searching the Q minimum values of equation (44), we can get the estimated location.

3.4. The Steps of the W-SDF Algorithm. We make a list of the following 5 steps about W-SDF algorithm. Figure 6 shows the flowchart of the algorithm.

Step 1. Establish a direct positioning scene model.

Step 2. For the nested array, we use the spatial smoothing method and the sum difference array method to get a larger array aperture.

Step 3. Calculate the covariance matrix and get the noise subspace.

Step 4. Generate the weighting coefficient w_l and use the dimension reduction method to set up the loss function $f_{SW-SDF}(\mathbf{p})$.

Step 5. Obtain the value of spectral peak through spectral peak search, which is the corresponding coordinate $(\widehat{x}_q, \widehat{y}_q)$.

4. Performance Analysis

In this section, the available DOF and the complexities of the W-SDF, SDF, Capon, and W-Capon algorithms are analyzed. Finally, we elaborate the advantages of W-SDF algorithm.

4.1. Achievable DOFs. We define that M means the number of dense uniform subarray, N means the number of sparse subarray, and H means the whole number of array elements. After spatial smoothing, the DOF of W-SDF algorithm is $MN + 2M + N$. DOF of proposed algorithm for circular sources with uniform linear subarray is H, DOF of proposed algorithm for noncircular sources with uniform linear subarray is $2H$, and DOF for circular sources with nested array is $MN + N$. It is obviously that the DOF has increased a lot.

4.2. Complexity Analysis. We define that H means numbers of array element, Q means numbers of source, L means numbers of observation station, and K means numbers of snapshots. The X orientation is separated into L_x equivalent

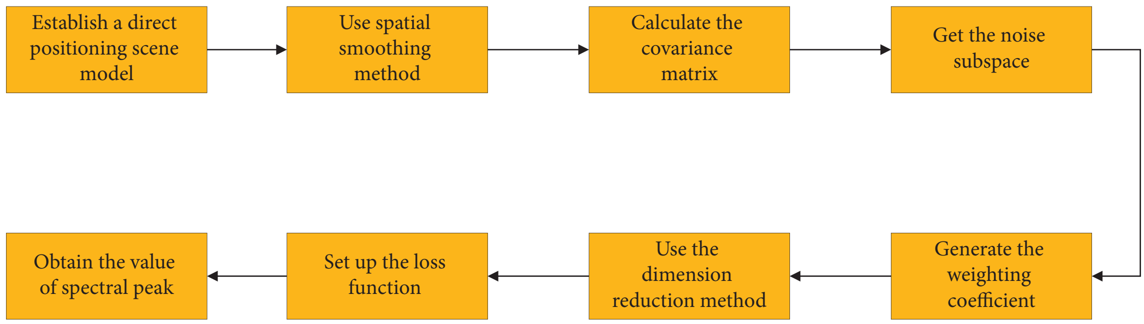

FIGURE 6: Algorithm flowchart.

portions, and Y orientation is separated into L_y equivalent portions [10]. Noncircular phase is separated into L_φ equivalent portions. The computer configuration is Intel(R) Core i7-10700F, and CPU frequency is 2.90 GHz.

The computing complexity for DPD mainly includes four portions: the complexity of covariance matrix is $O(4H^2LK)$, the computing complexity of covariance after spatial smoothing is $O[F^2VL]$, where $F = MN + M + 2N$, $V = MN + N$. The eigenvalue decomposition of the covariance matrix is $O[F^3L]$, and the computing complexity of spatial spectral peak searching value after SNR weighting is $O[LL_xL_y(3F^2 + 9F + F^2(F-Q) + 39]$. Table 1 lists the computing complexity of the W-SDF, SDF, Capon, and W-Capon algorithms and running time of these algorithms.

The W-SDF algorithm of computational complexity without dimension reduction is $O[4M^2LK + F^2VL + F^3L + LL_xL_yL_\varphi(F^2 + F + F^2(F-Q))]$.

The W-SDF algorithm of computational complexity with dimension reduction is $O[4M^2LK + F^2VL + F^3L + LL_xL_y(3F^2 + 9F + F^2(F-Q) + 39)]$.

It is obviously that the computational complexity is lessened after dimension reduction.

It can be seen from Figure 7 that W-SDF has the same computational complexity as the SDF algorithm and W-Capon has the same complexity as the Capon algorithm. W-SDF has lower computational complexity compared with W-Capon and Capon algorithm.

4.3. Advantages. We expound on the advantages about the proposed method from degree of freedom, computing complexity, and positioning accuracy.

(1) The proposed method makes use of noncircular sources and nested array features to expand aperture. The degree of freedom has been greatly improved.

(2) We make use of dimension reduction method to decrease computational complexity of algorithms for noncircular sources. The computing complexity is obviously lessened.

(3) We integrate the weighting method into SDF and obtain high accuracy. We make use of noncircular sources and nested arrays and get higher positioning accuracy.

5. Simulation Results

In this section, we emulate the proposed method and get the pattern of spatial spectrum and scatter diagram. We emulate the RMSE results of the proposed method under different parameters.

5.1. Estimated Results Concerning Proposed Method. Multiple nested arrays are located at multiple targets $\mathbf{P}_1 = [300m, 300m]$, $\mathbf{P}_2 = [500m, 500m]$, and $\mathbf{P}_3 = [800m, 800m]$. The noncircular phase is $(\pi/6, \pi/4, \pi/3)$. The observation stations are $\mathbf{U}_1 = [-2000m, -100m]$, $\mathbf{U}_2 = [-1000m, -100m]$, $\mathbf{U}_3 = [0m, -100m]$, $\mathbf{U}_4 = [1000m, -100m]$, and $\mathbf{U}_5 = [2000m, -100m]$. Figure 8 shows pattern of spatial spectrum and Figure 9 shows scatter diagram of three targets. The real location and estimated location are shown in Figure 8. The proposed W-SDF algorithm can locate three source targets accurately.

The location estimation performance is analyzed through computing Monte Carlo (MC) simulation times. The root mean squares error (RMSE) can be indicated as follows [9]:

$$RMSE = \frac{1}{Q}\sum_{q=1}^{Q}\sqrt{\frac{1}{MC}\sum_{mc=1}^{MC}\left[\left(\hat{x}_{q,mc} - x_q\right)^2 + \left(\hat{y}_{q,mc} - y_q\right)^2\right]}, \quad (45)$$

where MC means the number of Monte Carlo experiment times, Q means the number of targets, (x_q, y_q) means the true location of the qth target source, and $(\hat{x}_{q,mc}, \hat{y}_{q,mc})$ means the estimated position for the qth target in the $mcth$ experiment. We set Monte Carlo simulation times as 500.

5.2. Performance of W-SDF and SDF Algorithms under Different Sources and Arrays. Multiple targets are $\mathbf{P}_1 = [300m, 300m]$, $\mathbf{P}_2 = [500m, 500m]$, and $\mathbf{P}_3 = [800m, 800m]$. The number of snapshots is 300. The number of nested array element is $(M, N) = (3, 3)$. Figure 10 shows the performance of SDF algorithm and W-SDF algorithm under noncircular sources with different arrays. Figure 10 also shows that the performance of SDF algorithm and W-SDF algorithm for different sources under uniform linear array. The performance of weighted SDF algorithm is superior to SDF algorithm. The performance of SDF and

Table 1: Computing complexity and working time.

Different algorithms	Computing complexity	Working time (s)
SDF	$O[4M^2LK + F^2VL + F^3L + LL_xL_y(3F^2 + 9F + F^2(F - Q) + 39)]$	145.378111
W-SDF	$O[4M^2LK + F^2VL + F^3L + LL_xL_y(3F^2 + 9F + F^2(F - Q) + 39)]$	146.294961
Capon	$O[4M^2LK + F^2VL + LL_xL_y(3F^2 + 9F + F^3 + 39)]$	1360.93077
W-Capon	$O[4M^2LK + F^2VL + LL_xL_y(3F^2 + 9F + F^3 + 39)]$	1369.73693

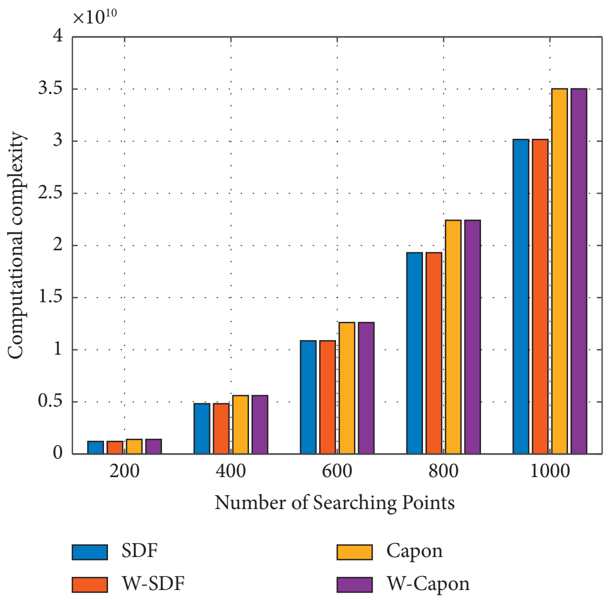

Figure 7: Computational complexity of different algorithms.

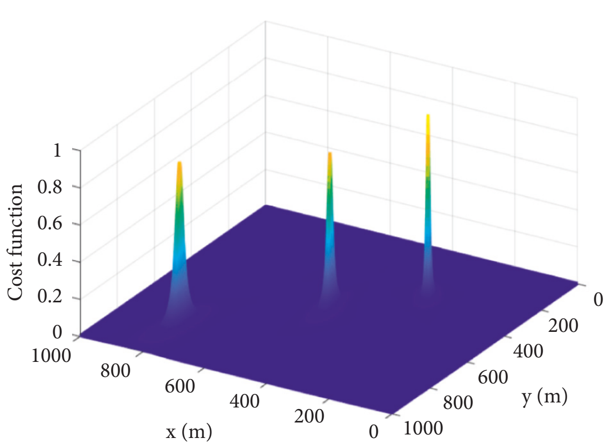

Figure 8: Multiple targets direct position.

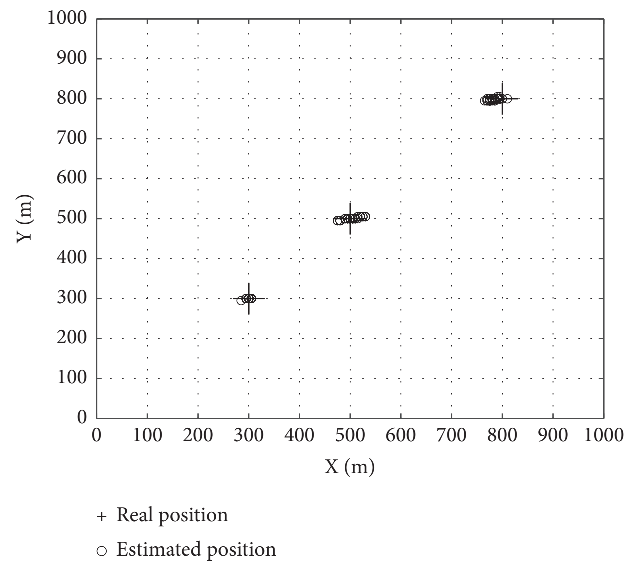

Figure 9: Scatter diagram of three targets.

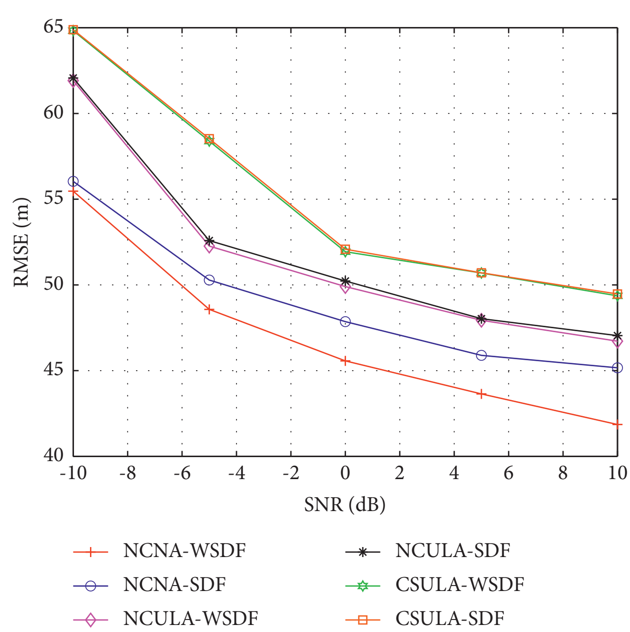

Figure 10: W-SDF and SDF algorithms for different arrays and sources.

W-SDF algorithms for noncircular sources is superior to that of circular sources. The performance of SDF and W-SDF algorithms for nested array is superior to that of uniform linear array.

5.3. Performance of Different Algorithms for Noncircular Sources. The number of snapshots is 300. Multiple targets are $\mathbf{P}_1 = [300m, 300m]$, $\mathbf{P}_2 = [500m, 500m]$, and $\mathbf{P}_3 = [800m, 800m]$. The number of nested array element is $(M, N) = (3, 3)$. Figure 11 shows the performance of W-SDF, SDF, W-Capon, Capon, and W-PM and PM algorithms under nested arrays and noncircular sources. Under noncircular sources and nested array, the performance of the W-SDF algorithm is superior to W-Capon and

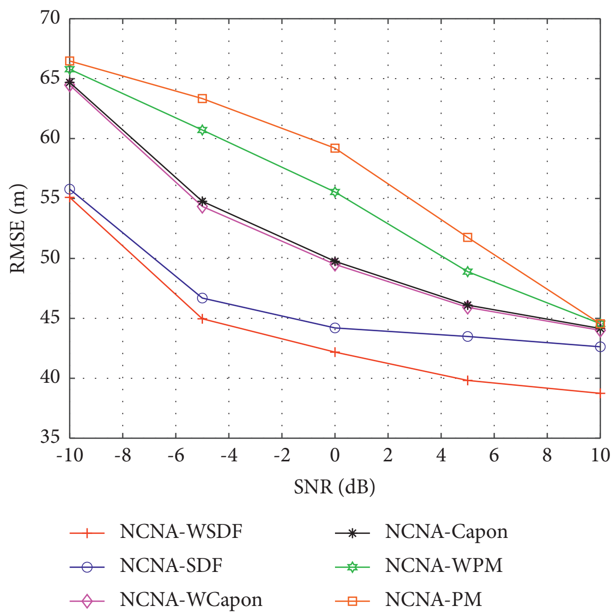

FIGURE 11: Different algorithms comparison for noncircular sources.

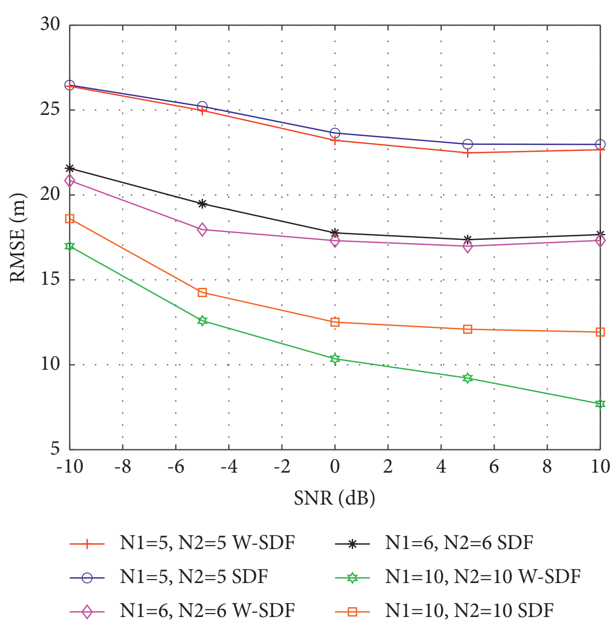

FIGURE 12: W-SDF and SDF algorithms for different element numbers.

W-PM algorithms. The performance of W-SDF algorithm is superior to SDF, Capon, and PM algorithm.

5.4. Performance of W-SDF and SDF Algorithms with Increment of Array Element Numbers. Multiple targets are $\mathbf{P}_1 = [300m, 300m]$, $\mathbf{P}_2 = [500m, 500m]$, and $\mathbf{P}_3 = [800m, 800m]$. The number of snapshots is 300. Figure 12 shows the performance of W-SDF and SDF under nested array $(M, N) = (5, 5), (6, 6), (10, 10)$. With the

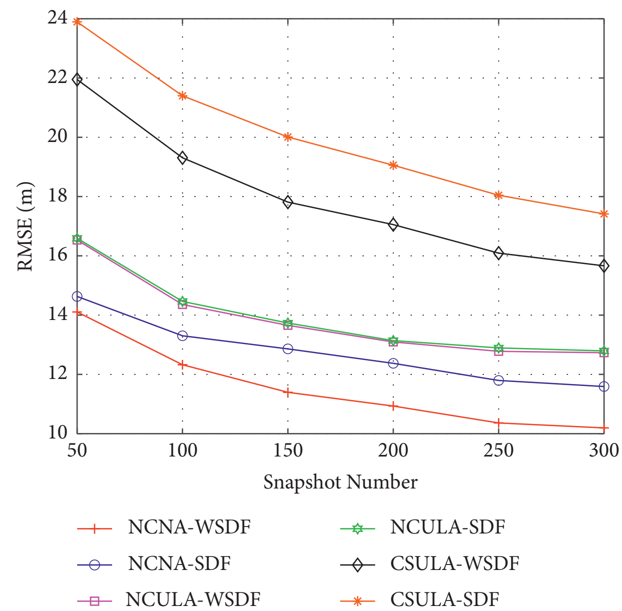

FIGURE 13: W-SDF and SDF algorithms with different snapshot numbers.

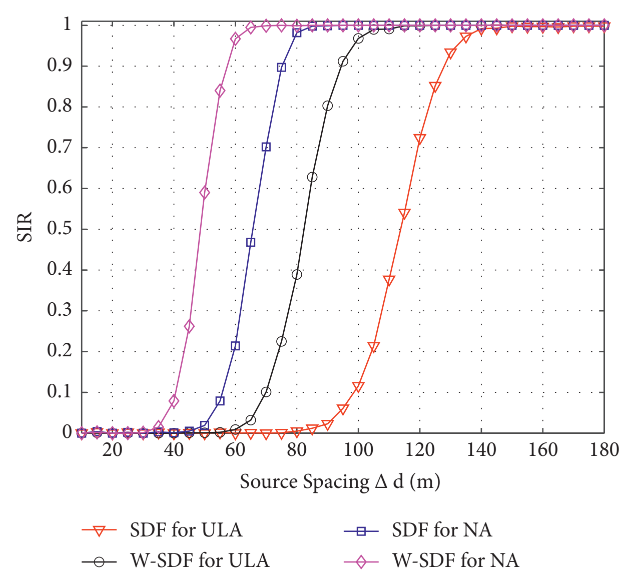

FIGURE 14: Resolution about W-SDF and SDF algorithms.

number of array elements increment, the performance of SDF and W-SDF for nested array and noncircular sources is better.

5.5. Performance of W-SDF and SDF Algorithms with Different Snapshot Numbers. Figure 13 shows the performance of SDF and W-SDF algorithms under different number of snapshots. Multiple targets are $\mathbf{P}_1 = [300m, 300m]$, $\mathbf{P}_2 = [500m, 500m]$, and $\mathbf{P}_3 = [800m, 800m]$. The SNR is set as 15 dB. The nested array element number is $(M, N) = (3, 3)$. With the increment of snapshot number, it is clearly to see that the performance for nested arrays and noncircular sources is better.

5.6. Resolution about Source Spacing with Different Arrays. Figure 14 shows resolution about the distance between two sources. SNR is set as 5 dB. Positions are set as $\mathbf{p}_1 = [300m, 300m]$ and $\mathbf{p}_2 = [\Delta dm, 300m]$, where Δd changes from 10 m to 180 m. It can be seen that the resolution of weighted SDF algorithm is better than that of SDF algorithm with noncircular sources, and the resolution of algorithm under nested array is better than that under uniform array.

6. Conclusion

This article studies SNR weighted SDF algorithm on account of noncircular sources and nested arrays for direct position determination. For noncircular sources, the dimension reduction method is used to decrease the computing complexity and remove the noncircular phase. For SDF algorithm vulnerable to noise and inferior stability, we use SNR weighted SDF algorithm to improve location accuracy. For the aperture limited, we introduce nested arrays to expand array aperture. We use spatial smoothing technology and use sum and difference co-array to deal with the nested array. Simulation results show that the proposed method decreases the complexity of the algorithm and improves the location accuracy, degree of freedom, and resolution. In the future, we can study an optimal station position. Three-level nested arrays and other sparse arrays for the direct positioning are also needed researched in the future.

Data Availability

The data used to support the findings of this study are included within the article.

Conflicts of Interest

The authors declare that they have no conflicts of interest.

Acknowledgments

This work was supported by the China NSF (Grant nos. 61971217, 61971218, and 61631020), Jiangsu NSF (Grant no. BK20200444), Suzhou Key Research and Development Project(Grant no. SGC2021069), and National Key Research and Development Project, (Grant no. 2020YFB1807602).

References

[1] Y. Wang and Y. Wu, "An efficient semidefinite relaxation algorithm for moving source localization using TDOA and FDOA measurements," *IEEE Communications Letters*, vol. 21, no. 1, pp. 80–83, 2017.

[2] Y. Xie, Y. Wang, P. Zhu, and X. You, "Grid-search-based hybrid TOA/AOA location techniques for NLOS environments," *IEEE Communications Letters*, vol. 13, no. 4, pp. 254–256, 2009.

[3] T. Qiao, Y. Zhang, and H. Liu, "Nonlinear expectation maximization estimator for TDOA localization," *IEEE Wireless Communications Letters*, vol. 3, no. 6, pp. 637–640, 2014.

[4] F. Wen, Q. Wan, and L. Y. Luo, "Time-difference-of-arrival estimation for noncircular signals using information theory," *AEU-International Journal of Electronics and Communications*, vol. 67, no. 3, pp. 242–245, 2013.

[5] Q. Liu, J. Xu, Z. Ding, and H. C. So, "Target localization with jammer removal using frequency diverse array," *IEEE Transactions on Vehicular Technology*, vol. 69, no. 10, pp. 11685–11696, 2020.

[6] O. Bialer, D. Raphaeli, and A. J. Weiss, "Maximum-likelihood direct position estimation in dense multipath," *IEEE Transactions on Vehicular Technology*, vol. 62, no. 5, pp. 2069–2079, 2013.

[7] K. Hao and Q. Wan, "High resolution direct detection and position determination of sources with intermittent emission," *IEEE Access*, vol. 7, pp. 43428–43437, 2019.

[8] Y. Qian, Z. Yang, and H. Zeng, "Direct position determination for augmented coprime arrays via weighted subspace data fusion method," *Mathematical Problems in Engineering*, vol. 2021, pp. 1–10, Article ID 2825025, 2021.

[9] Y. Qian, D. Zhao, and H. Zeng, "Direct position determination of noncircular sources with multiple nested arrays: reduced dimension subspace data fusion," *Wireless Communications and Mobile Computing*, vol. 2021, pp. 1–10, Article ID 9950518, 2021.

[10] X. Shi, X. Zhang, and H. Zeng, "Direct position determination of non-circular sources for multiple arrays via weighted euler ESPRIT data fusion method," *Applied Sciences*, vol. 12, no. 5, 2022.

[11] F. Ma, Z. M. Liu, and F. Guo, "Direct position determination in asynchronous sensor networks," *IEEE Transactions on Vehicular Technology*, vol. 68, no. 9, pp. 8790–8803, 2019.

[12] T. Zhou, W. Yi, and L. Kong, "Direct position determination of multiple coherent sources using an iterative adaptive approach," *Signal Processing*, vol. 161, pp. 203–213, 2019.

[13] J. Yin, D. Wang, and Y. Wu, "An efficient direct position determination method for multiple strictly noncircular sources," *Sensors*, vol. 18, no. 2, p. 324, 2018.

[14] Y. K. Zhang, H. Y. Xu, B. Ba, D. M. Wang, and W. Geng, "Direct position determination of non-circular sources based on a Doppler-extended aperture with a moving coprime array," *IEEE Access*, vol. 6, pp. 61014–61021, 2018.

[15] P. Pal and P. P. Vaidyanathan, "Nested arrays: a novel approach to array processing with enhanced degrees of freedom," *IEEE Transactions on Signal Processing*, vol. 58, no. 8, pp. 4167–4181, 2010.

[16] Y. Wang, W. Wu, X. Zhang, and W. Zheng, "Transformed nested array designed for DOA estimation of non-circular signals: reduced sum-difference Co-array redundancy perspective," *IEEE Communications Letters*, vol. 24, no. 6, pp. 1262–1265, 2020.

[17] C. L. Liu and P. P. Vaidyanathan, "Super nested arrays: linear sparse arrays with reduced mutual coupling–part I: fundamentals," *IEEE Transactions on Signal Processing*, vol. 64, no. 15, pp. 3997–4012, 2016.

[18] W. Si, Z. Peng, C. Hou, and F. Zeng, "Improved nested arrays with sum-difference co array for DOA estimation," *IEEE Sensors Journal*, vol. 19, no. 16, pp. 6986–6997, 2019.

[19] P. Gupta and M. Agrawal, "Design and analysis of the sparse array for DOA estimation of noncircular signals," *IEEE Transactions on Signal Processing*, vol. 67, no. 2, pp. 460–473, 2019.

[20] J. Shi, F. Wen, and T. Liu, "Nested MIMO radar: coarrays, tensor modeling and angle estimation," *IEEE Transactions on Aerospace and Electronic Systems*, vol. 57, no. 1, pp. 573–585, 2021.

[21] M. Yang, L. Sun, X. Yuan, and B. Chen, "Improved nested array with hole-free DCA and more degrees of freedom," *Electronics Letters*, vol. 52, no. 25, pp. 2068–2070, 2016.

[22] P. P. Vaidyanathan and P. Pal, "Sparse sensing with coprime samplers and arrays," *IEEE Transactions on Signal Processing*, vol. 59, no. 2, pp. 573–586, 2011.

[23] P. Gounon, C. Adnet, and J. Galy, "Location angulaire de signaux non circulares," *Traitement du Signal*, vol. 15, no. 1, pp. 17–23, 1998.

[24] J. X. Yin, Y. Wu, and D. Wang, "Direct position determination of multiple noncircular sources with a moving array," *Circuits, Systems, and Signal Processing*, vol. 36, no. 10, pp. 4050–4076, 2017.

[25] Y. Zhang, B. Ba, D. Wang, W. Geng, and H. Xu, "Direct position determination of multiple non-circular sources with a moving coprime array," *Sensors*, vol. 18, no. 5, p. 1479, 2018.

[26] J. Liu, Z. Huang, and Y. Zhou, "Extended 2q-MUSIC algorithm for noncircular signals," *Signal Processing*, vol. 88, no. 6, pp. 1327–1339, 2008.

[27] B. Picinbono, "On circularity," *IEEE Transactions on Signal Processing*, vol. 42, no. 12, pp. 3473–3482, 1994.

[28] Y. Wang, J. Shen, X. Zhang, Y. He, and X. Dai, "Noncircular signals for nested array: sum-difference co-array and DOA estimation algorithm," *IET Radar, Sonar & Navigation*, vol. 14, no. 1, pp. 27–35, 2019.

[29] J. Steinwandt, F. Roemer, and M. Haardt, "ESPRIT-type algorithms for a received mixture of circular and strictly non-circular signals," *IEEE International Conference on Acoustics, Speech and Signal Processing*, vol. 14, no. 1, pp. 2809–2813, 2015.

Hindawi
Mathematical Problems in Engineering
Volume 2022, Article ID 5429488, 12 pages
https://doi.org/10.1155/2022/5429488

Research Article

A Computationally Efficient Algorithm for DOA Estimation with Unfolded Coprime Linear Array

Gong Pan [1] **and Yin Huafei** [2]

[1] *College of Electronic Engineering, Nanjing Vocational University of Industry Technology, Nanjing 211106, China*
[2] *Research Institute of China Aerospace Science and Industry Corporation, Nanjing 210007, China*

Correspondence should be addressed to Gong Pan; 2020101091@niit.edu.cn

Received 28 April 2022; Accepted 27 July 2022; Published 5 September 2022

Academic Editor: Ardashir Mohammadzadeh

In this paper, we investigate the direction of arrival (DOA) estimation problem with unfolded coprime linear array (UCLA) and propose a low computational complexity signal-subspace fitting (SF) algorithm. SF algorithm is able to achieve excellent DOA estimation performance while it requires global angular search (GAS). Especially in the several source signals situation, expensive complexity cost causes. To decrease computational complexity, we propose an initialized based SF (ISF) algorithm, which involves the several one dimensional (1D) partial angular search (PAS) instead of the multidimensional GAS. Consequently, the complexity is significantly decreased. Due to the full utilization of the array aperture, the proposed method in UCLA can attain better performance than general CLA (GCLA). In addition, as the SF is attractive in practical application, the proposed ISF algorithm lowers the computational cost, while achieving almost approximate estimation performance as traditional SF and noise subspace fitting (NF). Moreover, numerical simulations are provided and verify the effectiveness and the superiority of the proposed algorithm for the UCLA.

1. Introduction

Direction of arrival (DOA) estimation is one of the fundamental issues for the array signal processing scenery and has been applied in engineering fields, including sonar, radar, navigation, and wireless communications [1–6]. In the past decades, many subspace based algorithms have been proposed [7–10], like multiple signals classification (MUSIC) based algorithms [7–10], and estimation of signal parameters via rotational invariance techniques (ESPRIT) [11–13]. These are subspace based algorithms. The propagator method (PM) [14, 15] can reduce the computational complexity by employing a linear partition operation instead of eigenvalue decomposition (EVD). These algorithms were initially designed for uniform array [16–19]. Nevertheless, for the conventional uniform arrays, the interelement spacing is required to be no larger than half-wavelength. As a result, the phase ambiguity problem can be avoided [20].

Over these years, coprime array [21] attracts much attention. It can effectively increase the degrees of freedom (DOFs) [22, 23], relieve the mutual coupling (MC) effects [16, 24], and improve the angle estimation performance. Because of these advantages, the coprime array is widely used in wireless communication systems and radar location [25, 26]. Specifically, a general coprime linear array (GCLA) incorporates two sparse uniform linear subarrays with M and N sensors, where M and N are coprime integers. And, the interelement spacing of these two subarrays are $(N\lambda/2)$ and $(M\lambda/2)$, respectively. And, λ means the wavelength. This design concept breaks the conventional half-wavelength and can achieve the higher angle resolution compared with the classic uniform array in the same conditions.

In these years, various algorithms have been proposed for DOA estimation with GCLA. Zhou proposed a total spectral search (TSS) algorithm in [27]. By combining the DOA estimates of two subarrays to attain the final DOA estimates. This algorithm results in significantly computational complexity because of the global angular search (GAS). A partial spectral searching algorithm [28], which investigates the linear relationship to obtain all estimates, was proposed. Moreover, it transforms the GAS into partial sector one. These algorithms treat the array separately, so they only employ the auto-information of two subarrays. An efficient method which can resolve the ambiguity in DOA estimation was proposed in [29]. The method offers good generalization and robustness in resolving the ambiguity problem. It achieves full degrees of freedom (DOF) with reduced complexity. An ambiguity-free algorithm via utilizing the total matrix information, such as auto-covariance information and mutual covariance information, was proposed in [30]. However, it involves high computational complexity. Along with pursuing the high resolution and DOA estimation performance, the computational complexity is also a challenging but promising task [31, 32].

It is known that subspace fitting techniques [33, 34] are popular in array signal processing [35, 36]. Compared with maximum likelihood [37], signal subspace fitting (SF) and noise subspace fitting (NF) [33] algorithms obtain the similar angle estimation performance [37], while these algorithms involve high computational complexity due to the GAS, especially in the multiple signals situation. A successive scheme of SF has proposed in [38], which incorporates the coprime linear array and SF to decrease the complexity. To further expand the array aperture, we link the SF into unfolded coprime linear array (UCLA), which enlarges the array aperture and we transform the multidimensional searching into several one dimensional (1D) searching. Moreover, we replace the GAS by partial angular search (PAS). Specifically, by PM, we can attain the initial DOAs of two subarrays. And, we recover all estimates and obtain the unique initial DOA estimates according to coprime property. Then, we employ the initial estimates to reconstruct the steering matrix and transform the multidimensional search into several 1D one. Consequently, computational complexity cost can be significantly decreased. Meanwhile, via the initial estimates, we replace the GAS by PAS. The proposed ISF can acquire better DOA estimation performance with UCLA than that with GCLA due to the larger array aperture. And, it acquires similar DOA estimation performance compared with SF and NF, while ISF has the lowest complexity. Moreover, Cramer–Rao Bound (CRB) is presented as a theoretical lower bound [39]. Finally, the effectiveness and superiority of the proposed ISF algorithm for the UCLA is demonstrated by the numerical simulations.

Specifically, we summarize the main contributions of this paper as follows:

(1) We integrate the UCLA with the subspace fitting method which can obtain a larger array aperture compared with GCLA. Simulations verify that the proposed algorithm with UCLA can realize more excellent estimation performance than GCLA.

(2) We propose an initialization based algorithm for DOA estimation, which can effectively decrease the complexity of the classic SF algorithm. By utilizing PM to initialize and obtain coarse estimation, and operating fine searching among a small sector, so we can achieve lower complexity.

(3) We demonstrate that the proposed algorithm can achieve the approximately the same DOA estimation performance as the classical SF and NF algorithms. And, the proposed algorithm outperforms the classic PM algorithm in DOA estimation performance.

The remaining parts of this paper are organized as follows: in Section 2, we elaborate the UCLA geometry and signal model. Subsequently, the proposed algorithm is introduced in Section 3. Complexity analysis and advantages are given in Section 4. Numerical simulations are provided in Sections 5 and 6 conclude this paper.

Notations: we utilize lower-case (upper-case) bold characters as vectors (matrices). And, we use $(\cdot)^T$ and $(\cdot)^H$ to represent the transpose and the conjugate transpose, respectively. $\odot$ and $\otimes$ represent the Khatri–Rao product and Kronecker product, respectively. $\mathrm{diag}(\cdot)$ denotes a diagonal matrix which employs the elements of the matrix to be its diagonal elements. $E(\cdot)$ represents statistical expectation. $\min(\cdot)$ is getting the minimum element. $D_m(\cdot)$ is a diagonal matrix that the m-th row of the matrix is employed. $\mathrm{angle}(\cdot)$ and $\arctan(\cdot)$ denote phase operator and the arctangent function, respectively.

2. Signal Model

In this paper, we employ an unfolded coprime linear array (UCLA) configuration which is able to further enlarge the array aperture and promote DOA estimation performance.

An UCLA configuration incorporates two uniform linear subarrays. One subarray has M sensors with $d_1 = (N\lambda/2)$, where λ represents the wavelength. The other subarray is with N sensors and the interelement spacing is denoted as $d_2 = (M\lambda/2)$. So the total number of the sensors is denoted as $T_{UCLA} = M + N - 1$. Figure 1 is an example of UCLA configuration where $M = 3$ and $N = 4$.

Assume that there are K uncorrelated far-field narrowband signals $s_k(t)$ impinging on the UCLA from distinct angles where $t \in [1, L]$ and L represents the number of snapshots. The angles are denoted as $\Theta = [\theta_1, \theta_2, \ldots, \theta_K]$, where $\theta_k \in [0, \pi/2]$, $(k = 1, 2, \ldots, K)$. Here, we assume the number of sources K is known. The received signal of the array can be denoted as follows:

$$x(t) = \mathrm{As}(t) + n(t) = \begin{bmatrix} x_1(t) \\ x_2(t) \end{bmatrix} = \begin{bmatrix} A_1 \\ A_2 \end{bmatrix} s(t) + \begin{bmatrix} n_1(t) \\ n_2(t) \end{bmatrix}, \tag{1}$$

where $A = [A_1^T, A_2^T]^T = [a(\theta_1), a(\theta_2), \ldots, a(\theta_K)]$ is the direction matrix and the steering vector is defined by $a(\theta_k) = [a_1(\theta_k)^T, a_2(\theta_k)^T]^T$, $n(t) = [n_1(t)^T, n_2(t)^T]^T$ is the additive white Gaussian noise with zero mean and variance σ_n^2. And, the noise signal is independent of the signal resources. And $\mathbf{s}(t) = [s_1(t), s_2(t), \ldots, s_K(t)]^T$ denotes the

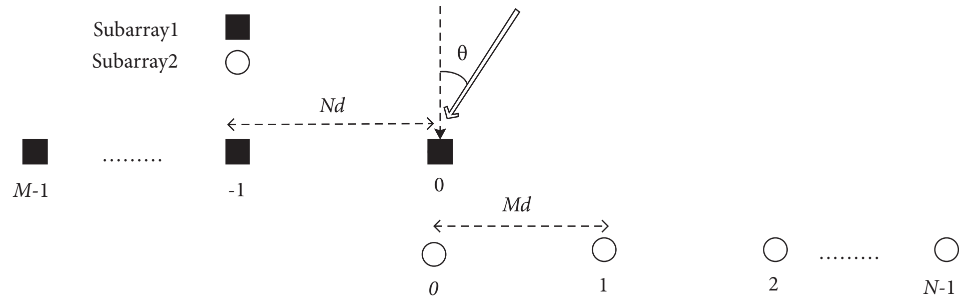

Figure 1: Structure of unfolded coprime linear array.

signal vector, where $t = 1, 2, \ldots, L$, L means the number of snapshots. $A_1 = [a_1(\theta_1), a_1(\theta_2), \ldots, a_1(\theta_K)]$ represents the directional matrix and the corresponding steering vector is denoted as $a_1(\theta_k) = [e^{j(M-1)N\pi\sin\theta_k}, e^{j(M-2)N\pi\sin\theta_k}, \ldots, 1]^T$ $(k = 1, 2, \ldots, K)$. And, the directional matrix of subarray 2 is denoted as $A_2 = [a_2(\theta_1), a_2(\theta_2), \ldots, a_2(\theta_K)]$ and the corresponding steering vector is represented as $a_2(\theta_k) = [e^{-jM\pi\sin\theta_k}, \ldots, e^{-j(N-1)M\pi\sin\theta_k}]^T$.

Practically, the covariance matrix is approximately computed with L snapshots [7].

$$\widehat{R} = \left(\frac{1}{L}\right)\sum_{t=1}^{L} \mathbf{x}(t)\mathbf{x}^H(t). \tag{2}$$

Then, perform eigenvalue decomposition [7].

$$\widehat{R} = \widehat{U}_s\widehat{D}_s\widehat{U}_s^H + \widehat{U}_n\widehat{D}_n\widehat{U}_n^H, \tag{3}$$

where $\widehat{D}_s$ and $\widehat{D}_n$ are the diagonal matrices composed of the largest K eigenvalues of $\widehat{\mathrm{R}}$ and the diagonal matrix containing the remaining eigenvalues, respectively. And, $\widehat{U}_s$ denotes the signal subspace which consists of the eigenvectors corresponding to the largest K eigenvalues. $\widehat{U}_n$ is the noise subspace including the rest eigenvectors.

In the noise-free case, we can get the following equation:

$$\mathrm{space}\{U_s\} = \mathrm{space}\{A\}. \tag{4}$$

It exists a full rank matrix $\Gamma \in \mathbb{C}^{(K\times K)}$ [7] to make (5) hold.

$$\widehat{\mathrm{U}}_s = \mathbf{A}\Gamma. \tag{5}$$

3. Proposed Method for DOA Estimation

3.1. Initialization Processing. In this subsection, we first utilize subarray 1 to introduce the proposed algorithm. And we can operate the subarray 2 by the similar method.

By partitioning the directional matrix A_1, we can get A_{11} and A_{12}, which contain the first K rows and $(M-K)$ rows, respectively.

For the subarray 1, we first partition the steering matrix A_1 as follows:

$$A_1 = \left[\frac{A_{11}}{A_{12}}\right], \tag{6}$$

where $A_{11} \in \mathbb{C}^{K\times K}$ represents the matrix contains the first K rows of A_1 and $A_{12} \in \mathbb{C}^{(M-K)\times K}$ stands for the matrix with the remaining $(M-K)$ rows of $\mathbf{A}_1$, respectively.

Assume that $\mathbf{A}_{11}$ is a full rank matrix, then we can obtain $\mathbf{A}_{12}$ by the following equation:

$$\mathbf{A}_{12} = \mathbf{P}_{1c}\mathbf{A}_{11}, \tag{7}$$

where $\mathbf{P}_{1c}$ is the propagator method of the subarray 1. And $\mathbf{P}_{1c} \in \mathbb{C}^{(M-K)\times K}$ [14].

Then, we define the following equation:

$$\mathbf{P}_1 = \left[\frac{\mathbf{I}_{1K}}{\mathbf{P}_{1c}}\right], \tag{8}$$

where $\mathbf{I}_{1K}$ is a unit matrix of $\mathbf{I}_{1K} \in \mathbb{C}^{K\times K}$.

So we have the following equation:

$$\mathbf{P}_1\mathbf{A}_{11} = \left[\frac{\mathbf{I}_{1K}\mathbf{A}_{11}}{\mathbf{P}_{1c}\mathbf{A}_{11}}\right] = \left[\frac{\mathbf{A}_{11}}{\mathbf{A}_{12}}\right] = \mathbf{A}_1. \tag{9}$$

Then, we partition the matrix of $\mathbf{P}_1$ and can get $\mathbf{P}_{1a}$ and $\mathbf{P}_{1b}$

$$\mathbf{P}_1 = \left[\frac{\mathbf{P}_{1a}}{\boldsymbol{\Gamma}_\xi}\right] = \left[\frac{\Xi_\zeta}{\mathbf{P}_{1b}}\right], \tag{10}$$

Where $\mathbf{P}_{1a}$ and $\mathbf{P}_{1b}$ denote the first $(M-1)$ rows and last $(M-1)$ rows of $\mathbf{P}_1$, respectively. And, Ξ_ξ and Ξ_ζ, respectively, represent the last row and the first row of $\mathbf{P}_1$.

Then, we partition $\mathbf{A}_1$ by the following equation:

$$\mathbf{A}_1 = \left[\frac{\mathbf{A}_{1a}}{\boldsymbol{\Sigma}_\xi}\right] = \left[\frac{\boldsymbol{\Sigma}_\zeta}{\mathbf{A}_{1b}}\right], \tag{11}$$

where $\mathbf{A}_{1a}$ and $\mathbf{A}_{1b}$ denote the first $(M-1)$ rows and last $(M-1)$ rows of $\mathbf{A}_1$, respectively. Σ_ξ represents the last row and Σ_ζ is the first row of $\mathbf{A}_1$.

Then, we can get the following equation:

$$\begin{cases} \mathbf{P}_1\mathbf{A}_{11} = \left[\frac{\mathbf{P}_{1a}}{\boldsymbol{\Gamma}_\xi}\right]\mathbf{A}_{11} = \left[\frac{\Xi_\zeta}{\mathbf{P}_{1b}}\right]\mathbf{A}_{11}, \\ \mathbf{A}_1 = \left[\frac{\mathbf{A}_{11}}{\mathbf{A}_{12}}\right] = \left[\frac{\mathbf{A}_{1a}}{\boldsymbol{\Sigma}_\xi}\right] = \left[\frac{\boldsymbol{\Sigma}_\zeta}{\mathbf{A}_{1b}}\right]. \end{cases} \tag{12}$$

According to (10), we have the following equation:

$$\begin{cases} \mathbf{P}_{1a}\mathbf{A}_{11} = \mathbf{A}_{1a} \\ \mathbf{P}_{1b}\mathbf{A}_{11} = \mathbf{A}_{1b} \end{cases} \tag{13}$$

So it has the following equation:

$$\left[\frac{\mathbf{P}_{1a}}{\mathbf{P}_{1b}}\right]\mathbf{A}_{11} = \left[\frac{\mathbf{A}_{1a}}{\mathbf{A}_{1b}}\right] = \left[\frac{\mathbf{A}_{1a}}{\mathbf{A}_{1a}\mathbf{\Phi}_{1r}}\right]. \tag{14}$$

Then, we have the following equation:

$$\mathbf{P}_{1a}^{+}\mathbf{P}_{1b} = \mathbf{A}_{11}\mathbf{\Phi}_{1r}\mathbf{A}_{11}^{-1}, \tag{15}$$

where $\mathbf{P}_{1a}^{+} = (\mathbf{P}_{1a}^{H}\mathbf{P}_{1a})^{-1}\mathbf{P}_{1a}^{H}$ gives the pseudoinverse of $\mathbf{P}_{1a}$ and Φ_{1r} is a diagonal matrix which is denoted as follows: $\Phi_{1r} = \mathrm{diag}(e^{j\pi N sin\theta_1}, e^{j\pi N sin\theta_2}, \ldots, e^{j\pi N sin\theta_K}) \in \mathbb{C}^{K\times K}$.

We define the following equation:

$$\mathbf{\Psi}_{1r} = \mathbf{P}_{1a}^{+}\mathbf{P}_{1b}. \tag{16}$$

Because $\mathbf{A}_{11}$ is a full rank matrix, so Ψ_{1r} is the similar transformation of Φ_{1r}.

As Φ_{1r} is a diagonal matrix of eigenvalues, Ψ_{1r} and Φ_{1r} possess the same eigenvalues. As a result, operate eigenvalues decomposition of Ψ_{1r}, then we can obtain the diagonal elements $\delta_{1,k}$. And, we can get the initial DOA estimates $\sin\overrightarrow{\theta}_{1,k}(k = 1, 2, \ldots, K)$ of subarray 1, which is denoted as follows:

$$\sin\overrightarrow{\theta}_{1,k} = \mathrm{angle}\frac{(\delta_{1,k})}{(N\pi)}, \tag{17}$$

where angle$(\cdot)$ means angle function.

By the similar conduction, we process the subarray 2.

Separate the directional matrix $\mathbf{A}_2$ into two parts and we can get $\mathbf{A}_{21}$ and $\mathbf{A}_{22}$, which contain the first K rows and $(N - K)$ rows, respectively.

The steering matrix of $\mathbf{A}_2$ is separated as follows:

$$\mathbf{A}_2 = \left[\frac{\mathbf{A}_{21}}{\mathbf{A}_{22}}\right], \tag{18}$$

where $\mathbf{A}_{21} \in \mathbb{C}^{K\times K}$ represents the matrix contains the first K rows of $\mathbf{A}_2$ and $\mathbf{A}_{22} \in \mathbb{C}^{(N-K)\times K}$ represents the matrix with the remaining $(N - K)$ rows of $\mathbf{A}_2$, respectively.

Assume that $\mathbf{A}_{21}$ is a full rank matrix, then we can obtain $\mathbf{A}_{22}$ by the following equation:

$$\mathbf{A}_{22} = \mathbf{P}_{2c}\mathbf{A}_{21}, \tag{19}$$

where $\mathbf{P}_{2c}$ is the propagator method of the subarray 1. And $\mathbf{P}_{2c} \in \mathbb{C}^{(N-K)\times K}$.

Then, we define the following equation:

$$\mathbf{P}_2 = \left[\frac{\mathbf{I}_{2K}}{\mathbf{P}_{2c}}\right], \tag{20}$$

where $\mathbf{I}_{2K}$ is a unit matrix of $\mathbf{I}_{2K} \in \mathbb{C}^{K\times K}$.

Similar to equation 15 we have the following equation:

$$\mathbf{P}_2\mathbf{A}_{21} = \left[\frac{\mathbf{I}_{2K}\mathbf{A}_{21}}{\mathbf{P}_{2c}\mathbf{A}_{21}}\right] = \left[\frac{\mathbf{A}_{21}}{\mathbf{A}_{22}}\right] = \mathbf{A}_2. \tag{21}$$

Then, we partition the matrix of $\mathbf{P}_2$ and can get $\mathbf{P}_{2\mathrm{a}}$ and $\mathbf{P}_{2b}$

$$\mathbf{P}_2 = \left[\frac{\mathbf{P}_{2a}}{\mathbf{\Gamma}_{2\xi}}\right] = \left[\frac{\Xi_{2\zeta}}{\mathbf{P}_{2b}}\right], \tag{22}$$

where $\mathbf{P}_{2\mathrm{a}}$ and $\mathbf{P}_{2b}$ denote the first $(N - 1)$ rows and last $(N - 1)$ rows of $\mathbf{P}_2$, respectively. And, $\Xi_{2\xi}$ and $\Xi_{2\zeta}$, respectively, represent the last row and the first row of $\mathbf{P}_2$.

Then, we partition $\mathbf{A}_2$ by the following equation:

$$\mathbf{A}_2 = \left[\frac{\mathbf{A}_{2a}}{\mathbf{\Sigma}_{2\xi}}\right] = \left[\frac{\mathbf{\Sigma}_{2\zeta}}{\mathbf{A}_{2b}}\right], \tag{23}$$

where $\mathbf{A}_{2\mathrm{a}}$ and $\mathbf{A}_{2b}$ denote the first $(N - 1)$ rows and last $(N - 1)$ rows of $\mathbf{A}_2$, respectively. $\Sigma_{2\xi}$ represents the last row and $\Sigma_{2\zeta}$ is the first row of $\mathbf{A}_2$.

Then, we can get the following equation:

$$\begin{cases} \mathbf{P}_2\mathbf{A}_{21} = \left[\frac{\mathbf{P}_{2a}}{\mathbf{\Gamma}_{\xi}}\right]\mathbf{A}_{11} = \left[\frac{\Xi_{\zeta}}{\mathbf{P}_{2b}}\right]\mathbf{A}_{21}, \\ \mathbf{A}_2 = \left[\frac{\mathbf{A}_{21}}{\mathbf{A}_{22}}\right] = \left[\frac{\mathbf{A}_{2a}}{\mathbf{\Sigma}_{\xi}}\right] = \left[\frac{\mathbf{\Sigma}_{\zeta}}{\mathbf{A}_{2b}}\right]. \end{cases} \tag{24}$$

According to (22), we have the following equation:

$$\begin{cases} \mathbf{P}_{1a}\mathbf{A}_{11} = \mathbf{A}_{1a} \\ \mathbf{P}_{1b}\mathbf{A}_{11} = \mathbf{A}_{1b} \end{cases} \tag{25}$$

Then, we can get the following equation:

$$\left[\frac{\mathbf{P}_{2a}}{\mathbf{P}_{2b}}\right]\mathbf{A}_{21} = \left[\frac{\mathbf{A}_{2a}}{\mathbf{A}_{2b}}\right] = \left[\frac{\mathbf{A}_{2a}}{\mathbf{A}_{2a}\mathbf{\Phi}_{2r}}\right]. \tag{26}$$

Then, we have the following equation:

$$\mathbf{P}_{2a}^{+}\mathbf{P}_{2b} = \mathbf{A}_{21}\mathbf{\Phi}_{2r}\mathbf{A}_{21}^{-1}, \tag{27}$$

where $\mathbf{P}_{2a}^{+} = (\mathbf{P}_{2a}^{H}\mathbf{P}_{2a})^{-1}\mathbf{P}_{2a}^{H}$ gives the pseudo-inverse of $\mathbf{P}_{2a}$ and Φ_{2r} is a diagonal matrix which is denoted as follows: $\Phi_{2r} = \mathrm{diag}(e^{j\pi M sin\theta_1}, e^{j\pi M sin\theta_2}, \ldots, e^{j\pi M sin\theta_K}) \in \mathbb{C}^{K\times K}$.

We define the following equation:

$$\mathbf{\Psi}_{2r} = \mathbf{P}_{2a}^{+}\mathbf{P}_{2b}. \tag{28}$$

Because $\mathbf{A}_{21}$ is a full rank matrix, so Ψ_{2r} is the similar transformation of Φ_{2r}.

As Φ_{2r} is a diagonal matrix of eigenvalues, Ψ_{2r} and Φ_{2r} possess the same eigenvalues. As a result, operate eigenvalues decomposition of Ψ_{2r}, then we can obtain the diagonal elements $\delta_{2,k}$. And, we can get the initial DOA estimates $\sin\widehat{\theta}_{2,k}$ of subarray 2, which is denoted as follows:

$$\sin\widehat{\theta}_{2,k} = \mathrm{angle}\left(\delta_{2,k}\right)/(M\pi), \tag{29}$$

where $k = 1, 2, \ldots, K$ and angle$(\cdot)$ is the angle function.

3.2. Ambiguity Elimination Based on Coprime Property. In this part, according to the obtained angles, we first recover all the estimates. Then, we eliminate the ambiguity problem based on the coprime property.

It is known that there exists $2k\pi\,(k \in \mathbb{Z})$ between the real and ambiguous angles for the sinusoid function [28].

$$\left(\frac{2\pi d_i \sin \widehat{\theta}_i}{\lambda - 2\pi d_i}\right)\left(\frac{\sin\widehat{\theta}_{i,am}}{\lambda = 2Q_i\pi}\right), \tag{30}$$

where $Q_i \in \mathbb{Z}$, $d_1 = N\,d$, $d_2 = M\,d$, $\theta_{i,am}$ means the ambiguous angle of the subarray i. It has the following equation:

$$\begin{aligned}\left(\frac{\sin \overrightarrow{\theta}_{1,k}}{\lambda - \sin \widehat{\theta}_{1,am}}\right) &= \left(\frac{2Q_1}{N}\right),\\ \left(\frac{\sin \overrightarrow{\theta}_{2,k}}{\lambda - \sin \widehat{\theta}_{2,am}}\right) &= \left(\frac{2Q_2}{M}\right).\end{aligned} \tag{31}$$

According to the variation range of θ, it is indicated that $Q_1 \in [-(N-1), N-1)]$ and $Q_2 \in [-(M-1), (M-1)]$, where M and N are integers [27].

Then, we have the following equation:

$$\frac{2Q_1}{N} = \frac{2Q_2}{M}. \tag{32}$$

It is known that the interelement spacing of a uniform linear array is no larger than half wave length to avoid the phase ambiguity. As a result, no phase ambiguity problem results in. But the coprime array, due to the element spacing larger than half wavelength, arises phase ambiguity.

To illustrate the phase ambiguity problem, we provide the simulation about the coprime array. Figure 2 depicts the DOA estimation with the three different element spacing, where there is one signal $\theta = 25^\circ$ arrives at the array. And it can be noticed that there are ambiguous angles when $d = 3\lambda/2$ and $d = 5\lambda/2$.

Due to the coprime property of M and N, there only exists $Q_1 = Q_2 = 0$ which makes the equation (32) satisfied.

Via equations (33) and (34), all the DOA estimates are obtained.

$$\widehat{\theta}_{M,k} = \arcsin\left(\frac{\left(\mathit{sin}\overrightarrow{\theta}_{1,k} - 2Q_1\right)}{N}\right), \tag{33}$$

$$\widehat{\theta}_{N,k} = \arcsin\left(\frac{\left(\mathit{sin}\overrightarrow{\theta}_{2,k} - 2Q_2\right)}{M}\right), \tag{34}$$

where $k = (1, 2, \ldots, K)$, $\widehat{\theta}_M = [\widehat{\theta}_{M,1}, \widehat{\theta}_{M,2}, \ldots, \widehat{\theta}_{M,k}]$ and $\widehat{\theta}_N = [\widehat{\theta}_{N,1}, \widehat{\theta}_{N,2}, \ldots, \widehat{\theta}_{N,k}]$.

Practically, considering that noise exists, to attain the overlapped angle estimation is always difficult. Consequently, we replace searching the overlap by finding the nearest angles from $\widehat{\theta}_M^{\xi}$ and $\widehat{\theta}_N^{\zeta}$, which contain all the estimates of two subarrays, respectively.

$$\min_{\widehat{\theta}_M^{\xi}, \widehat{\theta}_N^{\zeta}} \left|\widehat{\theta}_M^{\xi} - \widehat{\theta}_N^{\zeta}\right| (\xi = 1, 2, \ldots, N,\ \zeta = 1, 2, \ldots, M). \tag{35}$$

By equation (36), we can get the initial DOA estimates.

$$\widehat{\theta}_k^{ini} = \frac{\widehat{\theta}_M^{\xi} + \widehat{\theta}_N^{\zeta}}{2}\ (k = 1, 2, \ldots, K). \tag{36}$$

3.3. Initialization Based Algorithm. Via equation (37), we get the covariance matrix [7].

$$\mathbf{R} = \mathbf{A}\mathbf{R}_s\mathbf{A}^H + \sigma_n^2\mathbf{I}_{(M+N)\times(M+N)}, \tag{37}$$

where $\mathbf{R}_s$ is the covariance matrix of the signals and $\sigma_n^2\mathbf{I}_{(M+N)\times(M+N)}$ denotes the power of noise.

From equations (3) and (37), it has the following equation:

$$\mathbf{A}\mathbf{R}_s\mathbf{A}^H + \sigma_n^2\mathbf{I}_{(M+N)\times(M+N)} = \mathbf{U}_s\mathbf{D}_s\mathbf{U}_s^H + \sigma_n^2\mathbf{U}_n\mathbf{U}_n^H. \tag{38}$$

Due to the orthogonality of the signal and noise subspace, it exists $\mathbf{I} = \mathbf{U}_s\mathbf{U}_s^H + \mathbf{U}_n\mathbf{U}_n^H$. So equation (38) can be rewritten as follows:

$$\begin{aligned}&\mathbf{A}\mathbf{R}_s\mathbf{A}^H + \sigma_n^2\mathbf{I}_{(M+N)\times(M+N)}\\ &\quad = \mathbf{U}_s\mathbf{D}_s\mathbf{U}_s^H + \sigma_n^2\left(\mathbf{I}_{(M+N)\times(M+N)} - \mathbf{U}_s\mathbf{U}_s^H\right).\end{aligned} \tag{39}$$

Then, we can get the following equation:

$$\mathbf{A}\mathbf{R}_s\mathbf{A}^H + \sigma_n^2\mathbf{U}_s\mathbf{U}_s^H = \mathbf{U}_s\mathbf{D}_s\mathbf{U}_s^H. \tag{40}$$

As $\mathbf{U}_s = \mathbf{A}\Gamma$ and $\mathbf{U}_s^H\mathbf{U}_s = \mathbf{I}_{(M+N)\times(M+N)}$, we have the following equation:

$$\Gamma = \mathbf{R}_s\mathbf{A}^H\mathbf{U}_s\left(\mathbf{D}_s - \sigma_n^2\mathbf{I}_{(M+N)\times(M+N)}\right)^{-1}. \tag{41}$$

However, the noise exists. To solve this problem, establish a fitting relationship to compute the matrix Γ.

$$\theta, \widehat{\Gamma} = \min\left\|\widehat{\mathrm{U}}_s - \widehat{A}\widehat{\Gamma}\right\|_{\mathrm{F}}^2, \tag{42}$$

which can make the equation (5) hold.

By utilizing the least square (LS) criterion, we can get the following equation:

$$\widehat{\Gamma} = \left(\widehat{\mathbf{A}}^H\widehat{\mathbf{A}}\right)^{-1}\widehat{\mathbf{A}}^H\widehat{\mathbf{U}}_s = \widehat{\mathbf{A}}^+\widehat{\mathbf{U}}_s. \tag{43}$$

Incorporate (36) and (37), then we have the following equation:

$$\begin{aligned}\theta &= \min\left\|\widehat{U}_s - \widehat{A}\widehat{A}^+\widehat{U}_s\right\|_{\mathrm{F}}^2\\ &= \min\ \mathrm{tr}\left\{\left\{\mathbf{I} - \widehat{A}\left(\widehat{A}^H\widehat{A}\right)^{-1}\widehat{A}^H\right\}\widehat{U}_s\widehat{U}_s^H\right\}\\ &= \max\ \mathrm{tr}\left\{\widehat{A}\left(\widehat{A}^H\widehat{A}\right)^{-1}\widehat{A}^H\widehat{U}_s\widehat{U}_s^H\right\}.\end{aligned} \tag{44}$$

When there are numerical signals, the problem of equation (44) is becoming a multidimensional SF problem. Consequently, it will have a higher computational cost. In view of this, we utilize the initialization based method to

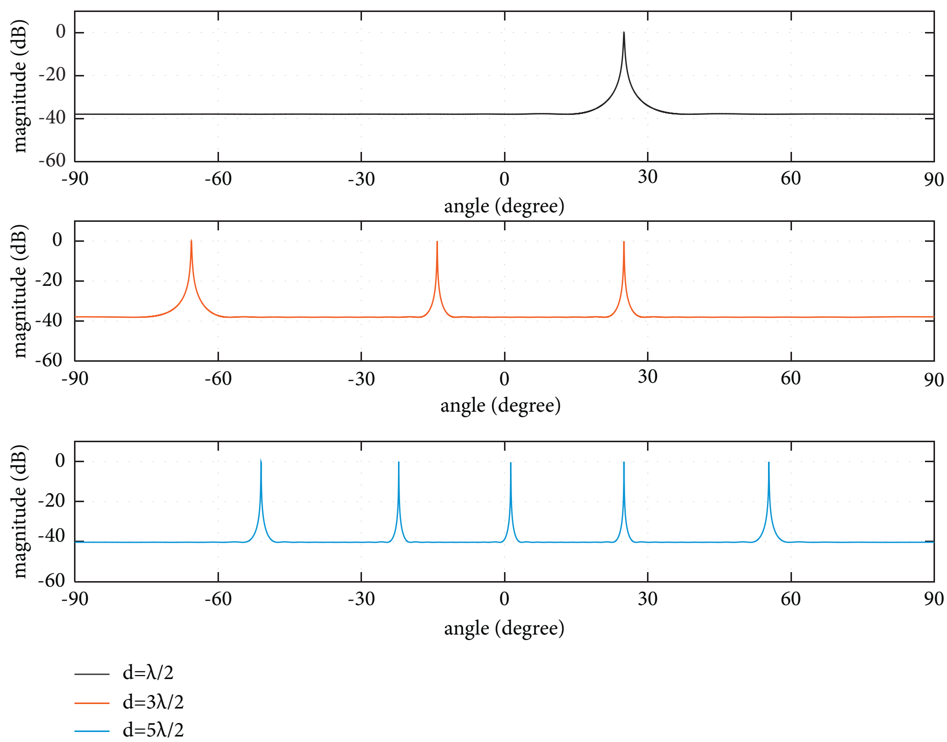

FIGURE 2: DOA estimation with the varying element spacing.

reconstruct the steering matrix and search within a small sector. In this way, complexity gets significantly decreased.

According to the obtained initial DOA estimates $\widehat{\theta}^{\text{in}} = [\widehat{\theta}_1^{in}, \widehat{\theta}_2^{in}, \ldots, \widehat{\theta}_K^{in}]$, the new manifold matrix $\widehat{A}^{(1)}$ is obtained.

$$\widehat{A}^{(1)} = \left[\mathbf{a}(\theta), \mathbf{a}\left(\widehat{\theta}_2^{in}\right), \ldots, \mathbf{a}\left(\widehat{\theta}_K^{in}\right)\right]. \tag{45}$$

Then, the angle θ_1 can be computed by the following equation:

$$\widehat{\theta}_1 = \underset{\theta\in\left[\widehat{\theta}_1^{in}-\Delta\theta, \widehat{\theta}_1^{in}+\Delta\theta\right]}{\operatorname{argmin}} \left\| \widehat{U}_s - \widehat{A}^{(1)}\widehat{A}^{(1)}\widehat{U}_s \right\|_{\mathrm{F}}^2. \tag{46}$$

It can be noted the searching region is $\theta \in [\widehat{\theta}_1^{in} - \Delta\theta, \widehat{\theta}_1^{in} + \Delta\theta]$, where $\Delta\theta$ is a tiny value. In this way, we can get the more accurate DOA estimate of θ_1.

From equation (46), we can obtained $\widehat{\theta}_1$. Then, we keep $[\widehat{\theta}_1, \widehat{\theta}_3^{in}, \ldots, \widehat{\theta}_K^{in}]$ unchanged and elaborate a new directional matrix $\widehat{A}^{(2)}$.

$$\widehat{A}^{(2)} = \left[\mathbf{a}\left(\widehat{\theta}_1\right), \mathbf{a}(\theta), \mathbf{a}\left(\widehat{\theta}_3^{in}\right), \ldots, \mathbf{a}\left(\widehat{\theta}_K^{in}\right)\right]. \tag{47}$$

Here, θ is the angle that we will estimate in the following step.

By equation (48), we can obtain the estimate of θ_2 by PAS within $\theta \in [\widehat{\theta}_2^{in} - \Delta\theta, \widehat{\theta}_2^{in} + \Delta\theta]$.

$$\widehat{\theta}_2 = \underset{\theta\in\left[\widehat{\theta}_2^{in}-\Delta\theta, \widehat{\theta}_2^{in}+\Delta\theta\right]}{\operatorname{argmin}} \left\| \widehat{U}_s - \widehat{A}^{(2)}\widehat{A}^{(2)} + \widehat{U}_s \right\|_F^2. \tag{48}$$

Similarly, keep $[\widehat{\theta}_1, \widehat{\theta}_2, \widehat{\theta}_4^{in}, \ldots, \widehat{\theta}_K^{in}]$ unchanged. And we employ $\widehat{\theta}_2$ to establish $\widehat{A}^{(3)}$,

$$\widehat{A}^{(3)} = \left[\mathbf{a}\left(\widehat{\theta}_1\right), \mathbf{a}\left(\widehat{\theta}_2\right), \mathbf{a}(\theta), \mathbf{a}\left(\widehat{\theta}_4^{in}\right), \ldots, \mathbf{a}\left(\widehat{\theta}_K^{in}\right)\right]. \tag{49}$$

It is noted that $\widehat{\theta}_1$ and $\widehat{\theta}_2$ is estimated via equations (46) and (48), and θ is the goal that we are to estimate in the next step.

Via equation (50), we can get the more accurate DOA estimate of θ_3 within a small searching region $\theta \in [\widehat{\theta}_3^{in} - \Delta\theta, \widehat{\theta}_3^{in} + \Delta\theta]$.

$$\widehat{\theta}_3 = \underset{\theta\in\left[\widehat{\theta}_3^{in}-\Delta\theta, \widehat{\theta}_3^{in}+\Delta\theta\right]}{\arg\min} \left\| \widehat{U}_s - \widehat{A}^{(3)}\widehat{A}^{(3)}\widehat{U}_s \right\|_{\mathrm{F}}^2. \tag{50}$$

By the similar method, we reconstruct the new directional matrix $\widehat{A}^{(K)}$ via using $[\widehat{\theta}_1, \widehat{\theta}_2, \ldots, \widehat{\theta}_{K-1}]$.

$$\widehat{A}^{(K)} = \left[\mathbf{a}\left(\widehat{\theta}_1\right), \mathbf{a}\left(\widehat{\theta}_2\right), \ldots, \mathbf{a}\left(\widehat{\theta}_{K-1}\right), \mathbf{a}(\theta)\right]. \tag{51}$$

Then. we can attain the estimate of θ_K by the following equation:

$$\widehat{\theta}_K = \underset{\theta\in\left[\widehat{\theta}_K^{ini}-\Delta\theta, \widehat{\theta}_K^{ini}+\Delta\theta\right]}{\operatorname{argmin}} \left\| \widehat{U}_s - \widehat{A}^{(K)}\widehat{A}^{(K)} + \widehat{U}_s \right\|_F^2. \tag{52}$$

Here, the angle searches within a small region $\theta \in [\widehat{\theta}_K^{\text{ini}} - \Delta\theta, \widehat{\theta}_K^{\text{ini}} + \Delta\theta]$.

Due to transforming the multi-dimensional GAS of SF into initialization based 1D PAS, the computational complexity is significantly reduced.

Step 1: compute the covariance matrix $\widehat{R}$ according to equation (2)
Step 2: operate the EVD of $\widehat{R}$ and get the signal subspace by equation (3)
Step 3: via propagator method, obtain the initial angle estimation and recover all the DOA estimates by equations (33) and (34)
Step 4: ambiguity problem is solved via the coprime property and initial estimates $\widehat{\theta}_k^{in}, k = 1, 2, \ldots, K$ are achieved
Step 5: compute fine DOA estimates according to equation (52)

Algorithm 1: The details of the proposed ISF algorithm.

Table 1: Comparison of the computational complexity.

Algorithms	Computational complexity
ISF	$O\left(\begin{array}{c}(M^2+N^2)L + M^3 + N^3 + 2[(M-1)^2 + (N-1)^2]K + (M-1)^3 + \\ (N-1)^3 + [(M-1)+(N-1)]K^2 + G_1[4K(M^2+N^2) + (M^3+N^3)]\end{array}\right)$
SF	$O((M^2+N^2)L + M^3 + N^3 + G_2[4K(M^2+N^2) + (M^3+N^3)])$
NF	$O(M^2+N^2)L + M^3 + N^3 + G_2[M(M-K)K + N(N-K)K])$
TSS	$O((M^2+N^2)L + M^3 + N^3 + G_3[M(M-K) + N(N-K)])$

3.4. Detailed Steps. The detailed steps of the proposed method are (Algorithm 1) as follows:

4. Discussions

4.1. Complexity. In this part, we give the computational complexity comparison results of the proposed ISF algorithm, SF [2], NF [2], and TSS [27]. For ISF, it has the complexity of $(M^2+N^2)L+M^3+N^3+2[(M-1)^2+(N-1)^2]K+(M-1)^3+(N-1)^3+[(M-1)+(N-1)]K^2]+\Pi_1[4K(M^2+N^2)+(M^3+N^3)]$ where $\Pi_1 = K\cdot 2\Delta/\mathrm{ds}$ means the search times and $ds = 0.001$ is the search step, Δ denotes a tiny search value. Moreover, we provide the computational complexity comparison of the different algorithms in Table 1, including SF, NF, and TSS. The comparison of the computational complexity versus number of snapshots and sensors are illustrated in Figures 3 and 4, where $M=3, N=4, K=3, ds=0.001$ and $N=[4,5,7,8]$, respectively. As the proposed method transforms the GAS into PAS and searches over a small sector, it shows clearly that its complexity is much lower than SF, NF, and TSS. Figure 5 depicts the complexity comparison versus the search step. It is seen that ISF can significantly relieve the computational complexity burden.

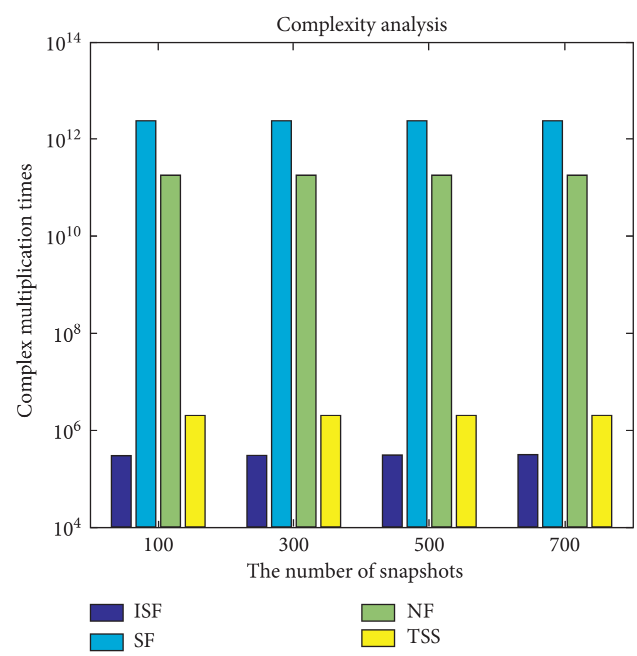

Figure 3: Complexity versus the number of snapshots.

4.2. Cramer-Rao Bound. Here, we derive the CRB [37] of the UCLA.

Elaborate the manifold matrix of the UCLA as follows:

$$\mathbf{A}_t = \left[\frac{\mathbf{A}_1}{\mathbf{A}_{2p}}\right], \tag{53}$$

where $\mathbf{A}_{2p}$ denotes the rows from the second one to the last one of the $\mathbf{A}_2$.

$$\mathbf{CRB} = \frac{\sigma_n^2}{2L}\left\{\mathrm{Re}\left[\mathbf{D}^H\left[\mathbf{I} - \mathbf{A}_t\left(\mathbf{A}_t^H\mathbf{A}_t\right)^{-1}\mathbf{A}_t^H\right]\mathbf{D}\oplus\mathbf{R}_s\right]\right\}^{-1}, \tag{54}$$

where $\mathbf{R}_s = (1/L)\sum_{t=1}^{L}\mathbf{s}(t)\mathbf{s}^H(t)$, $\mathbf{D} = [(\partial\mathbf{a}_{t,1}/\partial\theta_1), (\partial\mathbf{a}_{t,2}/\partial\theta_2), \ldots, (\partial\mathbf{a}_{t,K}/\partial\theta_K)]$, $\oplus$ means the Hadamard operation. And $\mathbf{a}_{t,k}$ is the K^{th} column of $\mathbf{A}_t$.

4.3. Advantages. We give the advantages of the proposed ISF algorithm in the following:

(1) We incorporate the signal subspace fitting method into UCLA, which can achieve the more superior performance than GCLA due to the larger array aperture. It is seen in Figure 5.

(2) When there are multiple signals, the proposed ISF transforms the conventional multi-dimensional search into several 1D search, which can remarkably decrease the computational complexity. It is seen in Figure 2.

(3) By employing the obtained initial DOA estimates, the GAS is transformed into PAS. In this way, the

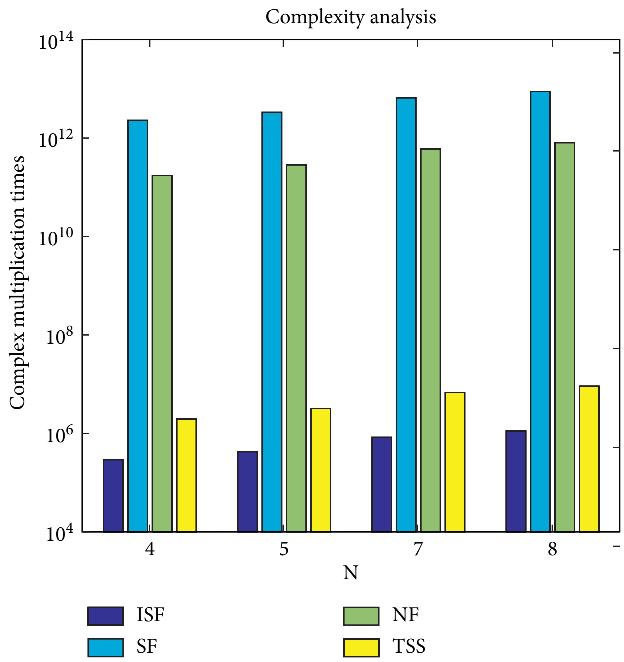

Figure 4: Complexity versus element number.

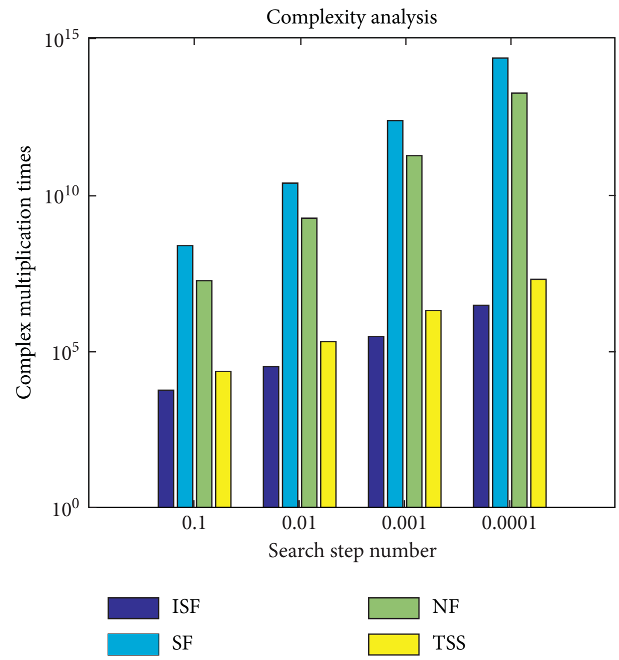

Figure 5: Complexity versus search step number.

complexity has an effective reduction, which can be seen in Section 4.

(4) The proposed ISF is able to attain similar DOA estimation performance as traditional SF and NF algorithms and outperform ESPRIT and PM, which is seen in Section 5.

5. Simulations

In the simulation section, the root mean square error (RMSE) is used as the performance comparison metric, which is defined as follows:

$$\mathrm{RMSE} = \sqrt{\sum_{p=1}^{Q} \sum_{k=1}^{K} \frac{\left(\widehat{\theta}_{k,p} - \theta_k\right)^2}{PK}}, \tag{55}$$

where P is the number of Monte Carlo simulations, $\widehat{\theta}_{k,p}$ stands for the estimate of the p-th trial for the k-th theoretical angle θ_k. And, in this paper, we set $P = 1000$.

5.1. Scattering Figure of the Proposed ISF with UCLA. The scattering figure of the proposed ISF algorithm with UCLA for three distant sources $\theta = [10^\circ, 30^\circ, 50^\circ]$ is presented in Figure 6, where $M = 3, N = 4$, $L = 200$, $\mathrm{SNR} = 5\,\mathrm{dB}$. And, we define the search step and the tiny searching restrain as $ds = 0.001$ and $\Delta = 0.5$. It is shown clearly that the proposed ISF algorithm detects the source signals successfully.

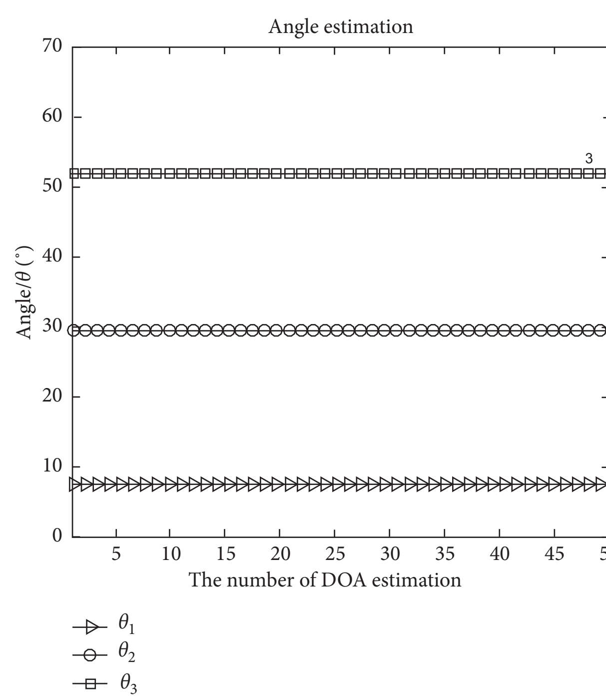

Figure 6: Scattering figure via ISF algorithm.

5.2. Comparison of Different Arrays with the Same Algorithm. The RMSE comparison versus SNR and snapshots with different configurations, including UCLA and GCLA, for two sources $(\theta_1, \theta_2) = [25^\circ, 45^\circ]$ is given in Figures 7 and 8 by the same algorithm. It is defined that $L = 200$ and $\mathrm{SNR} = 5\,\mathrm{dB}$, respectively. From these two figures, we can notice that the UCLA is able to obtain the lower CRB and better DOA estimation performance than the GCLA. Moreover, the proposed ISF algorithm can attain the better DOA estimation performance with the UCLA than that with the GCLA because of the extension of the array aperture.

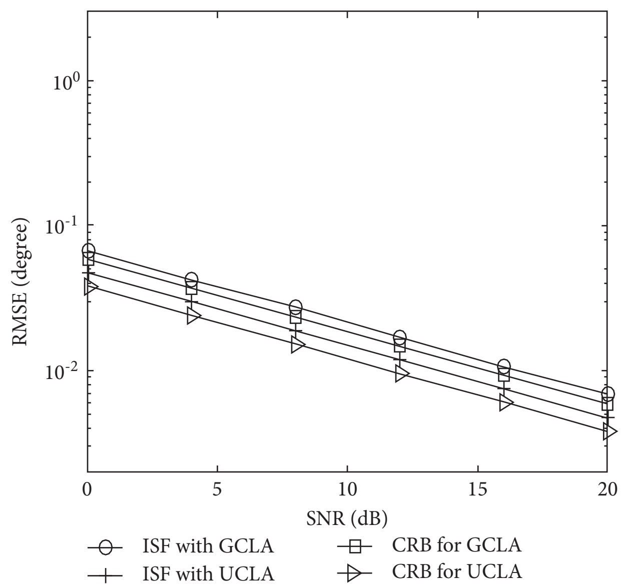

FIGURE 7: RMSE performance versus SNR for different configurations.

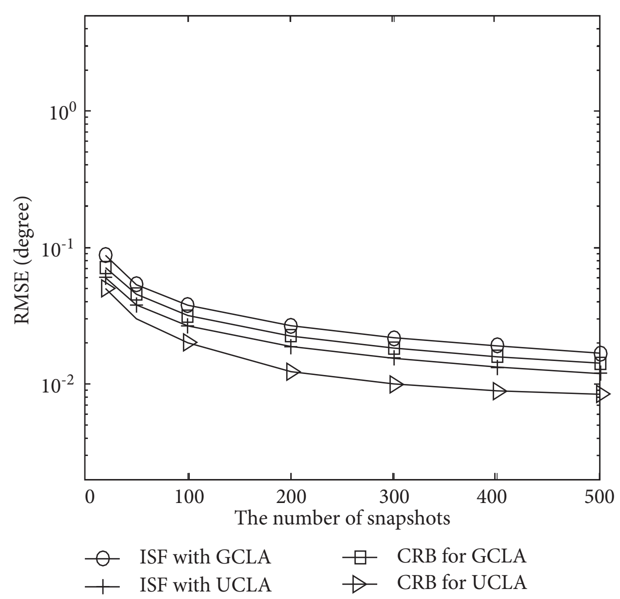

FIGURE 8: RMSE performance versus the number of snapshots for different configurations.

5.3. Comparison of Different Algorithms with the UCLA. In this subsection, the RMSE comparison of the proposed ISF algorithm, SF [33], NF [33], TSS [27], S-SF [38], ESPRIT [11], and PM [14] versus SNR and the number of snapshots is given in Figures 9 and 10, where $M = 3, N = 4$ and $(\theta_1, \theta_2) = [25°, 45°]$ It is defined that $L = 200$ and SNR = 5 dB, respectively. From these two figures, we can notice that ISF can achieve nearly similar estimation performance as SF, NF, and TSS but with the lower complexity due to the initialization operation to decrease the complexity which is verified in Figure 2. What's more, ISF performs the better DOA estimation than ESPRIT and PM.

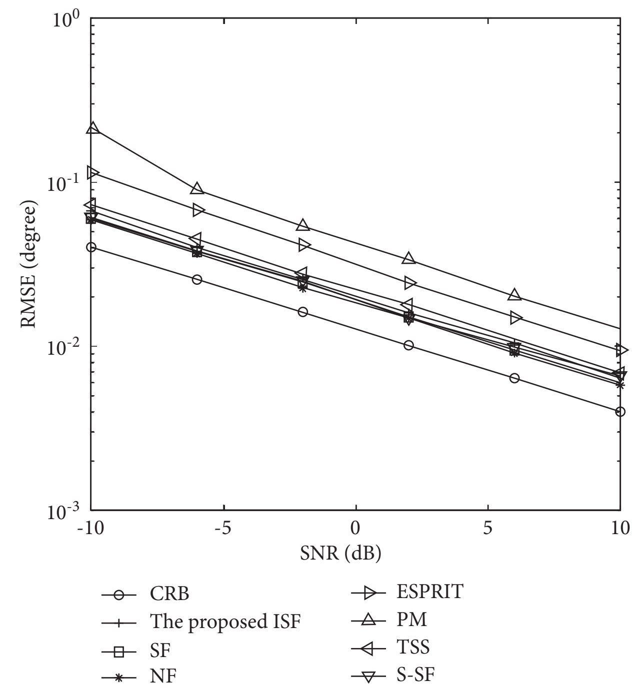

FIGURE 9: RMSE performance versus SNR.

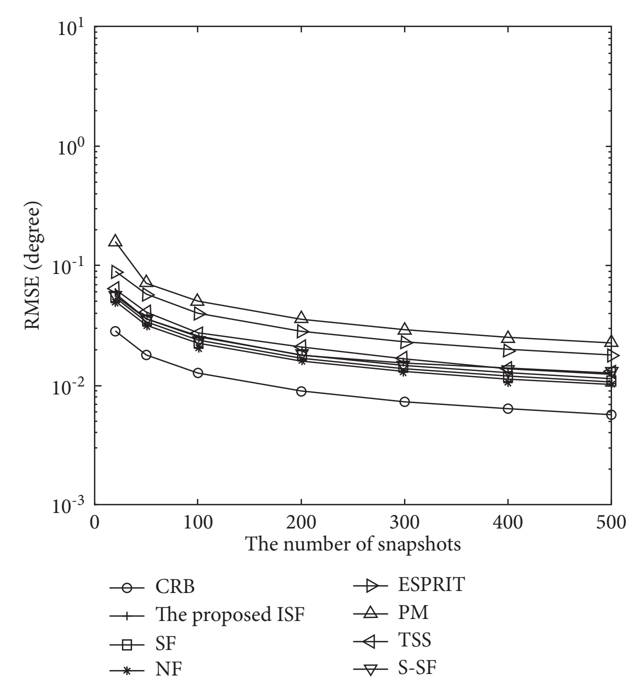

FIGURE 10: RMSE performance versus the number of snapshots.

5.4. RMSE with Different Snapshots and SNR. Figures 11 and 12 compare the estimation performance with a different number of snapshots and SNR, respectively. It shows clearly that the performance of angle estimation becomes better with the number of snapshots and SNR increasing.

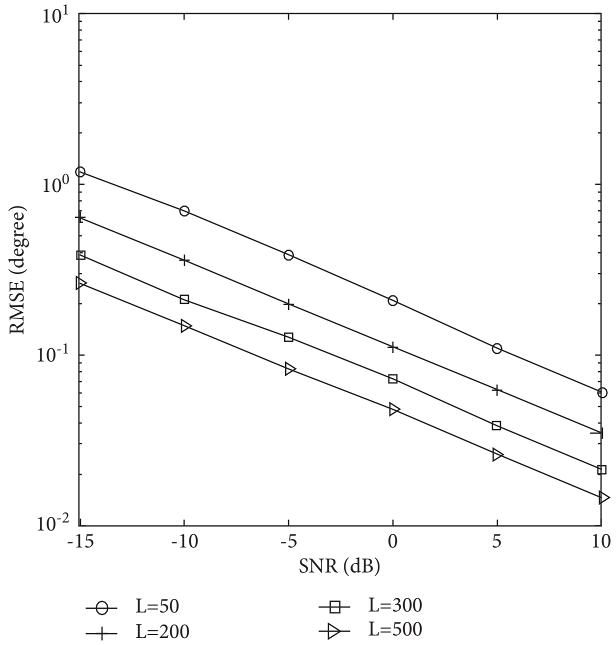

Figure 11: RMSE performance with different (L).

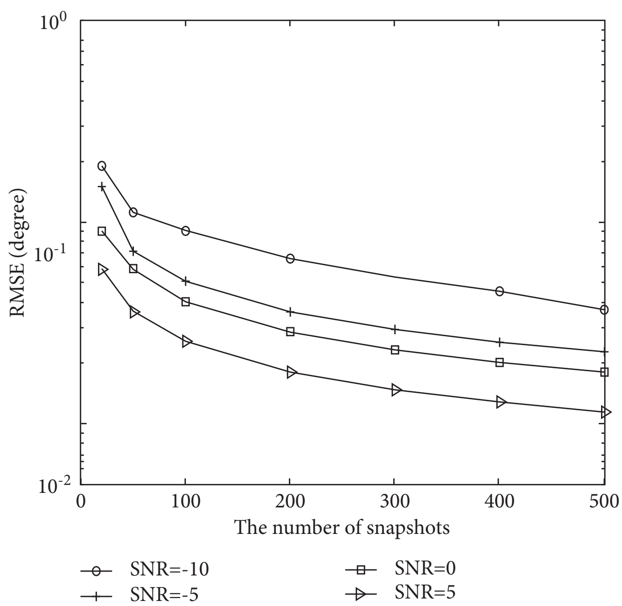

Figure 12: RMSE performance with different SNR.

5.5. Estimation Probability Comparison of Different Algorithms. Figures 13 and 14 depict the estimation probability versus the number of SNR and snapshots of the proposed ISF algorithm, SF [33], NF [33], TSS [27], S-SF [37], ESPRIT [11], and PM [14]. Suppose two closely located targets impinging on the arrays, where $SNR = 5\text{dB}$, $K = 2$, $(\theta_1, \theta_2) = (20^\circ, 21^\circ)$. The two sources can be resolved if $|\theta - \widehat{\theta}| < |\theta_1 - \theta_2|/2$ where $\theta = (\theta_1, \theta_2)$, $\widehat{\theta} = (\widehat{\theta}_1, \widehat{\theta}_2)$ [40]. We can clearly see that the proposed ISF algorithm performs the almost the same estimation probability than SF, NF, and TSS. It can be also inferred that ISF outperforms the ESPRIT and PM algorithms.

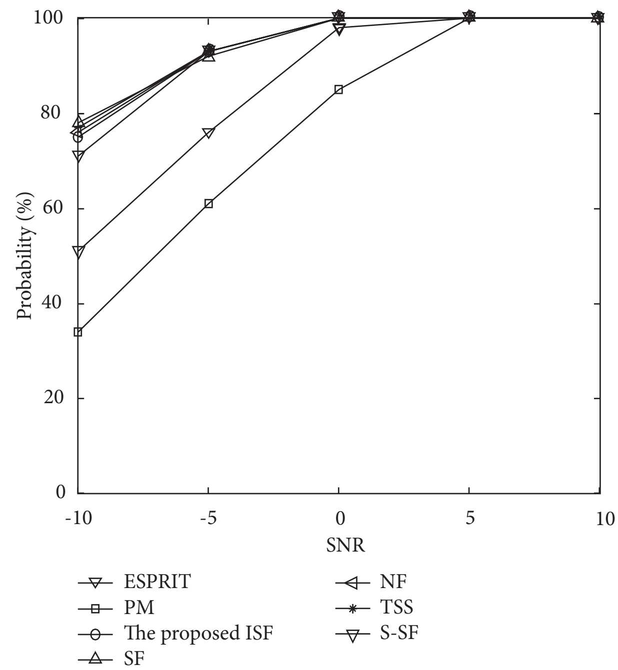

Figure 13: Estimation probability versus SNR.

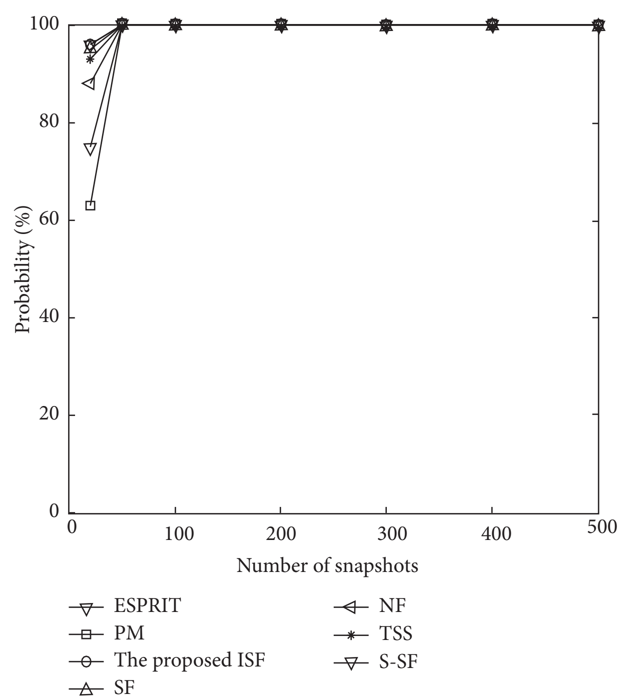

Figure 14: Estimation probability versus snapshots.

6. Conclusions

In this paper, we propose an ISF algorithm for DOA estimation with UCLA and verify that UCLA behaves the better DOA estimation performance than GCLA due to the larger array aperture. In the multiple signals scenery, the classic SF needs severe computational complexity cost due to the multidimensional GAS. To solve this problem, we transform the multi-dimensional search into several 1D one. In addition, GAS is changed to be PAS. Specifically, the propagator method is employed to obtain the initial DOA estimation. By initialization, we can transform the multi-dimensional GAS into several 1D partial one. As a result, the complexity is significantly reduced. CRB is presented and the simulations verify the effectiveness of the proposed algorithm.

Data Availability

The data used to support the findings of this study are included within the article.

Conflicts of Interest

The authors declare that they have no conflicts of interest.

Acknowledgments

This work was supported by China NSF under Grant nos. 61371169, 61601167, 61601504, and 62004100, Jiangsu NSF under Grant no. BK20161489, the open research fund of National Mobile Communications Research Laboratory, Southeast University under Grant no. 2015D03, Natural Science Research Project of Higher Education in Jiangsu Province under Grant no. 20KJD430010, and Jiangsu Wind Power Engineering Technology Center of Research on wind farm data acquisition system based on 5G and University level scientific research under Grant nos. YK20-02-11 and YK19-02-06.

References

[1] F. Wen, J. Shi, and Z. Zhang, "Joint 2D-DOD, 2D-DOA and polarization angles estimation for bistatic EMVS-MIMO radar via PARAFAC analysis," *IEEE Transactions on Vehicular Technology*, vol. 69, no. 2, pp. 1626–1638, 2019.

[2] X. Zhang, L. Xu, L. Xu, and D. Xu, "Direction of departure (DOD) and direction of arrival (DOA) estimation in MIMO radar with reduced-dimension MUSIC," *IEEE Communications Letters*, vol. 14, no. 12, pp. 1161–1163, 2010.

[3] R. Shafin, L. Liu, J. Zhang, and Y. C. Wu, "DoA estimation and capacity analysis for 3-D millimeter wave massive-MIMO/FD-MIMO OFDM systems," *IEEE Transactions on Wireless Communications*, vol. 15, no. 10, pp. 6963–6978, 2016.

[4] Y Huang and J. Liu, "Exclusive Sparsity Norm Minimization with Random Groups via Cone Projection," *IEEE Transactions on Signal Processing*, vol. 64, no. 4, pp. 995–1006, 2015.

[5] A. M. Ahmed, U. S. K. P. M. Thanthrige, A. E. Gamal, and A. Sezgin, "Deep learning for DOA estimation in MIMO radar systems via emulation of large antenna arrays," *IEEE Communications Letters*, vol. 25, no. 5, pp. 1559–1563, 2021.

[6] N. Dey, A. S. Ashour, F. Shi, and R. S. Sherratt, "Wireless capsule gastrointestinal endoscopy: direction-of-arrival estimation based localization survey," *IEEE Reviews in Biomedical Engineering*, vol. 10, pp. 2–11, 2017.

[7] R. O. Schmidt, "Multiple emitter location and signal parameter estimation," *IEEE Transactions on Antennas and Propagation*, vol. 34, no. 3, pp. 276–280, 1986.

[8] M. L. Bencheikh and Y. Wang, "Joint DOD-DOA estimation using combined ESPRIT-MUSIC approach in MIMO radar," *Electronics Letters*, vol. 46, no. 15, pp. 1081–1083, 2010.

[9] X. Gong, Z. Liu, and Y. Xu, "Quad-quaternion MUSIC for DOA estimation using electromagnetic vector sensors," *EURASIP Journal on Applied Signal Processing*, vol. 2009, pp. 1–14, 2008.

[10] J. Li, X. Zhang, R. Cao, and M. Zhou, "Reduced-Dimension MUSIC for angle and array gain-phase error estimation in bistatic MIMO radar," *IEEE Communications Letters*, vol. 17, no. 3, pp. 443–446, 2013.

[11] R. Roy and T. Kailath, "ESPRIT-estimation of signal parameters via rotational invariance tech-niques," *IEEE Transactions on Acoustics, Speech, & Signal Processing*, vol. 37, no. 7, pp. 984–995, 2002.

[12] F. Gao and A. B. Gershman, "A generalized ESPRIT approach to direction-of-arrival estimation," *IEEE Signal Processing Letters*, vol. 12, no. 3, pp. 254–257, 2005.

[13] X. Zhang and D. Xu, "Low-complexity ESPRIT-based DOA estimation for colocated MIMO radar using reduced-dimension transformation," *Electronics Letters*, vol. 47, no. 4, pp. 283-284, 2011.

[14] S. Marcos, A. Marsal, and M. Benidir, "The propagator method for source bearing estimation," *Signal Processing*, vol. 42, no. 2, pp. 121–138, 1995.

[15] J. Li, X. Zhang, and H. Chen, "Improved two-dimensional DOA estimation algorithm for two-parallel uniform linear arrays using propagator method," *Signal Processing*, vol. 92, no. 12, pp. 3032–3038, 2012.

[16] Z. Ye, J. Dai, X. Xu, and X. Wu, "DOA estimation for uniform linear array with mutual coupling," *IEEE Transactions on Aerospace and Electronic Systems*, vol. 45, no. 1, pp. 280–288, 2009.

[17] C. Qi, Y. Wang, Y. Zhang, and H. Chen, "DOA estimation and self-calibration algorithm for uniform circular array," *Electronics Letters*, vol. 41, no. 20, pp. 1092–1094, 2005.

[18] S. Ren, X. Ma, S. Yan, and C. Hao, "2-D unitary ESPRIT-like direction-of-arrival (DOA) estimation for coherent signals with a uniform rectangular array," *Sensors*, vol. 13, no. 4, pp. 4272–4288, 2013.

[19] Z. Ye and X. Xu, "DOA estimation by exploiting the symmetric configuration of uniform linear array," *IEEE Transactions on Antennas and Propagation*, vol. 55, no. 12, pp. 3716–3720, 2007.

[20] B. D. Steinberg, *Principles of Aperture and Array System Design*, Wiley, NY, USA, 1976.

[21] P. Pal and P. Vaidyanathan, "Coprime sampling and the music algorithm," in *Proceedings of the Digital Sig. Proc. Workshop and IEEE Signal Proc. Edu. Workshop Proceeding of the*, pp. 289–294, Sedona, AZ, USA, January 2011.

[22] G. Zheng and J. Tang, "DOD and DOA estimation in bistatic MIMO radar for nested and coprime array with closed-form DOF," *International Journal of Electronics: Theoretical & Experimental*, vol. 104, no. 5, pp. 885–897, 2017.

[23] H. Zhai, X. Zhang, W. Zheng, and P. Gong, "DOA Estimation of Noncircular Signals for Unfolded Coprime Linear Array: Identifiability, DOF and Algorithm," *IEEE Access*, vol. 6, pp. 29382–29390, 2018.

[24] E. Boudaher, F. Ahmad, M. G. Amin, and A. Hoorfar, "DOA Estimation with Co-prime Arrays in the Presence of Mutual coupling," in *Proceedings of the 2015 23rd European Signal Processing Conference Proceeding of the*, IEEE, Fajardo, PR, USA, August 2015.

[25] Y. Qin, Y. Liu, J. Liu, and Z. Yu, "Underdetermined wideband DOA estimation for off-grid sources with coprime array using sparse bayesian learning," *Sensors*, vol. 18, no. 1, p. 253, 2018.

[26] Q. Si, Y. D. Zhang, and M. G. Amin, "Sparsity-based Multi-Target Localization Exploiting Multi-Frequency Coprime array," in *Proceedings of the 2015 IEEE China Summit & International Conference on Signal & Information Processing Proceeding of the*, IEEE, Chengdu, China, July 2015.

[27] C. Zhou, Z. Shi, Y. Gu, and X. Shen, "DECOM: DOA estimation with combined MUSIC for coprime array," in *Proceedings of the 2013 IEEE International Conference on Wireless Communication and Signal Proceeding Proceeding of the*, pp. 1–5, Hangzhou, October 2013.

[28] F. Sun, P. Lan, and B. Gao, "Partial spectral search-based DOA estimation method for co-prime linear arrays," *Electronics Letters*, vol. 51, no. 24, pp. 2053–2055, 2015.

[29] C. Ashok and N. Venkateswaran, "An efficient method for resolving ambiguity in DOA estimation with coprime linear array," *Circuits, Systems, and Signal Processing*, vol. 41, no. 4, pp. 2411–2427, 2021.

[30] W. Zheng, X. Zhang, P. Gong, and H. Zhai, "DOA estimation for coprime linear arrays: an ambiguity-free method involving full DOFs," *IEEE Communications Letters*, vol. 22, no. 3, pp. 562–565, 2018.

[31] M. Shinagawa, K. Ichige, and H. Arai, "Accuracy and computational complexity of DOA estimation algorithms with beamspace transformation IEICE technical report," *Antennas and propagation*, vol. 102, 2003.

[32] L. Zhao, X. Li, L. Wang, and G. Bi, "Computationally efficient wide-band DOA estimation methods based on sparse bayesian framework," *IEEE Transactions on Vehicular Technology*, vol. 66, no. 12, pp. 11108–11121, 2017.

[33] M. Viberg, "Subspace fitting concepts in sensor array processing," *Signal Processing*, vol. 19, p. 345, 1990.

[34] C. Gong, B. Shi, and H. Chen, "Joint-PSO Algorithm for Weighted Subspace Fitting of DOA Estimation," *Computer Systems & Applications*, vol. 12, 2018.

[35] E. A. Santiago, "Noise Subspace Based Iterative Direction of Arrival Estimation technique," *Dissertations & Theses-Gradworks*, vol. 49, no. 4, pp. 2281–2295, 2013.

[36] M. Viberg, B. Ottersten, and T. Kailath, "Detection and estimation in sensor arrays using weighted subspace fitting," *IEEE Transactions on Signal Processing*, vol. 39, no. 11, pp. 2436–2449, 1991.

[37] P. Stoica and A. Nehorai, "MUSIC, maximum likelihood, and Cramer-Rao bound," *IEEE Transactions on Acoustics, Speech, & Signal Processing*, vol. 37, no. 5, pp. 720–741, 1989.

[38] P. Gong, X. Zhang, and T. Ahmed, "Computationally efficient DOA estimation for coprime linear array: a successive signal subspace fitting algorithm," *International Journal of Electronics*, vol. 107, no. 2, 2020.

[39] P. Stoica and A. Nehorai, "Performance study of conditional and unconditional direction-of-arrival estimation," *IEEE Transactions on Acoustics, Speech, & Signal Processing*, vol. 38, no. 10, pp. 1783–1795, 1990.

[40] R. Schmidt, *A Signal Subspace Approach to Multiple Emitter Location and Spectral Estimation*, Ph.D. dissertation. Stanford University, Stanford, CA, Nov, 1982.

Hindawi
Mathematical Problems in Engineering
Volume 2022, Article ID 1265658, 11 pages
https://doi.org/10.1155/2022/1265658

Research Article

Two-Dimensional Transceiver Beamforming for Mainlobe Jamming Suppression with FDA-MIMO Radar

Pengfei Wan[1,2] **Guisheng Liao**[1] **Jingwei Xu**[1] **and Guimei Zheng**[2]

[1]*National Laboratory of Radar Signal Processing, Xidian University, Xi'an, Shaanxi 710071, China*
[2]*Air Defence and Anti Missile College, Air Force Engineering University, Xi'an, Shaanxi 710051, China*

Correspondence should be addressed to Pengfei Wan; wanpengfei@stu.xidian.edu.cn

Received 7 March 2022; Revised 3 April 2022; Accepted 11 June 2022; Published 8 July 2022

Academic Editor: Ardashir Mohammadzadeh

With the rapid development of electronic warfare technology, the airborne electronic counter measures (ECM) system can generate mainlobe jamming using range gate pull-off (RGPO) strategy, which brings serious performance degradation of target tracking for the tracking and guidance radar. In this study, a two-dimensional transceiver beamforming approach is proposed to suppress the mainlobe jamming with frequency diverse array using multiple-input multiple-output (FDA-MIMO) radar. The mainlobe jamming signal differs from the real target echo in the joint transmit and receive domain due to the range dependence of FDA beampattern. The amplitude of RGPO signal is greater than the amplitude of real target echo. Thus, the transceiver beampattern can be designed to null out the jamming while maintaining the real target. The jamming suppression performance is studied in consideration of practical range constraint of RGPO. Simulation results are provided to verify the effectiveness of the proposed approach.

1. Introduction

Tracking and guidance radar plays an important role in national defense applications [1–4]. It provides sufficient antijamming ability against the jammers with the low side lobe antenna technique and large time-bandwidth products. However, with the development of electronic interference technique in the advanced weapons, tracking and guidance radar encounters extremely hostile environment in the mainlobe [5–7]. For example, the electronic counter measures (ECM) system has been developed to generate strong jamming in the mainlobe [8–10], which becomes a great challenge for the traditional phased array radar systems.

The mainlobe jamming is not easy to implement and also difficult to suppress. Especially, the multidimensional modulation deceptive jamming signal from the mainlobe seriously affects the performance of the radar system [11–14]. Deceptive jamming intercepts the radiation signal of radar by airborne electronic support measures (ESM) and modulates the range and speed in multiple dimensions, and then a deceptive jamming pattern similar to the real radar detection waveform is generated, that is, the false target is generated by the way of "intercept-modulation-forward," which can make the radar system mistakenly regard the false target as the real target. Therefore, deceptive jamming has serious consequences such as increased false alarm, missing of real target, and extremely heavy computational burden [15–17].

RGPO is an effective technique for deceptive jamming of radar range information. Because it has the advantages of low interference power and strong flexibility, it has become a hot research topic in recent years [18, 19]. Greco et al. [20] studied the working mechanism of RGPO and analyzed the influence of delay quantization based on digital radio frequency memory (DRFM) on jamming signals. Öztürk et al. [21] adopted the RGPO of bidirectional false target, which can effectively resist the pulse leading edge or trailing edge tracking technology adopted by radar. Xie et al. [22] proposed a range gate RGPO method based on bidirectional false targets, which is verified by evaluating radar measurements. In the study by Rui-xing and Jian-yun [23], a jamming power compensation technique was proposed to improve the success rate of range gate RGPO, and the output peak value of pulse compression was used to evaluate the RGPO effect. Xue and Yang [24] optimized the realization mode of range gate RGPO and put forward a method to improve the effect of range gate RGPO by frequency shift technology.

In order to counter the RGPO, this study presents a method of countering the range gate RGPO based on frequency diverse array (FDA)-multiple-input multiple-output (MIMO) radar [25]. It is a new radar system that combines frequency diversity array and MIMO radar [26–29]. Because of the multiantenna transmission single frequency step system, it forms a three-dimensional range-angle-time-dependent pattern in the far field, and the research shows that the range-angle dependence of FDA's transmission pattern is different from that of traditional radar [30]. However, in order to make full use of this characteristic, it is necessary to effectively separate the transmitter signal, and MIMO radar technology is an effective means to obtain the freedom of transmission [31]. Zhang and Xie [32] extracted the phase difference of adjacent array elements by analyzing the influence of each link in radar signal processing and realized the suppression of false targets. In [33], the antijamming ability was improved by joint optimization of transmission polarization and transmission frequency step interval. Reference [34] adopted a method based on eigenvector to improve jamming suppression ability.

This study, according to the analysis of the principle of RGPO, takes advantage of the characteristic that the amplitude of RGPO signal is larger than the amplitude of the real target echo, a method is proposed for the FDA-MIMO radar to eliminate RGPO corresponding to the large eigenvalue, which improves the antijamming ability of the radar system and keeps the stable tracking.

The structure of this article is as follows: Section 2 introduces the signal model and the fundamentals of FDA-MIMO radar followed by the introduction of the algorithm to eliminate the jamming signal with range constraint in Section 3. Subsequently, simulation and analysis are given in Section 4. Finally, Section 5 draws a conclusion and summarizes this study.

Notation: $\otimes$ and $\odot$ denote Kronecker product and Hadamard product, respectively. The letter $j \triangleq \sqrt{-1}$ represents the imaginary unit. The transpose and conjugate transpose of a matrix or vector are denoted by $(\cdot)^T$ and $(\cdot)^H$. Boldfaced lowercase letters such as x represent a vector, boldfaced uppercase letters such as R denote a matrix, and italic letters such as a represent a scalar. For the vector x, we use $[x]_n$ to denote the nth element of vector x. For matrix R, we use $[R]_{m,n}$ to denote the element of R in the mth row and the nth column. Finally, $[a, b]$ indicates a closed interval in real number space.

2. Fundamentals of FDA-MIMO Radar

It is considered that the FDA-MMO radar system is an isometric linear array composed of M transmitting antenna elements and N receiving antenna elements [35]. Under the condition of ignoring the antenna element pattern and array error, the transmitting and receiving antenna elements are omni-directional radiation, which are identical and uniform. The transmission signal form of the mth transmitting unit can be written as [36]

$$s_m(t) = rect\left(\frac{t}{T_p}\right)\varphi_m(t)\exp\{j2\pi f_m t\}, \tag{1}$$

where t is the elapsed time of pulse propagation since the start of the pulse, $rect(t/T_p) = \begin{cases} 1, 0 \le t \le T_P \\ 0, else \end{cases}$ is the pulse modulation function, $\varphi_m(t)$ is the baseband modulation signal corresponding to the mth transmitting unit [37], and f_m is the transmitting frequency corresponding to the mth transmitting unit:

$$f_m = f_0 + (m-1)\Delta f, \quad m = 1, 2, \ldots, M, \tag{2}$$

where f_0 is the frequency of the reference array element (the first array element) and Δf is the frequency offset between array elements.

Assuming that there is a target at a certain position (R, θ) in space, the echo from the mth transmitting antenna unit received by the nth receiving antenna unit can be written as

$$\begin{aligned} x_{s,m,n}\left(t-\tau_{m,n}\right) = \beta_{s0} rect\left(\frac{t-\tau_{m,n}}{T_p}\right)\varphi_m\left(t-\tau_{m,n}\right) \\ \cdot \exp\left\{j2\pi f_0\left(t-\tau_{m,n}\right)\right\}, \end{aligned} \tag{3}$$

where β_{s0} represents the complex coefficient of the target echo including the full link of radar transmitting and receiving, $\tau_{m,n} = \tau_0 - d(m-1)\cos(\theta)/c - d(n-1)\cos(\theta)/c$ represents the echo delay difference corresponding to the mth transmitting unit and the nth receiving unit, and d is the interelement spacing. Because the working frequency of each transmitting element of FDA-MIMO radar is different, when equation (3) expresses the approximate model under the assumption of far-field narrowband, the phase term introduced by frequency stepping cannot be ignored. When equation (1) is brought into equation (3), we can get

$$\begin{aligned} x_{s,m,n}(t-\tau_0) \approx \beta_{s0} rect\left(\frac{t-\tau_0}{T_p}\right)\exp\{j\phi_m(t-\tau_0)\} \\ \cdot \exp\left\{j2\pi\Delta f(m-1)\left(t-\tau_{m,n}\right)\right\} \\ \cdot \exp\left\{j2\pi f_0\left(t-\tau_{m,n}\right)\right\}, \end{aligned} \tag{4}$$

where $\tau_0 = 2R/c$ is the reference delay of the target echo. The target echo received by the nth receiving antenna unit can be approximately written as

$$\begin{aligned} x_{s,n}(t-\tau_0) \approx \sum_{m=1}^{M} \beta_{s0} rect\left(\frac{t-\tau_0}{T_p}\right)\exp\{j\phi_m(t-\tau_0)\} \\ \cdot \exp\left\{j2\pi\Delta f(m-1)\left(t-\tau_{m,n}\right)\right\} \\ \cdot \exp\left\{j2\pi f_0\left(t-\tau_{m,n}\right)\right\}. \end{aligned} \tag{5}$$

The target echo is amplified and matched filtered, and the range unit where the target is located can express the signal as a concise form:

$$s = \beta_s a(R, \theta) \otimes b(\theta), \tag{6}$$

where β_s represents the complex coefficient of the target echo after pulse compression; $a(R, \theta)$ and $b(\theta)$ are the transmit and receive steering vectors of the target, respectively, and $\otimes$ is the Krnoecker product:

$$\begin{aligned} a(R,\theta) &= a_r(R) \odot a_\theta(\theta) = \\ &\cdot \left[1,\ \exp\left(-j4\pi\Delta f \frac{R}{c}\right), \ldots,\ \exp\left(-j4\pi\Delta f \frac{(M-1)R}{c}\right)\right]^T \odot \\ &\cdot \left[1.\ \exp\left(j2\pi \frac{d\ \sin\ \theta}{\lambda}\right), \ldots,\ \exp\left(j2\pi \frac{(M-1)d\ \sin\ \theta}{\lambda}\right)\right] = \\ &\cdot \left[1,\ \exp\left\{-j4\pi \frac{\Delta f R}{c} + j2\pi \frac{d}{\lambda}\cos(\theta)\right\}, \cdots,\ \exp\left\{-j4\pi \frac{\Delta f R}{c}(M-1) + j2\pi \frac{d}{\lambda}(M-1)\cos(\theta)\right\}\right]^T, \end{aligned} \tag{7}$$

$$b(\theta) = \left[1,\ \exp\left\{j2\pi \frac{d}{\lambda}\cos(\theta)\right\}, \cdots,\ \exp\left\{j2\pi \frac{d}{\lambda}(N-1)\cos(\theta)\right\}\right]^T, \tag{8}$$

where $\odot$ denotes the Hadamard product, $a_r(R)$ and $a_\theta(\theta)$ mean the launch range and launch angle steering vectors, respectively [38], and T is the transpose operator. As can be seen from equation (7), compared with the traditional radar, the range guidance vector of FDA-MIMO radar contains the range information R of the target signal, and its range guidance vector is correlated with angle and range in two dimensions. Because of the two-dimensional correlation between angle and range, FDA-MIMO radar has the ability to distinguish targets with different ranges in the transmitting space, that is, it can distinguish different targets on the close range gate with the same angle, which provides great practical value for radar to counter the jamming from mainlobe.

Assuming that airborne ESM on space far-field target intercepts radar tracking signal and releases self-defense RGPO, the intercepted radar signal is stored and transmitted with the delay to form a false target jamming signal in the fast time dimension. The jamming signal is stronger than the target echo, and the signal form corresponding to the mth transmitting unit and the nth receiving unit can be expressed as the signal form of the mth transmitting unit and the nth receiving unit:

$$x_{j,m,n}(t-\tau_j) \approx \beta_{j,p} rect\left(\frac{t-\tau_j}{T_p}\right)\exp\{j\phi_m(t-\tau_j)\}\exp\{j2\pi\Delta f(m-1)(t-\tau_{j,m,n})\}\exp\{j2\pi f_0(t-\tau_{j,m,n})\}, \tag{9}$$

where $\tau_j = R_i/c$ is the reference delay of the RGPO jamming signal generated by the jammer and $\tau_{j,m,n} = \tau_j - d(m-1)\cos(\theta)/c - d(n-1)\cos(\theta)/c$ represents the echo delay difference between the mth transmitting unit and the nth receiving unit.

As can be seen from equation (9), the pull-off jamming signal of the range map is completely consistent with the target echo. The time delay between the target echo and jamming is different. After the above analysis of RGPO, the jamming delay signal τ_j and the real target echo delay time τ_0 are located in the same range gate. According to the traditional radar processing method, the radar range tracking center will be greatly affected. It is necessary to combine the radar prior knowledge and jamming characteristics to design antijamming. The specific analysis is introduced in the next section. For the convenience of description, the output signal form after matched filtering is given after considering the target signal, jamming, and noise comprehensively

$$x(t) = s(t) + j(t) + n(t) = \beta_s(t)a(R,\theta) \otimes b(\theta) + \beta_j(t)a(R_j,\theta) \otimes b(\theta) + n(t). \tag{10}$$

Among them, $\beta_s(t) = \beta_s\delta(t - \tau_0)$ is the time delay corresponding to the range gate where the target located is τ_0 and $\beta_j(t) = \beta_j\delta(t - \tau_j)$ is the time delay of the jammer generating RGPO is τ_j.

3. Principle and Method of Anti-RGPO for FDA-MIMO Radar

In Section 2, the real target echo and jamming signal in FDA-MIMO radar system are studied. The echo of the target releasing self-defense jamming is completely consistent with the jamming signal in angle dimension, but its range dimension is slightly deviated. Whether the range dimension deviation can be effectively used to suppress the jamming is the key to resist this kind of mainlobe jamming. Based on the analysis of jamming mechanism and mathematical model, combined with radar signal and information processing flow, this section expounds the application of FDA-MIMIO radar against RGPO in range dimension and gives the antijamming conditions and methods.

3.1. Mechanism of RGPO. RGPO is a kind of self-defense jamming. Usually, the airborne ESM system intercepts the radar radiation signal after finding that it is tracked and locked by the tracking and guidance radar and forwards the jamming signal with a certain delay through fast storage, so that the range tracking gate center of the enemy radar deviates from the real target and locks on the released false target, thus tracking the lost technical method. In the actual radar system, after tracking the target, the angle, range, and speed of the target can be predicted with high data rate, and the target position at the next moment can be interception in a certain range, which is called wave gate. If the jamming signal deviates greatly from the real target and exceeds the wave gate range, it may be eliminated as outliers or cannot form an effective jamming track in the data processing stage, and the jamming effect would not be achieved.

RGPO can be divided into front-gate-pull-off jamming and back-gate-pull-off jamming according to different delay time functions [39]. For the jamming in front of the wavefront, the forwarding delay of the jamming signal gradually decreases for the radar tracking system, which results in an "illusion" that the false target is gradually approaching the radar system relative to the real target. For the back-gate-pull-off jamming, the delay of jamming signal forwarding increases gradually, resulting in a "phenomenon" that the range the false target is gradually apart from the real target in radar system. As for that front-gate-pull-off jamming, one or more pulse repetition stages need to be delayed. If the radar adopts frequency agility technology, the jamming effect would not be achieved. For back-gate-pull-off jamming, the time delay of the jamming signal needs to be within the same range gate as the target echo. If the radar adopts leading edge tracking technology, it can also effectively resist deceptive jamming. However, for the radar system, the time delay of the real echo received is inaccurate, and it is impossible to accurately determine the jamming style it is, so a new antijamming technology is needed to deal with the pull-off jamming with different ranges. This study focuses on countering the back-gate-pull-off jamming, and the proposed algorithm is also suitable for the front-gate-pull-off jamming.

For RGPO, it is generally divided into three stages: interception stage, pull-off stage, and stop stage:

Interception stage: after intercepting the tracking signal, the airborne ESM system stores and quickly forwards a jamming signal. Usually, the time delay of the jamming signal needs to basically coincide with the target echo in time dimension. A_s represents the amplitude of the target echo and A_j represents the amplitude of the jamming signal $A_j/A_s \approx 1.3 \sim 1.5$

Pull-off stage: in order to make the range gate center of radar deviate from the real echo of the target and avoid two echo peaks at the same time, ESM system needs to gradually increase the delay time of forwarding every time it intercepts a radar tracking signal, so that the range gate center gradually leaves the target position until the range gate deviates from the target echo by a predetermined range.

Stopping stage: when the ESM system judges that the radar has deviated from the real target by enough range from the center of the wave gate, it stops radiating jamming signals, which leads to the radar losing the target or increasing the tracking error, so it is necessary to search and find the target again.

If the above three steps are repeated, the radar can get rid of the tracking of the target or increase the tracking error of the radar.

3.2. Mathematical Model of RGPO. RGPO is mainly aimed at the radar working in tracking mode. Because the tracking filter has started to work, the radar has a priori information about the position and speed of the target, and through this priori information, the three-dimensional information of the target in the next working cycle can be predicted. In order to get rid of radar tracking, the target releases RGPO. Assuming that the pull-off range of RGPO to the center of echo is ΔR at the i pulse repetition interval (PRI) of radar, the time delay of radar receiving jamming signal is

$$\tau_j = \tau_{s,i} + \Delta\tau_{j,i}. \tag{11}$$

In the equation, τ_j is the delay time of the jamming signal [40], $\tau_{s,i}$ is the delay time of the real target echo, $\Delta\tau_{j,i} = \Delta R/c$ is the time corresponding to the pull-off jamming range of the i frame, and $\tau_{j,i} > \tau_{j,i-1}$. The pull-off range gradually increases, as shown in Figure 1.

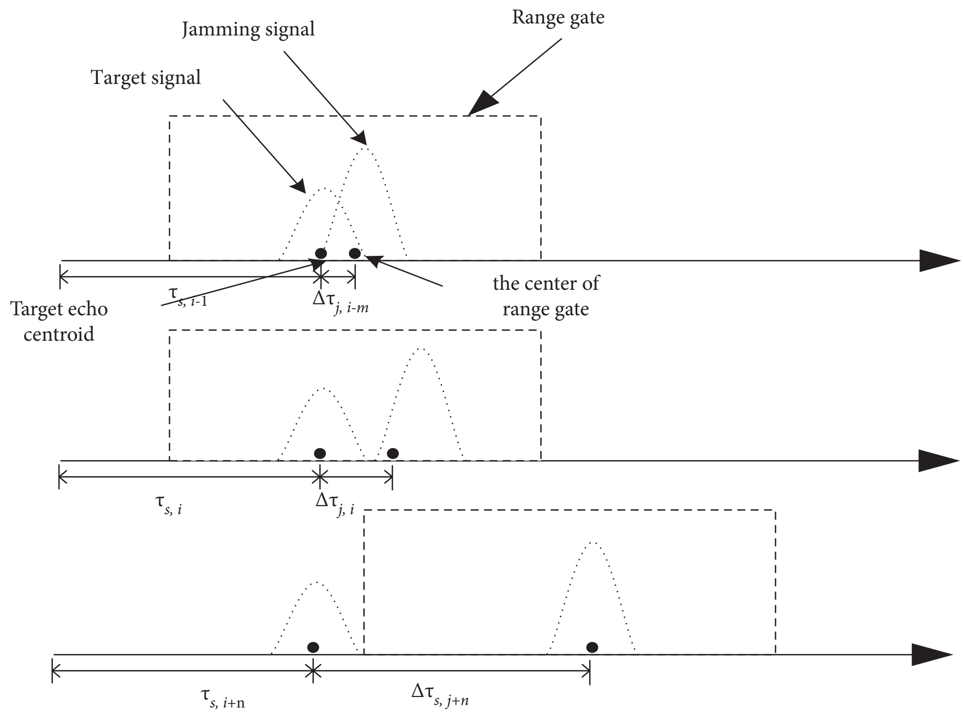

FIGURE 1: Schematic diagram of RGPO.

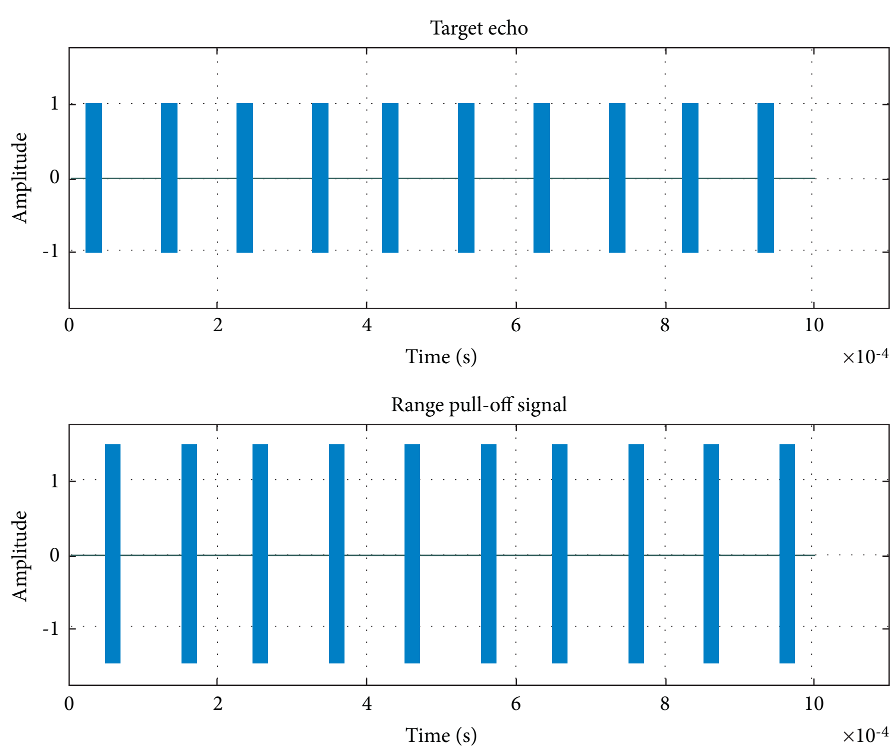

FIGURE 2: Schematic diagram of time domain waveform of RGPO signal.

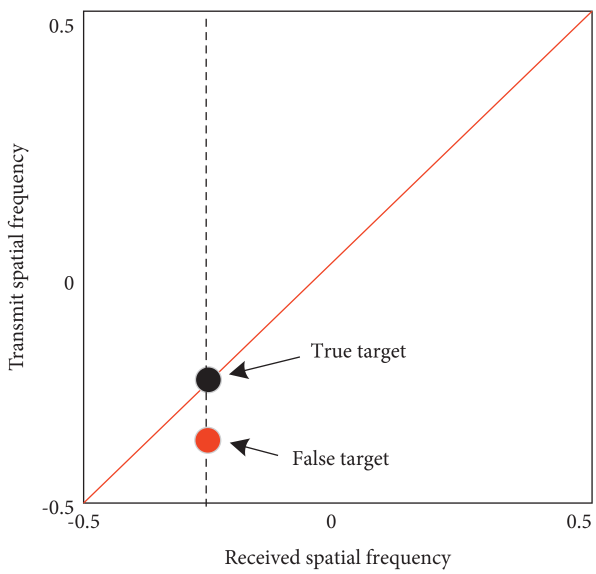

FIGURE 3: Distribution of real target and false target in transmitting-receiving two-dimensional spatial frequency domain after range pull-off.

The time delay information $\Delta\tau_{j,i}$ of false target caused by range gate RGPO jamming can be expressed as

$$\Delta\tau_{j,i} = \begin{cases} 0 & 0 \le i < \mathrm{m}\ \text{Interception stage}, \\ \dfrac{2v(i-m)}{c} \text{ or } \dfrac{a(i-m)^2}{c}, & m \le i < \mathrm{n}\ \text{Pull}-\text{off stage}, \\ \text{Pull}-\text{off stop}, & n \le i < T\text{Stopping stage}. \end{cases} \tag{12}$$

Among them, a represents the pull-off acceleration in the process of uniform acceleration pull-off and v is the pull-off speed in the process of uniform acceleration pull-off. Figure 2 is a schematic diagram of time domain waveform of RGPO signal.

3.3. Jamming Suppression Method. It can be concluded that the RGPO has the following characteristics:

Feature 1: in order to deviate the center of radar gate, the amplitude of RGPO signal must be greater than the amplitude of real target echo

Feature 2: because the jamming signal and the target echo are basically consistent in time dimension during the interception stage, the jamming suppression processing cannot be carried out in time domain during the interception stage

Feature 3: during the pull-off stage, because the jamming signal gradually deviates from the target echo, the delay time of the jamming signal is different from that of the target real echo in time dimension

Assuming that the jamming parameter is (R_j, θ_j) and the transmitting space frequency and receiving space corresponding to the jamming signal are, respectively,

$$f_{Tj} = -\frac{2\Delta f R_j}{c} + \frac{d}{\lambda}\cos\left(\theta_j\right), \tag{13}$$

$$f_{Rj} = \frac{d}{\lambda}\cos\left(\theta_j\right). \tag{14}$$

Assume that the parameter of the target is (R_s, θ_s), where $\theta_s = \theta_j$, $R_s = R_j - \Delta R$, and ΔR are the pull-off range.

Then, the transmitting spatial frequency and receiving spatial frequency corresponding to the target scattering signal are

$$f_{Ts} = -\frac{2\Delta f R_s}{c} + \frac{d}{\lambda}\cos\left(\theta_s\right), \tag{15}$$

$$f_{Rs} = \frac{d}{\lambda}\cos\left(\theta_s\right). \tag{16}$$

It can be seen from the above equation that for RGPO, the receiving spatial frequency is completely consistent with the backscattered signal of the target, but the transmitting spatial frequency is different. In order to ensure the difference of transmitting spatial frequencies, the jamming suppression algorithm proposed in this study is mainly completed during the pull-off stage.

Because the release time of RGPO is that the radar has been working in the target tracking state, the relevant prior information of the target has been obtained, including the distance and angle of the target. It is assumed that the predicted position of the radar for the target is (R_y, θ_y), and the target and jamming position are extended and constrained, so that the jamming and target signals fall into the constrained range. The specific method is to set the range tracking accuracy of the radar to be σ_R. Centered on the target position predicted by the radar, and search inside $R_l = \pm 3\sigma_R$, namely:

$$\begin{cases} R_s \in \left[R_y - R_l, R_y + R_l\right] = R_h \\ R_j \in \left[R_y - R_l, R_y + R_l\right] = R_h \end{cases}, \tag{17}$$

where R_l is the range constraint value and R_h is the range in the constructed target steering vector.

According to the working principle of RGPO, assuming that the jammer releases a pull-off signal that is greater than the target echo amplitude, the covariance matrix R_X of the constrained azimuth echo can be expressed by eigenvector:

$$R_X = \sum_{k=1}^{2} \lambda_k u_k u_k^H + \sum_{k=3}^{N^2} \lambda_k u_k u_k^H. \tag{18}$$

The first term of equality coordinates u_k is the eigenvector corresponding to the signal subspace and λ_k is the eigenvalue corresponding to the signal subspace. Under the ideal condition of not considering false alarm, because the echo and jamming signal are independent,

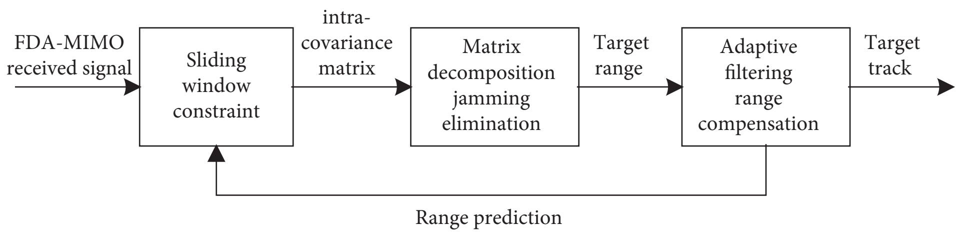

Figure 4: Flowchart of FDA-MIMO radar anti-RGPO.

Table 1: Radar simulation parameters.

Parameter	Parameter value	Parameter	Parameter value
Operating frequency	10 GHz	Pulse repetition frequency	10 kHz
Sampling frequency	5 MHz	Number of receiving array elements	10
Number of transmitting array elements	10	Receiving array element spacing	0.015 m
Launching element spacing	0.015 m	Range tracking error	40 m
Target state noise	20 m	Target motion model	Constant velocity model
SNR	10 dB	Tracking filter	Standard Kalman
Target range	10 km	Target angle	0°
RGPO JNR	15 dB	Target speed	100 m/s
Pull-off time	30 s	Range pull-off speed	10 m/s

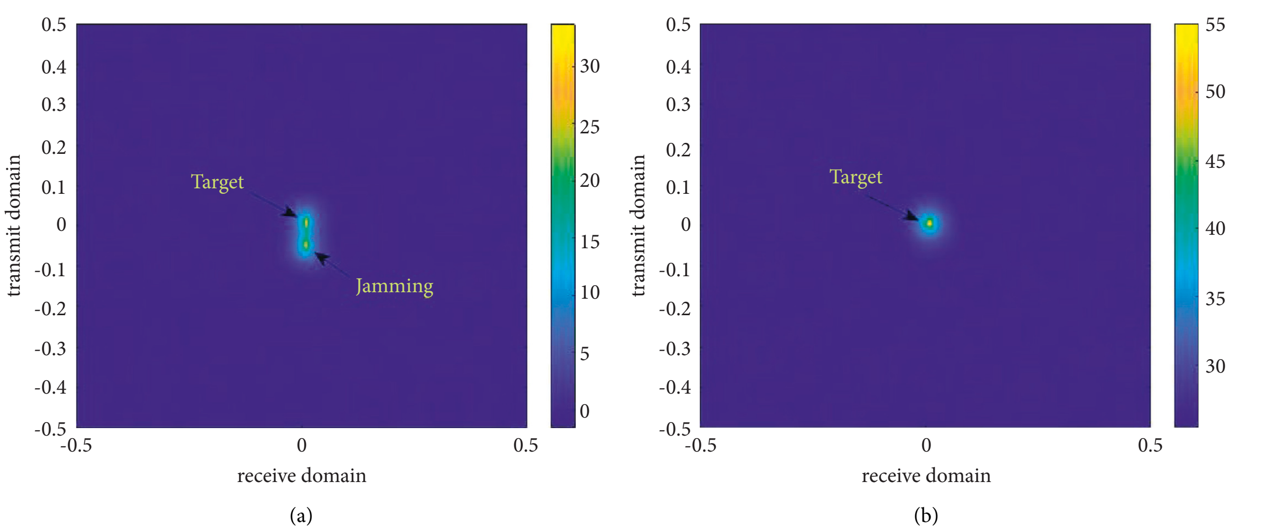

Figure 5: Power spectrum characteristics of real target and pull-off jamming. (a) Power spectrum pull-off by range. (b) Power spectrum after antijamming.

two large eigenvalues can be obtained after the eigendecomposition of the received covariance matrix. Because the signal strength of pull-off jamming is stronger than that of target echo. The eigenvalues are arranged in sequence from large to small, the jamming signal corresponding to the largest eigenvalue is eliminated, and the rest is the range corresponding to the target signal, and then the transmission angular frequency compensation is carried out according to the range of the target signal. The transmission spatial frequencies of the compensated target signal and the pull-off jamming signal are as follows:

$$\widehat{f}_{Ts} = \frac{d}{\lambda}\cos(\theta_s), \tag{19}$$

$$\widetilde{f}_{Tj,p} = -\frac{2\Delta f \Delta R}{c} + \frac{d}{\lambda}\cos(\theta_j). \tag{20}$$

After compensation, the pull-off jamming signal can be clearly distinguished from the target signal, as shown in Figure 3.

As shown in the figure, the real target is distributed diagonally in the transmit-receive spatial frequency, and the pull-off jamming needs to deviate from the center of the gate,

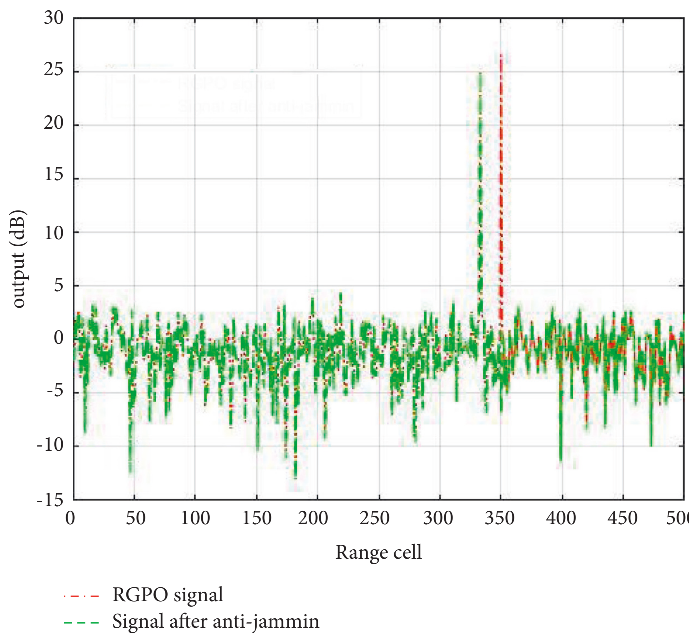

Figure 6: Output results of signal processing before and after antijamming.

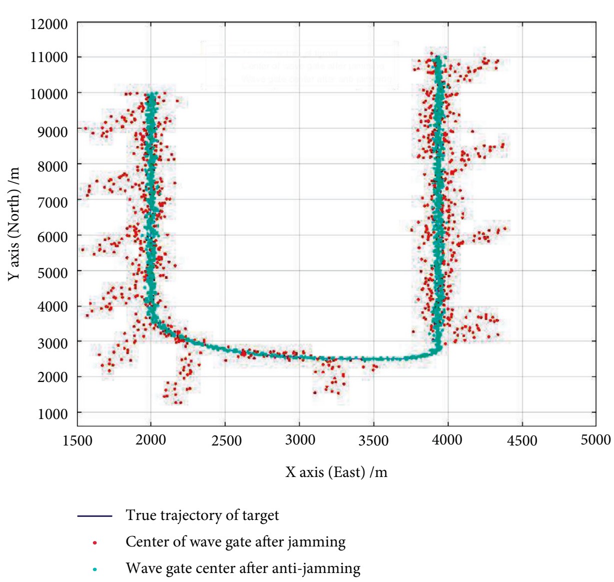

Figure 7: Change of wave gate center before and after radar jamming.

which is obviously different from the real target in the transmit spatial frequency.

Based on the analysis of real target and RGPO signal characteristics, combined with the characteristics of FDA-MIMO radar, two-dimensional beamforming technology is used to suppress pull-off jamming signal. Its beamformer weights can be expressed as

$$w_{MF} = a\left(\hat{f}_T\right) \otimes b\left(\hat{f}_R\right). \tag{21}$$

After the target range compensation, the weights of the two-dimensional filter are independent of the range parameters, but only related to the angle parameters of radar detection. However, the weights of two-dimensional filters are affected by the following two factors:

(1) The accuracy of radar prediction of target range, which would cause the loss of matching output

(2) The accuracy of radar angle estimation, which directly affects the accuracy of weights

The adaptive beamformer based on the minimum lossless response criterion can overcome the above influence factors, which can be expressed as

$$\begin{aligned} &\min_{w_{AMF}} E\left\{\left|w_{AMF}^H \tilde{x}\right|^2\right\} \\ &s.t. w_{AMF}^H\left[a\left(\hat{f}_T\right) \otimes b\left(\hat{f}_R\right)\right] = 1. \end{aligned} \tag{22}$$

where $\tilde{x}$ is the compensated data. After adaptive beamforming, the influence of range gate pull-off jamming can be effectively suppressed.

In this study, the flow of the specific method proposed is shown in Figure 4:

Step 1: use the radar's predicted value of the target range dimension to constrain the target steering vector according to equation (16), and set the constraint range to within $\pm 3\sigma_R$ the radar tracking accuracy, so that the real target and the jamming signal are both within the constrained steering vector range;

Step 2: perform eigendecomposition on the covariance matrix R_X, including the target echo and the jamming signal, and use the characteristic that the jamming signal is stronger than the target echo to eliminate the jamming signal range corresponding to the large eigenvalue to obtain the true range of the target;

Step 3: after obtaining the true range of the real target, compensate the launch angle frequency, distinguish the jamming signal and the target echo in the launch-receive spatial frequency, use the MVDR criterion to form an adaptive filter, complete the range

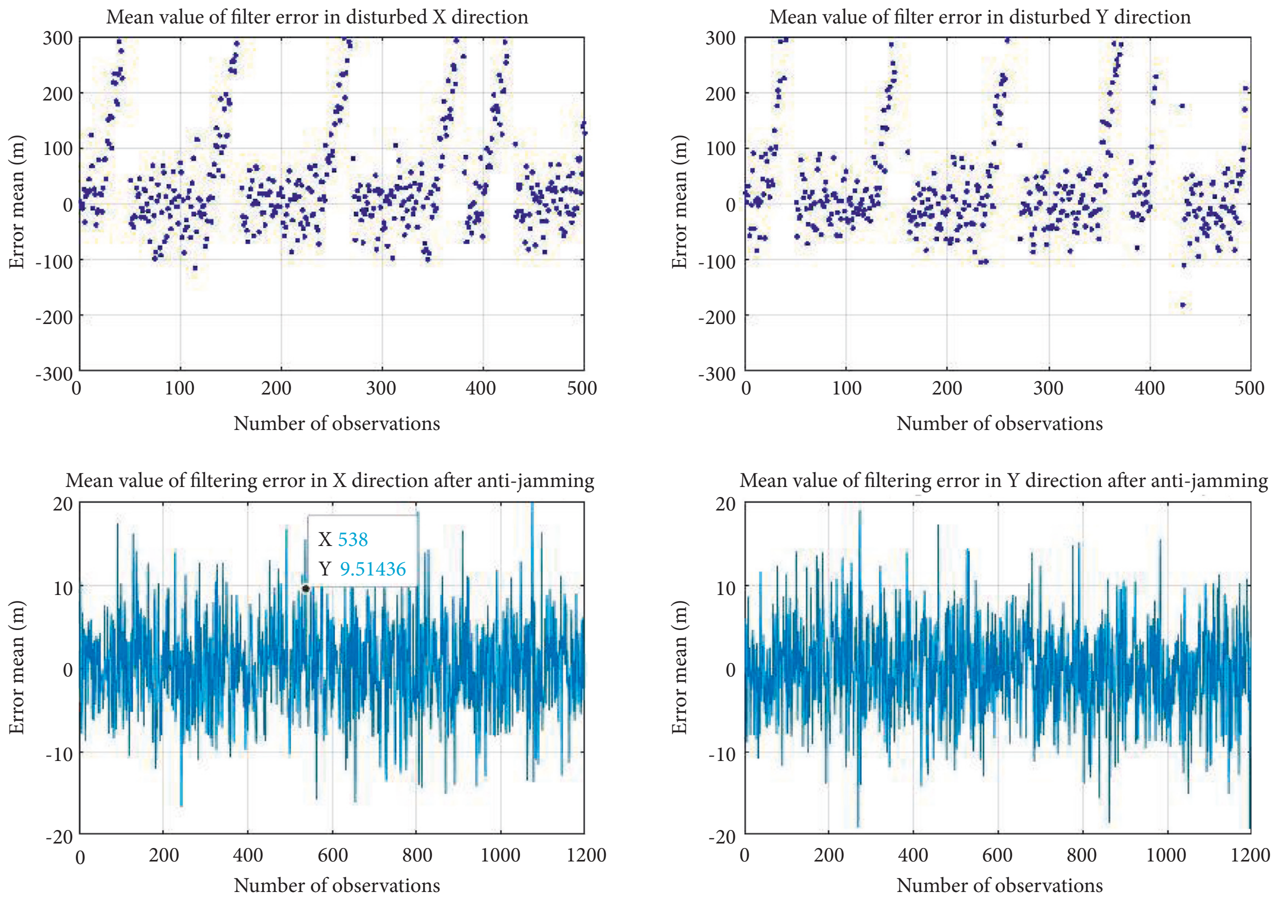

Figure 8: The average change of tracking error before and after radar antijamming.

compensation in the launch dimension, and complete the target track.

4. Simulation Verification

In this section, the effectiveness of the proposed approach is verified by simulation examples. Without losing generality, assume that the radar receives the jamming signal radiated by the enemy when it has stably tracked the target, and the jammer intercepts the radar tracking signal and tows it to release the RGPO. The relevant parameters of simulation are given in Table 1.

4.1. Power Spectrum Analysis before and after Antijamming. Figure 5 shows the simulation comparison results of echo before and after processing the antijamming approach proposed in the transmission-reception frequency domain. It can be seen from the simulation results that because the echo in FDA-MIMO system contains the range dimension information of the echo in the transmitting frequency domain, the radar cannot accurately distinguish the real target echo because the amplitude of the jamming signal is greater than that of the echo after receiving the RGPO signal, and the range between the jamming signal and the target echo is close during the pull-off stage. After constrained and large signal is proposed, the transmission frequency domain can be compensated, and the true echo of the target can be accurately detected. It should be noted that due to the target motion and radar detection error, the position of the compensated target may change slightly. Figure 6 shows the signal strength distribution after pulse compression in range dimension before and after antijamming. In this simulation, with receiving the jamming signal, the maximum amplitude of the output is about 28 dB and the range cell is 350 where the jamming is, after processing antijamming, the maximum amplitude of the output is about 25 dB and the range cell is 333 where the real target is.

4.2. Tracking Performance Analysis. The tracking performance before and after antijamming is analyzed. In order to accurately show the experimental results, it is assumed that the flying height of the target remains unchanged in the northeast coordinate system, and the tracking performance is mainly analyzed on X axis and Y axis. Figure 7 shows the change of the whole range segment of the range-dimensional tracking gate center before and after the radar is jammed by range pull-off. It can be seen from the example that after receiving the RGPO, the range tracking gate center of the radar would gradually deviate from the real target position, resulting in increased tracking error or even out of tolerance, and the target would be lost after the jamming signal disappears. Figure 8 shows the average tracking error of X axis and Y axis in the radar tracking process. It can be seen that the tracking error increases dramatically after receiving the RGPO. After filtering, the two-dimensional range error is about ±300 m, which is far greater than the radar tracking accuracy. After antijamming, the two-dimensional range error changes ±40 m, and the radar can keep stable tracking of the target.

5. Conclusion

Tracking and guidance radar is usually affected by the mainlobe jamming. In this study, focused on the principle and application of FDA-MIMO radar against range gate pull-off jamming, an effective way to solve the problem that the center of range gate deviates from the real target greatly due to pull-off jamming is provided on the basis of analyzing the principle and working process of RGPO. Based on two-dimensional transceiver beamforming and range eliminating, the jamming signal can be suppressed. The experimental results verify the effectiveness and feasibility of the proposed method from two important links of detection and tracking radar.

Data Availability

The data used to support the findings of this study are available from the corresponding author upon request.

Conflicts of Interest

The authors declare that there are no conflicts of interest.

Acknowledgments

This work was supported by the Nature Science Foundation of China (NSFC) (61931016).

References

[1] G. Li, Y. Zhou, W. Xia, and J. Cao, "A Simulation Technique Service Training Method of Guidance Radar Equipment Based on Visual Simulation," in *Proceedings of the 2016 2nd IEEE International Conference on Computer and Communications (ICCC)*, pp. 2864–2868, Chengdu, October 2016.

[2] D. Tarchi, F. Oliveri, and P. F. Sammartino, "MIMO radar and ground-based SAR imaging systems: equivalent approaches for remote sensing," *IEEE Transactions on Geoscience and Remote Sensing*, vol. 51, no. 1, pp. 425–435, January. 2013.

[3] A. Basit, S. Y. Nusenu, S. Wali, and S. Wali, "FDA based QSM for mmWave wireless communications: frequency diverse transmitter and reduced complexity receiver," *IEEE Transactions on Wireless Communications*, vol. 20, no. 7, pp. 4571–4584, 2021.

[4] X. Li, D. Wang, X. Ma, and W. Q. Wang, "FDS-MIMO radar low-altitude beam coverage performance analysis and optimization," *IEEE Transactions on Signal Processing*, vol. 66, no. 9, pp. 2494–2506, 2018.

[5] A. Basit, S. Y. Nusenu, S. Wali, and S. Yaw Nusenu, "Transmit beamspace design for FDA–MIMO radar with alternating direction method of multipliers," *Signal Processing*, vol. 180107832 pages, 2021.

[6] M. Soumekh, "SAR-ECCM using phase-perturbed LFM chirp signals and DRFM repeat jammer penalization," *IEEE Transactions on Aerospace and Electronic Systems*, vol. 42, no. 1, pp. 191–205, January. 2006.

[7] L. Lan, M. Rosamilia, A. Aubry, A. D. Maio, and G. Liao, "Single-snapshot angle and incremental range estimation for FDA-MIMO radar," *IEEE Transactions on Aerospace and Electronic Systems*, vol. 57, no. 6, pp. 3705–3718, 2021.

[8] L. Lan, G. Liao, J. Xu, Y. Zhang, and B. Liao, "Transceive beamforming with accurate nulling in FDA-MIMO radar for imaging," *IEEE Transactions on Geoscience and Remote Sensing*, vol. 58, no. 6, pp. 4145–4159, 2020.

[9] S. Zhao and Z. Liu, "Main-Lobe jamming suppression method in multiple-radar system," in *Proceedings of the IGARSS 2019 IEEE International Geoscience and Remote Sensing Symposium*, pp. 2276–2279, Yokohama, Japan, August 2019.

[10] Z. Xiang, B. Chen, and M. Yang, "Polarization optimization for mainlobe interference suppression," *International Conference on Radar Systems (Radar)*, vol. 12, pp. 1–5, 2017.

[11] Y. Yuan, G. Cui, M. Ge, X. Yu, and L. Kong, "Active repeater jamming suppression via multistatic radar elliptic-hyperbolic location," *Proc. IEEE Radar Conference*, vol. 45, pp. 692–697, May 2017.

[12] F. Bandiera, A. Farina, D. Orlando, and G. Ricci, "Detection algorithms to discriminate between radar targets and ECM signals," *IEEE Transactions on Signal Processing*, vol. 58, no. 12, pp. 5984–5993, December, 2010.

[13] G. Zheng, Y. Song, and C. Chen, "Height Measurement for with wave polarimetric MIMO radar: signal model and MUSIC algorithm," *Signal Processing*, vol. 190, 2022.

[14] P. Wan, Y. Weng, J. Xu, and G. Liao, "Range gate pull-off mainlobe jamming suppression approach with FDA-MIMO radar theoretical formalism and numerical study," *Remote Sensing*, vol. 14, no. 6, p. 1499, 2022.

[15] J. Shi, Z. Yang, and Y. Liu, "On parameter identifiability of diversity-smoothing-based MIMO radar," in *IEEE Transactions on Aerospace and Electronic Systems*, November 2021.

[16] J. Zhang, X. Zhu, and K. E. Wang, "A waveform diversity technique for countering RGPO," *2009 IET International Radar Conference*, vol. 58, pp. 1–4, 2009.

[17] T. Cheng, Z. He, and Y. Li, "An Effective Target Tracking Algorithm with Anti-RGPO Ability," in *Proceedings of the 10th IEEE International NEWCAS Conference*, pp. 117–120, Montreal, QC, Canada, June 2012.

[18] X. Yong, Y. Fang, S. Chen, and Y. Wu, "Sensor registration algorithm considering RGPO deception," *2015 Chinese Automation Congress (CAC)*, vol. 6, pp. 1874–1878, 2015.

[19] R. Jia, T. Zhang, Y. Wang, and Y. Deng, "An Intelligent Range Gate Pull-Off (RGPO) Jamming Method," in *Proceedings of the 2020 International Conference on UK-China Emerging Technologies*, pp. 1–4, UCET), Glasgow, UK, August 2020.

[20] M. Greco, F. Gini, and A. Farina, "Combined effect of phase and RGPO delay quantization on jamming signal spectrum," *IEEE International Radar Conference*, vol. 77, pp. 37–42, 2005.

[21] M. T. Öztürk, Y. Dalveren, and A. Kara, "Spectrum analysis of parabolic range gate pull-off (RGPO) signals," in *Proceedings of the 2015 23nd Signal Processing and Communications Applications Conference (SIU)*, pp. 1026–1029, Malatya, Turkey, May 2015.

[22] M. Xie, L. Liu, C. Zhang, and X. Fu, "Bidirectional false targets RGPO jamming," in *Proceedings of the 2018 13th IEEE Conference on Industrial Electronics and Applications (ICIEA)*, pp. 2345–2348, Wuhan, China, May 2018.

[23] G. Rui-xing and Z. Jian-yun, "Jamming power compensate method related to RGPO retransmission time delay," *Fire Control and Command Control*, vol. 43, no. 06, pp. 107–110+117, 2018.

[24] y. Xue and Ai ping Yang, "Analysis and simulation of range gate pull jamming method based on frequency," *ShiftShipboard Electronic Countermeasure*, vol. 41, no. 03, pp. 42–44+95, 2018.

[25] J. Xiong, W. Q. Wang, and K. Gao, "FDA-MIMO radar range-angle estimation: CRLB, MSE, and resolution analysis," *IEEE Transactions on Aerospace and Electronic Systems*, vol. 54, no. 1, pp. 284–294, February. 2018.

[26] L. Lan, J. Xu, G. Liao, Y. Zhang, F. Fioranelli, and H. C. So, "Suppression of mainbeam deceptive jammer with FDA-MIMO radar," *IEEE Transactions on Vehicular Technology*, vol. 69, no. 10, pp. 11584–11598, 2020.

[27] J. Xu, S. Zhu, and G. Liao, "Range ambiguous clutter suppression for airborne FDA-STAP radar," *IEEE Journal of Selected Topics in Signal Processing*, vol. 9, no. 8, pp. 1620–1631, December, 2015.

[28] J. Xu, G. Liao, Y. Zhang, H. Ji, and L. Huang, "An adaptive range-angle-Doppler processing approach for FDA-MIMO radar using three-dimensional localization," *IEEE Journal of Selected Topics in Signal Processing*, vol. 11, no. 2, pp. 309–320, March 2017.

[29] G. Zheng and Y. Song, "Signal model and method for joint angle and range estimation of low-elevation target in meter-wave FDA-MIMO radar," *IEEE Communications Letters*, vol. 26, no. 2, pp. 449–453, February. 2022.

[30] L. Lan, J. Xu, S. Zhu, and G. Liao, "Advances in anti-jamming using waveform diverse array radar," *Systems Engineering and Electronics*, vol. 43, no. 6, pp. 1437–1451, 2021.

[31] J. Xu, J. Kang, G. Liao, and H. C. So, "Mainlobe Deceptive Jammer Suppression with FDA-MIMO Radar," in *Proceedings of the 2018 IEEE 10th Sensor Array and Multichannel Signal Processing Workshop (SAM)*, pp. 504–508, Sheffield, UK, July 2018.

[32] Z. Zhang and J. Xie, "Discrimination method of range deception jamming based on FDA-MIMO," *Journal of Beijing University of Aeronautics and Astronautics*, vol. 43, no. 4, pp. 738–746, 2016.

[33] R. Gao and Y. Quan, "Main-lobe decetive Jamming suppression with FDA-MIMO radar based on BSS," *Systems Engineering and Electronics*, vol. 42, no. 9, pp. 1927–1934, 2020.

[34] H. Chen and R. Li, "FDA-MIMO radar main-lobe dense false target jamming suppression based on feature vector eliminating," *Journal of Air Force Early Warning Academy*, vol. 32, no. 6, pp. 397–401, 2018.

[35] Q. Liu, J. Xu, Z. Ding, and H. C. So, "Target localization with jammer removal using frequency diverse array," *IEEE Transactions on Vehicular Technology*, vol. 69, no. 10, pp. 11685–11696, 2020.

[36] L. Lan, G. Liao, J. Xu, Y. Zhang, and F. Fioranelli, "Suppression approach to main-beam deceptive jamming in FDA-MIMO radar using nonhomogeneous sample detection," *IEEE Access*, vol. 6, pp. 34582–34597, 2018.

[37] Z. Ding and J. Xie, "Joint transmit and receive beamforming for cognitive FDA-MIMO radar with moving target," *IEEE Sensors Journal*, vol. 21, no. 18, pp. 20878–20885, 2021.

[38] J. Xu, G. Liao, S. Zhu, L. Huang, and H. C. So, "Joint range and angle estimation using MIMO radar with frequency diverse array," *IEEE Transactions on Signal Processing*, vol. 63, no. 13, pp. 3396–3410, July, 2015.

[39] H. Zhou, C. Dong, R. Wu, X. Xu, and Z. Guo, "Feature fusion based on bayesian decision theory for radar deception jamming recognition," *IEEE Access*, vol. 9, pp. 16296–16304, 2021.

[40] J. Yang, X. Fu, C. Zhang, X. Yin, P. Cong, and S. Su, "Anti-Time-Delay Repeater Jamming under Sea Surface Target Spatial Position Constraint," in *Proceedings of the 2019 IEEE 4th International Conference on Signal and Image Processing (ICSIP)*, pp. 425–429, Wuxi, China, July 2019.

Hindawi
Mathematical Problems in Engineering
Volume 2022, Article ID 9717413, 11 pages
https://doi.org/10.1155/2022/9717413

Research Article

Joint Design Method of Transmit-Receive for Airborne MIMO Radar Based on Feasible Point Pursuit

Jianchong Huang,[1] Zhihui Li ,[1] Xiaobo Li,[1] Chunsheng Liu,[1] Chaoyang Niu,[1] Xiaoxing Feng,[1] and Qiang Wang[2]

[1]*College of Electronic Engineering, National University of Defense Technology, Hefei 230037, China*
[2]*College of Information and Communication, National University of Defense Technology, Wuhan, China*

Correspondence should be addressed to Zhihui Li; lizhihui_16@163.com

Received 29 March 2022; Accepted 25 May 2022; Published 13 June 2022

Academic Editor: Wang Zheng

Consider the moving target detection performance degradation of airborne multiple-input multiple-output (MIMO) radar in the presence of inaccurate target prior information. This paper proposes a joint design method of transmit waveform and receive filter bank of airborne MIMO radar based on feasible point pursuit successive convex approximation (FPP-SCA). Firstly, a set of receive filter banks is designed in the region where the target may appear on the angle-Doppler plane, and the worst-case output signal-to-clutter-plus-noise ratio (SCNR) is maximized as the optimization criterion. Secondly, considering the energy constraint and similarity on the transmit waveform, the maximin joint design problem is formulated to improve the robustness of the MIMO space-time adaptive processing (STAP) radar against the uncertainty of target parameters. Finally, an FPP-SCA algorithm is employed to solve the maximin nonconvex joint design problem. Simulation results demonstrate the effectiveness of the proposed method in terms of better output SCNR, lower computational load, and more robustness against the errors of target parameters.

1. Introduction

As the information hub of the modern battlefield environment, early warning aircraft can effectively improve the combat effectiveness of the battlefield. As the core of early warning aircraft, airborne radar can expand the detection range of radar to ground, ocean, and air targets [1]. However, the airborne radar suffers from intense ground/sea clutter due to its down-looking mode. The clutter is strongly coupled in the space-time domains, which leads to the weak target signal completely submerged by the clutter and makes it more difficult for airborne radar to detect the moving target [2]. Collecting the received data of the space-time domain, space-time adaptive processing (STAP) can effectively suppress side-lobe clutter and main-lobe clutter and improve the detection performance of moving targets under clutter background [3]. Nevertheless, the airborne radar is faced with threats such as low observable targets, low-altitude target, and advanced integrated electronic jamming in the contemporary battlefield environment. It is necessary to develop new system airborne radar and corresponding new theory and technology of signal processing [4].

Multiple-input multiple-output (MIMO) radar can flexibly transmit different waveforms through different antennas [5]. Utilizing the property of waveform diversity, MIMO radar can design different transmit waveform, which makes it superior to traditional-phased array radar in target detection, parameter estimation, recognition, and classification [6–10]. In addition, making full use the information of the target and environment, the cognitive radar extends the adaptive technology from the receiver to the transmitter [11]. Thus, the cognitive radar forms a fully adaptive radar processing system with a dynamic closed-loop receiver, transmitter, and environment. According to the prior information of the dynamic environment database and the environment information obtained by the radar in real time, cognitive radar can infer and decide the optimal waveform or the waveform parameters suitable for the current radar working scene. By adaptively adjusting and optimizing the resource allocation of the radar system and the transmit waveform, cognitive radar can obtain the optimal target detection performance in the complex and changeable environment. Inspired by the cognitive idea and MIMO radar, and based on the actual prior environment information, it is possible for the airborne MIMO radar to jointly design the transmit waveform and receive filter to realize the best matching between the system and the environment and improve the target detection performance in the complex environment.

In the past decades, joint design of transmit waveform and receive filter for airborne collocated MIMO radar system has received considerable attention. These research studies can be divided into two categories. The first category deals with the joint design of transmit-receive exploiting the accurate prior information [12–19]. In [12], maximizing the output signal-to-interference-plus-noise ratio (SINR) under the practical waveform constraints (i.e., the energy constraint, constant-envelope constraint, and similarity constraint), the joint design problem is formulated in an earlier time and five iterative algorithms based on generalized Rayleigh quotient, relaxation and waveform extracting, and fractional programming are proposed. In 2016, Setlur and Rangaswamy of the US Air Force Research Laboratory studied the waveform design problem in STAP, which assumed that the clutter response was related to the transmit waveform [13]. Since the objective function of the weight vector and waveform vector is joint nonconvex, while the objective function of a single weight vector and waveform is convex, the constrained selection minimization technology is proposed to iteratively optimize another vector while keeping one vector unchanged. O'Rourke Sean et al. [14] studied the joint design problem of transmit signal and receive beamformer under the signal-dependent STAP, and proposed a relaxed biquadratic optimization method to find a feasible solution. In addition, they extended the energy constraint on waveform to constant-modulus and similarity constraint [15]. In [16], the minorization-maximization (MM) technique is employed to solve the resultant quartic waveform optimization problem. Compared with the semidefinite programming (SDP) method, the joint design algorithm based on MM technique exhibits faster convergence speed and better SINR performance. In [17, 18], the Riemannian geometry optimization method is first applied to the joint design of MIMO-STAP radar, and the Riemannian gradient descent algorithm and the Riemannian trust region algorithms are proposed to solve the joint design problem.

However, the performance of MIMO-STAP radar is severely degraded when the prior information is inaccurate. Then, the second category addresses the robust joint design of transmit-receive in the presence of prior information uncertainties. In [20], considering the presence of target space-time steering vector mismatch, the worst-case output SINR over the set of the target space-time steering vector is maximized as a figure of merit for the robust joint design. However, the waveform covariance matrix obtained by the relaxation constraint of the target steering vector and the diagonal loading technique is still suboptimal. To solve this problem, Tang Bo et al. [21] used a more general uncertainty set to describe the steering vector error, and then accurately derived the worst target steering vector that minimizes the output SINR. This method abandoned the heuristic diagonal loading method to find the globally optimal waveform covariance matrix which is robust to the target steering vector error. In [22], considering the uncertainty of target Doppler frequency and angle, the joint design of MIMO-STAP radar with peak-to-average power ratio (PAPR) and transmit power constraints is studied. However, this method has high computational complexity, and only three independent interference is considered in the simulation scene. In [23], based on the known target Doppler frequency and spatial angle statistical distribution, the averaged output signal-to-clutter-plus-noise ratio (SCNR) is deduced as the optimization criterion, and four robust joint design methods-based SDP relaxation and fractional programming with power method-like are proposed. In [24], the maximin joint design of transmit waveform and receive filter bank under the energy constraint, flexible modulus constraint, and similarity constraint are considered. In [25], with the prior knowledge of target and clutter statistics, the averaged SINR is formulated as a figure of merit to maximize. Then, an iterative algorithm based on Dinkelbach transformation and alternating direction penalty method (ADPM) is proposed to solve the robust joint design problem.

In this paper, focusing on the joint design problem of transmit waveform and receive filter bank of airborne MIMO radar when the target angle and Doppler parameters are inaccurate, a set of filters that are matched with the target possible region is designed. The worst-case output SCNR is maximized as a figure of merit under the constant-modulus constraint and similarity constraint on the transmit waveform. Then, the joint design problem is formulated by maximizing the worst-case SCNR, and a sequential optimization algorithm based on feasible point pursuit successive convex approximation (FPP-SCA) is developed to solve the resultant problem. Simulation results are provided to demonstrate the performance of the proposed algorithm. The main contributions of the paper are summarized as follows: (1) By employing a set of receive filter tuned over the possible spatial angle and Doppler frequency of target, the objective function of joint design is obtained by maximizing the worst-case output SCNR. (2) A sequential optimization algorithm based on FPP-SCA is derived to solve the robust joint design problem. Specifically, an auxiliary variable is introduced to transform the maximin problem into a minimization problem. Then, the nonconvex constant-modulus constraint is solved by utilizing the SCA method. Thus, the waveform optimization problem can be addressed by using the CVX tool box. (3) Several simulation results indicate that the proposed joint design algorithm performs better than the algorithm based on SDP and randomization method in terms of better output SCNR and lower computational time. In addition, the performance of the proposed joint design method is against the target parameters errors.

The remainder of this paper is organized as follows: In Section 2, the signal model of MIMO-STAP radar is provided. The problem formulation and the robust joint design problem are discussed in Section 3. The sequential optimization algorithm based on FPP-SCA is presented in Section 4. Simulation results are provided in Section 5 to demonstrate the performance of the proposed algorithm. Finally, conclusions are drawn in Section 6.

2. Signal Model

We consider an airborne collocated MIMO radar system with N_T transmit antennas and N_R receive antennas, as shown in Figure 1. The transmit antenna and receive antenna are uniform linear array (ULA) with interelement spacing being d_T and d_R, respectively. The radar transmits M pulses during a coherent processing interval (CPI) with the pulse repetition frequency (PRF) f_r. The radar platform is flying along the X-axis at velocity V_p. Assuming that $\mathbf{s}_n \in \mathbb{C}^{L\times 1}$ represents the sampled waveform emitted by the nth transmit antenna, then the transmit waveform matrix of the radar system can be expressed as $\mathbf{S} = [\mathbf{s}_1, \mathbf{s}_2, \ldots, \mathbf{s}_{N_T}]^T \in \mathbb{C}^{N_T\times L}$, where L represents the number samples of a pulse and each pulse emits the same waveform.

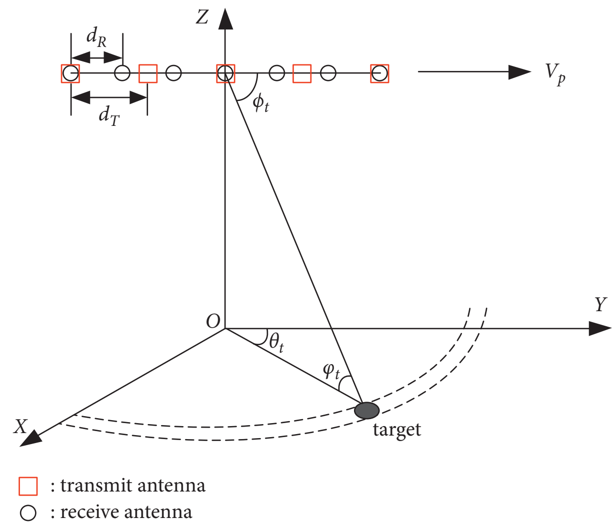

Figure 1: Configuration of airborne MIMO radar.

2.1. Target.

Assuming that the spatial angle of the moving target relative to the platform is ϕ_t and the normalized Doppler frequency is f_t, then the target echo of the mth pulse received by the airborne MIMO radar can be expressed as

$$\mathbf{y}_{t,m} = \alpha_t e^{j2\pi(m-1)f_t}\left(\mathbf{I}_L \otimes \left(\mathbf{b}(\phi_t)\mathbf{a}^T(\phi_t)\right)\right)\mathbf{s}, \quad (1)$$

where α_t represents the target complex amplitude, $\mathbf{I}_L$ is the $L\times L$ identity matrix, $\otimes$ is the Kronecker product, $(\cdot)^T$ stands for the transpose operation, $\mathbf{s} = \mathrm{vec}(\mathbf{S})$, $\mathbf{a}(\phi_t)$ and $\mathbf{b}(\phi_t)$ represent the transmit spatial steering vector and receive steering vector of target, respectively, and they have the form of

$$\mathbf{a}(\phi_t) = \left[1, e^{(j2\pi d_T\cos(\phi_t)/\lambda)}, \ldots, e^{(j2\pi(N_T-1)d_T\cos(\phi_t)/\lambda)}\right]^T, \quad (2)$$

$$\mathbf{b}(\phi_t) = \left[1, e^{(j2\pi d_R\cos(\phi_t)/\lambda)}, \ldots, e^{(j2\pi(N_R-1)d_R\cos(\phi_t)/\lambda)}\right]^T, \quad (3)$$

where λ denotes the wavelength of the system.

Let $\mathbf{y}_t = [\mathbf{y}_{t,1}^T, \ldots, \mathbf{y}_{t,M}^T]^T \in \mathbb{C}^{LMN_R\times 1}$, then the received target echo of a CPI can be expressed as

$$\mathbf{y}_t = \alpha_t \mathbf{V}(f_t, \phi_t)\mathbf{s}, \quad (4)$$

where $\mathbf{V}(f_t,\phi_t) = (\mathbf{u}(f_t)\otimes\mathbf{I}_L\otimes(\mathbf{b}(\phi_t)\mathbf{a}^T(\phi_t)))$, and $\mathbf{u}(f_t) = [1, e^{j2\pi f_t}, \ldots, e^{j2\pi(M-1)f_t}]^T$ represents the time steering vector of target.

2.2. Clutter.

The clutter of airborne MIMO radar system is the signal-dependent clutter echo, which is distributed in the whole azimuth domain and range domain. Clutter echo received by a single range bin consists of all clutter patches of the range bin. Then, the clutter echo received by the airborne MIMO radar can be expressed as

$$\mathbf{y}_c = \sum_{p=-P}^{P}\sum_{k=1}^{N_c}\alpha_{c,p,k}\mathbf{V}\left(f_{c,p,k}, \phi_{c,p,k}\right)\mathbf{s}, \quad (5)$$

Where P denotes the number of range bin around the range under test, $\alpha_{c,p,k}$, $f_{c,p,k}$, and $\phi_{c,p,k}$ represent the complex amplitude, normalized Doppler frequency, and spatial angle of the kth clutter patch in the pth range bin, respectively, $f_{c,p,k} = 2V_p\cos(\phi_{c,p,k})/(\lambda f_r)$, N_c is the clutter patch number in a range bin. $\mathbf{V}(f_{c,p,k}, \phi_{c,p,k}) = (\mathbf{u}(f_{c,p,k})\otimes\mathbf{J}_P^T\otimes(\mathbf{b}(\phi_{c,p,k})\mathbf{a}^T(\phi_{c,p,k})))$, let $\mathbf{V}_{c,p,k}$ denote $\mathbf{V}(f_{c,p,k}, \phi_{c,p,k})$ for convenience, where $\mathbf{J}_p = \mathbf{J}_{-p}^T \in \mathbb{C}^{L\times L}$ denotes the shift matrix, which is calculated by

$$\mathbf{J}_p(i,j) = \begin{cases} 1, & i-j+p=0, \\ 0, & i-j+p\neq 0. \end{cases} \quad (6)$$

Total received echo: therefore, the echo received by the airborne radar containing the target (which may exist), signal-dependent clutter, and noise can be expressed as

$$\mathbf{y} = \mathbf{y}_t + \mathbf{y}_c + \mathbf{y}_n, \quad (7)$$

where $\mathbf{y}_n$ denotes the complex Gaussian white noise whose mean value is zero and covariance matrix is $\sigma_n^2\mathbf{I}_{LMN_R}$, where σ_n^2 is noise power.

3. Problem Formulation

Considering that the accurate normalized Doppler frequency and spatial angle of the target are unknown, it is assumed that the approximate region of the target in the angle-Doppler plane can be known through spatial angle estimation and Doppler frequency estimation, as shown in cyan area in Figure 2. The normalized Doppler frequency and spatial angle range of the target can be expressed as $\Psi = [f_{tmin}, f_{tmax}]\,(f_t\in\Psi)$ and $\Omega = [\phi_{tmin}, \phi_{tmax}]\,(\phi_t\in\Omega)$, respectively, and are then discretized into I and J grid points, respectively. Then, we can obtain the discretized normalized Doppler frequency-spatial angle pair, that is, $(f_t^{n_1}, \phi_t^{n_2}), n_1 \in \mathcal{I} = \{1, \ldots, I\}, n_2 \in \mathcal{J} = \{1, \ldots, J\}$. Next, a set of $LMN_R \times 1$ filters $\mathbf{w}_{n_1,n_2} \in \mathcal{W} = \{\mathbf{w}_{n_1,n_2} | n_1 \in \mathcal{I}, n_2 \in \mathcal{J}\}$ is used to process the received signal, and each received filter is tuned to a specific normalized Doppler frequency-spatial angle pair of targets $(f_t^{n_1}, \theta_t^{n_2})$. Therefore, the output SCNR corresponding to the (n_1, n_2) th filter branch can be expressed as

$$\mathrm{SCNR}_{n_1,n_2}(\mathbf{s}, \mathbf{w}_{n_1,n_2}) = \frac{\sigma_t^2 \left| \mathbf{w}_{n_1,n_2}^H \mathbf{V}(f_t^{n_1}, \phi_t^{n_2}) \mathbf{s} \right|^2}{\mathbf{w}_{n_1,n_2}^H \mathbf{R}_{\mathrm{cn}}(\mathbf{s}) \mathbf{w}_{n_1,n_2}}, \tag{8}$$

where $\sigma_t^2 = \mathbb{E}\{|\alpha_t|^2\}$, $\mathbb{E}(\cdot)$ denotes the statistical expectation, $(\cdot)^H$ denotes the conjugate transpose operation, $\mathbf{R}_{\mathrm{cn}}(\mathbf{s})$ is the clutter plus noise covariance matrix, which can be expressed as

$$\mathbf{R}_{\mathrm{cn}}(\mathbf{s}) = \sum_{p=-P}^{P} \sum_{k=1}^{N_c} \sigma_{c,p,k}^2 \mathbf{V}_{c,p,k} \mathbf{s}\mathbf{s}^H \mathbf{V}_{c,p,k}^H + \sigma_n^2 \mathbf{I}_{LMN_R}. \tag{9}$$

Assumed that the prior information of clutter (including $\sigma_{c,p,k}^2$, $f_{c,p,k}$ and $\phi_{c,p,k}$) is known, which can be obtained from the terrain database. Therefore, maximizing the worst-case output SCNR over all possible normalized Doppler frequencies and spatial angles of the target, we can obtain the optimization of the joint design to deal with the uncertainty of the target parameters. Concretely, the joint design of transmit waveform and receive filter bank for airborne MIMO radar in the presence of target uncertainty can be formulated as

$$\overline{\mathrm{SCNR}}(\mathbf{s}, \mathbf{w}_{n_1,n_2}) \triangleq \min_{n_1 \in \mathcal{I}, n_2 \in \mathcal{J}} \mathrm{SCNR}_{n_1,n_2}(\mathbf{s}, \mathbf{w}_{n_1,n_2}). \tag{10}$$

In practical radar system, constant-modulus constraint is applied to the transmit waveform to prevent overloading of the amplifier, i.e., $|\mathbf{s}(n)| = 1/\sqrt{N_T L}$, $n = 1, \ldots, N_T L$. At the same time, in order to obtain the good characteristics for the transmit waveform, for example, good ambiguity function, it is necessary to impose similarity constraints on the transmit waveform, namely, $\|\mathbf{s} - \mathbf{s}_0\|_\infty \le \delta$, where, $\|\cdot\|_\infty$ represents the infinite norm of a matrix, δ is used to control the similarity between the optimized waveform and the reference waveform $\mathbf{s}_0$ ($\|\mathbf{s}_0\|^2 = 1$), and $\|\cdot\|$ represents the Euclidean norm of a matrix.

Considering the constant-modulus constraint and similarity constraint of the transmit waveform, the joint design problem of transmit waveform and receive filter bank of airborne MIMO radar based on maximizing the worst-case output SCNR can be expressed as

$$\begin{aligned} &\max_{\mathbf{s}, \mathbf{w}_{n_1,n_2} \in \mathcal{W}} \mathrm{SCNR}_{n_1,n_2}(\mathbf{s}, \mathbf{w}_{n_1,n_2}), \\ &\text{s.t.} \quad |\mathbf{s}(n)| = \frac{1}{\sqrt{N_T L}}, \quad n = 1, \ldots, N_T L, \\ &\qquad \|\mathbf{s} - \mathbf{s}_0\|_\infty \le \delta, \end{aligned} \tag{11}$$

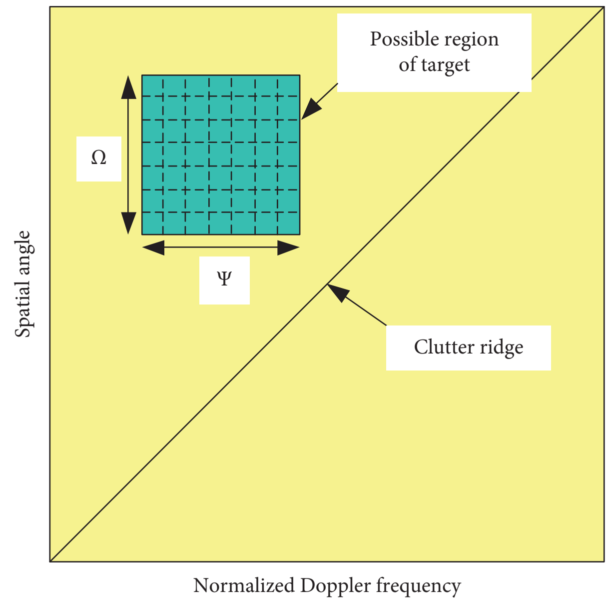

Figure 2: Possible region of target in angle-doppler plane.

The problem (11) is NP hard owing to the nonconvex objective function and the nonconvex waveform constraints. In the next section, we proposed a sequential algorithm to address the problem (11).

4. Joint Design Method Based on FFP-SCA

In this section, a sequential algorithm based on FPP-SCA is proposed to solve the maximin problem (11), which can obtain monotonically increasing worst-case output SCNR during the iterative procedure. Specifically, the transmit waveform $\mathbf{s}$ is first fixed, and the receive filter banks $\mathbf{w}_{n_1,n_2} \in \mathcal{W}$ are optimized by maximizing $\overline{\mathrm{SCNR}}(\mathbf{s}, \mathbf{w}_{n_1,n_2})$. Then, the receive filter banks $\mathbf{w}_{n_1,n_2} \in \mathcal{W}$ are fixed and the transmit waveform $\mathbf{s}$ is optimized.

4.1. Receive Filter Bank Optimization. At the ith iteration, the optimization of the receive filter bank $\mathbf{w}_{n_1,n_2} \in \mathcal{W}$ can be expressed as

$$\max_{\mathbf{w}_{n_1,n_2} \in \mathcal{W}} \frac{\left| \mathbf{w}_{n_1,n_2}^H \mathbf{V}(f_t^{n_1}, \phi_t^{n_2}) \mathbf{s}^{(i-1)} \right|^2}{\mathbf{w}_{n_1,n_2}^H \mathbf{R}_{\mathrm{cn}}(\mathbf{s}^{(i-1)}) \mathbf{w}_{n_1,n_2}}. \tag{12}$$

The optimization problem (12) has IJ independent objective functions corresponding to $\mathbf{w}_{n_1,n_2}$. Therefore, the problem (12) can be transformed into optimization of each $\mathbf{w}_{n_1,n_2}$, and the closed solution of $\mathbf{w}_{n_1,n_2}$ can be obtained by

$$\mathbf{w}_{n_1,n_2}^{(i)} = \frac{\mathbf{R}_{\mathrm{cn}}^{-1}(\mathbf{s}^{(i-1)}) \mathbf{V}(f_t^{n_1}, \theta_t^{n_2}) \mathbf{s}^{(i-1)}}{(\mathbf{s}^{(i-1)})^H \mathbf{V}^H(f_t^{n_1}, \theta_t^{n_2}) \mathbf{R}_{\mathrm{cn}}^{-1}(\mathbf{s}^{(i-1)}) \mathbf{V}(f_t^{n_1}, \theta_t^{n_2}) \mathbf{s}^{(i-1)}}. \tag{13}$$

4.2. Transmit Waveform Optimization Based on FPP-SCA. With a fixed receive filter bank $\mathbf{w}_{n_1,n_2}$, the optimization of the transmit waveform $\mathbf{s}$ can be expressed as

$$\begin{aligned}
&\max_{\mathbf{s}} \min_{n_1\in\mathcal{I},n_2\in\mathcal{J}} \frac{\left|\left(\mathbf{w}_{n_1,n_2}^{(i)}\right)^H \mathbf{V}\left(f_t^{n_1},\phi_t^{n_2}\right)\mathbf{s}\right|^2}{\left(\mathbf{w}_{n_1,n_2}^{(i)}\right)^H \mathbf{R}_{\text{cn}}\left(\mathbf{s}^{(i-1)}\right)\mathbf{w}_{n_1,n_2}^{(i)}},\\
&\text{s.t.}\quad |\mathbf{s}(n)| = \frac{1}{\sqrt{N_T L}},\quad n=1,\cdots,N_T L,\\
&\qquad \left\|\mathbf{s}-\mathbf{s}_0\right\|_\infty \le \delta.
\end{aligned} \tag{14}$$

Substituting (13) into the objective function of problem (14), and after some mathematical deduction, the problem (14) can be transformed into

$$\begin{aligned}
&\max_{\mathbf{s}} \min_{n_1\in\mathcal{I},n_2\in\mathcal{J}} \mathbf{s}^H \mathbf{V}^H\left(f_t^{n_1},\phi_t^{n_2}\right)\mathbf{R}_{\text{cn}}^{-1}\left(\mathbf{s}^{(i-1)}\right)\mathbf{V}\left(f_t^{n_1},\theta_t^{n_2}\right)\mathbf{s},\\
&\text{s.t.}\quad |\mathbf{s}(n)| = 1/\sqrt{N_T L},\ n=1,\cdots,N_T L,\\
&\qquad \left\|\mathbf{s}-\mathbf{s}_0\right\|_\infty \le \delta.
\end{aligned} \tag{15}$$

Problem (15) is a nonconvex maximin problem, and it is difficult to find the optimal waveform in the polynomial time. A computationally efficient algorithm is derived to solve this problem. By introducing an auxiliary variable t, the maximin problem (15) can be transformed as

$$\begin{aligned}
&\min_{\mathbf{s},t} -t,\\
&\text{s.t.}\ (1),\quad \mathbf{s}^H \mathbf{Q}^{n_1,n_2}\left(\mathbf{s}^{(i-1)}\right)\mathbf{s} \ge t,\ n_1\in\mathcal{I},\ n_2\in\mathcal{J},\\
&\qquad (2),\quad |\mathbf{s}(n)| = \frac{1}{\sqrt{N_T L}},\ n=1,\cdots,N_T L,\\
&\qquad (3),\quad \left\|\mathbf{s}-\mathbf{s}_0\right\|_\infty \le \delta.
\end{aligned} \tag{16}$$

where

$$\mathbf{Q}^{n_1,n_2}\left(\mathbf{s}^{(i-1)}\right) = \mathbf{V}^H\left(f_t^{n_1},\phi_t^{n_2}\right)\mathbf{R}_{\text{cn}}^{-1}\left(\mathbf{s}^{(i-1)}\right)\mathbf{V}\left(f_t^{n_1},\theta_t^{n_2}\right). \tag{17}$$

The objective function of problem (16) is convex, but the constraints are nonconvex. Then, the SCA technique is employed to deal with the nonconvex waveform constrains.

For the first constraint (1) in problem (16), since $\mathbf{Q}^{n_1,n_2}(\mathbf{s}^{(i-1)})$ is a semidefinite matrix, for any feasible solution $\mathbf{s}_f \in \mathbb{C}^{N_T L\times 1}$ of problem (14), the following inequality holds:

$$\left(\mathbf{s}-\mathbf{s}_f\right)^H \mathbf{Q}^{n_1,n_2}\left(\mathbf{s}^{(i-1)}\right)\left(\mathbf{s}-\mathbf{s}_f\right) \ge 0. \tag{18}$$

Expanding the left side of (18), we can obtain

$$\mathbf{s}^H \mathbf{Q}^{n_1,n_2}\left(\mathbf{s}^{(i-1)}\right)\mathbf{s} \ge 2\text{Re}\left(\mathbf{s}^H \mathbf{Q}^{n_1,n_2}\left(\mathbf{s}^{(i-1)}\right)\mathbf{s}_f\right) - \mathbf{s}_f^H \mathbf{Q}^{n_1,n_2}\left(\mathbf{s}^{(i-1)}\right)\mathbf{s}_f. \tag{19}$$

Substituting inequality (19) into the first constraint of problem (16), we have

$$\begin{aligned}
&\mathbf{s}_f^H \mathbf{Q}^{n_1,n_2}\left(\mathbf{s}^{(i-1)}\right)\mathbf{s}_f - 2\text{Re}\left(\mathbf{s}^H \mathbf{Q}^{n_1,n_2}\left(\mathbf{s}^{(i-1)}\right)\mathbf{s}_f\right)\\
&\quad + t \le 0,\ n_1\in\mathcal{I}, n_2\in\mathcal{J}.
\end{aligned} \tag{20}$$

For the second constraint (2) in problem (16), it can be expressed as the intersection of $|\mathbf{s}(n)|^2 - 1/N_T L \le 0$ and $1/N_T L - |\mathbf{s}(n)|^2 \le 0$. The former is convex while the latter is nonconvex. Then, the first order condition of convex function is used to approximate the lower bound of $|\mathbf{s}(n)|^2$

$$\begin{aligned}
|\mathbf{s}(n)|^2 &\ge \left|\mathbf{s}_f(n)\right|^2 + \text{Re}\left\{\left(\frac{\partial|\mathbf{s}(n)|^2}{\partial\mathbf{s}(n)}\Big|_{\mathbf{s}_f(n)}\right)^*\left(\mathbf{s}(n)-\mathbf{s}_f(n)\right)\right\}\\
&= \left|\mathbf{s}_f(n)\right|^2 + \text{Re}\left\{2\mathbf{s}_f^*(n)\left(\mathbf{s}(n)-\mathbf{s}_f(n)\right)\right\}.
\end{aligned} \tag{21}$$

Thus, the constraint $1/N_T L - |\mathbf{s}(n)|^2 \le 0$ can be approximately expressed as

$$\frac{1}{N_T L} - |\mathbf{s}(n)|^2 \le \frac{1}{N_T L} - \left|\mathbf{s}_f(n)\right|^2 - \text{Re}\left\{2\mathbf{s}_f^*(n)\mathbf{s}(n) - 2\left|\mathbf{s}_f(n)\right|^2\right\} \le 0. \tag{22}$$

After some mathematical transformation, the second constraint (2) can be formulated as

$$\frac{1}{N_T L} - 2\text{Re}\left\{\mathbf{s}_f^*(n)\mathbf{s}(n)\right\} + \left|\mathbf{s}_f(n)\right|^2 \le 0. \tag{23}$$

Expanding the third constraint (3) in problem (16), it can be expressed as $N_T L$ independent quadratic constraints, that is,

$$\left|\mathbf{s}(n) - \mathbf{s}_0(n)\right|^2 \le \delta^2,\quad n=1,\ldots,N_T L. \tag{24}$$

Therefore, by replacing the nonconvex constraints of problem (16) with convex approximate representations (20), (23), and (24), the convex approximate representation of problem (16) can be obtained

$$\begin{aligned}
&\min_{\mathbf{s},t} -t,\\
&\text{s.t.}\quad
\begin{cases}
\mathbf{s}_f^H \mathbf{Q}^{n_1,n_2}\left(\mathbf{s}^{(i-1)}\right)\mathbf{s}_f - 2\mathrm{Re}\left(\mathbf{s}^H \mathbf{Q}^{n_1,n_2}\left(\mathbf{s}^{(i-1)}\right)\mathbf{s}_f\right) + t \le 0, \quad n_1 \in \mathcal{I}, n_2 \in \mathcal{J},\\
|\mathbf{s}(n)|^2 - \dfrac{1}{N_T L} \le 0, \quad \forall n,\\
\dfrac{1}{N_T L} - 2\mathrm{Re}\left\{\mathbf{s}_f^*(n)\mathbf{s}(n)\right\} + \left|\mathbf{s}_f(n)\right|^2 \le 0, \quad \forall n,\\
\left|\mathbf{s}(n) - \mathbf{s}_0(n)\right|^2 \le \delta^2, \quad \forall n.
\end{cases}
\end{aligned} \tag{25}$$

However, since there is only one intersection of $|\mathbf{s}(n)|^2 - 1/N_T L \le 0$ and $1/N_T L - 2\mathrm{Re}\left\{\mathbf{s}_f^*(n)\mathbf{s}(n)\right\} + |\mathbf{s}_f(n)|^2 \le 0$, problem (25) has only a single feasible solution. Inspired by the iterative optimization algorithm and FPP algorithm [26–28], a nonnegative auxiliary variable was introduced to the third constraint of problem (25) and $\|\mathbf{u}\|_1$ is added to the objective function at the same time. At the ith iteration, problem (25) could be transformed into

$$\begin{aligned}
&\min_{\mathbf{s},t,\mathbf{u}} -t + \rho\|\mathbf{u}\|_1 + \kappa\left\|\mathbf{s} - \mathbf{s}^{(i-1)}\right\|^2\\
&\text{s.t.}\quad
\begin{cases}
\left(\mathbf{s}^{(i-1)}\right)^H \mathbf{Q}^{n_1,n_2}\left(\mathbf{s}^{(i-1)}\right)\mathbf{s}^{(i-1)} - 2\mathrm{Re}\left(\mathbf{s}^H \mathbf{Q}^{n_1,n_2}\left(\mathbf{s}^{(i-1)}\right)\mathbf{s}^{(i-1)}\right) + t \le 0, \quad n_1 \in \mathcal{I}, n_2 \in \mathcal{J},\\
|\mathbf{s}(n)|^2 - \dfrac{1}{N_T L} \le 0, \ \forall n,\\
\dfrac{1}{N_T L} - 2\mathrm{Re}\left\{\left(\mathbf{s}^{(i-1)}(n)\right)^* \mathbf{s}(n)\right\} + \left|\mathbf{s}^{(i-1)}(n)\right|^2 - \mathbf{u}(n) \le 0, \ \forall n,\\
\left|\mathbf{s}(n) - \mathbf{s}_0(n)\right|^2 \le \delta^2, \ \forall n,\\
\mathbf{u}(n) \ge 0, \ \forall n,\\
t \ge t^{(i-1)},
\end{cases}
\end{aligned} \tag{26}$$

where ρ and κ represent the positive penalty parameters. Supposing $(\mathbf{s}^{(i)}, t^{(i)})$ is the solution of the problem (26) at the ith iteration, and then the solution of the original problem (15) (or problem (16)) can be obtained by solving the optimization problem iteratively. It is worth noting that the norm $\|\mathbf{s} - \mathbf{s}^{(i-1)}\|^2$ is added to the objective function to ensure that a unique specific solution can be obtained when the problem (26) converges. The constraint $t \ge t^{(i-1)}$ is added to ensure that the algorithm obtains increasing solutions during the iteration. The question (26) belongs to the quadratically constrained quadratic programming (QCQP) problem, and it can be solved by transforming into second-order cone programming (SOCP). The interior point method (convex optimization tool kit [29]) is applied to obtain the optimal solution, whose computational complexity is $\mathcal{O}((N_T L)^3)$. The whole solution of transmit waveform is completed within the framework of the FPP-SCA algorithm, so it is called the transmit waveform optimization algorithm based on FPP-SCA.

4.3. Joint Design Method for Airborne MIMO Radar Based on FPP-SCA. The proposed joint design method based on FPP-SCA to solve problem (11) is summarized in Algorithm 1. The main computational complexity of the proposed method is dependent on the number of iterations and the computational complexity per iteration. In each iteration, the optimization of $\mathbf{w}_{n_1,n_2} \in \mathcal{W}$ for fixed $\mathbf{s}$ involves $\mathcal{O}((LMN_R)^3)$ complexity. The optimization of $\mathbf{s}$ for a given $\mathbf{w}_{n_1,n_2} \in \mathcal{W}$ has a complexity of $\mathcal{O}((N_T L)^3)$. The robust joint design method based on SDP and randomization (SDP-R) [30] can also address the problem (11), whose optimal waveform is obtained by interior point method involving $\mathcal{O}((N_T L)^{4.5})$ complexity. It is seen that the computational complexity of the proposed joint design method is lower than that based on SDP-R.

Remark 1. The objective function $\overline{\text{SCNR}}(\mathbf{s}^{(i)}, \mathbf{w}_{n_1,n_2}^{(i)})$ obtained by the joint design method based on FPP-SCA monotonically increases and converges to a specific value.

It is seen from (26) that the optimized value satisfies $t^{(i)} \geq t^{(i-1)}$. Thus, we have

$$\begin{aligned}\overline{\text{SCNR}}\left(\mathbf{s}^{(i-1)}, \mathbf{w}_{n_1,n_2}^{(i-1)}\right) &= \min_{n_1\in\mathcal{I},n_2\in\mathcal{J}} \left(\mathbf{s}^{(i-1)}\right)^H \mathbf{V}^H\left(f_t^{n_1}, \phi_t^{n_2}\right)\mathbf{\Phi}_{\text{cn}}^{-1}\left(\mathbf{s}^{(i-1)}\right)\mathbf{V}\left(f_t^{n_1}, \theta_t^{n_2}\right)\mathbf{s}^{(i-1)} \\ &\leq \min_{n_1\in\mathcal{I},n_2\in\mathcal{J}} \left(\mathbf{s}^{(i)}\right)^H \mathbf{V}^H\left(f_t^{n_1}, \phi_t^{n_2}\right)\mathbf{\Phi}_{\text{cn}}^{-1}\left(\mathbf{s}^{(i-1)}\right)\mathbf{V}\left(f_t^{n_1}, \theta_t^{n_2}\right)\mathbf{s}^{(i)} \\ &= \overline{\text{SCNR}}\left(\mathbf{s}^{(i)}, \mathbf{w}_{n_1,n_2}^{(i-1)}\right).\end{aligned} \tag{27}$$

5. Simulation Results

In this section, simulation results are implemented to validate the effectiveness of the proposed FPP-SCA based joint design method. The simulation scenario is set as follows: consider an airborne collocated MIMO radar with the transmit antenna and receive antenna being ULA, the number of transmit array is $N_T = 4$, the number of receive array is $N_R = 4$, the interelement spacing of the transmit antenna and receive antenna is $d_T = d_R = \lambda/2$, the pulse number within the coherent processing interval is $M = 4$, the PRF is $f_r = 2000$, and the sampling number of single pulse is $L = 8$. The platform altitude is 8000 m and the flight speed is $V_p = 140$ m/s. We consider the clutter of five range bin ($P = 2$) is received, the number of clutter patches of a single range bin is $N_c = 181$, and the clutter power is $\sigma_{c,p,k}^2 = R_0/R_p$, $p = -P, \cdots, P$, $k = 1, \cdots, N_c$, where R_0 and R_p, respectively, represent the distance from the range under test and the pth range bin to the platform. The noise power is 0 dB. The real position of the target on the space-time two-dimensional plane is (0.2, -0.2), the target uncertainty set is $\Psi = [0.1, 0.3]$ and $\Omega = [-0.3, -0.1]$, and the uniform sampling step is 0.02. Then, the number of sampling points of normalized Doppler frequency and normalized spatial frequency are 11, thus forming 121 groups of normalized Doppler frequency-spatial frequency pairs, and 121 groups of receive filters are required to process the received signals. The SNR is 20 dB. The orthogonal linear frequency modulation waveform is used as the reference waveform, i.e,

$$\mathbf{S}_0\left(n_t, l\right) = \frac{\exp\left\{j2\pi n_t (l-1)/L\right\}\exp\left\{j\pi (l-1)^2/L\right\}}{\sqrt{N_T L}}, \tag{28}$$

where $n_t = 1, \cdots, N_T$, $l = 1, \cdots, L$, and $\mathbf{s}_0 = \text{vec}(\mathbf{S}_0)$. The parameters of FPP-SCA are set as follows: $\rho = 1$, $\eta = 10^{-4}$, and $\kappa = 10^{-5}$. The comparison algorithm is the robust joint design method based on SDP-R [30]. The iteration termination condition of SDP-R is 10^{-4} and the number of random trials of SDP-R is 1000. The simulation experiment platform is notebook (I7–9750U CPU and 32 GB RAM) Matlab 2016b.

Figure 3 shows the worst-case output SCNR versus the number of iterations. The similarity parameters are $\gamma = 0.4$, $\gamma = 1$, and $\gamma = 2$, respectively, where $\gamma = \delta\sqrt{N_T L}$. As can be seen from Figure 3, the worst-case output SCNR obtained by both FPP-SCA and SDP-R gradually increases with the increase of iterations. In addition, it is seen that all the worst-SCNR curves obtained by the proposed FPP-SCA remain unchanged when the number of iterations is greater than 5. This shows that the proposed algorithm is convergent. When the similarity parameter increases, the worst-case output SCNR of FPP-SCA and SDP-R also increases. It is worth noting that, when $\gamma = 0.4$, 1, and 2, the $\gamma = 0.4$ worst output SCNR obtained by the proposed FPP-SCA is significantly better than that obtained by SDP-R. For example, FPP-SCA is about 5.27 dB higher than SDP-R when $\gamma = 2$.

Table 1 provides the iteration number and runtime comparison of FPP-SCA and SDP-R, where $\gamma = 0.4$,1, and 2. As can be seen from Table 1, the total runtime of SDP-R is apparently larger than FPP-SCA for all γ. In addition, when $\gamma = 0.4$, 1, and 2, the running time change of FPP-SCA and SDP-R in a single iteration is relatively small. In particular, the running time of FPP-SCA and SDP-R in a single iteration is the largest when $\gamma = 0.4$ while the smallest when $\gamma = 1$. For fixed γ, the running time of a single iteration of FPP-SCA is significantly smaller than SDP-R. In fact, SDP-R method involves the solution of two SDP problems, and we can obtain from [30] that the computational complexity is $\mathcal{O}((LMN_R)^{4.5})$ and $\mathcal{O}((LN_T)^{4.5})$, respectively. Thus, the total computational complexity of the SDP-R method is $\mathcal{O}(\widetilde{I}((LMN_R)^{4.5} + t(LN_T)^{4.5}))$, where $\widetilde{I}$ denotes the number of iterations. Contrarily, the total computational complexity of FPP-SCA is $\mathcal{O}(\widetilde{I}((LMN_R)^3 + t(LN_T)^3))$, which is much smaller than that of SDP-R. In addition, the more constraints exist, the longer the running time of the SDP-R algorithm. For example, 121 groups of receive filters are set in this paper, and the number of constraints including receive filters is 121. Thus, the computational load is much heavy, which leads to a much longer running time required for a single iteration.

Figure 4 depicts the worst-case output SCNR versus the target uncertainty value, where the target normalized Doppler frequency error and the target spatial frequency error both increase from 0 to 0.2. In addition, the FPP-SCA-ROB represents "robust design," where the worst-case output SCNR is obtained by the proposed FPP-SCA iterative

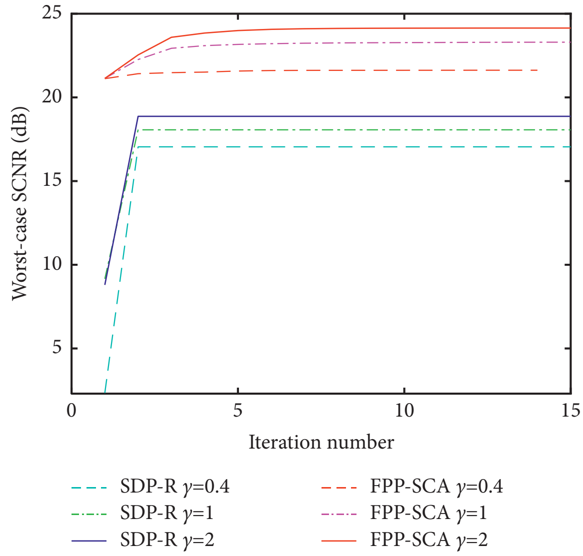

FIGURE 3: Worst-case output SCNR versus the iteration number.

Input: $\mathbf{V}(f_t^{n_1}, \phi_t^{n_2}), n_1 \in \mathcal{F}, n_2 \in \mathcal{J}$, $\mathbf{R}_{\text{cn}}(\mathbf{s})$, $\mathbf{w}_{n_1,n_2}^{(0)} \in \mathcal{W}$, $\mathbf{s}^{(0)}$, η
Output: The optimal solution to problem (11) $(\mathbf{s}^*, \mathbf{w}_{n_1,n_2}^* \in \mathcal{W})$.
Iteration:
Step 1: $i = 1$.
Step 2: Calculate $\mathbf{R}_{\text{cn}}(\mathbf{s}^{(i-1)})$ with (9) and $\mathbf{s}^{(i-1)}$, compute $\mathbf{w}_{n_1,n_2}^{(i)} \in \mathcal{W}$ with (13).
Step 3: Obtain the optimal waveform $\mathbf{s}^{(i)}$ by solving problem (26) with FPP-SCA algorithm.
Step 4: If $|\overline{\text{SCNR}}(\mathbf{s}^{(i)}, t\mathbf{w}_{n_1,n_2}^{(i)}) - \overline{\text{SCNR}}(\mathbf{s}^{(i-1)}, t\mathbf{w}_{n_1,n_2}^{(i-1)})| \le \eta$, stop the iteration, otherwise, go step 2.
Step 5: Output $\mathbf{s}^* = \mathbf{s}^{(i)}$ and $\mathbf{w}_{n_1,n_2}^* = \mathbf{w}_{n_1,n_2}^{(i)}$.

ALGORITHM 1: Joint design method based on FPP-SCA to solve (11).

TABLE 1: Iteration number and runtime comparison of different algorithm.

Algorithm	Total runtime (s)	Iteration number	Average runtime (s)
SDP-R ($\gamma = 0.4$)	494.82	3	164.94
SDP-R ($\gamma = 1$)	430.83	3	143.61
SDP-R ($\gamma = 2$)	438.81	3	146.27
FPP-SCA ($\gamma = 0.4$)	27.72	14	1.98
FPP-SCA ($\gamma = 1$)	31.96	17	1.88
FPP-SCA ($\gamma = 2$)	28.65	15	1.91

algorithm (where the number of receive filters is set as 121), while FPP-SCA-NROB denotes the "nonrobust design," where the output SCNR is obtained by the presumed target position (where the number of receive filters is set as 1). We can see that the output SCNR curves obtained by FPP-SCA-ROB and FPP-SCA-NROB all utilize the FPP-SCA iterative algorithm, where the difference between them lies in the number of receive filter bank. The more the number of receive filters, the stronger the robustness of the algorithm. The FPP-SCA-NROB is not robust against the target uncertainty value since the number of filter banks is set as 1. As can be seen from Figure 4, the worst-case output SCNR of FPP-SCA-NROB is a little better than FPP-SCA-ROB when the target uncertainty value is small. The reason is that more degree of freedom of the system is utilized to deal with the target uncertainty. It is seen that the worst-case output SCNR of FPP-SCA-ROB is higher than that of FPP-SCA-NROB when the target uncertainty value is larger than 0.08. Furthermore, the larger the value of target uncertainty value is, the more worst-case output SCNR of FPP-SCA-NROB decreases, while FPP-SCA-ROB decreases slowly. The simulation results demonstrate that the proposed FPP-SCA-ROB is robust to the target uncertainty parameters.

Figure 5 shows the worst-case output SCNR versus the target position, where the target normalized Doppler frequency ranges from 0 to 0.4, the target normalized spatial frequency ranges from −0.4 to 0, and the real position of the target is (0.2, −0.2). As can be seen from Figure 5, when the target is near the actual target location, the worst-case output SCNR of FPP-SCA-NROB is superior to that of FPP-SCA-ROB. However, when the target is far from the real location, the worst-case output SCNR of FPP-SCA-NROB is

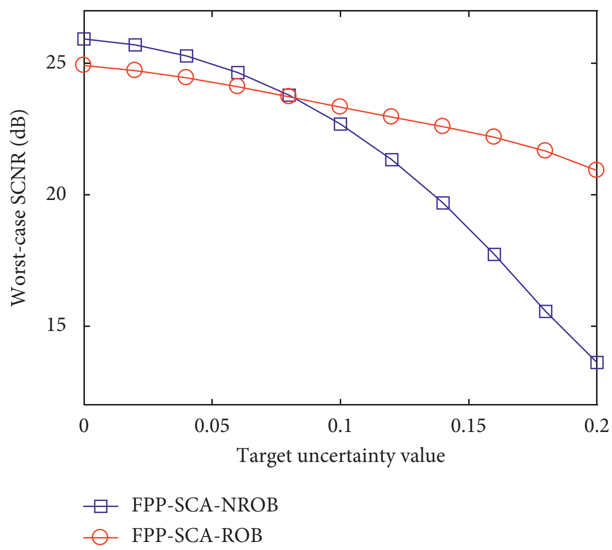

FIGURE 4: Worst-case output SCNR versus the target uncertainty value.

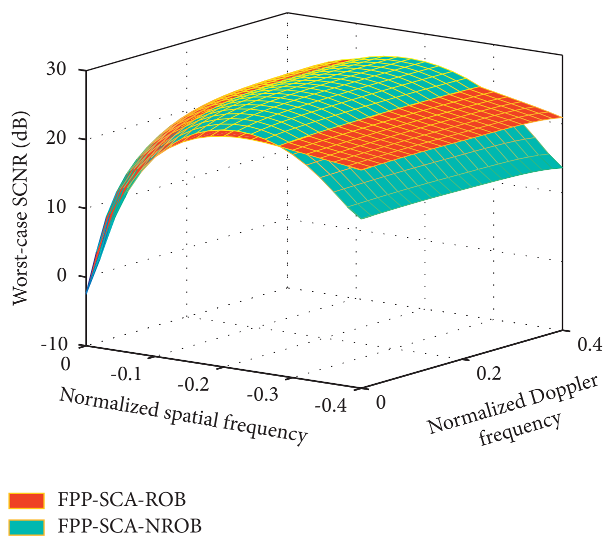

FIGURE 5: Worst-case output SCNR versus the target position.

significantly reduced, while the worst-case output SCNR of FPP-SCA-ROB remains relatively high value. This is consistent with the conclusion obtained in Figure 4. In addition, it can be observed from Figure 5 that when the target position tends to (0, 0), the worst-case output SCNR of both FPP-SCA-NROB and FPP-SCA-ROB decreases dramatically. The reason is that the point (0, 0) is the location of clutter, and the worst-case output SCNR forms a deep notch near the clutter ridge.

6. Conclusion

In order to improve the target detection performance of airborne MIMO radar when the target parameters have errors, a joint design method for transmit-receive of airborne MIMO radar based on FPP-SCA iteration is proposed in this paper. By designing a set of receive filters in the region where the target might appear, we can solve the SCNR degradation caused by the uncertain target parameters. Considering the constant-modulus constraint and similarity constraint of the transmit waveform, an FPP-SCA algorithm was designed to obtain the optimal waveform. Simulation results show that: (1) compared with the traditional joint design method based on SDP and randomization, the proposed method avoids the use of randomization to find the optimal waveform. In addition, we observe that for different similarity parameters γ, apparent worst-case output SCNR improvement is obtained by the proposed method with relatively small computational load. (2) The achieved worst-case SCNR becomes worse when the inaccuracy on the target parameters increases. Nevertheless, adopting more receive filters can provide a better robustness against these uncertainties than only one receive filter.

However, it should be mentioned that the number of receive filters is large in this work. In fact, the larger the number of receive filters, the greater the computational burden of the algorithm. The interval model, ball model, ellipsoidal model, and norm model are good choice to describe the target uncertain parameters [31]. Besides, the spectral constraint on the transmit waveform is considered to ensure the spectrum coexistence with other communication systems [32–34]. Thus, all these directions are pursued in the future research.

Data Availability

The data used to support the findings of this study are available from the corresponding author upon request.

Conflicts of Interest

The authors declare that there are no conflicts of interest regarding the publication of this paper.

Acknowledgments

This work was supported in part by the National Natural Science Foundation of China under Grants 61901511, 62001510, and 62001479, and in part by the Anhui Provincial Natural Science Foundation under Grant 2108085QF257, and in part by the Research Program of National University of Defense Technology under Grants ZK19-10, ZK19-28 and ZK20-33.

References

[1] J. Ward, "Space-time adaptive processing for airborne radar," Technical report 1015, MIT Lincoln Laboratory, Lexington, MA, USA, 1994.

[2] R. Klemm, *Principles of Space-Time Adaptive Processing*, IET, London, UK, 3rd edition, 2006.

[3] W. L. Melvin, "Space-time adaptive radar performance in heterogeneous clutter," *IEEE Transactions on Aerospace and Electronic Systems*, vol. 36, no. 2, pp. 621–633, 2000.

[4] L. Lan, J. Xu, G. Liao, Y. Zhang, F. Fioranelli, and H. C. So, "Suppression of mainbeam deceptive jammer with FDA-MIMO radar," *IEEE Transactions on Vehicular Technology*, vol. 69, no. 10, Article ID 11598, 2020.

[5] J. Li and P. Stoica, "MIMO radar with colocated antennas," *IEEE Signal Processing Magazine*, vol. 24, no. 5, pp. 106–114, 2007.

[6] I. Bekkerman and J. Tabrikian, "Target detection and localization using MIMO radars and sonars," *IEEE Transactions on Signal Processing*, vol. 54, no. 10, pp. 3873–3883, 2006.

[7] J. Li and P. Stoica, *MIMO Radar Signal Processing*, John Wiley & Sons, incorporated, Hoboken, NJ, USA, 2009.

[8] H. Godrich, A. M. Haimovich, and R. S. Blum, "Target localization accuracy gain in MIMO radar-based systems," *IEEE Transactions on Information Theory*, vol. 56, no. 6, pp. 2783–2803, 2010.

[9] S. D. Blunt and E. L. Mokole, "Overview of radar waveform diversity," *IEEE Aerospace and Electronic Systems Magazine*, vol. 31, no. 11, pp. 2–42, 2016.

[10] J. Shi, Z. Yang, and Y. Liu, "On parameter identifiability of diversity-smoothing-based MIMO radar," *IEEE Transactions on Aerospace and Electronic Systems*, vol. 58, no. 3, pp. 1660–1675, 2022.

[11] S. Haykin, "Cognitive radar: A way of the future," *IEEE Signal Processing Magazine*, vol. 23, no. 1, pp. 30–40, 2006.

[12] B. Tang and J. Tang, "Joint design of transmit waveforms and receive filters for MIMO radar space-time adaptive processing," *IEEE Transactions on Signal Processing*, vol. 64, no. 18, pp. 4707–4722, 2016.

[13] P. Setlur and M. Rangaswamy, "Waveform design for radar STAP in signal dependent interference," *IEEE Transactions on Signal Processing*, vol. 64, no. 1, pp. 19–34, 2016.

[14] S. M. O'Rourke, P. Setlur, M. Rangaswamy, and A. L. Swindlehurst, "Relaxed biquadratic optimization for joint filter-signal design in signal-dependent STAP," *IEEE Transactions on Signal Processing*, vol. 66, no. 5, pp. 1300–1315, 2018.

[15] S. M. O'Rourk, P. Setlur, M. Rangaswamy, and A. L. Swindlehurst, "Quadratic semidefinite programming for waveform-constrained joint filter-signal design in STAP," *IEEE Transactions on Signal Processing*, vol. 68, pp. 1744–1759, 2020.

[16] S. Shi, Z. He, and Z. Wang, "Joint design of transmitting waveforms and receiving filter for MIMO-STAP airborne radar," *Circuits, Systems, and Signal Processing*, vol. 39, no. 3, pp. 1489–1508, 2020.

[17] J. Li, G. Liao, Y. Huang, and A. Nehorai, "Manifold optimization for joint design of MIMO-STAP radars," *IEEE Signal Processing Letters*, vol. 27, pp. 1969–1973, 2020.

[18] J. Li, G. Liao, Y. Huang, Z. Zhang, and A. Nehorai, "Riemannian geometric optimization methods for joint design of transmit sequence and receive filter on MIMO radar," *IEEE Transactions on Signal Processing*, vol. 68, pp. 5602–5616, 2020.

[19] Z. Li, Y. Mao, Q. Zhou, J. Shi, and B. Li, "Joint design of transmit beamforming and receive filter for transmit subaperturing MIMO STAP radar," *Multidimensional Systems and Signal Processing*, vol. 33, no. 1, pp. 143–165, 2022.

[20] H. Wang, G. Liao, J. Li, and H. Lv, "Waveform optimization for MIMO-STAP to improve the detection performance," *Signal Processing*, vol. 91, no. 11, pp. 2690–2696, 2011.

[21] B. Tang, J. Li, Y. Zhang, and J. Tang, "Design of MIMO radar waveform covariance matrix for Clutter and Jamming suppression based on space time adaptive processing," *Signal Processing*, vol. 121, pp. 60–69, 2016.

[22] Y. Wang, W. Li, Q. Sun, and G. Huang, "Robust joint design of transmit waveform and receive filter for MIMO radar space-time adaptive processing with signal-dependent interferences," *IET Radar, Sonar & Navigation*, vol. 11, no. 8, pp. 1321–1332, 2017.

[23] Q. Zhou, Z. Li, J. Shi, and Y. Mao, "Robust cognitive transmit waveform and receive filter design for airborne MIMO radar in signal-dependent clutter environment," *Digital Signal Processing*, vol. 101, pp. 1–15, 2020.

[24] Z. Li, B. Tang, J. Shi, and Q. Zhou, "Maximin joint design of transmit waveform and receive filter bank for MIMO-STAP radar under target uncertainties," *IEEE Signal Processing Letters*, vol. 29, pp. 179–183, 2022.

[25] Z. Li, J. Shi, W. Liu, J. Pan, and B. Li, "Robust joint design of transmit waveform and receive filter for MIMO-STAP radar under target and clutter uncertainties," *IEEE Transactions on Vehicular Technology*, vol. 71, no. 2, pp. 1156–1171, 2022.

[26] O. Mehanna, K. Huang, B. Gopalakrishnan, A. Konar, and N. D. Sidiropoulos, "Feasible point pursuit and successive approximation of non-convex QCQPs," *IEEE Signal Processing Letters*, vol. 22, no. 7, pp. 804–808, 2015.

[27] S. Imani and S. A. Ghorashi, "Sequential quasi-convex-based algorithm for waveform design in colocated multiple-input

multiple-output radars," *IET Signal Processing*, vol. 10, no. 3, pp. 309–317, 2016.

[28] X. Yu, K. Alhujaili, G. Cui, and V. Monga, "MIMO radar waveform design in the presence of multiple targets and practical constraints," *IEEE Transactions on Signal Processing*, vol. 68, pp. 1974–1989, 2020.

[29] M. Grant and S. Boyd, "Cvx package," 2012, http://www.cvxr.com/cvx.r.

[30] S. M. Karbasi, A. Aubry, A. De Maio, and M. H. Bastani, "Robust transmit code and receive filter design for extended targets in clutter," *IEEE Transactions on Signal Processing*, vol. 63, no. 8, pp. 1965–1976, 2015.

[31] Y. Xu, X. Zhao, and Y.-C. Liang, "Robust power control and beamforming in cognitive radio networks: A survey," *IEEE Communications Surveys & Tutorials*, vol. 17, no. 4, pp. 1834–1857, 2015.

[32] Z. Cheng, B. Liao, Z. He, Y. Li, and J. Li, "Spectrally compatible waveform design for MIMO radar in the presence of multiple targets," *IEEE Transactions on Signal Processing*, vol. 66, no. 13, pp. 3543–3555, 2018.

[33] A. Aubry, A. De Maio, M. A. Govoni, and L. Martino, "On the design of multi-spectrally constrained constant modulus radar signals," *IEEE Transactions on Signal Processing*, vol. 68, pp. 2231–2243, 2020.

[34] J. Yang, A. Aubry, A. De Maio, X. Yu, and G. Cui, "Multi-spectrally constrained transceiver design against signal-dependent interference," *IEEE Transactions on Signal Processing*, vol. 70, pp. 1320–1332, 2022.

Hindawi
Mathematical Problems in Engineering
Volume 2022, Article ID 3483778, 10 pages
https://doi.org/10.1155/2022/3483778

Research Article

Joint DOD and DOA Estimation of Bistatic MIMO Radar for Coprime Array Based on Array Elements Interpolation

Zhiyuan You,[1,2] Guoping Hu ,[2] Guimei Zheng,[2] and Hao Zhou[2]

[1]*Graduate College, Air Force Engineering University, Xi'an 710051, China*
[2]*Air and Missile Defense College, Air Force Engineering University, Xi'an 710051, China*

Correspondence should be addressed to Guoping Hu; hgp6068@163.com

Received 25 February 2022; Revised 29 March 2022; Accepted 6 May 2022; Published 21 May 2022

Academic Editor: Ardashir Mohammadzadeh

This paper proposes a method to address the problem of the joint direction of departure (DOD) and direction of arrival (DOA) estimation with augmented coprime array (CPA) bistatic multiple input multiple output (MIMO) radar using interpolating sensors. At first, we deduce the regular pattern of hole positions in the virtual array and interpolate a small number of sensors to augmented CPA to form a partially contiguous virtual array. Then, we use the diversity smoothing algorithm to reconstruct the Toeplitz matrix to obtain a spatial smoothing matrix. Finally, we combine the RD-MUSIC algorithm with the spatial smoothing matrix to estimate the spatial spectrum and achieve automatic matching of DODs and DOAs for the targets. Simulation results clearly illustrate the superiority of the method.

1. Introduction

Direction of arrival (DOA) estimation and Kalman filter algorithm for target tracking [1] are significant areas of research in array signal processing. It can estimate the angular position of different signals in a certain airspace and plays a key role in radar, sonar, and other target detection fields. Since the last century, DOA estimation has gone through three stages, which are beamforming [2], subspace fitting [3–6], and compressed sensing [7], and made a great contribution to the development of the DOA estimation algorithm. Bistatic multiple input multiple output (MIMO) radar has the advantages of waveform diversity [8] and spatial separation; it estimates target angle including DOA and direction of departure (DOD), so the joint estimation of DOD and DOA [9, 10] has also become the focus of research. Although the uniform linear array (ULA) can also solve the related problems of DOA estimation, it still has certain limitations. For example, the number of physical array sensors usually cannot be less than the number of signal sources; otherwise, the estimation accuracy will be badly affected, and thus the degree of freedom (DOF) is limited by physical array elements and other factors [11]. In order to solve these problems, a sparse array is introduced by scholars. The difference between the sparse array [12, 13] and the traditional uniform array mainly includes that the sparse array is formed by setting different interelement spacings in the array to form a sparse array structure, and part of the sparse array has a larger element spacing, so it forms longer virtual array to increase DOF. Coprime array (CPA) [14, 15] has been widely studied by scholars because of its larger element spacing. Thus, the CPA has a low mutual coupling effect and high accuracy of target angle estimation. Moreover, the CPA can construct a longer virtual array through its own differential coarray [16] and use its equivalent vector to estimate DOA. However, although the virtual array formed by CPA has a long virtual array aperture [17], there are array holes that make the virtual array discontinuous, which limits the expansion of DOF. Scholars have conducted a series of studies to settle the question.

A method was advanced to fill the virtual array hole by moving the sparse array in [18], and it used the differential coarray of the original array and the differential coarray of the moved array to form a composite array without holes to estimate DOA effectively. But this method has a small estimated error that originated from array movement distance and signal source movement distance, and its theoretical feasibility is insufficient. Interpolated virtual array element was considered in [19] and solved the problem of virtual array discontinuity caused by virtual array holes, but the method will be affected when there are continuous virtual holes, and its DOF will reduce. Some scholars utilize the virtual array element interpolation theory [19] to the joint estimation of DOD and DOA of bistatic radar targets; this method reduces redundancy of the virtual array and improved DOF and estimated target resolution, but this method required more calculations. Combined with the traditional ESPRIT algorithm [20], Li et al. proposed a joint estimation of target DOD and DOA with bistatic CPA MIMO radar based on virtual aperture expansion in [21]. This method achieved better estimation performance than the traditional method, but it did not use discrete virtual array elements. Recently, a method which interpolated array elements in CPA was proposed to solve the virtual array hole problem in [22], but augmented CPA which the method used cannot nicely reflected the advantage of the interpolated array elements to expand the virtual array aperture. We propose a joint DOD and DOA estimation of bistatic MIMO radar for coprime array based on array elements interpolation. The method uses augmented CPAs as the transmit array and receive array and interpolates a small number of sensors to the particular holes in the virtual array to expand the aperture. Then, the method uses the selection matrix to reconstruct the Toeplitz matrix based on diversity smoothing to estimate the DODs and DOAs of the sources.

The remaining sections are as follows: in Section 2, we reduce the math model of the bistatic CPA MIMO radar. We deduce the law of hole position and propose a diversity smoothing algorithm for reconstructing the Toeplitz matrix to estimate the DODs and DOAs of the targets in Section 3. We perform the same simulation experiments with the proposed method and other methods, which clearly illustrates the superiority of the method in Section 4. Finally, we present conclusions for this paper in Section 5.

Notations: we use italicized boldface characters to represent vectors and matrices in this paper. Superscripts $(.)^T$ and $(.)^H$ represent transpose and conjugate-transpose, respectively, diag $[\cdot]$ denotes diagonal matrix, and $\otimes$ and $\circ$ denote the Kronecker product and the Hadamard product, respectively.

2. Mathematical Model

The conventional bistatic CPA MIMO radar model is presented in Figure 1. Transmit array and receive array in the model are augmented CPA which consists of two uniform linear arrays (ULA). One ULA has $2M_1 - 1$ sensors in transmit array, and red circles represent sensors of subarray 1; another ULA of transmit array has N_1 sensors, and the black circle represents sensors of subarray 2. Similarly, receive array contains two ULAs, which, respectively, have $2M_2 - 1$ sensors and N_2 sensors, where M_1 and N_1 are two coprime integers and M_2 and N_2 are two coprime integers. The number of sensors of arrays are, respectively, $M = 2M_1 + N_1 - 1$ and $N = 2M_2 + N_2 - 1$. The unit interelement spacing of the array is d, which is

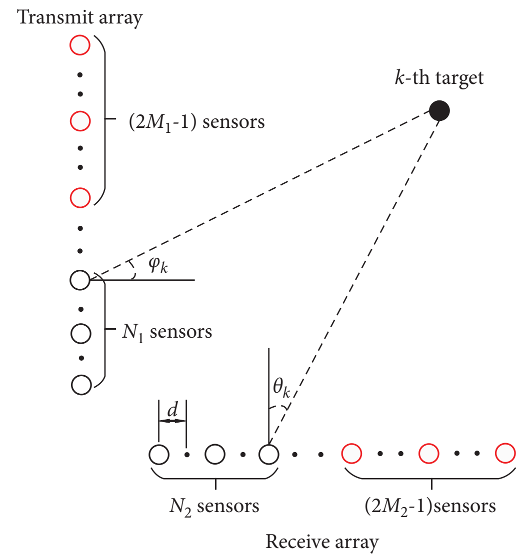

Figure 1: Conventional bistatic CPA MIMO radar model.

the half wavelength $(\lambda/2)$. The sensor positions are given by the following equation:

$$\mathbb{S}_t = \{-mN_1 d | 0 \le m \le 2M_1 - 1\} \cup \{2nM_1 d | 0 \le n \le N_1 - 1\},$$
$$\mathbb{S}_r = \{-mN_2 d | 0 \le m \le 2M_2 - 1\} \cup \{2nM_2 d | 0 \le n \le N_2 - 1\}. \quad (1)$$

Suppose there are K uncorrelated signals in the space, the DOD and DOA of signals are given by $\varphi = [\varphi_1, \varphi_2, \ldots, \varphi_K]$ and $\theta = [\theta_1, \theta_2, \ldots, \theta_K]$. $\mathbf{p}_t = [p_{t1}, p_{t2}, \ldots, p_{tM}]$ represents the position of the sensors in the transmit array, and $\mathbf{p}_r = [p_{r1}, p_{r2}, \ldots, p_{rN}]$ denotes the position of the sensors in the receive array. Set the reflection coefficient of signals as $\mathbf{s}(t) = [s_1(t), s_2(t), \ldots, s_K(t)]^T$, $t = 1, 2, \ldots, L$, and L represents the number of snapshots. The received signal after matched filtering is given by the following equation:

$$\begin{aligned}\mathbf{x}(t) &= [\mathbf{a_t}(\varphi_1) \otimes \mathbf{a_r}(\theta_1), \ldots, \mathbf{a_t}(\varphi_K) \otimes \mathbf{a_r}(\theta_K)]\mathbf{s}(t) + \mathbf{n}(t)\\ &= (\mathbf{A}_t \circ \mathbf{A}_r)\mathbf{s}(t) + \mathbf{n}(t)\\ &= \mathbf{A}\mathbf{s}(t) + \mathbf{n}(t),\end{aligned} \quad (2)$$

where $n(t)$ represents a matrix composed of Gaussian white noise and it follows the Gaussian distribution $\mathbf{n}(t) \sim (0, \sigma^2)$. $\mathbf{A}_t$ and $\mathbf{A}_r$ are also given by the following equation:

$$\begin{aligned}\mathbf{A}_r &= [\mathbf{a}_r(\theta_1), \mathbf{a}_r(\theta_2), \ldots, \mathbf{a_r}(\theta_k), \ldots, \mathbf{a}_r(\theta_K)],\\ \mathbf{A}_t &= [\mathbf{a}_t(\varphi_1), \mathbf{a}_t(\varphi_2), \ldots, \mathbf{a_t}(\varphi_k), \ldots, \mathbf{a}_t(\varphi_K)],\end{aligned} \quad (3)$$

where $\mathbf{a_t}(\varphi_k)$ and $\mathbf{a_r}(\theta_k)$, respectively, denote manifold matrices, and they are given by the following equation:

$$\begin{aligned}\mathbf{a}_t(\varphi_k) &= \left[e^{-j(2\pi/\lambda)p_{t1}\sin\varphi_k}, \ldots, e^{-j(2\pi/\lambda)p_{tM}\sin\varphi_k}\right]^T,\\ \mathbf{a}_r(\theta_k) &= \left[e^{-j(2\pi/\lambda)p_{r1}\sin\theta_k}, \ldots, e^{-j(2\pi/\lambda)p_{rN}\sin\theta_k}\right]^T.\end{aligned} \quad (4)$$

Therefore, the covariance matrix of the received signal $\mathbf{R}$ is given by the following equation:

$$\mathbf{R} = E\left[\mathbf{x}(t)\mathbf{x}^H(t)\right] = \mathbf{A}\mathbf{R}_s\mathbf{A}^H + \sigma_n^2\mathbf{I}_{MN}, \quad (5)$$

where $\mathbf{I}_{MN}$ represents an $MN \times MN$ dimensional identity matrix and $\mathbf{R}_s$ denotes the covariance matrix of the received target.

$$\mathbf{R}_s = E\left[\mathbf{s}(t)\mathbf{s}^H(t)\right] = \mathrm{diag}\left[\sigma_1^2, \sigma_2^2, \ldots, \sigma_k^2, \ldots, \sigma_K^2\right], \quad (6)$$

where σ_k^2 represents the power of the kth target signal.

3. Joint Diversity Smoothing DOD and DOA Estimation Algorithm Based on Interpolated Sensors

3.1. Expansion of Virtual Array by Interpolating Sensors to CPA Holes. In this section, we will interpolate sensors to CPA holes to expand a longer virtual array aperture and then we can obtain a new equivalent vector to execute transmit-receive diversity smoothing. Assume transmit array and receive array are identical augmented CPA, and taking transmit array as an example, sensors distribution is illustrated in Figure 2.

The virtual array is formed by the sum-difference array of CPA, and the position of virtual sensors $\mathbb{S}_c$ is given by the following equation:

$$\begin{aligned}\mathbb{S}_c &= \left\{S_c | S_c = S_{ct} + S_{cr} - \left(\widetilde{S}_{ct} + \widetilde{S}_{cr}\right), S_{ct}, \widetilde{S}_{ct} \in \mathbb{S}_t, S_{cr}, \widetilde{S}_{cr} \in \mathbb{S}_r\right\} \\ &= \left\{S_c | S_c = \left(S_{ct} - \widetilde{S}_{ct}\right) + \left(S_{cr} - \widetilde{S}_{cr}\right), S_{ct}, \widetilde{S}_{ct} \in \mathbb{S}_t, S_{cr}, \widetilde{S}_{cr} \in \mathbb{S}_r\right\}.\end{aligned} \quad (7)$$

According to (8), the virtual sensors are only generated by the difference coarray of transmit array and the difference coarray of receive array when DOD and DOA are estimated, respectively. Therefore, $(S_{ct} - \widetilde{S}_{ct})$ corresponds to parameter φ_k and $(S_{cr} - \widetilde{S}_{cr})$ corresponds to parameter θ_k.

The position of the virtual sensors that are formed by the difference coarray of transmit array is given by the following equation:

$$\begin{aligned}\mathbb{S}_{td} = \{S_{td} | S_{td} = \ &\pm (M_1 nd + N_1 md), 0 \le m \le 2M_1 \\ &- 1, 0 \le n \le N_1 - 1\},\end{aligned} \quad (8)$$

where the value range of $\mathbb{S}_{td}$ is $[-(3M_1N_1 - M_1 - N_1), 3M_1N_1 - M_1 - N_1]$.

Similarly, the position of the virtual sensors that are formed by the difference coarray of receive array is given by the following equation:

$$\begin{aligned}\mathbb{S}_{rd} = \{S_{rd} | S_{rd} = \ &\pm (M_2 nd + N_2 md), 0 \le m \le 2M_2 \\ &- 1, 0 \le n \le N_2 - 1\},\end{aligned} \quad (9)$$

where the value range of $\mathbb{S}_{rd}$ is $[-(3M_2N_2 - M_2 - N_2), 3M_2N_2 - M_2 - N_2]$.

For transmit array, M_1 and M_2 can determine the distribution of the virtual sensors and the length of the virtual array aperture, and the distribution of virtual sensors that are formed by augmented CPA is shown in Figure 3.

In Figure 3, black filled circles represent virtual sensors and dotted circles represent virtual holes. Although augmented

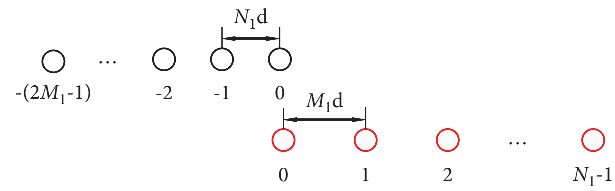

Figure 2: Sensors distribution of augmented CPA.

CPA can form more virtual sensors than traditional CPA, some virtual holes are located next to the center point. Therefore, other continuous virtual sensors cannot form a virtual array with a larger aperture.

With the purpose of settling the question, we present a method that utilizes a small number of sensors to interpolate a part of virtual holes. The originally discontinuous virtual array will become continuous to achieve more DOF.

We can know a special kind of holes next to the center point in Figure 3 and call them central virtual holes. Central virtual holes are continuous virtual holes which locate next to the center point. When $M_1 = 2$ and $M_2 = 3$, there are two central virtual holes in the virtual array; when $M_1 = 3$ and $M_2 = 4$, there are four central virtual holes in the virtual array; and when $M_1 = 3$ and $M_2 = 5$, there are four central virtual holes in the virtual array.

Assume we use sensors to interpolate the virtual central holes where next to the center point completely. Then, a new distribution of virtual sensors emerges in Figure 4.

From Figure 4, black filled circles represent virtual sensors, dotted circles represent virtual holes, red filled circles represent sensors, and red circles represent new formed virtual sensors. We found that we only need to interpolate the virtual holes located next to the center point to make the virtual array continuous. For example, when $M_1 = 3$ and $M_2 = 4$, we use two sensors to interpolate the virtual central holes which are located in {1d,2d}. Then, the array can form additional new virtual sensors which are located in {−1d,−2d,±5d}. Most of the original virtual holes are interpolated. Comparing Figure 3 with Figure 4, it can be found that the interpolated virtual array is a continuous virtual array that all the central virtual holes are replaced with sensors or new virtual sensors, and the DOF is 47. Therefore, we deduce the number of central virtual holes and DOF for different augmented CPAs from continuous experiments and find that the number of virtual holes to be interpolated is only related to M_1. The derived regular pattern and formulas are shown in Table 1.

In general, we interpolate $(M_1 - 1)$ sensors into the virtual holes which located next to the center point, the original virtual array becomes continuous, virtual array apertures become larger to $(4M_1N_1 - 1)$, and DOF also becomes larger to $(4M_1N_1 - 1)$.

3.2. Reconstructing Toeplitz Matrix Algorithm Based on Diversity Smoothing. In recent years, scholars have proposed some spatial smoothing algorithms for bistatic radars in [23–25]. This paper chooses an algorithm that reconstructs the Toeplitz matrix based on diversity smoothing.

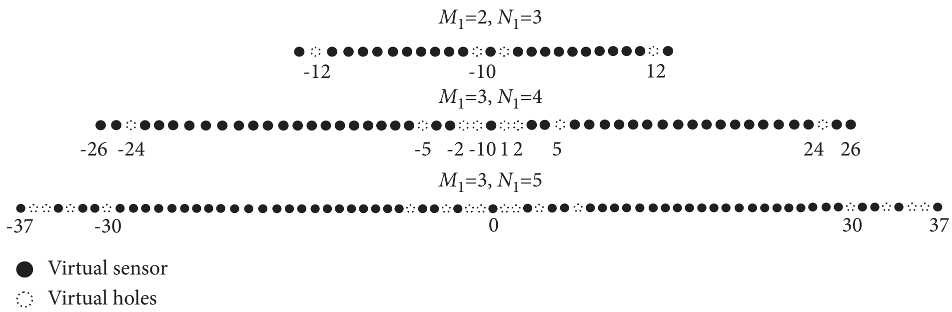

Figure 3: Distribution of virtual sensors and virtual holes.

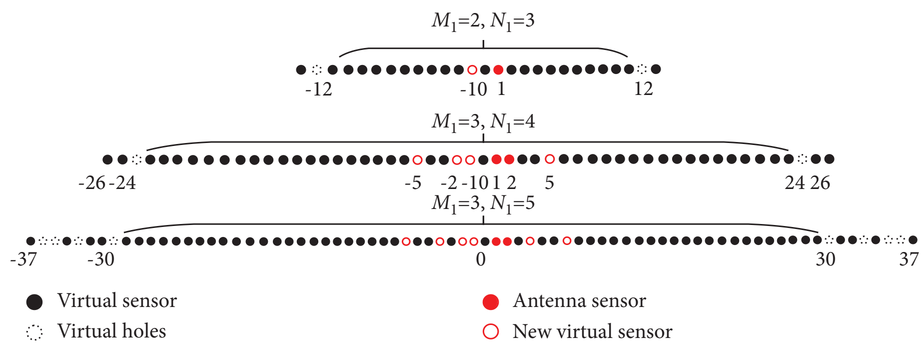

Figure 4: The new distribution of virtual array after interpolating sensors.

Table 1: Number of elements for augmented CPA.

	M_1	N_1	M	H_s	H_f	$\widetilde{M}$	DOF
$N_1 = M_1 + 1$	2	3	6	2	1	23	23
	3	4	9	4	2	47	47
	4	5	12	6	3	79	79
	...	...	...	...	...	...	...
$N1 = M_1 + 2$	3	5	10	4	3	59	59
	5	7	16	8	4	139	139
	7	9	22	12	6	251	251
	...	...	...	...	...	...	...
$N_1 = M_1 + 3$	4	7	14	6	3	111	111
	5	8	17	8	4	159	159
	7	10	23	12	6	279	279
	...	...	...	...	...	...	...
$N_1 = \mathrm{M}_1 + L$	M_1	N_1	$2M_1 + N_1 - 1$	$2(M_1 - 1)$	$M_1 - 1$	$4M_1N_1 - 1$	$4M_1N_1 - 1$

M denotes the number of array sensors, H_s denotes the number of central virtual holes located next to the center point, H_f denotes the number of interpolated sensors, $\widetilde{M}$ denotes the number of continuous virtual sensors, and DOF denotes the DOF after interpolating the holes.

After the sensors shave been interpolated, there are $\widetilde{M}$ continuous virtual sensors in the virtual array of transmit and $\widetilde{N}$ continuous virtual sensors in the virtual array of receive, and $\mathbf{p}_{\tilde{t}} = [p_{t1}, p_{t2}, \ldots, p_{t\widetilde{M}}]$ denotes the sensors' position in the virtual transmit array and $\mathbf{p}_{\tilde{r}} = [p_{r1}, p_{r2}, \ldots, p_{r\widetilde{N}}]$ denotes the sensors' position in the virtual receive array. Therefore, the steering matrices of transmit and receive virtual array are given by the following equation:

$$\widetilde{A}_{\tilde{t}} = \left[\widetilde{a}_{\tilde{t}}(\varphi_1), \widetilde{a}_{\tilde{t}}(\varphi_2), \ldots, \widetilde{a}_{\tilde{t}}(\varphi_k)\right],$$
$$\widetilde{A}_{\tilde{r}} = \left[\widetilde{a}_{\tilde{r}}(\theta_1), \widetilde{a}_{\tilde{r}}(\theta_2), \ldots, \widetilde{a}_{\tilde{r}}(\theta_k)\right], \tag{10}$$

where $\widetilde{a}_{\tilde{t}}(\varphi_k)$ and $\widetilde{a}_{\tilde{r}}(\theta_k)$, respectively, denote manifold matrices, and they are given by the following equation:

$$\widetilde{a}_{\tilde{t}}(\varphi_k) = \left[e^{-j(2\pi/\lambda)p_{t1}\sin\varphi_k}, \ldots, e^{-j(2\pi/\lambda)p_{t\widetilde{M}}\sin\varphi_k}\right]^T,$$
$$\widetilde{a}_{\tilde{r}}(\theta_k) = \left[e^{-j(2\pi/\lambda)p_{r1}\sin\theta_k}, \ldots, e^{-j(2\pi/\lambda)p_{r\widetilde{N}}\sin\theta_k}\right]^T. \tag{11}$$

A new covariance matrix $\widetilde{R}$ of the received signal can be formed by processing continuous virtual sensors. However, the ideal $\widetilde{R}$ is hard to get in practice, so $\widehat{R}$ is usually estimated by using L available snapshots and it is given by the following equation:

$$\widehat{R} = \frac{1}{L}\sum_{i=1}^{L}\widehat{x}(t)\widehat{x}^{H}(t), \tag{12}$$

where $\widehat{x}(t)$ is the new received signal of the virtual array.

The new covariance matrix is now vectorized to obtain a new equivalent vector as follows:

$$\widetilde{r} = \widetilde{A}\mathbf{p} + \sigma_n^2\widetilde{i} = \left(\widetilde{A}_t \circ \widetilde{A}_r\right)\mathbf{p} + \sigma_n^2\widetilde{i}, \tag{13}$$

where $\mathbf{p} = [\sigma_1^2, \sigma_2^2, \ldots, \sigma_K^2]$ and $\widetilde{i}$ is a $(\widetilde{M}\widetilde{N} \times 1)$ vector whose elements are all zeros except for the $(\widetilde{M}\widetilde{N} + 1)/2$th row.

In fact, we regard vector $\widetilde{r}$ as the received signal of a single snapshot in bistatic MIMO radar. According to the principles of spatial smoothing algorithms, the number of smoothing times should be no less than the number of overlapping subarrays to form a full rank covariance matrix. Since the number of virtual sensors is always an odd number, the best smoothing results are achieved when the number of smoothing times is equal to the number of overlapping subarrays. Therefore, we divide the virtual array of transmit into M_s overlapping subarrays to carry out M_s smoothing and divide the virtual array of receive into N_s overlapping subarrays to carry out N_s smoothing. Thus, $\widetilde{M} = 2M_s - 1$ and $\widetilde{N} = 2N_s - 1$.

Next, suppose there are two selection matrices $\mathbf{S}_m^t$ and $\mathbf{S}_n^r$ corresponding to the virtual array of transmit and the virtual array of receive, which are given by the following equations:

$$\mathbf{S}_m^t = \left[\mathbf{O}_{M_s\times(M_s-m)}\mathbf{I}_{M_s\times M_s}\mathbf{O}_{M_s\times(m-1)}\right], \tag{14}$$

$$\mathbf{S}_n^r = \left[\mathbf{O}_{N_s\times(N_s-n)}\mathbf{I}_{N_s\times N_s}\mathbf{O}_{N_s\times(n-1)}\right], \tag{15}$$

where $m = 1, \ldots, M_s$ and $n = 1, \ldots, N_s$. $\mathbf{O}_{M_s\times(M_s-m)}$ denote the $M_s \times (M_s - m)$ zero matrix, $\mathbf{I}_{M_s\times M_s}$ denote $M_s \times M_s$ identity matrix, and $\mathbf{O}_{M_s\times(m-1)}$ denote the $M_s \times (m-1)$ zero matrix. $\mathbf{S}_n^r$ is similar.

Utilize selection matrices $\mathbf{S}_m^t$ and $\mathbf{S}_n^r$ to form the transmission smoothing and receiving smoothing on the equivalent vector $\widetilde{r}$. Then, we can change the values of m and n to achieve the smoothing of overlapping subarrays in the virtual array, m and n represent smoothing times. So sub-vector $\widetilde{r}(m,n)$ is given by the following equation:

$$\begin{aligned}\widetilde{r}(m,n) &= \left(\mathbf{S}_m^t \otimes \mathbf{S}_n^r\right)\widetilde{r}\\ &= \left(\mathbf{S}_m^t\widetilde{A}_t\right)\circ\left(\mathbf{S}_n^r\widetilde{A}_r\right)\mathbf{p} + \sigma_n^2\widetilde{i}_{(m,n)}\\ &= \left(\overline{A}_t \circ \overline{A}_r\right)\mathbf{\Psi}_t^{m-1}\mathbf{\Psi}_r^{n-1}\mathbf{p} + \sigma_n^2\widetilde{i}_{(m,n)},\end{aligned} \tag{16}$$

where $\overline{A}_t = \mathbf{S}_1^t\widetilde{A}_t$, $\Psi_t = \mathrm{diag}[e^{-j\pi\sin\varphi_1}, \ldots, e^{-j\pi\sin\varphi_k}]$, $\overline{A}_r = \mathbf{S}_1^r\widetilde{A}_r$, $\Psi_r = \mathrm{diag}[e^{-j\pi\sin\theta_1}, \ldots, e^{-j\pi\sin\theta_k}]$, and $\widetilde{i}_{(m,n)}$ is the corresponding noise vector. The reconstructed Toeplitz matrix is given by the following equation:

$$\begin{aligned}\mathbf{R}_T &= \left[\widetilde{r}_{(1,1)}, \widetilde{r}_{(1,2)}, \ldots, \widetilde{r}_{(1,N_s)}, \widetilde{r}_{(2,1)}, \ldots, \widetilde{r}_{(M_s,N_s)}\right]\\ &= \left(\overline{A}_t \circ \overline{A}_r\right)\mathbf{R}_s\left(\overline{A}_t \circ \overline{A}_r\right)^H + \sigma_n^2\mathbf{I}_{M_sN_s}\\ &= \mathbf{A}_s\mathbf{R}_s\mathbf{A}_s^H + \sigma_n^2\mathbf{I}_{M_sN_s},\end{aligned} \tag{17}$$

where $\mathbf{A}_s$ represents the new steering matrix.

Therefore, the covariance matrix of each sub-array is given by the following equation:

$$\begin{aligned}\overline{R}_{(m,n)} &= \widetilde{r}_{(m,n)}\widetilde{r}_{(m,n)}^H\\ &= \mathbf{A}_s\mathbf{\Psi}_t^{m-1}\mathbf{\Psi}_r^{n-1}\mathbf{p}\mathbf{p}^H\mathbf{\Psi}_t^{1-m}\mathbf{\Psi}_r^{1-n}\mathbf{A}_s^H + \sigma_n^4\widetilde{i}_{(m,n)}\widetilde{i}_{(m,n)}^H\\ &\quad + \sigma_n^2\mathbf{A}_s\mathbf{\Psi}_t^{m-1}\mathbf{\Psi}_r^{n-1}\mathbf{p}\widetilde{i}_{(m,n)}^H + \sigma_n^2\widetilde{i}_{(m,n)}\mathbf{p}^{\mathrm{H}}\mathbf{\Psi}_t^{m-1}\mathbf{\Psi}_r^{n-1}\mathbf{A}_s^H.\end{aligned} \tag{18}$$

The values of m and n are changed to achieve the effect of spatial smoothing in the virtual array and the spatial smoothing algorithm is used to solve the single snapshot problem caused by the vectorized covariance matrix. The spatial smoothing matrix is given by the following equation:

$$\begin{aligned}\overline{R} &= \frac{1}{M_sN_s}\sum_{m=1}^{M_s}\sum_{n=1}^{N_s}\overline{R}_{(m,n)}\\ &= \frac{1}{M_sN_s}\left(\mathbf{A}_s\mathbf{R}_s\mathbf{A}_s^H\mathbf{A}_s\mathbf{R}_s\mathbf{A}_s^H + \sigma_n^4\mathbf{I}_{M_sN_s} + 2\sigma_n^2\mathbf{A}_s\mathbf{R}_s\mathbf{A}_s^H\right).\end{aligned} \tag{19}$$

Through comparison, we find that $\overline{R}$ and Toeplitz matrix $\mathbf{R}_{\mathrm{T}}$ have the same form, so the spatial smoothing matrix $\overline{R}$ is also given by the following equation:

$$\overline{R} = \frac{1}{M_sN_s}\mathbf{R}_T^2. \tag{20}$$

When performing spatial spectrum estimation, we choose the RD-MUSIC algorithm instead of the ESPRIT algorithm. Although we use the ESPRIT algorithm for spatial spectrum estimation to effectively reduce the complexity of the algorithm, the estimated DODs and DOAs of multiple targets need to be matched manually, whereas the RD-MUSIC algorithm can automatically match the DODs and DOAs of targets.

The RD-MUSIC algorithm is combined with $\overline{R}$ to estimate the spatial spectrum, and the spatial spectrum function is given by the following equation:

$$f_{\text{music}} = \frac{1}{\left[\widehat{a}_t(\varphi)\otimes\widehat{a}_r(\theta)\right]^H\mathbf{E}_n\mathbf{E}_n^H\left[\widehat{a}_t(\varphi)\otimes\widehat{a}_r(\theta)\right]}, \tag{21}$$

where $\mathbf{E}_n$ denotes signal subspace of the covariance matrix. $\widehat{a}_t(\theta)\otimes\widehat{a}_r(\theta)$ is also given by the following equation [25]:

$$\widehat{a}_t(\varphi)\otimes\widehat{a}_r(\theta) = \left[\widehat{a}_t(\varphi)\otimes\mathbf{I}_N\right]\widehat{a}_r(\theta). \tag{22}$$

Therefore, the spatial spectrum function is also given by the following equation:

$$\begin{aligned}f_{\text{music}} &= \frac{1}{\widehat{a}_r(\theta)^H\left[\widehat{a}_t(\varphi)\otimes\mathbf{I}_N\right]^H\mathbf{E}_n\mathbf{E}_n^H\left[\widehat{a}_t(\varphi)\otimes\mathbf{I}_N\right]\widehat{a}_r(\theta)}\\ &= \frac{1}{\widehat{a}_r(\theta)^H\mathbf{V}(\varphi)\widehat{a}_r(\theta)},\end{aligned} \tag{23}$$

where $\mathbf{V}(\varphi) = \left[\widehat{a}_t(\varphi)\otimes\mathbf{I}_N\right]^H\mathbf{E}_n\mathbf{E}_n^H\left[\widehat{a}_t(\varphi)\otimes\mathbf{I}_N\right]$. The DOA of the kth signal is given by the following equation:

Input: receive signal: $\mathbf{x}(t) = \mathbf{A}\mathbf{s}(t) + \mathbf{n}(t)$, $t = 1, 2, \ldots, L$;
Output: DODs and DOAs: $\{\widehat{\varphi}_k, \widehat{\theta}_k\}, k = 1, 2, \ldots, K$;
Step:
(1) estimate covariance matrix $\widehat{R}$ based on continuous virtual array as in (12);
(2) build the selection matrix of the transmit array $\mathbf{S}_m^t$ as in (14) and the selection matrix of receive array $\mathbf{S}_n^r$ as in (15);
(3) rebuild a new Toeplitz matrix $\mathbf{R}_T$ as in (17);
(4) form a spatial smoothing matrix $\overline{R}$ as in (18);
(5) utilize the RD-MUSIC algorithm, to estimate DODs and DOAs $\{\widehat{\varphi}_k, \widehat{\theta}_k\}$;

Algorithm 1: Array elements interpolation algorithm.

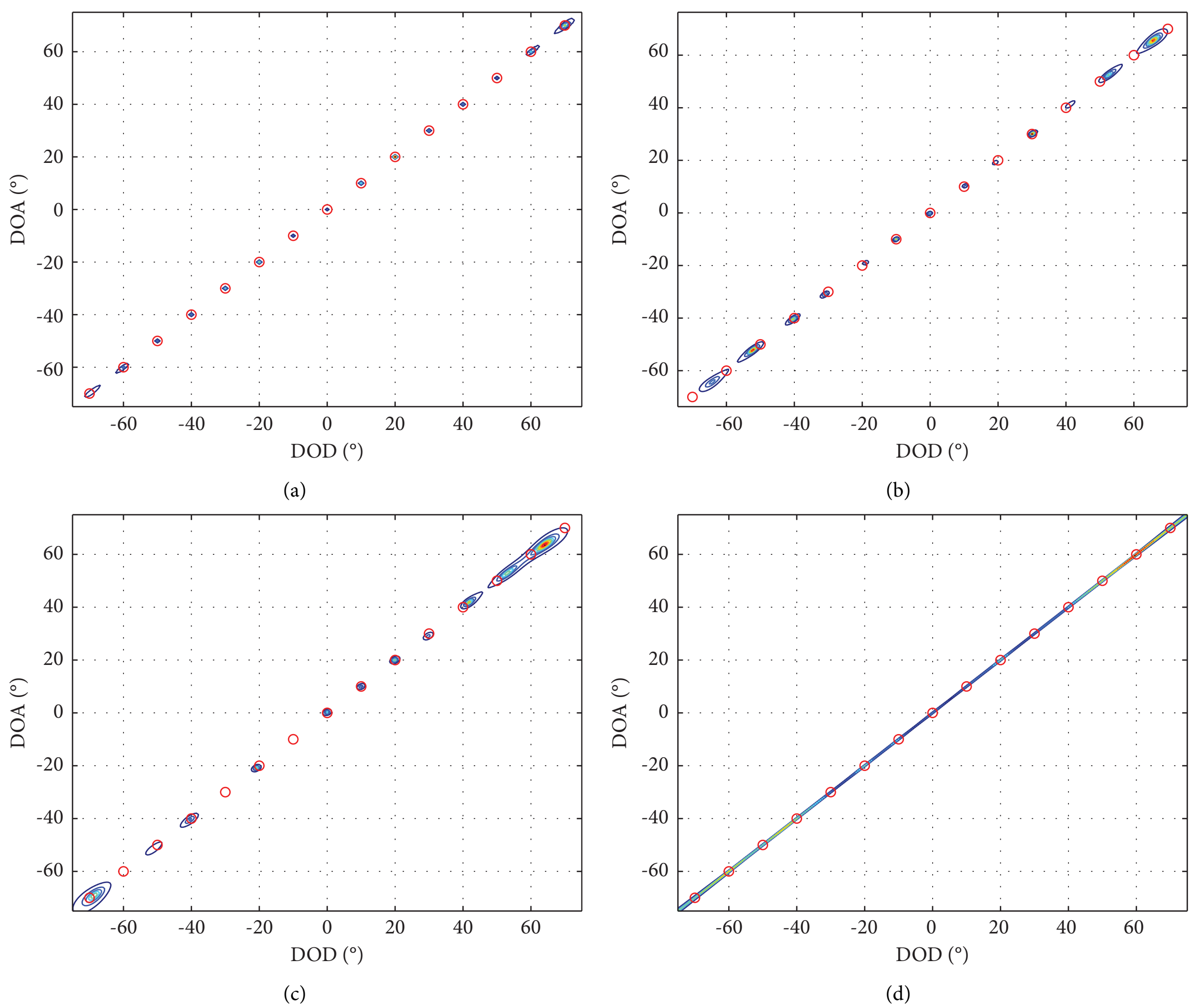

Figure 5: Results of detecting 15 targets by different methods: (a) CPA with DSIAS algorithm, (b) CPA with IVAE algorithm in [19], (c) CPA with CDS algorithm in [21], and (d) ULA with RD-MUSIC algorithm in [26].

$$\widehat{\theta}_k = \arg\min \frac{1}{\mathbf{e}_1^T \mathbf{V}^{-1}(\varphi_k)\mathbf{e}_1} = \arg\max\left(\mathbf{e}_1^T \mathbf{V}^{-1}(\varphi_k)\mathbf{e}_1\right), \quad (24)$$

where $\mathbf{e}_1 = [1, 0, \ldots, 0]^T$.

Similarly, The DOD of the kth signal is given by the following equation:

$$\widehat{\varphi}_k = \arg\min \frac{1}{\mathbf{e}_1^T \mathbf{V}^{-1}(\theta_k)\mathbf{e}_1} = \arg\max\left(\mathbf{e}_1^T \mathbf{V}^{-1}(\theta_k)\mathbf{e}_1\right). \quad (25)$$

The steps of the proposed Algorithm 1 are as follows.

4. Simulation Results

We assume the distance of array sensors $M_1 = M_2 = 2$, $N_1 = N_2 = 3$, the number of transmit and receive array sensors $M = N = 6$, and the original positions of transmit and receive sensors are [−9d, −6d, −3d, 0d, 2d, 4d]. The number of central virtual holes to be interpolated is $H_f = 1$, and the

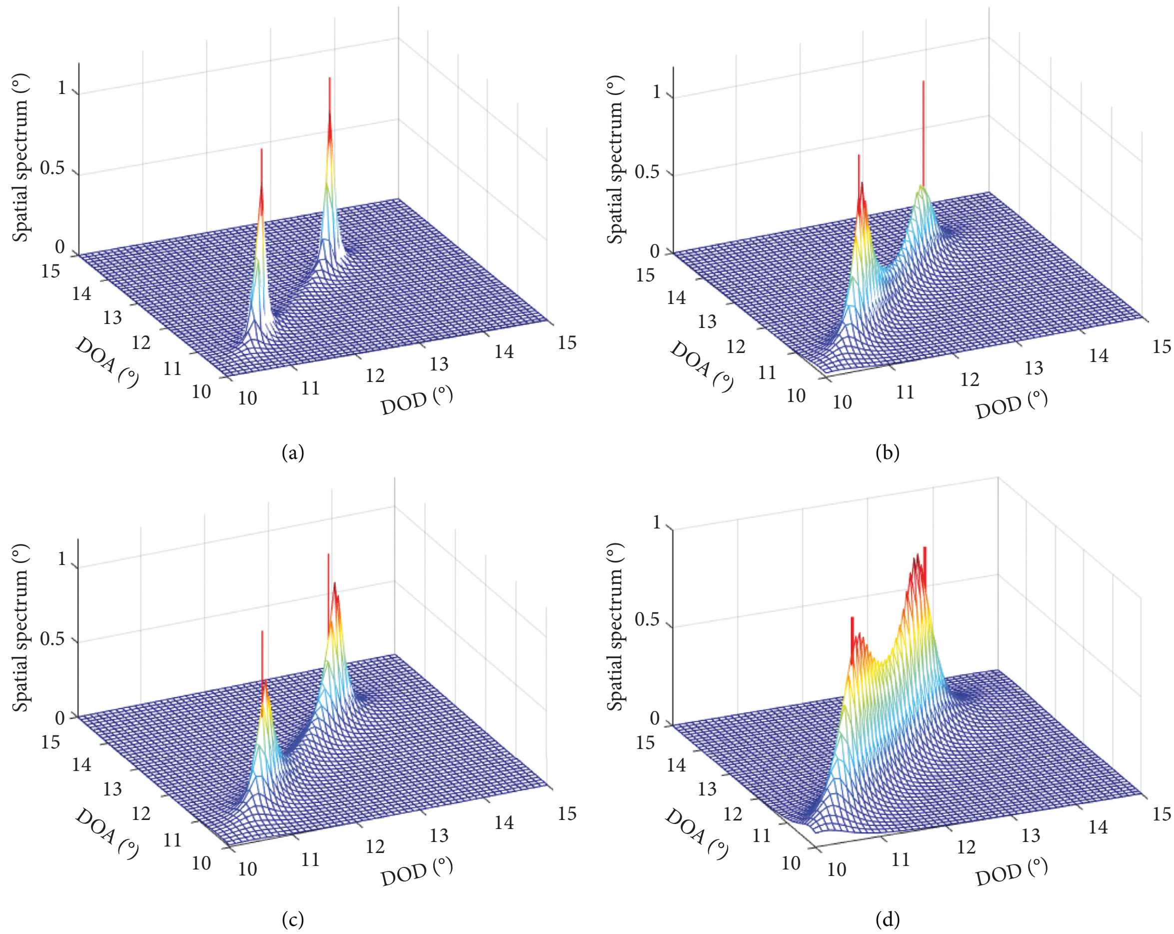

Figure 6: Results of the angular resolution of different methods: (a) CPA with DSIAS algorithm, (b) CPA with IVAE algorithm in [19], (c) CPA with CDS algorithm in [21], and (d) ULA with RD-MUSIC algorithm in [26].

positions of transmit and receive sensors after interpolating the holes are [−9d, −6d, −3d, 0d, 1d, 2d, 4d]. There are continuous virtual sensors in transmit array and receive array, overlapping subarrays of transmit and receive array, and smooth times are $Ms = Ns = 12$. The signals in the simulation are incoherent.

Compare the performance in target estimation of four methods which include diversity smoothing algorithm based on interpolating sensors (DSIAS) in this article, interpolation virtual array element algorithm (IVAE) in [19], conventional CPA diversity smoothing algorithm (CDS) in [21], and conventional ULA RD-MUSIC algorithm in [26]. It includes three specific simulation experiments, namely, target number detection and angular resolution. In the simulation of root mean square error (RMSE), we not only compared the above-given methods, we also added a unitary dual-resolution ESPRIT (U-ESPRIT) method [27] to the comparative simulation.

4.1. Number of Detectable Targets. In this part, the signal-to-noise ratio (SNR) is set as 10 dB and the number of snapshots is set as 200. There are 15 signal targets distributed over the range [−70°, 70°], where located at $\varphi = [-70^\circ, -60^\circ, -50^\circ, -40^\circ, -30^\circ, -20^\circ, -10^\circ, 0^\circ, 10^\circ, 20^\circ, 30^\circ, 40^\circ, 50^\circ, 60^\circ, 70^\circ]$ and $\theta = [-70^\circ, -60^\circ, -50^\circ, -40^\circ, -30^\circ, -20^\circ, -10^\circ, 0^\circ, 10^\circ, 20^\circ, 30^\circ, 40^\circ, 50^\circ, 60^\circ, 70^\circ]$. Figure 5 shows the results of DOD and DOA joint estimation of targets. The four pictures in Figure 5 represent the algorithms in this article, [18, 20], and [25], respectively. As shown in Figure 5, it shows the contour map of the spatial spectrum peak, red circles represent the true direction of 15 targets and the spectral peak contour represents the estimated direction of 15 targets. The spectral peak contour completely overlaps in the red circle in Figure 5(a), so the DSIAS algorithm can accurately estimate 15 targets. Other methods' spectral peak contours do not overlap completely in the red circle. The DSIAS algorithm is better than other methods for a number of detectable targets.

4.2. Angular Resolution. In this part, with the purpose of comparing the performance of the four algorithms in angular resolution, assume that the SNR is 10 dB and the number of snapshots is 200. Figure 6 shows situations of the angular resolution comparison of different algorithms. The position of two adjacent targets are $(\varphi_1, \theta_1) = (11^\circ, 11^\circ)$ and $(\varphi_2, \theta_2) = (13^\circ, 13^\circ)$, and the red line denotes the real target's direction. From the simulation results, we can also see that the MIMO radar which uses the DSIAS algorithm can estimate the targets well under the condition of two targets

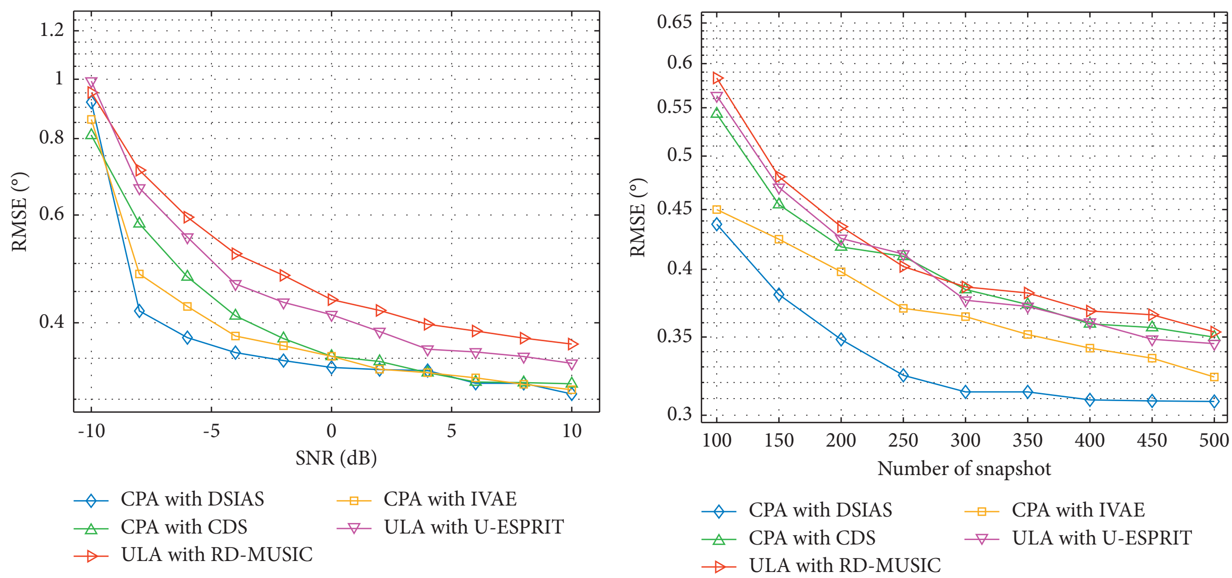

(a) (b)

Figure 7: RMSE versus SNR and number of snapshots for different methods (two targets): (a) RMSE versus SNR for different methods and (b) RMSE versus a number of snapshots for different methods.

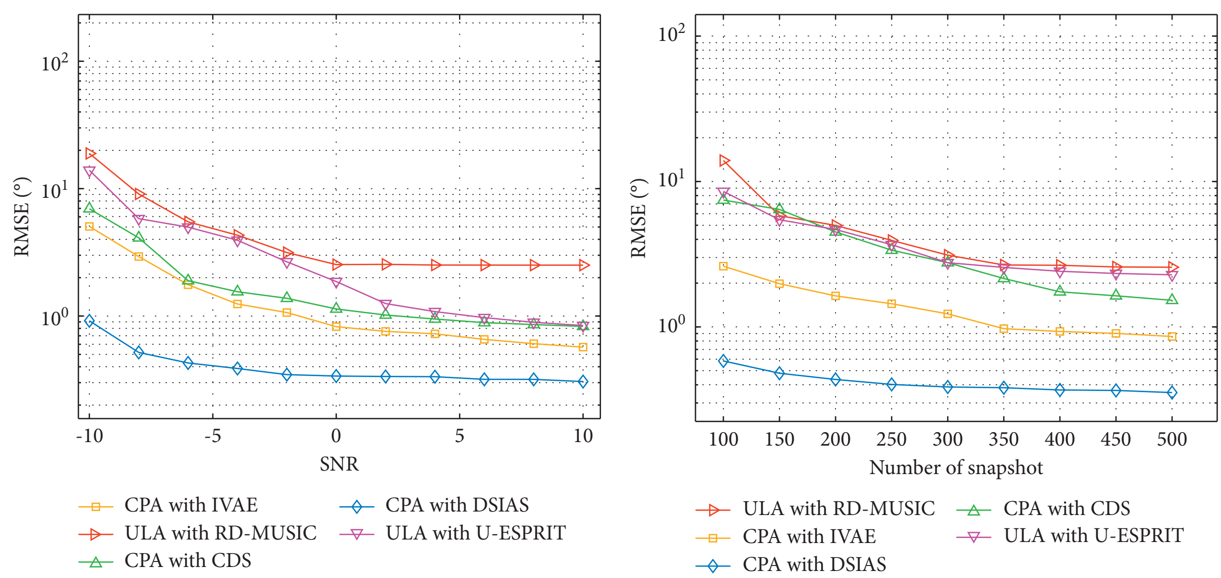

(a) (b)

Figure 8: RMSE versus SNR and number of snapshots for different methods (four targets): (a) RMSE versus SNR for different methods and (b) RMSE versus a number of snapshots for different methods.

close to each other, and the other three algorithms cannot accurately distinguish two similar targets.

4.3. Root Mean Square Error (RMSE). We compare the RMSEs of different algorithms. RMSE is a common standard that reflects the accuracy of angle estimation, and the average RMSE is defined by the following equation:

$$\mathrm{RMSE} = \sqrt{\frac{1}{2 \times QK} \sum_{i=1}^{Q} \sum_{k=1}^{K} \left[\left(\widehat{\varphi}_k^i - \varphi_k \right)^2 + \left(\widehat{\theta}_k^i - \theta_k \right)^2 \right]}, \quad (26)$$

where Q denotes Monte Carlo simulation times, K denotes the number of targets, and $(\widehat{\varphi}_k^i, \widehat{\theta}_k^i)$ denotes the joint estimated DOD and DOA of the kth target for the ith Monte Carlo simulation, $i = 1,2, \ldots, Q$. Estimation number of targets will affect the estimation accuracy. In order to reflect the comprehensiveness of the simulation results, we carried out simulation experiments for two targets and four targets, respectively, and the results of the simulation experiments are shown in Figures 7 and 8.

Figure 7 shows the relationship of RMSE with SNR and the number of snapshots under the condition of detecting two targets, and the targets locate at $(\varphi_1, \theta_1) = (10^\circ, 15^\circ)$, $(\varphi_2, \theta_2) = (20^\circ, 25^\circ)$. Figure 7(a) depicts the variation of the RMSE curve with SNR, where the number of snapshots is set as 200. The DSIAS algorithm has a higher estimation accuracy than other methods at low SNR but has similar performance with the other two methods [19, 21] at high SNR. Figure 7(b) depicts the variation of the RMSE curve with a number of snapshots, where the SNR is set as 10. The DSIAS algorithm has high estimation accuracy at a different number of snapshots.

As shown in Figure 7, the accuracy of all four algorithms is high when estimating two target angles, and the estimation accuracy of the DSIAS algorithm proposed in this paper is only slightly higher than the others. Figure 8 presents the relationship of RMSE with SNR and the number of snapshots under the condition of detecting four targets, and the targets locate at $(\varphi_1, \theta_1) = (10^\circ, 15^\circ)$, $(\varphi_2, \theta_2) = (20^\circ, 25^\circ)$, $(\varphi_3, \theta_3) = (30^\circ, 35^\circ)$, and $(\varphi_4, \theta_4) = (40^\circ, 45^\circ)$. Figure 8(a) depicts the variation of the RMSE curve with SNR, where the number of snapshots is set as 200. In contrast to the previous experiments, the DSIAS algorithm clearly performs better than other methods in estimation accuracy. Figure 8(b) depicts the variation of the RMSE curve with a number of snapshots, where the SNR is 10. It can be found that the DSIAS algorithm estimates more targets with greater accuracy by comparing two experiments which detects a different number of targets.

5. Conclusions

We propose a joint estimation of the DOD and DOA method that interpolate a small number of sensors to a specific location in an augmented CPA virtual array. The method can expand the aperture of the virtual array and maintains the maximum DOF of augmented CPA despite the virtual holes which cannot be exploited in the virtual array. Meanwhile, we reconstructed the Toeplitz matrix based on diversity smoothing to obtain a spatial smoothing matrix. Finally, we combined the RD-MUSIC algorithm with the spatial smoothing matrix to estimate the spatial spectrum and accurately estimate the DOD and DOA of the targets. Simulation results illustrate the proposed method has better performance than other methods.

Data Availability

The data used to support the findings of this study are available from the corresponding author upon reasonable request and with permission from the funders.

Conflicts of Interest

The authors declare that they have no conflicts of interest.

Acknowledgments

This study was supported by the National Natural Science Foundation of China under Grant No. 62071476.

References

[1] S. N. Qasem, A. Ahmadian, A. Mohammadzadeh, and S. B. Rathinasamy, "A type-3 logic fuzzy system: optimized by a correntropy based Kalman filter with adaptive fuzzy kernel size," *Information Sciences*, vol. 572, no. 3, pp. 424–443, 2021.

[2] J. Capon, "High-resolution frequency-wavenumber spectrum analysis," *Proceedings of the IEEE*, vol. 57, no. 8, pp. 1408–1418, 1969.

[3] R. Schmidt, "Multiple emitter location and signal parameter estimation," *IEEE Transactions on Antennas and Propagation*, vol. 34, no. 3, pp. 276–280, 1986.

[4] R. Roy and T. Kailath, "ESPRIT-Estimation of signal parameters via rotational invariance techniques," *IEEE Transactions on Acoustics, Speech, & Signal Processing*, vol. 37, no. 7, pp. 984–995, 1989.

[5] I. Ziskind and M. Wax, "Maximum Likelihood localization of multiple sources by alternating projection," *IEEE Transactions on Acoustics, Speech, & Signal Processing*, vol. 36, no. 10, pp. 1553–1560, 1988.

[6] M. Viberg, B. Ottersten, and T. Kailath, "Detection and estimation in sensor arrays using weighted subspace fitting," *IEEE Transactions on Signal Processing*, vol. 39, no. 11, pp. 2436–2449, 1991.

[7] D. L. Donoho, "Compressed sensing," *IEEE Transactions on Information Theory*, vol. 52, no. 4, pp. 1289–1306, 2006.

[8] P. Gong, Z. Shao, G. Tu, and Q. Chen, "Transmit beampattern design based on convex optimization for MIMO radar systems," *Signal Processing*, vol. 94, no. 6, pp. 195–201, 2014.

[9] D. Oh, Y. Li, J. Khodjaev, J. W. Chong, and J. H. Lee, "Joint estimation of direction of departure and direction of arrival for multiple-input multiple-output radar based on improved joint ESPRIT method," *IET Radar, Sonar & Navigation*, vol. 9, no. 3, pp. 308–317, 2015.

[10] T.-Q. Xia, "Joint diagonalization based DOD and DOA estimation for bistatic MIMO radar," *Signal Processing*, vol. 108, no. mar, pp. 159–166, 2015.

[11] B. Yao, Z. Dong, W. Zhang, and W. Q. Wang, "Degree-of-Freedom strengthened cascade array for DOD-DOA estimation in MIMO array systems," *Sensors*, vol. 18, no. 5, p. 1557, 2018.

[12] A. Moffet, "Minimum-redundancy linear arrays," *IEEE Transactions on Antennas and Propagation*, vol. 16, no. 2, pp. 172–175, 1968.

[13] P. Pal and P. P. Vaidyanathan, "Nested arrays: a novel approach to array processing with enhanced degrees of freedom," *IEEE Transactions on Signal Processing*, vol. 58, no. 8, pp. 4167–4181, 2010.

[14] P. P. Vaidyanathan and P. Pal, "Sparse sensing with co-prime samplers and arrays," *IEEE Transactions on Signal Processing*, vol. 59, no. 2, pp. 573–586, 2011.

[15] P. P. Vaidyanathan and P. Pal, "Sparse sensing with coprime arrays," in *Proceedings of the 44th Asilomar Conf. Signals*, pp. 1405–1409, Syst. Comput, Pacific Grove, CA, USA, November. 2010.

[16] W. Zheng, X. Zhang, and J. Shi, "Sparse extension array geometry for DOA estimation with nested MIMO radar," *IEEE Access*, vol. 5, pp. 9580–9586, 2017.

[17] B. Jiu, H. Liu, X. Wang, and L. Y. B. Zhang, "Knowledge-based spatial-temporal hierarchical MIMO radar waveform design method for target detection in heterogeneous clutter zone," *IEEE Transactions on Signal Processing*, vol. 63, no. 3, pp. 543–554, 2015.

[18] G. Qin, M. G. Amin, and Y. D. Zhang, "DOA estimation exploiting sparse array motions," *IEEE Transactions on Signal Processing*, vol. 67, no. 11, pp. 3013–3027, 2019.
[19] C. Zhou, Y. Gu, X. Fan, and Z. G. Y. D. Shi, "Direction-of-Arrival estimation for coprime array via virtual array interpolation," *IEEE Transactions on Signal Processing*, vol. 66, no. 22, pp. 5956–5971, 2018.
[20] M. Haardt, M. D. Zoltowski, C. P. Mathews, and J. Nossek, "2D unitary ESPRIT for efficient 2D parameter estimation," in *Proceedings of the 1995 International Conference on Acoustics, Speech, and Signal Processing*, pp. 2096–2099, IEEE, Detroit, MI, USA, May, 1995.
[21] J. Li, X. Zhang, and D. Jiang, "DOD and DOA estimation for bistatic coprime MIMO radar based on combined ESPRIT," *IEEE* in *Proceedings of the 2016 CIE International Conference on Radar*, vol. 05, pp. 10–13, Guangzhou, China, Octobar, 2016.
[22] G. Yu, "Algorithm to estimate direction of arrival with interpolated array elements for coprime array holes," *Mathematical Problems in Engineering*, vol. 2020, Article ID 1429628, 7 pages, 2020.
[23] F. Wen, J. Shi, and Z. Zhang, "Generalized spatial smoothing in bistatic EMVS-MIMO radar," *Signal Processing*, vol. 193, Article ID 108406, 2022.
[24] J. Shi, Z. Yang, and Y. Liu, "On parameter identifiability of diversity-smoothing-based MIMO radar," *IEEE Transactions on Aerospace and Electronic Systems*, p. 1, 2021.
[25] X. Zhang, L. Xu, L. Xu, and D. Xu, "Direction of departure (DOD) and direction of arrival (DOA) estimation in MIMO radar with reduced-dimension MUSIC," *IEEE Communications Letters*, vol. 14, no. 12, pp. 1161–1163, 2010.
[26] M. Jin, G. Liao, and J. Li, "Joint DOD and DOA estimation for bistatic MIMO radar," *Signal Processing*, vol. 89, no. 2, pp. 244–251, 2009.
[27] G. Zheng and B. Chen, "Unitary dual-resolution ESPRIT for joint DOD and DOA estimation in bistatic MIMO radar," *Multidimensional Systems and Signal Processing*, vol. 26, 2015.